Simulating feedback from Active Galactic Nuclei in galaxies, groups and clusters

A THESIS SUBMITTED TO THE UNIVERSITY OF MANCHESTER
FOR THE DEGREE OF

DOCTOR OF PHILOSOPHY

IN THE FACULTY OF ENGINEERING AND PHYSICAL SCIENCES

Richard D. A. Newton

2013

SCHOOL OF PHYSICS AND ASTRONOMY
JODRELL BANK CENTRE FOR ASTROPHYSICS
THE UNIVERSITY OF MANCHESTER

Simulating feedback from Active Galactic Nuclei in galaxies, groups & clusters

Doctor of Philosophy, PhD

The University of Manchester

Richard David Andrew Newton

Supervisor:
Dr. Scott T. Kay

September 9, 2013

By performing 542 high resolution *N*-body+SPH simulations of Milky-Way like galaxies, galaxy groups and clusters of galaxies, we investigate the effect of feedback by an active galactic nucleus (AGN) on the evolution of these objects and the black holes they host. We first analyse the role of AGN within isolated Milky-Way like galaxies and major mergers between them, utilising a selection of methods from the literature, additionally including supernova feedback. We find that AGN and supernova feedback are largely independent, and that although current AGN models are highly susceptible to numerical effects, the temperature to which gas is heated is important for determining the impact on the host. Having investigated the effects on galaxy-scales, we then apply the existing AGN models to idealised equilibrium groups and clusters of galaxies and identify the key components of an AGN model which is active in more massive systems. By simulating massive objects we learn of how AGN behave in a radically different regime where they are thought to perform a maintenance role and support the cluster against radiative cooling. Simulations of existing AGN models find that they do not provide sufficient heating to the wider cluster environment to prevent catastrophic cooling, whilst over-heating the galaxy groups. Finally, we develop and introduce an anisotropic feedback method which simulates jet AGN feedback, and a hybrid model which includes both jet and quasar feedback. Such descriptions better match observed phenomenology as they produce spatially concentrated feedback which penetrates its surroundings more effectively, producing jets and bubbles in the cluster gas. Through this work we have found that the inclusion of AGN is a crucial, if challenging, part of a modern galaxy evolution simulation, which is highly sensitive to the modelling of feedback.

Contents

Word Count: 47,562

List of Figures

List of Tables

List of Abbreviations

AMR Adaptive Mesh Refinement

BAO Baryon acoustic oscillation

BH Black Hole

CBE Collisionless Boltzmann Equation

CDM Cold Dark Matter

CIC Cloud-In-Cell

CMB Cosmic Microwave Background

DE Dark Energy

DM Dark Matter

EoS Equation of State

FFT Fast Fourier Transform

GPU Graphical Processing Unit

GRAPE GRAvity PipE

ICM Intra-Cluster Medium

IGM Inter-Galactic Medium

IMF Initial Mass Function

MACHO Massive Compact Halo Object

NGP Nearest Grid Point

P^3M Particle-Particle - Particle-Mesh

PM Particle-Mesh

PP Particle-Particle

PPM Piece-wise Parabolic Method

SHM Simple Harmonic Motion

SNe Supernovae

SNII Type II Supernovae

SPH Smoothed Particle Hydrodynamics

SSP Simple Stellar Population

TSC Triangular-Shaped Cloud

ULIRGs Ultra-Luminious Infra-Red Galaxies

VPH Voronoi Particle Hydrodynamics

WIMP Weakly Interacting Massive Particle

Declarations

No portion of the work referred to in this thesis has been submitted in support of an application for another degree or qualification of this or any other university or other institute of learning.

The author of this thesis (including any appendices and/or schedules to this thesis) owns certain copyright or related rights in it (the "Copyright") and s/he has given The University of Manchester certain rights to use such Copyright, including for administrative purposes.

Copies of this thesis, either in full or in extracts and whether in hard or electronic copy, may be made only in accordance with the Copyright, Designs and Patents Act 1988 (as amended) and regulations issued under it or, where appropriate, in accordance with licensing agreements which the University has from time to time. This page must form part of any such copies made.

The ownership of certain Copyright, patents, designs, trade marks and other intellectual property (the "Intellectual Property") and any reproductions of copyright works in the thesis, for example graphs and tables ("Reproductions"), which may be described in this thesis, may not be owned by the author and may be owned by third parties. Such Intellectual Property and Reproductions cannot and must not be made available for use without the prior written permission of the owner(s) of the relevant Intellectual Property and/or Reproductions.

Further information on the conditions under which disclosure, publication and commercialisation of this thesis, the Copyright and any Intellectual Property and/or Reproductions described in it may take place is available in the University IP Policy (see university website), in any relevant Thesis restriction declarations deposited in the University Library, The University Library's regulations (see university website) and in The University's policy on Presentation of Theses.

Supporting Publications

A study of AGN and supernova feedback in simulations of isolated and merging disc galaxies

Richard D. A. Newton; Scott T. Kay

Monthly Notices of the Royal Astronomical Society 2013; doi: 10.1093/mnras/stt1285
(This work forms the basis of Chapter 3.)

The Author

Originally from Lancaster, the author was schooled in Manchester from a young age. The completion of this thesis sees the fruition of a lifetime ambition to become a physicist.

The author obtained a first class (MPhys) degree in Physics with Astrophysics from the University of Manchester, performing work in his final year with Dr. Richard James and Dr. Scott Kay. Upon the completion of his undergraduate degree he then began a PhD in the summer of 2010 at the Jodrell Bank Centre for Astrophysics (JBCA), a part of the University of Manchester. The work presented in this thesis is the product of his time at the JBCA.

He leaves Jodrell Bank to become the inaugural Jim Buckee Fellow in Astrophysics at the International Centre for Radio Astronomy Research, based in the University of Western Australia.

Acknowledgements

Without my parents I would not have the drive to succeed and the work ethic that has taken me this far, I thank them for everything they have done.

Thank you to Dr. Taylor, my school physics teacher, for sharing his enthusiasm for science with me and answering all the annoying questions I asked of him - there were many.

I owe a lot to Bruno Maffei and Scott Kay for giving me the opportunities to prove myself, first through a summer project and then through my PhD, I could not have gotten this far without them. I am particularly thankful to Scott for all the guidance over the 4 years I've known him, and for his perfectionist approach (it takes one to know one).

A big thank you to everyone at the JBCA, Simon, Jon, Sarah, Jen, Marieke, Adam, Sam, Mel, Chris, Jonny, Abdul et al., for the innumerable interesting, often scientific and usually funny discussions. You helped me keep my sanity when my almost-perfect coding was being more almost than perfect.

Finally, I owe a debt of gratitude to Adam, Neal, Tim and Dan who made sure I grew up to be a semi-normal person. I am particularly indebted to Dan for subjecting himself to proof-reading a chapter of the following dry science.

For Sophie, you have made everything possible.

Space, is big.

Really big.

You just won't believe how vastly

hugely

mindbogglingly big it is.

I mean, you may think it's a long way down the road to the chemist's

but that's just peanuts to space.

DOUGLAS ADAMS

Chapter 1

Introduction

In the begining, there was nothing, which exploded.

SIR TERENCE "TERRY" PRATCHETT

1.1 The standard cosmological model

The current standard picture for the origin of the Universe begins with its formation in a (hot) *Big Bang*, after which it expanded from an incredibly hot, dense state to its current cool and diffuse one. Structures are thought to have been seeded by quantum fluctuations in the early universe, which were enlarged in a period of rapid inflation (enlarged by $\times 10^{26}$ within $10^{-34}\,\mathrm{s}$; see Baumann et al. 2009 for an overview of inflation) before growing as matter cooled and collapsed under gravity. The inflationary Big Bang model alone explains the existence of the Cosmic Microwave Background (CMB), the apparent flatness of the Universe (*the flatness problem*), observed isotropy and homogeneity, the large-scale correlated features of the CMB (*the horizon problem*) and the lack of observed topological defects (*the relic problem*) as well as a range of particle-physics phenomena. The rapid enlargement of quantum fluctuations in the early universe produced a nearly scale-independent field around which structures grew. The Universe may be broadly described as being filled with a mixture of ordinary matter (some of which is now visible as stars and galaxies), a Dark Matter (DM) component, and photons. The ratios of photons and ordinary matter change with time as the Universe cools and atoms form. The various matter components are commonly categorised dynamically as either collisional or collisionless, with the latter experiencing no pressure forces.

The DM component is thought to be composed of an, as yet, undiscovered fundamental particle which interacts solely through gravity. Specifically the paradigm favours *cold*

dark matter meaning that it has no initial velocity at the time of the big bang (see Frenk & White 2012 for an overview). This implies that the fundamental CDM particle has an infinite mass and it therefore decouples and becomes non-relativistic immediately at $t = 0$. An infinite mass would seem an unlikely prospect and is considered an unphysical, but useful, approximation; CDM particle candidates are commonly some form of massive super-symmetric particle or axion, however there remains much uncertainty about its true nature.

As well as the ordinary visible and the more alien DM components of the Universe, there is commonly thought to exist an even more exotic field which acts on large scales to oppose gravity and cause structures to separate, Dark Energy (DE; the simplest model for which was famously represented by Λ in Einstein's field equations, and so the combined model with CDM is often referred to as ΛCDM). That is to say, the mass within the universe slows its rate of expansion, whereas DE accelerates it. During different epochs the evolution of the Universe has been dominated by its different components. Initially photon pressure dominated, the Universe underwent a period of rapid expansion. However, as the Universe expanded, the photon energy density dropped faster than that of non-relativistic matter (due to red-shifting of the light), therefore the Universe transitioned into a matter dominated era where expansion slowed. Current observations (see Section 1.1.1) suggest that we are now entering the era dominated by DE where the rate of expansion increases exponentially.

General relativity tells us that the Universe has a curvature in (at least) a 4D space-time caused by gravity acting on its internal components. The curvature of a universe may be written as having three possible values $k = -1, 0, 1$. If we assume that matter dominates the Universe these values correspond to an *open* universe which evolves into free expansion, a *flat* universe, which slows its expansion over time and a *closed* universe, which eventually shrinks leading to the *Big Crunch*. However, observations indicate (see Section 1.1.1) that matter is not dominant, with the components of the Universe accounting for approximately $1/3$ of the current density and the DE around $2/3$. In this case DE may cause the Universe to continually expand independent of curvature. Indeed, current observations are consistent with $k = 0$ (e.g. Planck Collaboration et al. 2013b).

1.1.1 Observational cosmology and ΛCDM

We now discuss some of the key features of observational cosmology and the main methods in-use for its study, with a particular emphasis on the reasons for favouring a ΛCDM model.

The first evidence for dark matter came from observations of the Coma galaxy cluster

by Zwicky (1933). Zwicky applied the virial theorem (see Binney & Tremaine 1987 for a derivation) to the motions of the galaxies within the cluster and inferred the existence of an unseen matter component contributing to the gravitational potential. Further observations of the rotation curves of galaxies performed by Rubin & Ford (1970), Ostriker et al. (1974) and Einasto et al. (1974) strengthened the case for an unseen component of matter extending around galaxies, although the proposed explanations were not of some exotic particle but rather halos of faint stars and gas clumps respectively (broadly referred to as Massive Compact Halo Objects; MACHOs). Theoretically, the case for the existence of an unseen massive halo around galaxies was made by Ostriker & Peebles (1973), who showed that halos are required to dynamically stabilise observed thin galactic disks against the influence of bars. The cosmological context of these models was realised by White & Rees (1978), who proposed that galaxies form in the gravitational potential of DM structures as gas cools to form stars; this is the basis of the leading galaxy formation scenario in use today (although once again, faint stars were the proposed solution). This work layed the groundwork for the first cosmological simulations of structure growth (Aarseth et al. 1979), followed by those compatible with the modern CDM context performed by Davis et al. (1985).

The 'temperature' of a modern fundamental particle or Weakly Interacting Massive Particle (WIMP) dark matter model is due to the initial velocity field imparted to the particles before the time of decoupling, with more massive particles decoupling sooner. This gives rise to a free streaming length, below which structures are unable to form as the thermal motions of the particles dominate over dynamical effects. The dynamically 'hotter' the dark matter, the larger this length; therefore CDM has a zero free streaming length meaning that it does not inhibit structure growth on any scales. Early measurements of a massive ($30\,\mathrm{eV}$) neutrino motivated early studies to assume that such a particle comprised the unseen DM component of the Universe, and so hot DM was initially favoured. These studies then went on to predict structure formation by fragmentation, in a *top-down* fashion (Frenk & White 2012). This has since been ruled out as the free-streaming length would be so big that the cut-off would already have been observed; leading to acceptance of CDM as the leading paradigm. An intermediate solution in the form of warm dark matter with streaming lengths below galactic scales, however, remains a candidate. This is the focus of much ongoing study, although its simulation is often found to be numerically challenging (e.g. Hahn et al. 2012; Lovell et al. 2012; Benson et al. 2013; Schneider et al. 2013). The ΛCDM paradigm favoured today, gives rise to a picture of massive structures building up over time as smaller ones merge, in a process referred to as *bottom-up* structure growth.

We now move on to briefly summarise some of the techniques currently in use for

observationally characterising the cosmogony of the Universe.

Given a reliable measure of distance to an object, the expansion rate of the Universe may be deduced through the measurement of its redshift. A population of objects at different distances would therefore make it possible to constrain the expansion history of the Universe. Obtaining a reliable measure of distance over the large range of scales necessary is, however, a non-trivial problem in itself; one method involves the use of Cepheid variables. Cepheids are young, bright stars with a well-understood characteristic saw-tooth luminosity curve due to a pulsation of their atmosphere (Freedman et al. 2001). The period of the oscillation is related to the luminosity of the star, and therefore, gives us a method to deduce their distance. However, the method is limited to relatively short distances ($< 30\,\mathrm{Mpc}$) due to their relatively low luminosity. Additional complications arise due to scatter introduced by dust extinction, a metallicity dependence in the pulsation mechanism and crowding effects. (See Di Benedetto 2013 for a recent study of Cepheids for the use of cosmological parameter estimation.) At longer distances ($\sim 400\,\mathrm{Mpc}$; Freedman et al. 2001) the high luminosity and self-similar light curves of type Ia supernovae (SNe) makes them a useful measure of distance by acting as a 'standard candle'. Type Ia supernovae are produced in explosions which produce distinctive light-curves and colours that are correlated with the peak magnitude (see Campbell et al. 2013 for a recent study). The exact process forming the supernovae is still uncertain, however the classical picture is that white dwarf stars exceed the Chandrasekhar mass limit of $1.4\,M_{\odot}$ through accretion from a companion star and undergoes a runaway thermonuclear explosion. By calibrating the luminosity curves of observed SNe Ia to known distances of Cepheid variables residing in the same galaxies (e.g. Sandage et al. 2006) it is possible then to extend our distance measure out to greater distances.

Studying the CMB gives a route to observe primordial fluctuations in the radiation field just after recombination (at $z \sim 1000$). In measuring the CMB we are observing the redshifted photons emitted from the surface of last scattering as the Universe cooled and formed atoms, becoming optically thin. Soon after the CMB was discovered serendipitously by Penzias & Wilson (1965) it was realised that the CMB anisotropies would be a powerful probe of the nature of matter fluctuations in the early Universe and, therefore structure formation (e.g. Peebles 1967 and Silk 1968). The CMB anisotropy provides such a powerful test of cosmological theory, because the signals on different length scales correspond to different effects. On degree scales, the CMB anisotropy is primarily generated by the acoustic oscillations of the primordial plasma in the early universe; this is often regarded as the primary CMB signal. At intermediate angular scales the anisotropy power is damped by photon diffusion during recombination and on much smaller angular scales the signal becomes dominated by effects imprinted on the CMB at low redshift

(so-called secondary anisotropies; see e.g. Aghanim et al. 2008) due to effects such as the SZ effect (Sunyaev & Zeldovich 1970) and weak lensing (Story et al. 2012). (Some of the most important contemporary CMB experiments are described in Bennett et al. 2012, Story et al. 2012 and Planck Collaboration et al. 2013a.)

Baryon Acoustic Oscillations (BAO; Goldberg & Strauss 1998) provide a further tool constraining cosmological parameters through distance measurements. BAO are correlated fluctuations produced by primordial quantum perturbations exciting sound waves in the relativistic plasma soon after the big bang. The over-densities caused by the sound waves cause a clustering of baryonic matter with a characteristic length-scale that is set by the distance a sound wave propagating from a point source at the end of inflation would travel before decoupling shortly after recombination (at the baryon drag epoch; Percival et al. 2010). Therefore BAO provides a 'standard ruler' which may be detected across different redshifts, both by observing the CMB at high-z, and at lower redshifts by observing the large-scale distribution and clustering properties of galaxies, groups and clusters. BAO are therefore a probe of cosmology which lies orthogonal to the line-of-sight and therefore gives constraints complementary to those of SNe Ia and Cepheids.

Combining data from the above methods leads to powerful constraints on the composition, shape, history and fate of the Universe. We now go on to give a brief introduction to some of the relevant theory describing the early universe and the origins of structure formation.

1.1.2 Background cosmological theory

We begin by considering Einstein's General Theory of Relativity under the assumption of the weak Cosmological Principal, *we do not occupy a privileged point in space*, which implies that the universe must be both homogeneous and isotropic. Taken literally this is evidently untrue, but may hold at least on large scales. This assumption implies that the metric may vary only with time, i.e. it must be of the form,

$$\mathrm{d}s^2 = \mathrm{d}t^2 - a^2(t)\mathrm{d}x^2, \tag{1.1}$$

where $a(t)$ is the expansion factor and $x\ (= |\mathbf{x}|)$ is a co-moving distance which is invariant through the expansion of the universe as $\mathbf{r} = a(t)\mathbf{x}$, and correspondingly $\mathbf{v} = (\dot{a}/a)\mathbf{r}$. We note that the expansion rate of the Universe is observable on large distances and is seen to vary as

$$a = \frac{1}{1+z}. \tag{1.2}$$

If the universe is initially perfectly smooth, we may choose an arbitrary point to con-

sider as the centre of a spherical distribution of matter. If we consider the potential of a unit mass in such an expanding universe, the sum of its kinetic and gravitational potential energies are constant[1],

$$\frac{1}{2}v^2 - \frac{GM(r)}{r} = \text{const.} \tag{1.3}$$

Through substitution, for an expanding universe we obtain,

$$\frac{1}{2}\frac{\dot{a}^2}{a^2}r^2 - \frac{4\pi G}{3}\rho r^2 = -\frac{kc^2x^2}{2}, \tag{1.4}$$

where we have set chosen $kc^2x^2/2$ as our constants for simplicity at a later stage. Rearranging gives,

$$\frac{\dot{a}^2}{a^2} = \frac{8\pi G}{3}\rho - \frac{kc^2}{a^2}, \tag{1.5}$$

here we have obtained a form of the Friedmann equation. The equation must be properly derived using general relativity, however this result is exact except for the addition of the Cosmological Constant, Λ, and is alternatively written

$$H^2 = \frac{8\pi G}{3}\rho + \frac{\Lambda}{3} - \frac{kc^2}{a^2}, \tag{1.6}$$

where $H = \dot{a}/a$ is the Hubble parameter (expansion rate). The Friedmann equation describes the evolution of our homogeneous and isotropic universe, relating the internal density, shape and rate of expansion.

Completely specifying the fluid describing matter in a universe requires not only the Friedmann equation but also the fluid equation and an equation of state ($P = P(\rho, s)$ where ρ is the density and s is the specific entropy) to close the system. We obtain the fluid equation by considering a co-moving unit sphere undergoing the global expansion, for which we may write the energy as,

$$U = \frac{4\pi}{3}a^3\rho c^2. \tag{1.7}$$

The change in energy with time is then

$$\frac{\mathrm{d}U}{\mathrm{d}t} = 4\pi a^2\rho c^2\dot{a} + \frac{4\pi}{3}a^3\dot{\rho}c^2, \tag{1.8}$$

and the corresponding change in volume

$$\frac{\mathrm{d}V}{\mathrm{d}t} = 4\pi a^2\dot{a}. \tag{1.9}$$

[1]Now considering the non-relativistic limit, however the result is general.

Using the first law of thermodynamics, $\mathrm{d}U = T\mathrm{d}S - P\mathrm{d}V$, under the assumption that $\mathrm{d}S = 0$ (i.e. the expansion is reversible) we then obtain the fluid equation,

$$\dot{\rho} + 3\frac{\dot{a}}{a}\left(\rho + \frac{P}{c^2}\right) = 0. \tag{1.10}$$

Combining the Friedmann and fluid equations gives us a relationship describing the acceleration of the scale factor, commonly referred to as the acceleration equation,

$$\frac{\ddot{a}}{a} = -\frac{4\pi G}{3}\left(\rho + \frac{3P}{c^2}\right). \tag{1.11}$$

It is useful to define the following quantities in order to simplify future expressions. If we consider the simplifying case of a flat universe with no cosmological constant where $\Lambda = k = 0$ (an *Einstein-de Sitter* universe) we obtain the critical matter density,

$$\rho_{\mathrm{cr}} = \frac{3H^2}{8\pi G}. \tag{1.12}$$

The Friedmann equation at the present day, $z = 0$,

$$H_0^2 = \frac{8\pi G}{3}\rho_0(r) + \frac{\Lambda}{3} - \frac{kc^2}{a^2}, \tag{1.13}$$

may then be written as,

$$H_0^2 = H_0^2\frac{\rho_0}{\rho_{\mathrm{cr},0}} + \frac{\Lambda}{3} - kc^2. \tag{1.14}$$

This may be simplified further by defining the following normalised densities for the various components of the universe,

$$\Omega_{\mathrm{m}} = \frac{\rho_0}{\rho_{\mathrm{cr},0}}, \tag{1.15a}$$

$$\Omega_{\Lambda} = \frac{\Lambda}{3H_0^2}, \tag{1.15b}$$

$$\Omega_{\mathrm{k}} = -\frac{kc^2}{H_0^2}, \tag{1.15c}$$

where $\Omega_{\mathrm{m}} + \Omega_{\Lambda} + \Omega_{\mathrm{k}} = 1$. In the simplified form the Friedmann equation becomes

$$H^2 = H_0^2\left(\Omega_{\mathrm{m}}a^{-3} + \Omega_{\Lambda} + \Omega_{\mathrm{k}}a^{-2}\right), \tag{1.16}$$

$$= H_0^2E^2, \tag{1.17}$$

Table 1.1: Cosmological parameters from the Planck 2013 combined CMB, CMB polarisation, 'highL' and BAO datasets (Planck Collaboration et al. 2013b).

Parameter	Description	Value
$\Omega_{\rm b}h^2$	Baryon fraction	0.02214 ± 0.00024
$\Omega_{\rm c}h^2$	CDM fraction	0.1187 ± 0.0017
τ	Optical depth	0.092 ± 0.013
H_0	Hubble parameter $[\mathrm{Mpc}^{-1}\mathrm{kms}^{-1}]$	67.80 ± 0.77
$n_{\rm s}h^2$	Scalar index	0.9608 ± 0.0054
$\ln(10^{10}A_{\rm s})$	Scalar amplitude	3.091 ± 0.025
Ω_Λ	Dark energy density today	0.692 ± 0.010
σ_8	RMS matter fluctuations today in linear theory	0.826 ± 0.012
$z_{\rm re}$	Redshift at which Universe is half reionized	11.3 ± 1.1
t_0	Age of the Universe today [Gyr]	13.798 ± 0.037
$100\theta_*$	$100\times$ angular size of sound horizon at last scattering	1.04162 ± 0.00056
$r_{\rm drag}$	Comoving size of sound horizon at the drag epoch	147.68 ± 0.45

where $E^2 = (\Omega_{\rm m}a^{-3}+\Omega_\Lambda+\Omega_{\rm k}a^{-2})$. Considering again the simplest case of a flat universe with no cosmological constant ($k = \Lambda = 0$), then we can see from the Friedmann equation that the matter density evolves as

$$\rho(t) = \frac{1}{6\pi G t^2}, \tag{1.18}$$

while the Hubble parameter follows

$$H = \frac{2}{3t}. \tag{1.19}$$

These results show that the matter density in such a universe will decrease with time ($\rho \propto t^{-2}$) as it expands, and that the rate of its expansion too will decay ($\dot{a} \propto t^{-1/3}$).

Observational cosmological parameters

Cosmological models are commonly expressed in terms of 6 core parameters (e.g. Baumann et al. 2009), with additional variables necessary for more exotic models. Of the 6 parameters, $\{\Omega_{\rm b}h^2, \Omega_{\rm c}h^2, H_0, \tau\}$ describe the homogeneous background[2], whilst $\{n_{\rm s}, A_{\rm s}\}$ describe the primordial density fluctuations (Baumann et al. 2009). The most current dataset is commonly referred to as the *Planck Cosmology* (Planck Collaboration et al. 2013b), obtained from the best fit combined parameters derived from a combined dataset of CMB, CMB polarisation, 'highL' datasets and BAO is presented in Table 1.1. We addi-

[2]where $H_0 = 100\,h\,\mathrm{Mpc}^{-1}\mathrm{kms}^{-1}$

tionally include values for some commonly-used cosmological parameters for reference.

1.1.3 Linear structure formation

The growth of early structures are essentially determined by the competing affects of the expansion of the Universe and gravitational collapse of matter. Small over-densities in the nearly-homogeneous early-Universe, seeded by quantum fluctuations and expanded during inflation, collapse under their own gravity and grow to form structures. Dark matter, having no pressure, will collapse most readily at early times and attract baryonic material into the potential well.

The simplest case we may consider is the evolution of matter on large sub-horizon scales, which we may consider to be Newtonian with motion due to the Hubble expansion. However, due to the implicit homogeneity in this system, it would not collapse and form structure. Therefore we consider the next simplest case of a small linear perturbation to the density field. In this regime we may describe growth of fluctuations using a linear approximation and assuming that the gas pressure is negligible compared to its energy density (although the approximation of linearity breaks down at later times as structures grow upon themselves). This allows us to consider both ordinary baryonic and dark matter to be a single fluid described by the pressure-less fluid equation (cf. Equation 1.10)

$$\dot{\rho} + 3H\rho = 0, \tag{1.20}$$

together with the continuity, Euler and Poisson equations

$$\frac{\mathrm{D}\rho}{\mathrm{D}t} + \rho\nabla\cdot\mathbf{v} = 0, \tag{1.21}$$

$$\frac{\mathrm{D}\mathbf{v}}{\mathrm{D}t} + \nabla\phi = 0, \tag{1.22}$$

$$\nabla^2\phi - 4\pi G\rho = 0, \tag{1.23}$$

where ϕ is the gravitational potential and we have used the convective derivative,

$$\frac{\mathrm{D}}{\mathrm{D}t} = \frac{\partial}{\partial t} + (\mathbf{v}\cdot\nabla). \tag{1.24}$$

Considering the growth of structure from fluctuations it is convenient to follow the evolution of *over-densities* as they collapse under self-gravity. The over-density field is defined as

$$\delta(\mathbf{x}, a) = \frac{\rho(\mathbf{x}, a) - \bar{\rho}(a)}{\bar{\rho}(a)}, \tag{1.25}$$

i.e. the fractional excess in matter density compared to the universal mean at that time, $\bar{\rho}(a)$. This in turn leads to a linear modification of the potential field

$$\phi = \phi_0 + \delta\phi. \tag{1.26}$$

As we now allow the fluid to move relative to the background Hubble expansion, i.e. experience a *peculiar* velocity, we must allow for an additional term in the co-moving velocity defined earlier. We now write $\mathbf{v}(= \dot{\mathbf{r}})$ as

$$\mathbf{v}(\mathbf{r}, t) = H(t)\mathbf{r} + a(t)\dot{\mathbf{x}}(\mathbf{r}, t), \tag{1.27}$$

where as before $\mathbf{r} = a\mathbf{x}$ and the new second term (arising from allowing a changing $\mathbf{x}(\mathbf{r}, t)$) gives the peculiar velocity, $\mathbf{u} = a\dot{\mathbf{x}}$. Using the perturbed density field we can obtain the linearised equations of motion, starting by rewriting the equations governing the fluid (Equations 1.21, 1.22 and 1.23) in terms of the evolution of the linear over/under-densities which will seed structure formation. Beginning with the continuity equation, we substitute in Equations 1.26 and 1.25 giving

$$\frac{\mathrm{D}\delta}{\mathrm{D}t} + \nabla_{\mathbf{x}} \cdot [(1 + \delta)\mathbf{v}] = 0, \tag{1.28}$$

where $\nabla_{\mathbf{x}} = (1/a)\,\nabla$ is the co-moving derivative. This may be simplified in the limit of small fluctuations (where $\delta \ll 1$ and $\delta\phi \ll \phi_0$) to

$$\frac{\mathrm{D}\delta}{\mathrm{D}t} + \nabla_{\mathbf{x}} \cdot \mathbf{v} = 0. \tag{1.29}$$

Similarly, the Euler and Poisson equations may be rewritten

$$\ddot{\mathbf{x}} = -2H\dot{\mathbf{x}} - \frac{1}{a^2}\nabla_{\mathbf{x}}\delta\phi = 0, \tag{1.30}$$

$$\nabla^2_{\mathbf{x}}\delta\phi - 4\pi G\bar{\rho}a^2\delta = 0. \tag{1.31}$$

Therefore, assuming the fluctuations are small, Equation 1.30 gives the equation of motion in co-moving coordinates. The first term is known as the *Hubble Drag* and shows that the peculiar velocity decays with the expansion of the universe in the absence of potential fluctuations. The second term is due to the *peculiar gravitational acceleration* ($g \equiv \nabla_{\mathbf{x}}\delta\phi/a$) and corresponds to gravitational collapse. If we consider the simple case when the size of the perturbations tend to zero ($\delta = \delta\phi = 0$) but still allow an evolving co-moving spatial coordinate, i.e. inhomogeneous expansion of the universe, ($\dot{\mathbf{x}} \neq 0$) then

we obtain the solution for the so-called *vortical* modes (vortical with respect to the motion of matter undergoing gravitational collapse, g) for homogeneous universes. However, combining Euler's equation (Equation 1.30) and the continuity equation (Equation 1.29) gives

$$\ddot{\mathbf{x}} + 2H\dot{\mathbf{x}} = 0, \tag{1.32a}$$

$$\Rightarrow a^2\ddot{\mathbf{x}} + 2a\dot{a}\dot{\mathbf{x}} = 0, \tag{1.32b}$$

$$\Rightarrow \frac{\mathrm{D}}{\mathrm{D}t}(a^2\dot{\mathbf{x}}) = 0, \tag{1.32c}$$

$$\Rightarrow \dot{\mathbf{x}}(t) \propto \frac{1}{a^2}, \tag{1.32d}$$

which shows that the vortical modes, if present in the early universe, will decay with time. The evolution of the density contrast due to the *longitudinal* modes may be obtained by taking the divergence of Euler's equation and substituting in the continuity and Poisson's (Equation 1.31) equations

$$\ddot{\delta} + 2H\dot{\delta} - 4\pi G\bar{\rho}a^2\delta = 0, \tag{1.33}$$

where we have again assumed that the perturbations are small. Using this expression it is now possible to evaluate the characteristics of structure growth at early times for a given cosmogony, recalling that we have assumed that pressure terms are negligible (i.e. we are considering a *dust* universe).

At early times $\Omega \simeq 1$ and so we may assume an Einstein-de Sitter universe; we substitute Equations 1.18 and 1.19 into the above to obtain a description of structure growth in this case

$$\ddot{\delta} + \frac{4}{3t}\dot{\delta} - \frac{2}{3t^2}\delta = 0. \tag{1.34}$$

It is common to attempt a power law solution ($\delta \propto t^n$) which gives a general solution made up of a combination of growing and decaying modes

$$\delta(\mathbf{x}) = \delta_1(\mathbf{q})a + \delta_2(\mathbf{q})a^{-3/2} \tag{1.35}$$

$$= \delta_1(\mathbf{q})t^{2/3} + \delta_2(\mathbf{q})t^{-1}, \tag{1.36}$$

where $\mathbf{q}$ is the Lagrangian (initial) coordinate. Therefore, the mode corresponding to structures growing through gravitational collapse goes as $\propto a$. We express this in terms of a linear growth factor

$$D(a) = \frac{\delta(\mathbf{x})}{\delta(\mathbf{q})}, \tag{1.37}$$

which for the growing mode of small perturbations in an Einstein-de Sitter universe is simply $D = a$, i.e. structures will grow with the scale factor. A similar derivation may be

followed for the potential field, and one may show that the potential field evolves as

$$\delta\phi = \frac{D}{a}\delta\phi(\mathbf{q}), \tag{1.38}$$

i.e. linear potential fluctuations do not grow in an Einstein-de Sitter universe.

In reality, as density fluctuations grow over time their behaviour becomes non-linear ($\delta \rightarrow 1$) and the approximation of a single pressure-less fluid breaks down; the growth of structure may no longer be solved analytically and numerical solutions must be sought. Extensions of the theory into the non-linear regime may be made through the use of simplifying assumptions such as in the Spherical Top Hat Collapse model or the Press-Schechter formalism, however a discussion of such theory is beyond the scope of this work. Additionally, numerical solutions to the theory may be obtained through the assumption of simplifying geometries and adiabatic evolution (e.g. Peebles 1984 and Blumenthal et al. 1984) to obtain further insights without performing a full *N*-body simulation. However, in order to capture the full complexity of non-linear evolution with no assumed symmetries, the *N*-body method is essential.

1.2 The role of AGN in galaxy formation

As we have discussed, the ΛCDM model has been very successful in matching the observed large-scale structure of the Universe; however, additional baryonic physics is required to fully model the growth and evolution of galaxies, groups and clusters. This is seen in the observed galaxy mass function which differs from the CDM mass function. The under-abundance of high and low mass objects suggests that some baryonic process is suppressing the galaxy formation in these regimes (e.g. White & Frenk 1991; Bower et al. 2012; Leauthaud et al. 2012). This is illustrated in Fig. 1.1 which shows the observed halo mass versus stellar mass; if baryonic processes were unimportant we would expect the stellar mass fraction to be constant. Additionally, in groups and clusters we can see that the Intra-Cluster Medium (ICM) properties do not scale in the self-similar fashion expected if non-gravitational processes were not important on larger scales (see Kaiser 1986; Voit 2005; Borgani & Kravtsov 2009; Giodini et al. 2013). Furthermore, early models consisting of CDM and a simple hydrodynamical gas model with a prescription for radiative cooling produce too much cool gas, a lower-than-expected amount of hot gas and too many stars (e.g. Blumenthal et al. 1984; Katz et al. 1996; Schaye et al. 2010). AGN are thought to provide a source of feedback, along with supernovae, which offsets and slows cooling into galaxies and prevents this overproduction of stars; a model we now discuss in more detail.

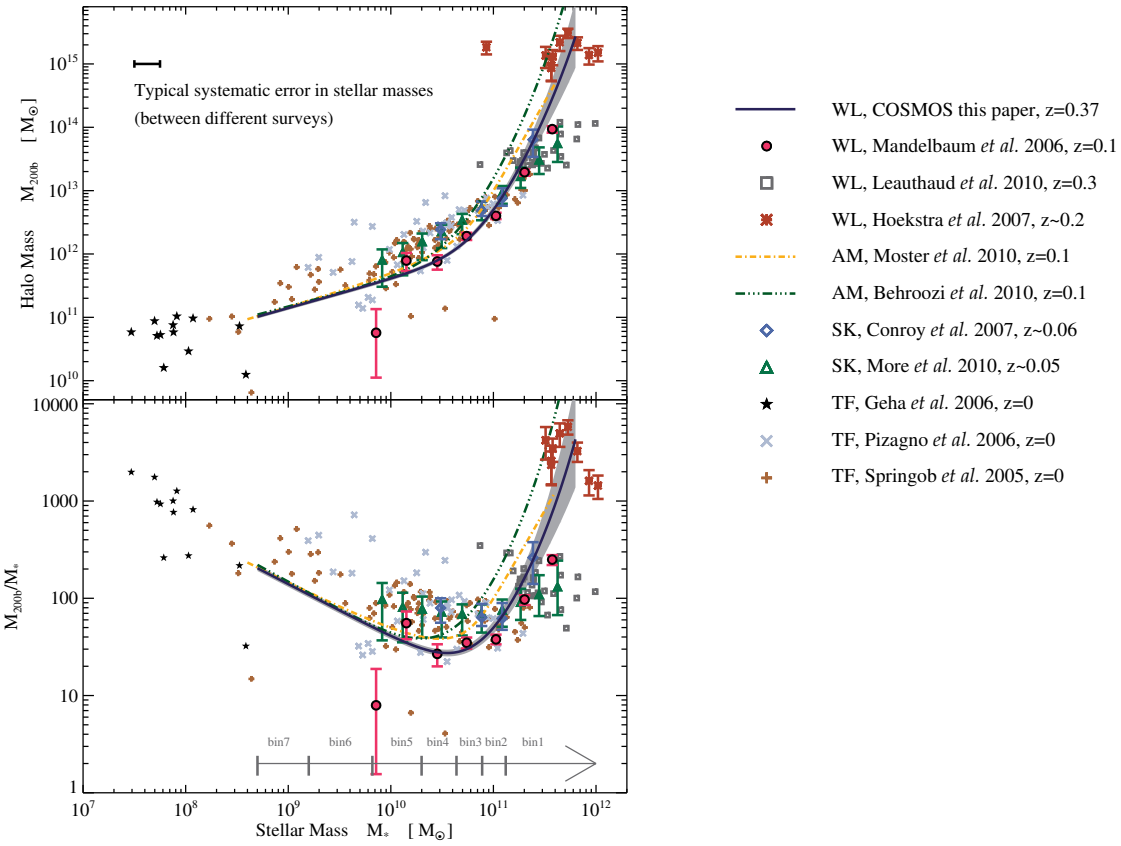

Figure 1.1: Observed halo mass versus stellar mass. The top panel shows the inferred stellar-to-halo mass relation in the z_1 redshift bin compared to other low-redshift measurements from weak lensing (WL), abundance matching (AM), satellite kinematics (SK), and the Tully-Fisher relation (TF). In the bottom panel, the dark-to-stellar mass ratio is shown as a function of stellar mass. If baryonic processes were unimportant we would expect the stellar mass fraction to be constant at the universal mean, however there is a larger stellar mass observed in more massive halos. This figure is reproduced from Leauthaud et al. (2012).

1.2.1 Observational evidence for AGN feedback

So far, 87 super-massive black holes have been observed in galaxies through dynamical modelling (Kormendy & Ho 2013; see Fig. 1.2 for an example of dynamical modelling around Sgr A*) and it is now thought that most, if not all galaxies host a super-massive black hole at their centre. The feedback from BHs is routinely observed across a range of wavelengths, embedded in a range of objects (e.g. McNamara & Nulsen 2012 and Kormendy & Ho 2013), appearing as far back as $z \sim 7$ (e.g. Fan et al. 2001; Kurk et al. 2007; Mortlock et al. 2011).

In galaxy bulges and at the centre of elliptical galaxies where black hole mass can be estimated, it has been shown that black hole mass correlates with the host's spheroid

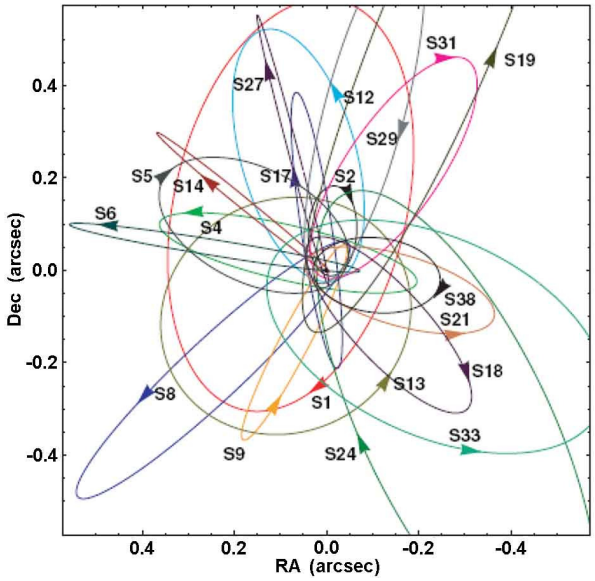

Figure 1.2: Black hole orbit observations around Sgr A*. Results are combined from Keck and Very Large Telescope observations. This figure is an updated form of the original by Genzel et al. (2010) reproduced from Kormendy & Ho (2013).

velocity dispersion (e.g. Ferrarese & Merritt 2000; Gebhardt et al. 2000; Tremaine et al. 2002). Since the dispersion is measured well outside the BHs gravitational range of influence this indicates that there exists some other mechanism leading to the co-evolution of these components. Furthermore, the observed galaxy luminosity and stellar masses (e.g. Magorrian et al. 1998; Häring & Rix 2004; Bennert et al. 2011; McConnell & Ma 2013) in known hosts of BHs also show a tight correlation, lending further weight to this interpretation. Current best fits for the observed relations from McConnell & Ma (2013) are illustrated in Fig. 1.3, specifically the observed relations are

$$\log(M_{\rm BH}/{\rm M}_\odot) = 8.32 + 5.64\log(\sigma/200\,{\rm kms}^{-1}), \tag{1.39}$$

$$\log(M_{\rm BH}/{\rm M}_\odot) = 9.32 + 1.11\log(L/10^{11}\,{\rm L}_\odot), \tag{1.40}$$

$$\log(M_{\rm BH}/{\rm M}_\odot) = 8.46 + 1.05\log(M_{\rm bulge}/10^{11}\,{\rm M}_\odot), \tag{1.41}$$

where σ is the stellar velocity dispersion, L is the V-band luminosity and $M_{\rm bulge}$ is the bulge stellar mass. We note that whether or not such a relationship linking BH mass to the DM halo and disc mass exists is unclear (e.g. Kormendy & Bender 2011 and Volonteri et al. 2011).

Whereas BH feedback in galaxies is typically observed as quasars, AGN activity in groups and clusters of galaxies is commonly linked to observations of hot, radio-emitting

plasma lobes embedded in cavities within the X-ray-emitting ICM (see e.g. McNamara & Nulsen 2007; Alexander & Hickox 2012 and references therein). By deducing the density, pressure and temperature inside and outside these lobes it is possible to estimate the work done inflating the bubble, how long they have been expanding and the ICM mass displaced by the growing cavity. Therefore, one may calculate the total energy the AGN deposits into the ICM through inflating the cavity, the gravitational potential energy released by gas sinking to replace the bubble as it rises and any shock fronts observed on the leading edge of the bubble. Additionally, unsharp-masked observations of clusters typically reveal the presence of sound waves related to weak shocks, caused by low power AGN outflows which may be contributing significant pressure to the ICM (e.g. Fabian et al. 2006). The total power from AGN in groups and clusters may therefore be in excess of $10^{43}\,\mathrm{ergs}^{-1}$, with associated energy outputs of the order $10^{61}\,\mathrm{erg}$ (e.g. McNamara & Nulsen 2007; Cavagnolo et al. 2010; Alexander & Hickox 2012).

With such a large amount of power deposited, it is interesting to investigate theoretically a link between AGN feedback and galaxy evolution on energetic grounds alone, a topic we now discuss.

1.2.2 Motivation and analytical AGN models

Although the exact origin of the observed correlations is not yet well understood (e.g. Jahnke & Macciò 2011), it is possible to obtain similar relationships between a BH and its host through simple physical arguments. Silk & Rees (1998) considered an AGN radiating proportionally to the Eddington luminosity (Equation 2.80) in a proto-galaxy described by an isothermal sphere and showed that for the BH to expel surrounding gas it must have a mass

$$M_{\mathrm{BH}} \sim \frac{f_{\mathrm{g}}\sigma_{\mathrm{T}}}{4\pi G^2 m_{\mathrm{p}} c}\sigma^5, \tag{1.42}$$

where f_{g} is the gas fraction, σ_{T} is the Thomson cross section, m_{p} is the proton mass and σ is the velocity dispersion (see Fabian 2012 for a derivation). We note that this early study was important in stimulating further work, and along with the observational paper of Magorrian et al. (1998) forged the perceived link between AGN and the formation of galaxies. By instead examining the momentum balance between the radiation field generated by an AGN and its gravitational pull, it is possible to obtain a similar relationship (via several possible derivations; e.g. Fabian 1999; King 2003; Fabian 2012)

$$M_{\mathrm{BH}} = \frac{f_{\mathrm{g}}\sigma_{\mathrm{T}}}{\pi G^2 m_{\mathrm{p}}}\sigma^4. \tag{1.43}$$

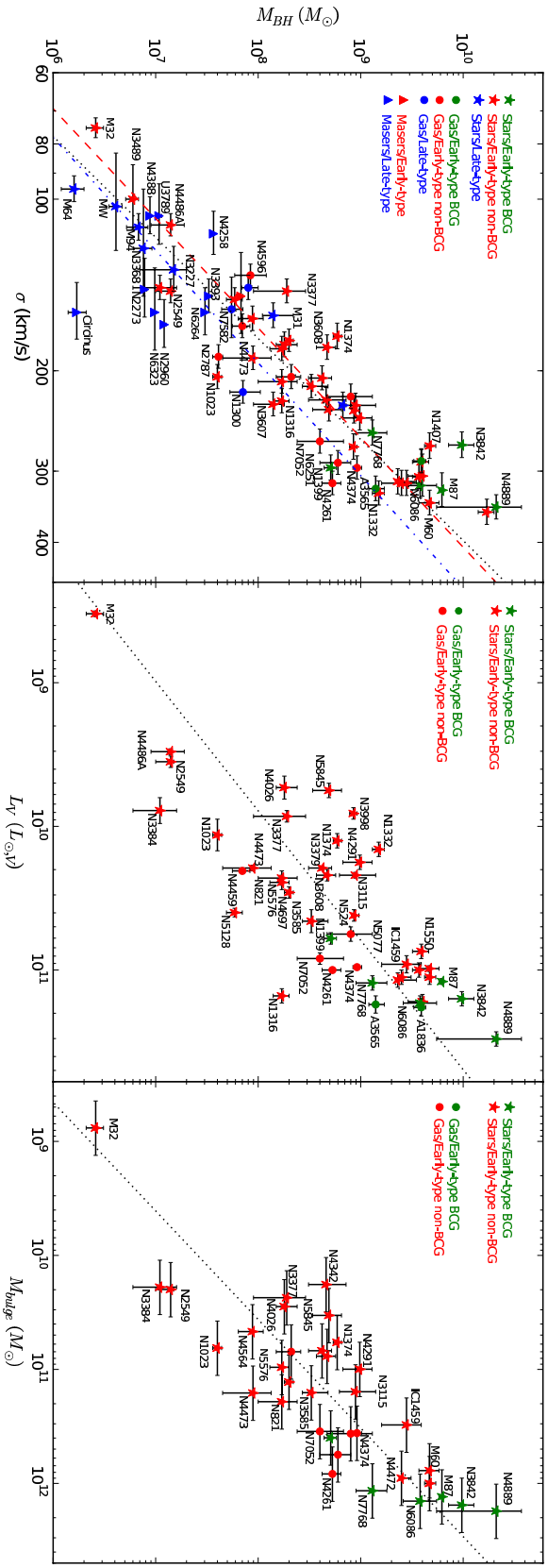

Figure 1.3: Observed correlations between the mass of 72 observed BHs and their host galaxy properties, shown top to bottom are stellar velocity dispersion, V-band luminosity and bulge stellar mass. This figure is adapted from McConnell & Ma (2013).

Each of these relationships are derived under the assumption that both the BH and star formation in the spheroid are fuelled by a sphere of cooling material which, upon the BH reaching a critical mass, is disrupted and blown out of the galaxy. Ishibashi & Fabian (2012) take an alternative view by evaluating a gas escape/trapping condition for different background DM density profiles and finding gas may not be fully ejected for the observed relations. Instead; the observed correlation may be an indicator of the AGN winds driving successive high-density gas shells which form stars.

Hoeft & Brüggen (2004) considered the stability of an analytical model of a galaxy cluster designed to match A2052 by integrating its entropy profile under the influence of radiative cooling, conduction and AGN heating. By tying the AGN luminosity to the mass inflow rate into the cluster-core and assuming that the AGN produced bubbles which did work on the surrounding gas as they rose, it was shown that it is possible to match observational temperature and entropy profiles by using AGN to offset cooling losses.

Therefore, analytical studies provide much circumstantial evidence linking AGN with galaxy evolution. AGN models are also an integral component of modern semi-analytical studies where their importance in galaxy formation theory is quantified by attempting to match the observable Universe.

1.2.3 AGN in semi-analytic models

Semi-analytic modelling is a process by which DM halo merger trees (commonly obtained either from using the extended Press-Schechter formalism or directly from N-body simulations; see e.g. Li et al. 2007) are combined with an often complex network of simple baryonic physics models which attempt to replicate the observable Universe. The first inclusion of BH growth in semi-analytics was performed by Kauffmann & Haehnelt (2000). The simple model assumed that the growth of BHs was due to gas finding its way onto the BH during a merger and accreting over a fixed timescale. Despite its simplicity, the model was moderately successful in modelling the quasar luminosity function and the $M - \sigma$ relation. Following from this, Benson et al. (2003) found that the amount of energy necessary to offset cooling in larger galaxies and obtain a fit to the galaxy luminosity function was larger than is feasible from SNe alone, citing AGN feedback as a necessary contribution. More modern semi-analytical modelling includes AGN as a central ingredient with more sophisticated recipes in use; accretion incorporates feeding from mergers and disc instabilities whilst feedback accounts for heating and ejection of gas (e.g. Bower et al. 2006; Croton et al. 2006; Guo et al. 2011). By incorporating BH feedback within the semi-analytic models it is possible to reproduce the sharp drop-off in number density at the bright end of the galaxy luminosity function (see also Binney 2004). The numerical

efficiency of semi-analytic modelling makes it ideal for characterising the importance of individual (baryonic) processes for galaxy formation and properties through the analysis of many permutations of parameters. However, the models are limited to giving statistical descriptions of the galaxy population rather than fully modelling individual objects; for this it is necessary to consider a full hydrodynamical treatment.

1.2.4 Numerical simulations of AGN feedback

As we have discussed, AGN activity on galactic and cluster scales is very dissimilar, showing substantially different phenomenology and effects on its environment. This dichotomy is often made explicit in numerical models where authors typically aim to simulate one of two distinct 'modes' of feedback (although some authors argue the case for 3 modes e.g. Fabian 2012). Which of the two modes the AGN resides in is thought to be determined by BH accretion rate (see the introduction of Russell et al. 2013 for an overview). The mode operating on group and cluster scales (corresponding to low accretion rates) is commonly referred to as a *radio* (also *jet* or *mechanical*) mode, named for the radio-emitting cavities inflated by jets. The physical process leading to the formation of jets around BHs is still poorly understood (Alexander & Hickox 2012), however a commonly-held view is that magnetic fields wound up in a geometrically thick accretion disc store large amounts of energy which are somehow tapped by the jets. The second mode considered is the *quasar* (also *radiative* or *cold*) mode which is associated with AGN producing high-power isotropic radiation fields and observed as quasars. In this regime the accretion disc is thought to collapse into a dense, optically thick, Shakura & Sunyaev (1973) accretion disc which emits the powerful quasar radiation field. We now go on to discuss how this mode is modelled in numerical galaxy formation simulations before discussing the radio mode.

The modelling of AGN in galaxy formation simulations set out by Springel et al. (2005) and Di Matteo et al. (2005, 2008), showed for the first time that black hole self regulation can be achieved and the observed $M_{\rm BH} - M_{\rm bulge}$ relation reproduced within a fully cosmological simulation. This method is now widely employed in simulations (e.g. Robertson et al. 2006; Di Matteo et al. 2008; Khalatyan et al. 2008; Johansson et al. 2009; Fabjan et al. 2010; DeGraf et al. 2012), although is by no means the only implementation currently in use and many aspects of the model are questioned. In the method, accretion onto the BH is assumed to be described by the Bondi-Hoyle-Lyttleton (Hoyle & Lyttleton 1939; Bondi & Hoyle 1944; Bondi 1952; 'Bondi') formula, which assumes spherically symmetric accretion from gas which is stationary at infinity. This has been challenged by a number of authors, for example Booth & Schaye (2009) dispute

the use of a simple multiplicative-factor correction for under-resolved accretion flows and central densities around the BH. Other authors further dispute the Bondi approach due to its inherent assumptions of spherical symmetry and negligible angular momentum (e.g. Debuhr et al. 2010; Power et al. 2011). Additionally, Hobbs et al. (2012) argue that a proper accretion rate estimate should take into account the gravitational potential of all matter, not just the BH. Each of these modifications, as well as others taking into account more complex physics such as BH spin (Fanidakis et al. 2011), will yield different accretion rates onto the BH and thus alter its final mass.

The method by which AGN feedback energy is deposited into the surrounding gas is also often varied. Some studies argue for thermally-driven feedback (e.g. Di Matteo et al. 2005; Booth & Schaye 2009; Sijacki & Springel 2006) and others for kinetic or momentum feedback (e.g. Debuhr et al. 2010; Power et al. 2011; Dubois et al. 2012) on various physical and numerical grounds. A key criticism of thermal feedback is that much of the energy used in raising the gas temperature is lost quickly through radiative cooling, a problem avoided in the method of Booth & Schaye (2009) which assumes that energy is stored until a gas particle can be heated to a high temperature. Comparatively, kinetic feedback schemes suffer from additional complications as heating of the gas relies on the imperfect shock-capturing ability of the code and the direction (as well as magnitude) of the outflows must be defined.

Key successes from AGN simulations on galaxy-scales include the ability to halt star formation in giant elliptical galaxies (Khalatyan et al. 2008), leading to a reproduction of the turn over at the high end of the luminosity function (Schaye et al. 2010)

We now turn our attention to the simulation of BH feedback on galaxy cluster scales. Such studies have typically been performed in isolated objects due to the large gas mass typically in the ICM ($\sim 10^{13}\,\mathrm{M}_{\odot}$) and the high resolution required to resolve the complex gas processes involved in simulating AGN outflows. Early work by Dalla Vecchia et al. (2004) within AMR (see Chapter 2 Section 2.1.2) simulations represented AGN-driven radio lobes as Gaussian spheres of heated gas injected at set time intervals within the ICM. They found that it was possible to prevent the over-cooling catastrophe by depositing feedback into the ICM with an energy budget in-line with characteristic AGN energy scales ($\sim 10^{60}\,\mathrm{erg}$). However, the model was unable to match observational constraints on the X-ray luminosity and temperature profiles. A similar approach was taken by Sijacki & Springel (2006), this time using Smoothed Particle Hydrodynamics (SPH; see Chapter 2 Section 2.1.2), for simulations of high resolution galaxy clusters. Again, this method injects bubbles into the cluster atmosphere without explicitly linking to an accreting BH. However, an advance was made in the more physically-motivated form of bubble heating used, which links the mass of the cluster and energy of the bubble to its size. An updated

scheme (Sijacki et al. 2007) derived the available feedback energy to the accretion rate onto a central BH and linked the bubble radius to physical properties of the simulation such as its internal energy and the density of the ICM. These studies showed that the radio mode of feedback can solve the over-cooling problem when modelled as thermal energy injection. However, a wealth of observational evidence suggests that the dominant mechanism by which AGN do work on cluster environments is momentum-driven feedback (e.g. McNamara & Nulsen 2012) leading to the adoption of this mechanism within simulations. An early work taking this approach by Cattaneo & Teyssier (2007) simulated the effect of AGN-driven ($\sim 1000\,\mathrm{kms}^{-1}$) outflows on a Virgo cluster mass object. By simulating jets in this way it was possible to reproduce the observed BH accretion rate and X-ray luminosity, reversing the effect of a cooling flow which initially. The failure at early times was attributed to the outflows carving out a 'chimney' from the ICM and reducing the influence of the feedback, only when the ICM becomes turbulent and breaks the jet into bubbles does the feedback become effective. More contemporary work by Gaspari et al. (2011) and Gaspari et al. (2013) has achieved great success in matching observations across a range of objects and masses with AMR simulations of kinetic AGN jet outflows. The potential shortcoming of this work is the need for the AGN heating efficiency to be tuned 'by hand' across the range of cluster masses to prevent under/over-heating the ICM.

So far we have discussed simulation methods which aim to replicate either the quasar or radio feedback modes, however a further class of models exists which combine both into a single framework. Sijacki et al. (2007) combined an updated treatment of the Sijacki & Springel (2006) radio with an implementation of quasar mode feedback described using the Springel et al. (2005) method. The two modes are assumed to operate at different BH accretion rates (as motivated by observations of X-ray binaries, see e.g. Alexander & Hickox 2012), the quasar mode providing the feedback at high accretion rates and the radio mode at low rates. The modified radio mode feedback no-longer produces a bubble at a pre-determined time interval, but when a critical amount of mass (1 per cent of M_{BH}) has been accreted onto the BH. The transition between the two modes is controlled by a threshold accretion rate

$$\lambda_{\mathrm{Edd,c}} = \frac{\dot{M}_{\mathrm{BH}}}{\dot{M}_{\mathrm{Edd}}}, \tag{1.44}$$

where the exact value of the threshold is a free parameter, but Sijacki et al. (2007) typically choose $\lambda_{\mathrm{Edd,c}} = 1$ per cent. The Sijacki hybrid method is employed by Cattaneo & Teyssier (2007) and Puchwein et al. (2008) in their work.

Vogelsberger et al. (2013) performed for the first time simulations incorporating AGN feedback represented through thermal, mechanical and electro-magnetic feedback incorporating radiative transfer in moving-mesh (see Chapter 2 Section 2.1.2) simulations of

galaxy formation. This work combines a modified form of the Sijacki et al. (2007) dual-mode feedback with an approximated effective quasar luminosity field to avoid the need for a full radiative transfer scheme. Once again, this study finds that powerful radio mode feedback is required to prevent an over-production of stars in high mass galaxy systems.

Whilst depositing the energy in a simplistic fashion has proven effective in many studies, some work suggests that a more complex description is necessary. Hopkins & Elvis (2010) show that incorporating a full radiative transfer treatment of a quasar radiation field can dramatically increase the effectiveness of even weak thermal feedback. However, performing full polychromatic radiative-transfer simulations remains beyond the reach of current cosmological simulations.

The remainder of this thesis is organised as follows, having now outlined previous research and theory, we discuss numerical methods and models appropriate to the studies we perform in Chapter 2. We then go on to perform and analyse simulations on disc galaxy scales including different AGN and supernovae models in Chapter 3 before then applying these same models to galaxy group and cluster scales in Chapter 4, we also present a new model here. Chapter 5 then covers the detailed analysis and characterisation of a novel 'hybrid' mode AGN model acting on groups and clusters, whilst Chapter 6 summarises the findings from all previous chapters.

Chapter 2

Methods

My definition of an expert in any field is a person who knows enough about what's really going on to be scared.

DR. PHILLIP "P. J." PLAUGER

Having discussed the role AGN in galaxy formation models, we now go on to outline some of the numerical methods relevant to its study. Whilst we present information on the broader methodology used for such work, the simulations presented in the following were performed using a modified version of the public code GADGET-2 (Springel 2005) and so we note specific details of this software where appropriate.

2.1 Cosmological simulation codes

There are a wide variety of computer programs for the simulation of physics on cosmological length and timescales within an expanding universe. Most early codes adopted the numerically and theoretically convenient simplification of a DM dominated universe. Due to the benefits of this approach it is still in use by many studies today. More complex programs also account for baryonic physics with various levels of sophistication, ranging from simply following the hydrodynamics of an ideal gas, to including sub-resolution recipes for cooling, star formation, AGN physics, metal enrichment, magnetic fields and radiative transfer.

Regardless of any additional methods, a core part of any of the codes is the numerical calculation of the gravitational force. In Section 2.1.1 we discuss common gravity solvers before going on to summarise leading hydrodynamics methods in Section 2.1.2 before finally outlining sub-grid models relevant to this work in Section 2.2.

2.1.1 *N*-body gravity solvers

When considering collisionless fluids such as DM and stellar populations it is convenient to use a system of Lagrangian tracer particles. These allow us to describe the properties of the collisionless fluid moving purely under gravity, by calculating self-interaction of the particles in a so-called *N*-body method. Fundamentally we evolve the 6-dimensional phase space given by $\mathbf{x}$ and $\mathbf{v}$ by solving Poisson's equation,

$$\nabla^2\Phi = 4\pi G\rho, \tag{2.1}$$

however utilising particles provides a conceptually simple method for calculating its evolution. The force exerted by particle j on particle i is

$$\mathbf{F}_{ij} = \frac{Gm_i m_j \mathbf{r}_{ij}}{(\varepsilon^2_{\rm soft} + |\mathbf{r}_{ij}|^2)^{3/2}}, \tag{2.2}$$

where m_i is the mass of particle i, and $\varepsilon_{\rm soft}$ is the gravitational softening parameter introduced to avoid singularities as the separation $\mathbf{r}_{ij}$ tends towards zero. The gravitational softening also prevents the time-step from becoming prohibitively small and reduces unwanted effects due to the artificially large quantisation of the mass, such as two-body scattering (discussed later in the this section).

Direct summation

The most obvious (and perhaps naive) method for evolving this system is to work-out the force on each particle from each other particle in turn, the so-called direct summation or Particle-Particle (PP) method. Numerically, this requires simply performing the summation of pairwise forces for all N particles. However doing so is computationally expensive, requiring $\frac{1}{2}N(N-1)$, i.e. $\mathcal{O}(N^2)$, evaluations of Equation 2.2, and quickly becomes prohibitive for large particle numbers.

Whilst it is possible to accelerate such brute-force calculations with parallel computing and specialised hardware such as gravity pipe (GRAPE) boards (Sugimoto et al. 1990) and more recently through the use of graphical processing units (GPUs; e.g. Portegies Zwart et al. 2007; Fluke et al. 2011), modern codes typically employ methods for simplifying and thus speeding up the calculation. This solution is chosen in situations where the required precision is not as high, and those using large datasets which encounter bottlenecks due to high transfer times between the host machine and specialised hardware. We now go on to discuss some of the methods for accelerating gravitational force calculations commonly employed in galaxy formation studies.

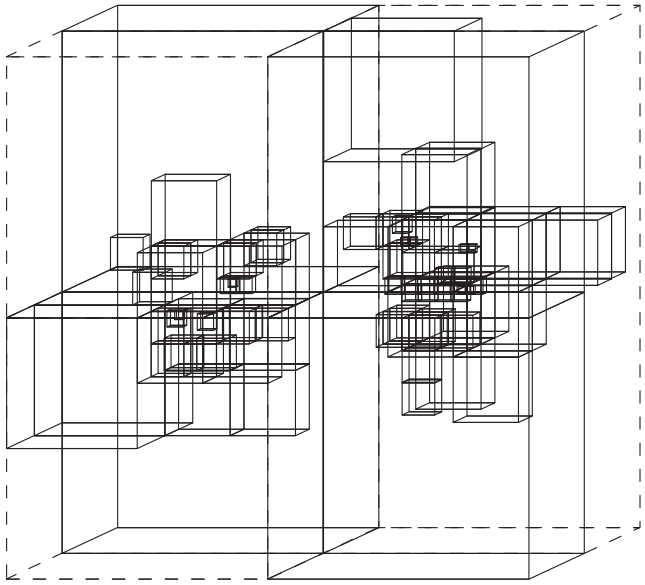

Figure 2.1: Example 3D Barnes-Hut oct-tree cell structure representing two adjacent groups of particles. The system of occupied cells adapts to the matter distribution, forming a range of cell sizes centred on the most dense areas. This figure is adapted from Barnes & Hut (1986).

Hierarchical tree

As an approximation to the direct method whereby a given particle feels the effect of all others, one may imagine a system whereby distant particles are grouped together to reduce the number of individual calculations. This is possible because any distribution of mass when viewed from infinity acts as a gravitational monopole, i.e. point mass. Therefore we may consider representing a mass distribution at a finite distance as an approximated facsimile, for example a distribution of monopoles or a multipole expansion about its centre of mass (however due to memory constraints this is often not used in practice). This approach was pioneered by Appel (1985) and first combined with SPH (see Section 2.1.2) for astrophysical applications by Hernquist & Katz (1989).

When constructing the tree, the particles are grouped into a series of increasingly large sets; it is with these *nodes* that the force calculation (Equation 2.2) will be performed. Upon calculating the net force for a given particle, nearby groups are 'opened' when the more accurate force determination is needed, based on the detailed mass distribution within it whilst distant groups are not opened and are instead considered en masse. By grouping more distant masses together progressively more coarsely we can reduce the number of interactions per force calculation to $\mathcal{O}(\log N)$ whilst incurring only minimal errors. The errors are determined by the level at which nodes are opened for a given distance, i.e. by the *opening angle*. For a given cell under consideration with side length l with a distance r between its centre of mass and the particle, the opening angle is given

by (Barnes & Hut 1986)

$$\theta = \frac{l}{r}. \tag{2.3}$$

The cell will then be opened if θ is greater than or equal to a fixed critical value controlling the force accuracy. A modified criterion compares is applied in GADGET-2 to limit absolute force accuracy, where a node is left closed if

$$\frac{GM}{r^2}\left(\frac{l}{r}\right)^2 \leq \alpha|\mathbf{a}|, \tag{2.4}$$

where α is a tolerance parameter and $\mathbf{a}$ is the particle acceleration obtained in the last time-step. This ensures higher force accuracy for a given computational cost than the classic criterion (Springel 2005).

In GADGET-2, the tree construction utilises a Barnes-Hut oct-tree method (Barnes & Hut 1986). In this method a cube spatially encompassing all particles is recursively subdivided into 8 smaller cubic volumes until each cube contains 1 or 0 particles. The force calculation for a particle is performed by 'walking' the branches of the tree considering each node in turn and opening them when necessary. Fig. 2.1 illustrates how the cell structure adapts to arbitrarily complex distributions of particles, resulting in a range of cell sizes.

The approach of grouping masses together to form an approximation is particularly useful in clumpy distributions of matter with high density contrasts over the simulation volume, as the tree method benefits from grouping distant clumps of particles. Such conditions are found in astronomical simulations of galaxies or low-redshift cosmological simulations. However, the tree method's weakness lies in simulations with low density contrast, such as at high redshifts in cosmological simulations where collapsed structures are yet to form. A radically different method must be considered to simulate this system efficiently.

Particle-Mesh

The particle-mesh method (PM; Hockney & Eastwood 1981; Klypin & Shandarin 1983; White et al. 1983; Efstathiou et al. 1985) utilises a different approach to both the PP and tree methods, performing more efficiently in regimes where the tree method fails. Simplistically, the particle mesh calculation may be broken down to four steps; assigning (smoothing) the density distribution onto a mesh, solving Poisson's Equation (Equation 2.1) on the mesh, calculating the forces on the mesh and finally interpolating the resulting forces back onto the particles. The details of the method vary greatly and different approaches offer advantages for simulating different systems; for example it is necessary

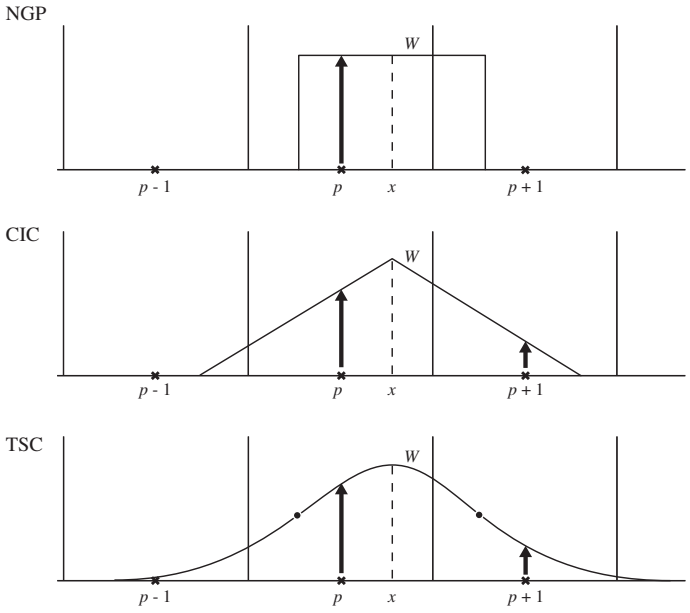

Figure 2.2: Example 1D mass assignment functions for a particle at position x in an equally-spaced mesh. The height at a mesh-point p shows the value of the mass assignment function W at that point. Top to bottom we show the NGP, CIC and TSC assignment functions respectively. This figure is adapted from Hockney & Eastwood (1981).

to consider the choice of periodic vs non-periodic boundaries, system geometries, mesh spacing and the accuracy-computational cost balance (Hockney & Eastwood 1981). We therefore limit our short overview to the method's most pertinent details.

The first step in the potential calculation requires the choice of a *mass assignment function*. This defines the nature of the smoothing by describing the weighting with which the particle's mass is attributed to its nearest grid-points. The simplest such function simply adds the mass of the particle to the nearest grid point (the NGP method); however it has the drawback of being discontinuous as the particle moves across boundaries. Alternative functions, produced by convolving the NGP window-function with itself one or more times give higher-order continuity. The cloud-in-cell (CIC; one convolution) function is continuous in density and the triangular-shaped cloud (TSC; two convolutions) in its first derivative. Fig. 2.2 shows the three mass assignment (weighting) functions schematically for a particle in a 1D mesh.

Solving the gravitational potential on a mesh is commonly performed using a Fast Fourier Transform (FFT) algorithm due to its numerical efficiency. We now outline some key theoretical steps in the approach. We may write the process of mass assignment as

$$\rho(\mathbf{r}_p) = \frac{1}{V_c} \sum_i^N m_i W(\mathbf{r}_i - \mathbf{r}_p), \tag{2.5}$$

where W is the weighting function, $V_{\rm c}$ is the cell volume (length/area in 1 and 2D respectively), m_i is the mass of particle i, and $\mathbf{r}_i$, $\mathbf{r}_p$ are the spatial coordinates of particle i and the centre of cell p respectively. The potential may be written as the sum of the pairwise interactions of each pair of cells

$$\Phi(\mathbf{r}_p) = V_{\rm c} \sum_{q}^{N_{\rm mesh}} \mathcal{G}(\mathbf{x}_p - \mathbf{x}_q)\rho(\mathbf{x}_q), \tag{2.6}$$

where $\mathcal{G}$ is the Green's function of the gravitational interaction, $\mathcal{G} = 4\pi G/\mathbf{k}^2$, and $\mathbf{k}$ is the wave-vector. (The Green's function takes this form due to the Laplacian operator in Equation 2.1.) Noting that the above is a quantisation of a convolution integral, we make use of the Fourier Convolution theorem, *"the Fourier transform of a convolution is equal to the product of the Fourier transforms of the individual quantities"*, to write

$$\check{\Phi}(\mathbf{k}) = \check{\mathcal{G}}(\mathbf{k})\check{\rho}(\mathbf{k}), \tag{2.7}$$

where $\check{\Phi}$ denotes the Fourier transform of Φ. Finally we may calculate the potential field due to all particles on a mesh by performing the inverse Fourier transform and interpolating back onto the particles after deconvolving the weighting function. The PM method requires $\mathcal{O}(N_{\rm mesh} \log N_{\rm mesh})$ calculations to compute the potential in this way, once the grid has been constructed, with $\mathcal{O}(N)$ additional calculations for interpolations onto and off the mesh. For a fixed mesh, one need only construct the mesh and calculate the corresponding Green's function once per simulation.

The computational benefit in this method comes from the loss of resolution involved in smoothing the particle distribution onto the grid as well as the use of efficient algorithms. Smoothing the density field means that sub-grid structure is lost, this is of no consequence in simulations with low density contrast as previously discussed, but can introduce large errors in some cases. An ideal method may then be one which combines the numerical efficiency of the PM method with an accurate force solver on short distances, two such methods are the P^{3}M and TreePM methods.

The Particle-Particle - Particle-Mesh (P^{3}M) method (Hockney et al. 1973; Hockney & Eastwood 1981) combines a mesh of minimum grid size approximately equal to a force splitting radius, $r_{\rm s}$, with a direct force calculation on sub-grid scales. The total force is then equal to the sum of the short-range and long range-forces. In practice P^{3}M codes tend to be slower (Xu 1995) than PM codes as even the reduced PP element is computationally expensive. In an effort to overcome this limitation, the AP^{3}M method (Couchman 1991) incorporated an adaptive mesh-refinement scheme which aimed to reduce the amount of

direct force calculations necessary in highly clustered regions. This method is combined with a hydrodynamics solver in the cosmological simulation code HYDRA (Couchman et al. 1995).

TreePM

Utilising the tree on short-ranges in combination with a large-scale PM grid eases the bottleneck caused by the direct summation component of the P^{3}M method. An early method by Xu (1995) first smooths all particles onto a grid and calculates the density field before splitting the force calculation. Grid cells above a density cut are then defined as tree cells, meaning that the particles contributing to them have a tree-calculated potential in addition to the long-range PM component. However, the approach utilised in GADGET-2 differs slightly in that the potential is instead explicitly split in Fourier space into short and long-range components, $\Phi_{\mathbf{k}} = \Phi_{\mathbf{k}}^{\mathrm{long}} + \Phi_{\mathbf{k}}^{\mathrm{short}}$, where

$$\Phi_{\mathbf{k}}^{\mathrm{long}} = \Phi_{\mathbf{k}} \exp(-\mathbf{k}^2 r_{\mathrm{s}}^2). \tag{2.8}$$

The small-scale potential at coordinate $\mathbf{x}$ is then solved in real-space using the tree to calculate

$$\Phi^{\mathrm{short}}(\mathbf{x}) = -G \sum_i \frac{m_i}{r_i} \mathrm{erfc}\left(\frac{r_i}{2r_{\mathrm{s}}}\right), \tag{2.9}$$

where r_i is the distance of the particle to point $\mathbf{x}$ (the minimum distance in the case of periodic boundaries) and r_{s} is the spatial scale of the force split. Springel (2005) notes that if r_{s} is set slightly larger than the mesh scale then it is possible to avoid the errors due to force anisotropies which affect PM methods.

Force softening

In many N-body methods it is common to *soften* the gravitational force between particles at short separations, i.e. the potential felt near to a particle is reduced compared to the Newtonian inverse-square law. In doing so the numerical singularity at $\mathbf{r}_{ij} = 0$ in the force calculation is avoided and also the effect of two-body encounters is reduced. The Lagrangian nature of the N-body method is susceptible to an inherent problem due to the discretisation of mass. The artificially-large quanta result in two-body scattering events which alter the dynamics of the fluid. The resulting effect may be characterised by a *relaxation time*; the time taken for a particle's velocity to change by order itself as a result of two-body interactions with the rest of the population (Binney & Tremaine 1987).

Beginning with the 2-body relaxation time assuming a random walk, it may be shown

$$\tau_{\rm relax} \approx \frac{1}{8}\frac{N}{\ln N}\tau_{\rm dyn} \tag{2.10}$$

where $\tau_{\rm dyn}$ is the dynamical time which we estimate to be (assuming simple harmonic motion on a circular orbit in a homogeneous sphere),

$$\tau_{\rm dyn} \approx \sqrt{\frac{3\pi}{16G\langle\rho\rangle}}, \tag{2.11}$$

where $\langle\rho\rangle$ is the mean density within r, therefore we may write

$$\tau_{\rm relax} \approx \frac{\pi}{16}\frac{N}{\ln N}\sqrt{\frac{r^3}{GM(<r)}}. \tag{2.12}$$

At a given time in the evolution of a system of particles one may then numerically solve the above relation for r to estimate the scale which has been substantially affected by collisional relaxation since the simulation began (Power et al. 2003).

However, the practice of *softening* the gravitational force at short distances in turn introduces its own error. Any structure on or below the scale of softening cannot be considered strictly physical since it has not been subject to an accurate Newtonian potential calculation.

We note that in practice GADGET-2 does not implement the gravitational force as laid out in Equation 2.2 due to the force split. Instead, the potential field of the point-particles are convolved with the SPH spline kernel of extent $2.8\varepsilon_{\rm soft}$ and so the potential is equivalent to that of a Plummer 'sphere' of size $\varepsilon_{\rm soft}$. Only structures larger than $2.8\varepsilon_{\rm soft}$, therefore, experience the Newtonian potential in simulations performed using GADGET-2 and are numerically reliable (however this is not a general rule as the exact length at which the calculations converge depends on the details of the force law used).

2.1.2 Hydrodynamical methods

This section gives a brief overview of some hydrodynamical methods currently in use in cosmological simulations, however this is by no means exhaustive as a wide variety of different and nuanced approaches are employed in modern codes. We first discuss the theoretical foundation of the method utilised in this work, Smoothed Particle Hydrodynamics (SPH) before briefly discussing some alternative hydrodynamics schemes.

Smoothed Particle Hydrodynamics

At the heart of SPH is the kernel interpolant, specifically a kernel summation defining the density of a fluid which may then be used to derive the rest of the core SPH equations. Any continuous field $F(\mathbf{r})$ may be described by

$$F(\mathbf{r}) = \int F(\mathbf{r}')\delta(\mathbf{r} - \mathbf{r}')\mathrm{d}\mathbf{r}' \tag{2.13}$$

where δ is the Dirac delta function, which we may then approximate with a smoothing kernel W with finite width h

$$F(\mathbf{r}) = \int F(\mathbf{r}')W(\mathbf{r} - \mathbf{r}', h)\mathrm{d}\mathbf{r}' + \mathcal{O}(h^2). \tag{2.14}$$

The smoothing kernel here must reduce to the Dirac delta function as $h \rightarrow 0$ and is normalised to unity, $\int_V W \mathrm{d}V' = 1$. Our choice of kernel must be symmetric with respect to $\mathbf{r} - \mathbf{r}'$ and have smooth derivatives, as well as providing low-noise evaluations of field quantities. An extreme choice of a spherical top hat kernel (constant weighting) would result in estimates highly susceptible to noise from small changes in either h or position as particles move in or out of the kernel, similarly a strong central peak would suffer from particle noise generated at low $\mathbf{r}$. It is desirable then for a kernel to decrease monotonically with $\mathbf{r}$ and have a centrally-flattened profile, i.e. to *smooth* the particle distribution. The natural choice which satisfies these conditions (and the function first used by Gingold & Monaghan 1977) is the Gaussian

$$W(\mathbf{r} - \mathbf{r}', h) = \frac{\sigma}{h^d} \exp\left[-\frac{(\mathbf{r} - \mathbf{r}')^2}{h^2}\right], \tag{2.15}$$

where $\sigma (= \pi^{-d/2})$ is a normalisation factor and d is the number of spatial dimensions. However, the Gaussian has practical drawbacks as a kernel due to its infinite extent (which we discuss later) and so it is common to adopt B spline approximations with finite support, such as the cubic spline with $W(\mathbf{r}, h) = w\left(|\mathbf{r}|/h\right)$

$$w(q) = \sigma \begin{cases} \frac{1}{4}(2-q)^3 - (1-q)^3 & 0 \leq q < 1, \\ \frac{1}{4}(2-q)^3 & 1 \leq q < 2, \\ 0 & q \geq 2, \end{cases} , \tag{2.16}$$

truncated at $2h$, where $q = |\mathbf{r}|/h$ and $\sigma = [2/3, 10/(7\pi), 1/\pi]$ is the normalisation factor in $[1, 2, 3]$ dimensions (although we note that GADGET uses a convention where the kernel is truncated at h and therefore has different normalisation constants). Therefore if we

know the value of the field at a set of points, $F_i = F(r_i)$ with known mass and density and an associated finite volume element $\Delta\mathbf{r}_i \sim m_i/\rho_i$ we can approximate the integral in Equation 2.14 as

$$F(\mathbf{r}) \simeq \sum_j \frac{m_j}{\rho_j} F_j W(\mathbf{r} - \mathbf{r}_j, h). \tag{2.17}$$

This is perhaps the most fundamental expression in SPH, and it is interesting to note that the field estimate is defined everywhere and not just at the positions of the particles.

Initially, the smoothing length, h, as implemented by Gingold & Monaghan (1977) was invariant in space and allowed only to vary globally in response to the maximum density at a given time. Clearly, it is advantageous for the smoothing length to be adaptive, taking advantage of the Lagrangian nature of SPH to resolve both sparsely populated and dense regions well. This may be achieved by holding the ratio of the smoothing length to mean particle separation approximately constant, i.e.

$$h(\mathbf{r}) \propto n(\mathbf{r})^{-1/d} \qquad n(\mathbf{r}) = \sum_j W(\mathbf{r} - \mathbf{r}_j, h(\mathbf{r})), \tag{2.18}$$

where n is the weighted number of neighbouring particles. It is apparent that such a link between n and ρ means that the two equations cannot be considered independently, as density is itself a function of the smoothing length. Indeed, for equal mass particles we have set the smoothing length, h, to be proportional to the density (since $n \equiv m/\rho$) and we therefore have two equations which must be solved iteratively

$$\rho(\mathbf{r}_i) = \sum_j m_j W(\mathbf{r}_i - \mathbf{r}_j, h_i), \tag{2.19}$$

$$h(\mathbf{r}_i) = \eta \left(\frac{m_i}{\rho_i}\right)^{1/d}. \tag{2.20}$$

where the scaling parameter, η, is the smoothing length in units of the mean particle spacing ($= (m/\rho)^{1/d}$). Defining the smoothing length in this way keeps the mass within the smoothing sphere approximately constant

$$M^i_{\rm tot} = \int_{V_i} \rho \, \mathrm{d}V \approx \frac{4}{3}\pi R^3_{\rm kern} \rho_i, \tag{2.21}$$

where $R_{\rm kern}$ is the kernel radius ($2h$ for the cubic spline). This mass may be used to define an equivalent number of neighbour particles given equal particle masses, $N^i_{\rm neigh} = M^i_{\rm tot}/m$, but we note this number need not be an integer as it is calculated via a weighted sum. Similarly, it is unlikely to have the same value as the number of particles within

$N(< R_{\rm kern}) = N_{\rm ngb}$ for an arbitrary mass distribution.

Evaluating the density summation for N particles utilising a given compact support kernel requires $\mathcal{O}(N_{\rm ngb}N)$ calculations. This is in contrast to the Gaussian kernel which, due to its infinite extent, requires N calculations for each particle giving a much more computationally expensive $\mathcal{O}(N^2)$ scaling.

Now we have obtained an expression for the density and an arbitrary field in the SPH formalism we move onto consider the dynamics of such a fluid.

The Euler equations governing inviscid gas dynamics may be written in the Lagrangian form as

$$\frac{\mathrm{D}\rho}{\mathrm{D}t} + \rho\nabla\cdot\mathbf{v} = 0, \tag{2.22}$$

$$\frac{\mathrm{D}\mathbf{v}}{\mathrm{D}t} + \frac{\nabla P}{\rho} = 0, \tag{2.23}$$

$$\frac{\mathrm{D}u}{\mathrm{D}t} + P\nabla\cdot\mathbf{v} = 0, \tag{2.24}$$

where u is the specific thermal energy and P is the gas pressure. This set of equations defines the behaviour of the gas, and expresses the conservation of mass, momentum and energy respectively. We now follow Springel (2010b) and Price (2012) in deriving the corresponding set of equations for a modern SPH implementation beginning only with the Lagrangian and the density estimate. Utilising the Lagrangian as a starting point provides multiple benefits including the derivation of a fully conservative SPH algorithm (aside from dissipative terms) and the inclusion of the Hamiltonian phase space properties. The Lagrangian is commonly given by,

$$L = T - V, \tag{2.25}$$

where T and V are the kinetic and (thermal) potential energies respectively. In the discretised form for a system of particles it becomes,

$$L = \sum_i m_i \left[\frac{1}{2}\mathbf{v}_i^2 - u_i(\rho_i, s_i)\right], \tag{2.26}$$

where $\mathbf{v} \equiv \mathrm{d}\mathbf{r}/\mathrm{d}t$, in general a function of density and entropy (ρ and s respectively). Deriving the equations of motion for this system can be derived through the principle of least action, i.e. minimising

$$S = \int L\,\mathrm{d}t, \tag{2.27}$$

where S is the action. We therefore wish to obtain equations for which S is unchanged by a small change in the particle coordinates, which we can write as $\delta S = \int \delta L\,\mathrm{d}t = 0$.

Therefore, if we assume that the Lagrangian is differentiable by $\mathbf{r}$ and $\mathbf{v}$ we have

$$\delta S = \int \left(\frac{\partial L}{\partial \mathbf{v}} \cdot \delta \mathbf{v} + \frac{\partial L}{\partial \mathbf{r}} \cdot \delta \mathbf{r} \right) \mathrm{d}t = 0, \tag{2.28}$$

$$= \int \left\{ \left[-\frac{\mathrm{d}}{\mathrm{d}t} \left(\frac{\partial L}{\partial \mathbf{v}} \right) + \frac{\partial L}{\partial \mathbf{r}} \right] \cdot \partial \mathbf{r} \right\} \mathrm{d}t, + \left[\frac{\partial L}{\partial \mathbf{v}} \cdot \partial \mathbf{r} \right]_{t_0}^{t} = 0. \tag{2.29}$$

Assuming that the variation vanishes at the start and end times then we have shown that the equations of motion are solutions to the Euler-Lagrange equation

$$\frac{\mathrm{d}}{\mathrm{d}t} \left(\frac{\partial L}{\partial \mathbf{v}_i} \right) + \frac{\partial L}{\partial \mathbf{r}_i} = 0, \tag{2.30}$$

shown here for a particle, i. In deriving this equation we have made two assumptions; the first being that the Lagrangian is smooth and differentiable (ignoring the possibility of discontinuities in initial conditions), and the second being that we have neglected the imperfections in the discrete numerical integration in time. Computing the derivatives in Equation 2.30 using Equation 2.26, we begin by writing

$$\frac{\partial L}{\partial \mathbf{v}_i} = m_i \mathbf{v}_i \qquad \frac{\partial L}{\partial \mathbf{r}_i} = -\sum_j m_j \left. \frac{\partial u_j}{\partial \rho_j} \right|_s \frac{\partial \rho_j}{\partial \mathbf{r}_i}, \tag{2.31}$$

where we have again assumed the fluid is dissipationless (s is constant). In order to move forward with the right-hand differentials we must consider the first law of thermodynamics

$$\mathrm{d}U = T\,\mathrm{d}S - P\,\mathrm{d}V, \tag{2.32}$$

where $\delta Q \equiv T\,\mathrm{d}S$ is the heat added to the system per unit volume and $\delta W \equiv P\,\mathrm{d}V$ is the pressure work done by expansion/compression of the fluid. As we are working in terms of quantities per unit mass and in SPH we calculate the density via $V = m/\rho$ (giving the change in volume as $\mathrm{d}V = -m/\rho^2 \mathrm{d}\rho$), we rewrite Equation 2.32 as

$$\mathrm{d}u = T\,\mathrm{d}s + \frac{P}{\rho^2}\mathrm{d}\rho, \tag{2.33}$$

or more conveniently as the change in specific thermal energy,

$$\left. \frac{\partial u_j}{\partial \rho_j} \right|_s = \frac{P}{\rho^2}. \tag{2.34}$$

Turning now to the density gradient term in Equation 2.31 we must make our first direct reference to the kernel interpolation method underpinning SPH. Taking the gradient of

the density estimate of particle j with respect to the coordinates of particle i yields

$$\frac{\partial \rho_j}{\partial \mathbf{r}_i} = f_j \sum_k m_k \frac{\partial W_{jk}(h_j)}{\partial \mathbf{r}_i}(\delta_{ji} - \delta_{ki}), \tag{2.35}$$

where we have introduced the shorthand $W_{jk}(h_j) \equiv W(\mathbf{r}_j - \mathbf{r}_k, h_j)$, δ_{ji} is the Dirac delta function and we have assumed the smoothing length is a function of density giving

$$f_i \equiv \left[1 - \frac{\partial h_i}{\partial \rho_i}\frac{\partial \rho_i}{\partial h_i}\right]^{-1}, \tag{2.36}$$

$$\equiv \left[1 - \frac{\partial h_i}{\partial \rho_i}\sum_j m_j \frac{\partial W_{ij}(h_i)}{\partial h_i}\right]^{-1}. \tag{2.37}$$

Under the standard SPH relationship, (Equation 2.20) the above derivative is simply

$$\frac{\partial h}{\partial \rho} = -\frac{h}{\rho d} \tag{2.38}$$

where d is the number of spatial dimensions. Finally we combine Equations 2.34, 2.35 and 2.31 obtaining

$$\frac{\partial L}{\partial \mathbf{r}_i} = -\sum_j m_j f_j \frac{P_j}{\rho_j^2} \sum_k m_k \frac{\partial W_{jk}(h_j)}{\partial \mathbf{r}_i}(\delta_{ji} - \delta_{ki}), \tag{2.39}$$

which allows us to write the equations of motion derived from the Euler-Lagrange equation, as

$$\frac{\mathrm{d}\mathbf{v}_i}{\mathrm{d}t} = -\sum_j m_j \left[f_i \frac{P_i}{\rho_i^2}\frac{\partial W_{ij}(h_i)}{\partial \mathbf{r}_i} + f_j \frac{P_j}{\rho_j^2}\frac{\partial W_{ij}(h_j)}{\partial \mathbf{r}_i}\right]. \tag{2.40}$$

For a constant smoothing length this simplifies to the standard SPH expression (Monaghan 1992)

$$\frac{\mathrm{d}\mathbf{v}_i}{\mathrm{d}t} = -\sum_j m_j \left(\frac{P_i}{\rho_i^2} + \frac{P_j}{\rho_j^2}\right) \nabla_i W_{ij}. \tag{2.41}$$

At this point we note that in the above formulation of SPH (and the one employed in this work) there is a non-zero pressure force acting on particles even when no pressure gradient exists. This gives rise to a spurious 'surface tension' across boundaries of gas at different phases which dampens mixing and prevents SPH from treating many instabilities such as Kelvin-Helmholtz and Rayleigh-Taylor instabilities properly (see e.g. Ritchie & Thomas 2001; Agertz et al. 2007; Read et al. 2010; Read & Hayfield 2012; Sijacki et al. 2012; Saitoh & Makino 2013). Clearly this is a weakness of the method and eliminating the spurious force is an area of active research. Finally we move on to the derivation of

the energy equation. Through the combination of Equations 2.19 and 2.34 we can write

$$\frac{\mathrm{d}u_i}{\mathrm{d}t} = \frac{P_i}{\rho_i^2}\frac{\mathrm{d}\rho_i}{\mathrm{d}t}, \tag{2.42}$$

$$\frac{\mathrm{d}u_i}{\mathrm{d}t} = f_i\frac{P_i}{\rho_i^2}\sum_j m_j(\mathbf{v}_i - \mathbf{v}_j)\cdot\nabla_i W_{ab}(h_a), \tag{2.43}$$

completing the set of equations defining the fluid. We now write again for convenience the set of three equations which specify an inviscid fluid modelled using SPH,

$$\rho(\mathbf{r}_i) = \sum_j m_j W(\mathbf{r}_i - \mathbf{r}_j, h_i), \tag{2.44}$$

$$\frac{\mathrm{d}\mathbf{v}_i}{\mathrm{d}t} = -\sum_j m_j\left[f_i\frac{P_i}{\rho_i^2}\frac{\partial W_{ij}(h_i)}{\partial \mathbf{r}_i} + f_j\frac{P_j}{\rho_j^2}\frac{\partial W_{ij}(h_j)}{\partial \mathbf{r}_i}\right], \tag{2.45}$$

$$\frac{\mathrm{d}u_i}{\mathrm{d}t} = f_i\frac{P_i}{\rho_i^2}\sum_j m_j(\mathbf{v}_i - \mathbf{v}_j)\cdot\nabla_i W_{ab}(h_a), \tag{2.46}$$

We note this discretised form of the equations explicitly conserves energy, momentum and angular momentum (see Price 2012 for a proof), as was implied by the use of the Lagrangian.

Practically, we are free to choose whether to numerically evolve either the internal energy or entropy, although it is arguably advantageous to evolve the entropy as it is computationally cheaper and eliminates time integration errors in Equation 2.43 (Springel 2010b), this is the approach taken in GADGET-2. So far we have discussed the purely inviscid form of the SPH equations, it is often useful for astronomical applications of SPH to introduce an *artificial* viscosity term to allow for the presence of shocks even when the microscopic properties of the gas are unknown. At shock fronts the differential form of the Euler equations may no longer be applied and we must instead consider their integral form, yielding the Rankine-Huginot jump conditions which relate the properties either side of the discontinuity. As an attempt to model the generation of entropy at such a shock front, it is common to add an artificial viscosity term to dampen the kinetic motion of particles and generate heat/entropy. In order to reduce spurious damping of gas motions we wish for the new viscosity term to activate only in truly shocking regions, a non-trivial problem. The artificial viscous force is often added to the equation of motion, Equation 2.40 as

$$\left.\frac{\mathrm{d}\mathbf{v}_i}{\mathrm{d}t}\right|_{\mathrm{visc}} = -\sum_j m_j\Pi_{ij}\overline{W}_{ij}, \tag{2.47}$$

where Π_{ij} is the viscosity factor and $\overline{W}_{ij} = [W_{ij}(h_i) + W_{ij}(h_j)]/2$ is the symmetrised ker-

nel. Given that the viscosity factor is chosen to be symmetric, the viscous force between the two particles will be anti-symmetric, meaning that linear and angular momentum are still conserved. In order to conserve total energy we need to account for the work done in the thermal energy of the gas

$$\left.\frac{\mathrm{d}u_i}{\mathrm{d}t}\right|_{\mathrm{visc}} = \frac{1}{2}\sum_j m_j \Pi_{ij}(\mathbf{v}_i - \mathbf{v}_j)\cdot\nabla_i \overline{W}_{ij}. \tag{2.48}$$

It is often convenient to consider the entropy form of Equation 2.43 when including the artificial viscosity. If we assume a form for the equation of state (EoS) of the gas

$$P_i = A_i(s)\rho_i^{\gamma} = (\gamma - 1)\rho_i u_i, \tag{2.49}$$

where A_i is an entropic function and γ is the adiabatic index (usually assumed to be $5/3$, the value for an ideal monatomic gas), we may write

$$u_i = \frac{A_i}{\gamma - 1}\rho^{\gamma-1}. \tag{2.50}$$

This, and using Equation 2.42 then gives the entropy change due to the artificial viscosity

$$\frac{\mathrm{d}A_i}{\mathrm{d}t} = \frac{\gamma-1}{\rho^{\gamma-1}}\left(\frac{\mathrm{d}u_i}{\mathrm{d}t} - \frac{P}{\rho^2}\frac{\mathrm{d}\rho}{\mathrm{d}t}\right), \tag{2.51}$$

$$= \frac{\gamma-1}{\rho^{\gamma-1}}\left.\frac{\mathrm{d}u_i}{\mathrm{d}t}\right|_{\mathrm{visc}}, \tag{2.52}$$

or in a similar form to Equation 2.48, as

$$\left.\frac{\mathrm{d}A_i}{\mathrm{d}t}\right|_{\mathrm{visc}} = \frac{1}{2}\frac{\gamma-1}{\rho^{\gamma-1}}\sum_j m_j \Pi_{ij}(\mathbf{v}_i - \mathbf{v}_j)\cdot\nabla_i \overline{W}_{ij}. \tag{2.53}$$

The form of the viscosity factor itself is relatively unconstrained, however a commonly employed function (Springel 2010b; a modified form of the original by Monaghan & Gingold 1983) is

$$\Pi_{ij} = \begin{cases} (\alpha c_{ij}\mu_{ij} + \beta\mu_{ij}^2)/\rho_{ij} & \text{if } \mathbf{v}_{ij}\cdot\mathbf{r}_{ij} < 0, \\ 0 & \text{otherwise,} \end{cases} \tag{2.54}$$

where

$$\mu_{ij} = \frac{h_{ij}\mathbf{v}_{ij}\cdot\mathbf{r}_{ij}}{|\mathbf{r}_{ij}|^2 + \varepsilon h_{ij}^2}, \tag{2.55}$$

we have denoted the arithmetic means of the smoothing length and density as h_{ij} and ρ_{ij}

respectively and c_{ij} is the mean sound speed of the two particles. The tuning parameters $\alpha(\simeq 0.5-1.0)$ and β set the strength of the viscosity (with the common choice $\beta = 2\alpha$), whilst $\varepsilon \simeq 0.1$ is a softening parameter included to prevent singularities. Here the artificial viscosity is a combination of a bulk and Von Neumann-Richtmyer viscosities, is always positive definite and vanishes for solid body rotation. The artificial viscosity as implemented in GADGET-2, however, is the improved formulation based on the Riemann problem presented by Monaghan (1997), which weights the viscous force towards particles with small separations. This parametrisation makes use of a signal velocity between two particles, $v_{ij}^{\rm sig} = \varepsilon_i + \varepsilon_j - 3w_{ij}$, and may be written as

$$\Pi_{ij} = -\frac{\alpha}{2}\frac{v_{ij}^{\rm sig} w_{ij}}{\rho_{ij}}, \tag{2.56}$$

where $w_{ij} = \mathbf{v}_{ij}\cdot\mathbf{r}_{ij}/|\mathbf{r}_{ij}|$ is the radial component of the relative velocity. However, in each of the two above forms the viscosity is spuriously active for pure shear flows, an aspect which may be solved by the inclusion of a Balsara switch (Balsara 1995; see also Cullen & Dehnen 2010) as utilised by GADGET-2.

Evolving either Equation 2.43 or 2.51 numerically requires the determination of an optimal time-step. GADGET-2 evolves all particles on independent time-steps, therefore it is important to ensure that the hydrodynamical forces are properly resolved by enforcing the Courant criterion

$$\Delta t_i \leq C_{\rm CFL}\frac{h_i}{c_i}, \tag{2.57}$$

where c_i is the sound speed of particle i. The fractional dimensionless parameter, $C_{\rm CFL} \sim 0.1-0.3$, adds a safety buffer to account for sudden changes in the sound speed. It has been shown that in environments with extreme spatial gradients in the sound speed such as near an explosion, the individual time-steps in GADGET may mean that particles cannot react to nearby changes as they are dormant when the explosion occurs, set on a longer time-step. A proposed method of overcoming this is to have the time-step of a particle informed by the time-steps of those around it. The so-called Saitoh and Makino (Saitoh & Makino 2009) switch, for example limits the spatial gradient in time-steps, so particles will be set on a short time-step if those around it are evolving rapidly (see also Durier & Dalla Vecchia 2012 for a GADGET-2 implementation).

Up to this point we have presented the fluid equations neglecting self-gravity. For astrophysical applications it is clearly necessary to include this term in the Lagrangian

$$L = \sum_i \left[\frac{1}{2}m_i\mathbf{v}_i^2 - m_i u_i(\rho_i, s_i)\right] - \frac{G}{2}\sum_{ij} m_i m_j \phi(r_{ij}, \varepsilon_{{\rm soft},j}), \tag{2.58}$$

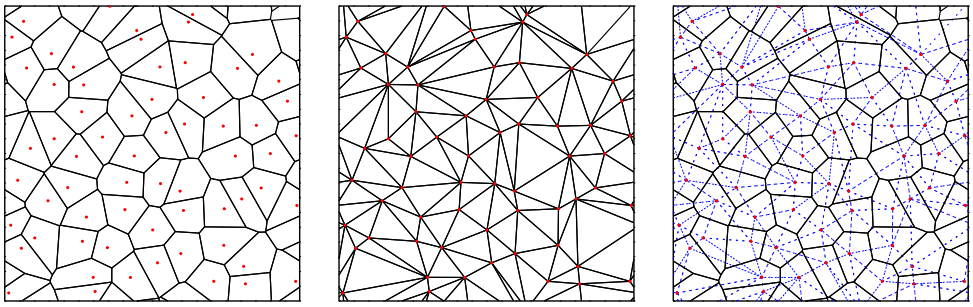

Figure 2.3: Example 2D Voronoi and Delauney tessellations for an arbitrary distribution of $N = 64$ particles with periodic boundary conditions. The unique Voronoi tessellation is shown in the left panel, the corresponding Delauney tessellation in the centre, and the superposition in the right hand panel (Delauney tessellation shown as blue dashed lines). This figure is reproduced from Springel (2010a).

where the right hand term is the gravitational field, $\phi(\mathbf{r}_{ij}, \varepsilon_{\mathrm{soft},j})$ is the corresponding potential and $\varepsilon_{\mathrm{soft},j}$ is the gravitational force softening length. The change imposed on the Lagrangian leads to an additional term in the equation of motion due to the gravitational force

$$m_i \left.\frac{\partial \mathbf{v}_i}{\partial t}\right|_{\mathrm{grav}} = -\frac{\partial E_{\mathrm{pot}}}{\partial \mathbf{r}_i}, \tag{2.59}$$

$$= -\sum_j G m_i m_j \frac{\mathbf{r}_{ij}}{r_{ij}} \frac{1}{2}\left[\frac{\partial \phi(r_{ij}, \varepsilon_i)}{\partial r_{ij}} + \frac{\partial \phi(r_{ij}, \varepsilon_{\mathrm{soft},j})}{\partial r_{ij}}\right] - \frac{1}{2}\sum_{jk} G m_j m_k \frac{\partial \phi(r_{jk}, \varepsilon_{\mathrm{soft},j})}{\partial \varepsilon_{\mathrm{soft},j}} \frac{\partial \varepsilon_{\mathrm{soft},j}}{\partial \mathbf{r}_i}. \tag{2.60}$$

The first term describes the ordinary gravitational force where the interaction is symmetrised by taking the average of the forces, and the second term gives the additional force component arising fue to the varying softening lengths.

Before discussing alternate methods we note that many aspects of SPH are currently experiencing advances, improving the accuracy and verisimilitude of the method. A full discussion of the topic is beyond this document, however key areas of advancement include the development of pressure-entropy (e.g. Ritchie & Thomas 2001; Hopkins 2013) or pressure-energy SPH, alternative kernels (e.g. Dehnen & Aly 2012) and the inclusion of artificial diffusion (e.g. Dalla Vecchia et al.; in prep.) or an alternative dissipation (e.g. Read & Hayfield 2012) switch.

AMR and Voronoi solvers

We now move on to discuss an alternative set of hydrodynamic solvers, so-called grid (also mesh) codes. Conventionally grid codes model the fluid in the Eulerian approach, that is solving the Euler equations in the 'lab frame'. In the most simplistic case grid codes utilise an evenly-spaced spatial grid upon which the fluid quantities are calculated. However, an even mesh leads to under-resolved flows when regions of high density form, a common occurrence in astrophysical problems which often model gravitational collapse. If the region of interest is known a priori this problem may be overcome by defining an unevenly spaced grid, with additional resolution where desired. However this is not always possible, in which case an Adaptive Mesh Refinement (AMR) method may be employed to increase resolution on the fly; this approach used by most modern astrophysical mesh codes. AMR codes dynamically split cells into smaller, higher resolution regions whenever necessary, as defined by multiple criteria such as gas/DM density, the presence of shocks, cooling time and the Jeans length.

AMR codes typically (e.g. FLASH, Fryxell et al. 2000; ENZO, O'Shea et al. 2004) solve the fluid equations outside of shocks using the piece-wise parabolic method (PPM; Colella & Woodward 1984; Bryan et al. 1995) , a higher order version of Godunov's method (Godunov 1959) with third-order piece-wise parabolic interpolation. This is then combined with a non-linear Riemann solver for treating entropy changes in shock-fronts. In Godunov's method the flow is divided into a series of slabs, each corresponding to a grid cell and the discontinuities between slabs are then solved using Riemann's shock tube problem at each cell wall. Solving the fluid equations in this way leads to more accurate treatment of shocks and mixing between fluids when compared to SPH. The poor performance in shock capturing is due to the SPH method smoothing over density discontinuities (Ritchie & Thomas 2001), and the spurious surface tension in the standard SPH formalism inhibits mixing, this is particularly evident when testing for the Rayleigh-Taylor instability (e.g. Agertz et al. 2007; Read et al. 2010; Saitoh & Makino 2013).

The traditional approach of utilising fixed grid codes does, however, suffer its own drawbacks. Arguably the most severe of these is the lack of Galilean invariance meaning that the hydrodynamics solver is sensitive to bulk velocities and can introduce multiple errors (see e.g. Tasker et al. 2008 for a comparison of SPH and AMR codes). For example, situations where gas is experiencing bulk flows with energy of order the thermal energy (common in cosmological problems) are susceptible to errors in pressure and temperature due to inherently limited machine precision. To address this shortcoming ENZO solves both the internal gas energy equation and total energy equation everywhere at all times. Their use of the *dual energy formalism* (Bryan et al. 1995) ensures correct entropy at

shocks, pressure and temperature in hypersonic flows. However, bulk velocities are a difficulty for AMR since the 'refined' area will have to move with the gas structures of interest and it is difficult to accurately predict their motion across the grid. A further problem lies in AMR's implicit mixing within cells which provides a spurious source of entropy. A practical problem relevant to cosmological simulations, is difficulty in capturing the (numerous) small initial density fluctuations properly at high redshift as they will be smoothed by the grid scale. This leads to reduced growth of the first collapsing DM structures.

An ideal hypothetical hydrodynamics solver for cosmological problems could be considered as a code with the Lagrangian method's moving resolution elements and automatic mass-dependent adaptive resolution, which may be combined with the discrete cell boundaries which allows the capture of shocks and eliminates spurious surface tension; clearly an ideal code would also not introduce unforeseen numerical errors. A potential avenue for advancement is offered by use of a Voronoi tessellation of a discrete set of free-moving points as implemented by AREPO (Springel 2010a) and the Voronoi Particle Hydrodynamics (VPH) code of Heß & Springel 2010.

A Voronoi tessellation creates a system of non-overlapping cells around a set of sites (particles) such that each cell contains the region of space closer to it than any other site. Following this definition leads to the creation of polyhedra (in 3D; polygons in 2D), with faces (edges) equidistant to the pair of mesh-generating points. Constructing the Voronoi tessellation requires the consideration of its topological dual, the Delauney tessellation. Simplistically put, whereas the Voronoi tessellation surrounds the sites with cell faces, the Delauney tessellation links them in a non-overlapping fashion. By definition, the Delauney tessellation connects the mesh-generating points to one another ensuring no cell contains another point; in 2D this corresponds to a triangulation of the domain, whereas in 3D tetrahedra are tessellated. The Voronoi and Delauney tessellations therefore have a duality, whereby the line joining two points in a Delauney tessellation is orthogonal to the edge/face of a Voronoi cell in two and three dimensions respectively. Fig. 2.3 is a schematic diagram of a 2D particle distribution and the corresponding Voronoi and Delauney tessellations.

Construction of the mesh is optimised through parallelisation and use of Peano-Hilbert space filling curves as well as a Barnes-Hut oct tree for neighbour finding; resulting in an overall scaling of $N \log N$ (noting SPH has $N \log N_{\rm ngb}$ scaling) and consumes 'slightly more' time than in an SPH code (Springel 2010a).

We now move on to briefly outline the theory supporting the hydrodynamic method employed by AREPO. Euler's hydrodynamical equations for an inviscid fluid (Equa-

tions 2.22, 2.23 and 2.24) may be written in a compact form by introducing a state vector

$$\mathbf{U}(\mathbf{x},t) = \begin{pmatrix} \rho \\ \rho\mathbf{v} \\ \rho e \end{pmatrix}, \tag{2.61}$$

where $\mathbf{v}$ is the velocity field, u is the internal (thermal) energy per unit mass and $e = u + \mathbf{v}^2/2$ is the total energy per unit mass. From this you can then define a flux function

$$\mathbf{F}(\mathbf{U}) = \begin{pmatrix} \rho\mathbf{v} \\ \rho\rho\mathbf{v}\mathbf{v}^T + P \\ \rho(\rho e + P)\mathbf{v} \end{pmatrix}, \tag{2.62}$$

combined with the usual equation of state to obtain the pressure, $P = (\gamma - 1)\rho u$. It is then possible to write the Euler equations in the compact form

$$\frac{\partial \mathbf{U}}{\partial t} + \nabla \cdot \mathbf{F} = 0, \tag{2.63}$$

the components of which are conservation laws for mass, momentum and energy respectively.

AREPO employs a *finite-volume* strategy where the system is discretised by subdividing it into a finite number of cells. Integrating over the fluid in a cell, i, allows us to define total mass, momentum and energy within the cell

$$\mathbf{Q}_i = \begin{pmatrix} m_i \\ \mathbf{p}_i \\ E_i \end{pmatrix} = \int_{V_i} \mathbf{U}\, \mathrm{d}V. \tag{2.64}$$

We can then calculate the change of these quantities in time with the help of Euler's equations. In order to rewrite the Euler equations into a form which we can solve, we first use Gauss' theorem to convert from a volume to a surface integral

$$\frac{\mathrm{d}\mathbf{Q}_i}{\mathrm{d}t} = -\int_{\partial V_i} [\mathbf{F}(\mathbf{U}) - \mathbf{U}\mathbf{w}^T]\, \mathrm{d}\mathbf{n}. \tag{2.65}$$

Here we have a term accounting for velocity of the cell boundary $\mathbf{w}$, for Eulerian codes where the cells are fixed $\mathbf{w} = 0$, and in the opposite limit $\mathbf{w} = \mathbf{v}$ for a fully Lagrangian method. Although the points move with the flow in AREPO it is not possible to ensure this is true at all points on the cell surface due to finite resolution. The Euler equations

may correspondingly be written in terms of the flux as

$$\mathbf{F}_{ij} = \frac{1}{A_{ij}} \int_{A_{ij}} [\mathbf{F}(\mathbf{U}) - \mathbf{U}\mathbf{w}^T] \, \mathrm{d}\mathbf{A}_{ij}, \tag{2.66}$$

so, combining with Equation 2.65, we obtain the Euler equations in finite-volume form

$$\frac{\mathrm{d}\mathbf{Q}_i}{\mathrm{d}t} = -\sum_j A_{ij}\mathbf{F}_{ij}. \tag{2.67}$$

This in turn leads to a conservative time discretisation

$$\mathbf{Q}_i^{(n+1)} = \mathbf{Q}_i^{(n)} - \Delta t \sum_j A_{ij}\hat{\mathbf{F}}_{ij}^{(n+1/2)}, \tag{2.68}$$

where $\hat{\mathbf{F}}_{ij}$ is now a time averaged approximation to the true flux and $\mathbf{Q}^{(n)}$ describes the state of the system on step n. In practice, solving for the flux consistently and accurately is difficult. Great care must be taken when considering the frame in which the Riemann problem is solved. A similar care is required when estimating the gradients of the field quantities between points, an important step in determining the surface values used in the Riemann solver. AREPO utilises a method which obtains gradients exact to linear order, an improvement on classical AMR codes.

The mesh-generating points in AREPO then move with the bulk fluid flow, although in contrast to a fully Lagrangian scheme (e.g. VPH, SPH) the cell masses need not remain constant. In fact in the extreme limit that the cells are held spatially fixed, AREPO is similar to a classical MUSCL-Hancock scheme (e.g. van Leer 1984, 2006).

So far we have discussed Voronoi tessellations from the point of view of AREPO, but another approach to solving the hydrodynamical equations, conceptually intermediate between AREPO and SPH, exists which too uses Voronoi tessellations. Combining the density estimate of Voronoi tessellations with the Lagrangian basis, and constant fluid-element mass, of SPH gives the VPH method of Heß & Springel (2010). Particles in VPH move due to pair-wise pressure forces (and gravitational acceleration) and have no mass flux between them, as in SPH. It is found that VPH benefits from an improved resolution of density contrasts and the removal of spurious surface tension which affects SPH, this leads to a more accurate treatment of mixing. However, the cell construction also has drawbacks. The movement of particles within cells, especially during gravitational collapse, can lead to noisy density estimates or even cell interpenetration. (Solving this problem in AREPO is much simpler as the movement of the particles does not affect the hydrodynamics directly, simply following the flow for the purposes of cell construc-

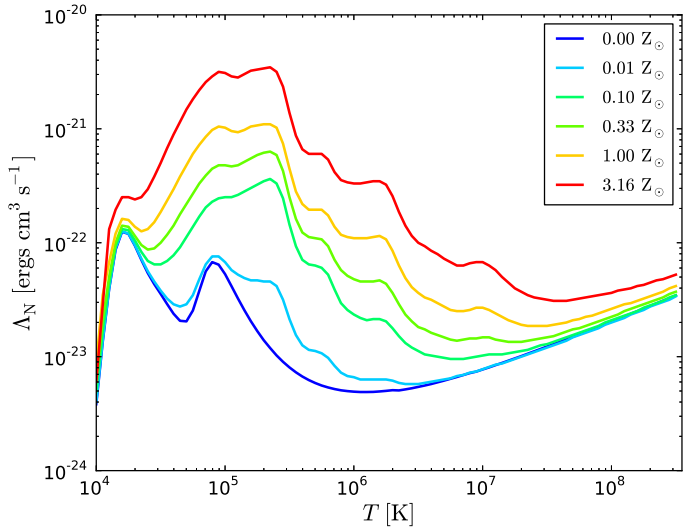

Figure 2.4: The adopted cooling function from Sutherland & Dopita (1993). We use the tabulated net cooling function computed across a range of temperatures and gas metallicities ranging from $Z = 0$ to $3.16\,\mathrm{Z}_\odot$, performing a bilinear interpolation for the desired value. Λ_N is the net cooling rate due to collisional line radiation, free-free and two-photon continuum, recombination processes, photoionization heating, collisional ionization and Compton heating, normalised for the ion and electron density.

tion.) This may be overcome either through modification of the artificial viscosity to act as a pair-wise restoring force, or by changing the underlying Lagrangian (Heß & Springel 2010). Although applying these changes improves the situation, they have the drawback of harming the code's ability to resolve Kelvin-Helmholtz instabilities as they re-introduce a spurious force inhibiting mixing.

2.2 Sub-grid modelling

All simulations discussed in the forthcoming chapters are performed using an independently developed and substantially modified version of the publicly available N-body + SPH (see Section 2.1.2) code GADGET-2 (Springel 2005). We outline our method for setting up disc galaxies and the physics used in the simulations here.

2.2.1 Radiative cooling, ISM & star-formation

Gas is allowed to cool radiatively following the method described by Kay (2004), who adopted the approach of Thomas & Couchman (1992). We utilise a tabulated equilibrium cooling function from Sutherland & Dopita (1993) for a metallicity $Z = 0.3\,\mathrm{Z}_\odot$ gas.

Fig. 2.4 shows the cooling function computed across a range of temperatures for metallicities ranging from $Z = 0$ to $3.16\,\mathrm{Z}_{\odot}$. The temperature of the gas is not permitted to fall below a critical value $T_{\mathrm{c}} = 10^4\,\mathrm{K}$, at which point we assume the gas temperature is maintained by the meta-galactic UV background.

The ISM and star formation model employed is that of Schaye & Dalla Vecchia (2008). We assume that the ISM is an ideal multi-phase gas which may be described by a polytropic equation of state above a critical value for the number density of hydrogen, $n_{\mathrm{H,c}}$

$$P = \begin{cases} A n_{\mathrm{H}}^{\gamma_{\mathrm{eff}}} & \text{if } n_{\mathrm{H}} > n_{\mathrm{H,c}}, \\ n_{\mathrm{H}} k_{\mathrm{B}} T_{\mathrm{c}} / (X\mu) & \text{otherwise,} \end{cases} \tag{2.69}$$

where A is a constant set by ensuring the pressure is continuous across the boundary $n_{\mathrm{H}} = n_{\mathrm{H,c}}$ and $\gamma_{\mathrm{eff}} = 4/3$. The critical density is set to $n_{\mathrm{H,c}} = 0.1\mathrm{cm}^{-3}$, the mean molecular weight, $\mu = 0.59$ and the hydrogen mass fraction, $X = 0.76$, the latter two having primordial values. Gas may leave the equation of state when it receives (AGN or supernova) feedback energy or if its thermal energy increases by $0.5\,\mathrm{dex}$ in a single time-step (as in Booth & Schaye 2009). Allowing particles to leave the equation of state in this fashion prevents artificial damping of feedback driven outflows.

A gas particle lying on the equation of state may be converted to a collisionless star particle representing a simple stellar population (SSP) described by a Salpeter Initial Mass Function (IMF). We again follow Schaye & Dalla Vecchia (2008) for our method, and as such our star formation implementation recovers the Kennicutt-Schmidt (Kennicutt 1998) law by construction (see Fig. 2.5). The volumetric star formation rate is designed to match the observed Kennicutt-Schmidt law (Kennicutt 1998) for a galaxy with disc gas fraction, $f_{\mathrm{g}} = 1$ (the commonly-employed value in cosmological simulations). Specifically, the law numerically reproduced here is

$$\dot{\Sigma}_{\star} = 2.5 \times 10^{-4} \mathrm{M}_{\odot}\,\mathrm{yr}^{-1}\mathrm{kpc}^{-2} \left(\frac{\Sigma_{\mathrm{g}}}{1\,\mathrm{M}_{\odot}\mathrm{pc}^{-2}} \right)^{1.4}, \tag{2.70}$$

where $\dot{\Sigma}_{\star}$ is the star formation rate surface density and Σ_{g} is the gas surface density. Fig. 2.5 demonstrates the good match between simulated and observed star formation rates, once the latter is adjusted for the disc gas fraction adopted for our initial conditions ($f_{\mathrm{g}} = 0.3$, lower than the value assumed in deriving the volumetric star formation rate; see Schaye & Dalla Vecchia 2008 for details) [1].

[1] We have also checked that our implementation reproduces the star formation rates found by Schaye & Dalla Vecchia (2008) when we adopt a zero metallicity gas, for both Salpeter and Chabrier IMFs.

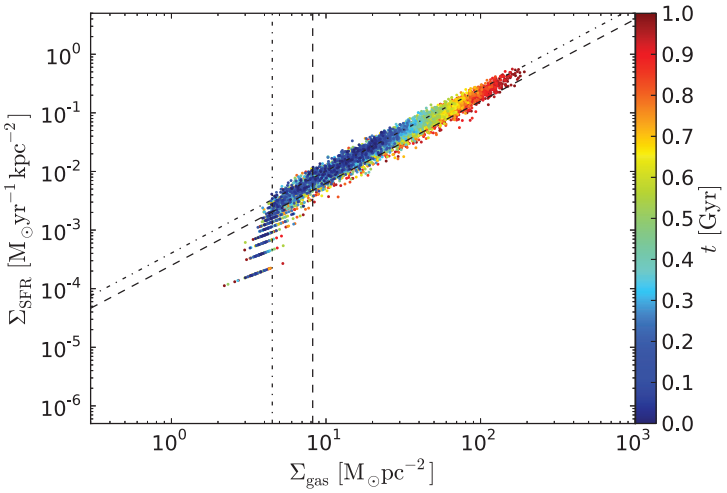

Figure 2.5: Recovered Kennicutt-Schmidt relation for a high resolution disc galaxy evolved for a time, $t = 1\,\mathrm{Gyr}$. Each point represents the star formation rate density averaged within an annulus centred on the galaxy rotation axis, while the colour represents the age of these stars at the end of the simulation (with red points being the oldest stars). The dashed lines show the input Kennicutt-Schmidt relation and density cut-off, while dot-dashed lines show these adjusted for $f_\mathrm{g} = 0.3$ (the value used in our initial conditions).

2.2.2 Supernova feedback

The supernova feedback implementation described here is motivated by the desire to ensure high temperature gas is produced which is more likely to influence the galaxy's evolution and is in this way similar to the recent work of Dalla Vecchia & Schaye (2012) (see also Kay et al. 2003). Gas with $T \gg 10^6\,\mathrm{K}$ cools more slowly than cooler gas allowing the heated material to interact hydrodynamically with its neighbours and escape the star forming region before cooling. By reducing the mass loading of the gas, we are able to utilise the energy liberated through supernovae to heat particles to a high temperature.

We assume that a fraction of the stars in each SSP will end their lives as type II supernovae (SNII), releasing energy to the environment. This typically occurs on a short timescale which we assume to be negligible. Therefore upon the formation of a star particle we promptly release energy equivalent to a temperature T_SN to the nearest N_heat gas particles to represent SNII feedback,

$$T_\mathrm{SN} = (\gamma - 1)\frac{\mu m_\mathrm{H}}{k_\mathrm{B}} u_\mathrm{SN}. \tag{2.71}$$

The amount of energy provided by SNII per unit mass of stars formed is calculated as

$$\begin{aligned} u_{\rm SN} &= E_{\rm SN}\, n_{\rm SNII}, \\ &= E_{\rm SN} \int_{M_0}^{M_1} \Phi(M)\, {\rm d}M, \\ &= 5.6 \times 10^{15}\, {\rm erg\, g^{-1}} \left(\frac{E_{\rm SN}}{10^{51}{\rm erg}}\right) \left(\frac{n_{\rm SNII}}{1.11 \times 10^{-2} {\rm M_\odot^{-1}}}\right), \end{aligned} \tag{2.72}$$

where $E_{\rm SN}$ is the energy per Type II supernova and $n_{\rm SNII}$ is the number of supernovae per unit mass, obtained by integrating over the IMF (Φ) between $M_0 = 0.1\,{\rm M_\odot}$ and $M_1 = 100\,{\rm M_\odot}$. The specific energy change imposed on the local gas is then

$$u_{\rm heat} = \epsilon_{\rm SN} \left[\frac{m_{\rm star}}{m_{\rm gas} N_{\rm heat}}\right] u_{\rm SN}, \tag{2.73}$$

where $\epsilon_{\rm SN}$ is a dimensionless supernova efficiency parameter (accounting for small-scale energy losses) and the term in brackets is the inverse mass loading factor (heating $N_{\rm heat}$ gas particles of mass $m_{\rm gas}$ for every new star particle with mass $m_{\rm star}$). The heating temperature can then be expressed as

$$\begin{aligned} T_{\rm heat} \approx 2.7 \times 10^7\, {\rm K} &\left(\frac{\epsilon_{\rm SN}}{N_{\rm heat}}\right) \left(\frac{m_{\rm star}}{m_{\rm gas}}\right) \\ &\left(\frac{E_{\rm SN}}{10^{51}{\rm erg}}\right) \left(\frac{\mu}{0.59}\right) \left(\frac{n_{\rm SNII}}{1.11 \times 10^{-2} {\rm M_\odot^{-1}}}\right). \end{aligned} \tag{2.74}$$

For the purpose of our fiducial simulations we set $T_{\rm heat} = 10^7\,{\rm K}$ and $N_{\rm heat} = 1$, yielding an assumed efficiency of $\epsilon_{\rm SN} \approx 0.4$ (this choice is investigated further in Section 3.4.5). When heated by supernovae, a gas particle is removed from the equation of state on its current time-step and tagged as a wind particle. However, should the particle meet the conditions for joining the equation of state on any subsequent time-step, it will return as normal.

2.2.3 Black hole growth and AGN feedback

There exists a large variety of work employing different methods for simulating AGN and their effects on the host galaxy. Here, we focus on the most widely used implementations. The models we investigate here are namely those by Springel et al. (2005); Booth & Schaye (2009); and a novel method based on the finite accretion radius model of Power et al. (2011).

The AGN models may be simplistically broken down into three processes: formation,

growth and feedback. The formation of black holes at high redshift is an interesting topic in itself and an active area of research, however this is beyond the scope of this work where we simply assume a galaxy contains a super-massive BH at its centre. We discuss the other two processes in turn.

Black hole growth: the Bondi method

Springel et al. (2005) and Booth & Schaye (2009) both used modified versions of the Bondi-Hoyle-Lyttleton (Hoyle & Lyttleton 1939; Bondi & Hoyle 1944; Bondi 1952) model to calculate the accretion rate onto the black hole from a surrounding gas reservoir, given by

$$\dot{M}_{\rm BH} = \alpha \frac{4\pi G^2 M_{\rm BH}^2 \rho_{\rm gas}}{(c_{\rm s}^2 + v^2)^{3/2}}, \tag{2.75}$$

where $\rho_{\rm gas}$ is the density of the surrounding gas, $c_{\rm s}$ its sound speed, and v the velocity of the BH relative to the gas. The additional factor α was added by Springel et al. (2005) to counteract an assumed underestimate for the accretion rate due to inadequate numerical resolution. Simulating the accretion fully requires proper resolution of the Bondi radius

$$r_{\rm B} \approx \frac{G M_{\rm BH}}{c_{\rm s}^2}, \tag{2.76}$$

which is considerably smaller than the force resolution in current simulations, for the case of galactic-scale black holes. Furthermore, one must also resolve the multiphase ISM and crucially its cold dense clouds, to allow accurate computation of the gas density and sound speed close to the BH.

Booth & Schaye (2009) modified the correction factor, α, arguing that the accretion is not always equally under-resolved and suggested the following scaling with density

$$\alpha = \begin{cases} 1 & \text{if } n_{\rm H} < n_{\rm H,c} \\ \left(\frac{n_{\rm H}}{n_{\rm H,c}}\right)^{\beta} & \text{otherwise,} \end{cases} \tag{2.77}$$

where $n_{\rm H,c}$ is the same critical value as for the ISM and star formation ($n_{\rm H,c} = 0.1\,{\rm cm}^{-3}$). The impact of varying the power-law index, β, was investigated by Booth & Schaye (2009) as well as varying the constant α value, as used in the more standard formalism. They found that observables are much more sensitive to the choice of α than to any reasonable change in β. We have implemented both methods as laid out in their original form.

A BH particle's mass is tracked by two variables: the *dynamical* mass which increases instantaneously when a particle is captured by the BH; and the smoothly integrated *inter-*

nal mass which is used to determine the accretion rate of the BH. In practice, the BH particle grows by stochastically capturing surrounding gas particles within the smoothing length at a rate which coarsely matches the internal black hole mass (see e.g. Di Matteo et al. 2005; Sijacki et al. 2007; Di Matteo et al. 2008; Booth & Schaye 2009). Upon accreting a particle the mass is added to that of the black hole. The potential drawback of using the SPH kernel is that gas particles may be captured at arbitrarily large distances from the sink particle due to the use of an adaptive smoothing length (discussed e.g. by Debuhr et al. 2010; Power et al. 2011).

Black hole growth: the accretion disc method

The Power et al. (2011) method does not use the Bondi-Hoyle-Lyttleton equation. Instead, it assumes that any particle which passes within a fixed accretion radius, $r_{\rm acc}$, is captured onto the *accretion disc* surrounding the BH. This mass is then moved to the BH on a viscous timescale. A key feature of this method is that, unlike the Bondi-Hoyle-Lyttleton accretion, only gas with low angular momentum is likely to be captured. In simulations lacking sufficient spatial resolution to simulate true accretion discs existing on sub-$\rm pc$ scales (e.g. Kato et al. 1998), it is favourable to set $r_{\rm acc}$ to the smallest resolvable length-scale, i.e. the gravitational softening length $\varepsilon_{\rm soft}$; this is the approach taken here ($\varepsilon_{\rm soft} = 50\,\rm pc$).

Preliminary testing of this method found it to be unphysical at the typical resolution of our simulations ($\sim 100\,\rm pc$), yielding an artificially large accretion rate, an overly-massive black hole and a large cleared-out area at the centre of the galaxy. Wurster & Thacker (2013) and Muldrew et al. (2013) attempt to overcome this problem by significantly reducing $r_{\rm acc}$ to limit mass accretion, with the precise value being varied as part of their investigation. It is, however, unphysical to take particles as point masses in this regime since capturing one whole corresponds to a gas cloud with radius of order the SPH smoothing length instantaneously collapsing onto the much smaller accretion disc. We take an alternative route by instead interpreting the accretion radius as a scale within which the captured material is gravitationally bound to the black hole system and will contribute to the mass of the accretion disc on a timescale set by the local free-fall time, $t_{\rm ff} = 1/\sqrt{G\langle\rho_{\rm gas}\rangle}$. Specifically, the gas mass is added to the disc at a rate given by

$$\frac{{\rm d}M_{\rm disc}}{{\rm d}t} = -\frac{\epsilon_{\rm ff} M_{\rm gas}(< r_{\rm acc})}{t_{\rm ff}}, \tag{2.78}$$

where $\epsilon_{\rm ff}$ is an efficiency parameter that may represent unresolved effects such as turbulence or residual angular momentum (we set $\epsilon_{\rm ff} = 0.1$, as discussed in the next section).

Motivating the large scale accretion via the free-fall timescale is similar in spirit to Hobbs et al. (2012), who did so by modifying the Bondi model. Mass is then added to the BH at the rate

$$\dot{M}_{\rm BH} = \min\left[\frac{M_{\rm disc}}{t_{\rm visc}}, \dot{M}_{\rm Edd}\right], \tag{2.79}$$

where the viscous timescale $t_{\rm visc}$ may be estimated from physical arguments and is typically set to $t_{\rm visc} \sim 10 - 100\,{\rm Myr}$ (Kato et al. 1998; Power et al. 2011; we set $t_{\rm visc} = 10\,{\rm Myr}$). For all three methods, we restrict the accretion rate to the Eddington limit

$$\dot{M}_{\rm Edd} = \frac{4\pi G M_{\rm BH} m_{\rm H}}{\epsilon_{\rm r}\sigma_{\rm T} c}, \tag{2.80}$$

where we assume the standard value for the radiative efficiency parameter, $\epsilon_{\rm r} = 0.1$.

Independent of accretion rate method, particles are numerically captured similarly to Springel et al. (2005). Particles are accreted only when the system mass (BH and accretion disc if applicable) exceeds the BH particle's dynamical mass. Accreted particles would ideally contribute momentum to the BH particle as it is clearly desirable to conserve momentum in all simulations. However we found that artificially large kicks and two-body scattering from other particles caused the black hole to become displaced from the centre of the galaxy, even in isolated quiescent galaxies. We therefore apply the approach of Di Matteo et al. (2005) and Booth & Schaye (2009) to all three methods, and re-centre the black hole particle on the neighbouring ($r_{ij} < h$) particle of minimum potential until it is a factor of 10 more massive than a single gas particle.

Feedback

The accretion rate onto the central BH is used to determine the energy budget for the AGN feedback. It is commonly assumed that a fraction of the accreted rest mass energy is released from the BH, with an additional multiplicative factor to represent the efficiency with which this then couples to the surrounding gas

$$\dot{E}_{\rm feed} = \epsilon_{\rm f} L_{\rm r} = \epsilon_{\rm f}\epsilon_{\rm r}\dot{M}_{\rm BH} c^2, \tag{2.81}$$

where $L_{\rm r}$ is the radiative luminosity, $\epsilon_{\rm r} = 0.1$ is the radiative efficiency as before and $\epsilon_{\rm f}$ is the feedback coupling efficiency.

The most accurate way to distribute this feedback energy, and the form it takes, is unclear. One method is to utilise an SPH-like approach and simply deposit the energy thermally in a kernel-weighted fashion; such an approach was taken by Springel et al. (2005). This method is numerically simple and characterises a high energy quasar radia-

tion field coupling isotropically to the surrounding gas. However, releasing the feedback energy in this way may not be able to provide gas hot enough to drive strong outflows. An alternative approach was taken by Booth & Schaye (2009). By 'bottling up' the energy it is ensured that a critical temperature change, $\Delta T_{\rm min}$, is reached before a heating event occurs. The energy which must be stored to heat $N_{\rm heat}$ gas particles by $\Delta T_{\rm min}$ is

$$E_{\rm crit} = \frac{N_{\rm heat} m_{\rm gas} k_{\rm B} \Delta T_{\rm min}}{(\gamma - 1)\mu m_{\rm H}}. \tag{2.82}$$

Once heated, it is then assumed that the gas will rise buoyantly in the ambient medium, mimicking outflows found in observations.

In the following sections we perform simulations that employ the methods for describing gas processes and feedback outlined above. Specifically, we simulate the Bondi accretion method with kernel-weighted feedback as set out by Springel et al. (2005); the Bondi method with 'strong' feedback by Booth & Schaye (2009); and the disc accretion method based on Power et al. (2011) with 'strong' feedback . We also consider a model with no AGN feedback and each model is performed both with and without supernovae.

2.3 GadgetX-2

The simulations which follow were all performed using a modified and extended version of the GADGET-2 code (Springel 2005). Specifically, the project begins with a version of the code extended to include a simple effective equation of state with star formation (Schaye & Dalla Vecchia 2008) and radiative cooling (Thomas & Couchman 1992) using the methods as discussed in Section 2.2.1.

Within this code various feedback mechanisms were incorporated as an additional entropy change calculated after the particle accelerations are computed at the end of the time-step. The BH methods discussed in the previous section are incorporated in a modular fashion so that the accretion and feedback mechanisms are fully interchangeable. We note that additional kinetic feedback methods were also incorporated into the code, however they are not investigated here and as such this is not discussed further.

The AGN accretion and feedback methods which do not utilise the ordinary SPH smoothing kernel to locate neighbours required the creation of additional neighbour-finding routines within GADGET which could act on an arbitrary particle-type. For the Booth & Schaye (2009) method (also used for the SN feedback) we utilise a neighbour-finding routine which calculates a new 'smoothing' length which contains a desired number (note, not *weighted* number as in the SPH kernel) of neighbours. In the case of feed-

back this number will be the number of particles to be heated, guaranteeing the gas nearest to the BH receives the entropy input. The GADGET code imposes a minimum smoothing length at $h = 2.8\,\varepsilon_{\rm soft}$, this is respected by the feedback routines which resort to probabilistic heating if there are more than $N_{\rm heat}$ particles within this radius.

In order to ensure that accretion onto the BH is properly resolved we impose an additional constraint on the time-step of the BH particle. We demand that the time-step is shorter than the time taken to accrete either the mass within the kernel or the BH internal mass at the current accretion rate. Specifically, the imposed limit is

$$t_{\rm BH} = a_{\rm BH}\frac{\min(m_{\rm gas}(< h), M_{\rm BH})}{\dot{M}}, \tag{2.83}$$

where $a_{\rm BH}\,(\leq 1)$ is a multiplicative factor which gives a safety margin in the case of rapid accretion rate changes ($a_{\rm BH} = 1 \times 10^{-4}$ is used throughout the following work, however this errs on the side of caution).

An additional improvement was made for the simulations in Chapters 4 and 5 where severe changes in the BH time-step were found to occur over short periods. In early tests this meant that using the duration of the previous time-step when integrating the BH mass could introduce substantial errors in some rare circumstances (which we verified did not occur in the earlier investigations). To circumvent this, the next time-step for the BH particle is calculated ahead of time within the accretion routines so that the mass can be integrated correctly even when its local environment evolves rapidly.

The code also includes several modules for additional or alternative physics not utilised here (however some have been employed in companion works) and will not be discussed in the main body of the text. These include additional BH accretion and (kinetic) feedback methods, a phase-dependent density calculation, a feedback mode switch similar to Sijacki et al. 2007 and a crude metal enrichment scheme.

Chapter 3

Simulations of disc galaxies with AGN feedback

Nothing shocks me. I'm a scientist.

DR. HENRY "INDIANA" JONES

In this chapter, we study how AGN and supernova feedback (both independently and combined) alter the star formation rate within simulations of isolated and merging disc galaxies. We particularly focus on the elements of the AGN models studied; how the assumptions made and how the implementation of the model affects both the evolution of the host galaxies and the BHs themselves.

Performing idealised simulations is a commonly employed method when studying such numerically demanding processes, allowing results to be produced with higher resolution than is normally possible in full cosmological simulations. Such systems have been used in the past to simulate a range of topics including galactic dynamics (e.g. Springel & White 1999), star formation (e.g. Schaye & Dalla Vecchia 2008), supernova feedback (e.g. Dalla Vecchia & Schaye 2008, 2012) and AGN implementations (e.g. Di Matteo et al. 2005; Debuhr et al. 2010). Our main results focus on three methods used in the literature for implementing black hole growth and AGN feedback, including a novel adaptation of the method suggested by Power et al. (2011). To simplify the interpretation of our results we adopt the same models for all other *sub-grid* physics included within our simulations (including supernova feedback, star formation and interstellar gas).

The interaction between feedback from AGN and supernovae is currently a topic of interest, as typically these two feedback mechanisms are treated separately in semi-analytic models (e.g. Bower et al. 2006; Croton et al. 2006; Guo et al. 2011). However, recent work by Booth & Schaye (2013) using cosmological hydrodynamical simulations, casts

doubt on the validity of this assumption. Their findings indicate that the combination of the two feedback processes has a weaker effect on the star formation rate than expected if they were acting independently. Due to the uncertainty in our present modelling of AGN feedback, it may be premature to assume that this interplay between AGN and supernovae is a physical effect and is not merely an outcome of the specific combination of models employed by Booth & Schaye (2013).

The remainder of the chapter is organised as follows. In Section 3.1 we describe how we set up our idealised galaxy initial conditions. Our main results are presented for isolated galaxies in Section 3.2 and merging galaxies in Section 3.3, while in Section 3.4 we take a closer look at some of our model assumptions. Finally, conclusions are drawn and future work outlined, in Section 3.5.

3.1 Creating equilibrium disc galaxies

The full method for constructing equilibrium disc galaxies is given here. We largely follow Springel et al. (2005) which builds on the work of Mo et al. (1998); however our approach differs in a few key areas such as our treatment of adiabatic contraction of the dark matter halo (see Section 3.1.1) and the ISM model used (Chapter 2 Section 2.2.1). The model galaxies created here consist of a DM halo surrounding a disc made up of stars and gas particles with a central stellar bulge. In summary we assume that the DM halo follow a Hernquist profile, and that the disc components are axisymmetric with an exponential surface density profile; both components having the same scale-length. The gas disc is assumed to be in hydrostatic equilibrium, whereas the stellar component is an isothermal sheet.

3.1.1 Particle positions

When defining the positions of the particles we begin with a so-called '*glass*', a volume of random and homogeneously distributed particles. We then modify the glass by adding additional constraints on the distribution of the particles to fit desired profiles. In this way any undefined aspect of the particle distribution is inherently random and we do not rely solely on pseudo-random number generators. Should the glass in use contain insufficient particles we copy and tile the existing glass until we obtain a cube large enough.

Dark matter halo & the stellar bulge

For the DM component we assume that it follows the Hernquist mass profile (Hernquist 1990),

$$\rho_{\rm h}(r) = \frac{M_{\rm h}}{2\pi}\frac{a}{r(r+a)^3}, \tag{3.1}$$

where $M_{\rm h}$ is the total halo mass ($M_{\rm h} = m_{\rm h}M$ where M is the total galaxy mass) and a is a constant scale-length which affects the central shape of the profile. The corresponding enclosed mass profile is then,

$$M_{\rm h}(<r) = M_{\rm h}\frac{r^2}{(r+a)^2}. \tag{3.2}$$

We choose this profile as it replicates the inner slope of the cosmologically motivated NFW profile (Navarro et al. 1996b) whilst having a mass profile which converges at large radii. In fact a conversion exists between the NFW concentration parameter, c, and a under the assumption that the two profiles contain the same mass within r_{200} (the radius at which the density of the system drops below $200\times$ the critical density required to close the universe at that redshift),

$$a = r_{\rm s}\sqrt{2[\ln(1+c) - c/(1+c)]}, \tag{3.3}$$

where $r_{\rm s} = r_{200}/c$ is the scale-length of the NFW halo. We then distribute the DM particles simply by sliding the particles to the radius found by interpolating Equation 3.2 at $M(<r) = (N+1)m_{\rm DM}$, where N is the number of particles already placed and $m_{\rm DM}$ is the mass of a DM particle. In this way the random angular position of the particle is maintained.

For the stellar bulge we also follow a Hernquist profile with the modification that a different (larger, Navarro et al. 1996b) scale-length b is employed instead of a and the particle mass is now $m_\star$,

$$M_{\rm b}(<r) = M_{\rm b}\frac{r^2}{(r+b)^2}. \tag{3.4}$$

Both a and b are free parameters of our model.

Stellar disc

For the stellar disc we define that its surface density is described by an axisymmetric exponential disc with scale-length h,

$$\Sigma_\star(R) = \frac{M_\star}{2\pi h^2}e^{(-R/h)}, \tag{3.5}$$

where $M_\star (= m_\star M)$ is the mass of the stellar disc and $m_\star$ is the stellar disc mass fraction ($m_\mathrm{d} = m_\star + m_\mathrm{g}$, $M_\mathrm{d} = M_\star + M_\mathrm{g}$). From this we deduce the enclosed mass profile and perform the same procedure as followed for the halo when setting the particle radii,

$$M_\star (< R) = M_\star \frac{(R+h)}{h} e^{(-R/h)}. \tag{3.6}$$

The scale-length, h, is set for both gaseous and stellar components by relating it to the angular momentum of the disc. We calculate the angular momentum by assuming that the baryonic matter which now makes up the disc was initially distributed identically to the surrounding DM halo forming a 'total' halo and then applying conservation of angular momentum. In this case the angular momentum of the disc is equal to a fraction of the 'total' halo angular momentum, i.e.

$$J_\mathrm{d} = j_\mathrm{d} J, \tag{3.7}$$

where we take the approach of Springel & White (1999) in assuming there is no angular momentum transport between the different galaxy components, under this assumption the angular momentum fraction is equal to the mass fraction of the disc ($j_\mathrm{d} = m_\mathrm{d}$). The spin of a halo is often described by the dimensionless spin parameter, λ,

$$\lambda = \frac{J|E|^{1/2}}{GM^{5/2}}, \tag{3.8}$$

where E is the total energy of the halo and we set $\lambda = 0.04$. For an NFW halo the kinetic energy is found to be, under the assumption that all particles move on circular orbits at the circular velocity (Springel & White 1999),

$$E_\mathrm{kin} = \frac{GM^2}{2r_{200}} f_\mathrm{c}, \tag{3.9}$$

where,

$$f_\mathrm{c} = \frac{c\left[1 - \frac{1}{(1+c)^2} - \frac{2\ln(1+c)}{1+c}\right]}{2\left[\ln(1+c) - \frac{c}{1+c}\right]^2}. \tag{3.10}$$

Although this relationship is strictly true for NFW profiles we assume it also holds for the Hernquist profile due to the similarity of the profiles in the central regions. Then applying the virial theorem so $E = -E_\mathrm{kin}$ and by substituting into Equation 3.8 we obtain an

expression for the halo angular momentum,

$$J = \lambda G^{1/2} M_{200}^{3/2} r_{200}^{1/2} \left(\frac{2}{f_{\rm c}}\right)^2, \tag{3.11}$$

We may then find a h value for which the numerically calculated $J_{\rm d}$ value agrees with the predicted value (in practice DM halo contraction must be simultaneously considered, see below. The angular momentum of any disc with known rotation curve and surface density may be found with (Mo et al. 1998),

$$J_{\rm d} = M_{\rm d} \int_0^\infty V_{\rm c}(R) R \times 2\pi R \, \Sigma(R) \, {\rm d}R, \tag{3.12}$$

where $V_{\rm c}$ is the circular velocity. For our model we substitute in Equation 3.5 to find,

$$J_{\rm d} = M_{\rm d} \int_0^\infty V_{\rm c}(R) \left(\frac{R}{h}\right)^2 \exp\left(-\frac{R}{h}\right) {\rm d}R \tag{3.13}$$

where $M_{\rm d} =$ is the total disc mass, and the circular velocity in our system may be written (as shown in e.g. Binney & Tremaine 1987 pg. 77),

$$V_{\rm c}^2(R) = \frac{G[M_{\rm h}(<R) + M_{\rm b}(<R)]}{R} + \frac{2GM_{\rm d}}{h} y^2 [I_0(y)K_0(y) - I_1(y)K_1(y)], \tag{3.14}$$

where $y = R/(2h)$ and I_n, K_n are Bessel functions.

For the vertical distribution we employ the model of an isothermal sheet with constant scale height z_0. From this we once again find the enclosed mass profile which can be rearranged to give the vertical positions,

$$\Sigma_\star(z) = \frac{M_\star}{2z_0} {\rm sech}^2\left(\frac{z}{2z_0}\right), \tag{3.15}$$

$$M_\star(<z) = M_\star {\rm tanh}\left(\frac{z}{2z_0}\right). \tag{3.16}$$

Here we follow Springel et al. (2005) in setting $z_0 = 0.2h$. For completeness, the 3D density and mass distribution of the stellar disc are described by,

$$\rho_\star(R,z) = \frac{M_\star}{4\pi z_0 h^2} {\rm sech}^2\left(\frac{z}{2z_0}\right) e^{(-R/h)}, \tag{3.17}$$

$$M_\star(<R,<z) = \frac{M_\star}{h} \tanh\left(\frac{z}{2z_0}\right) \left(h - e^{(-R/h)}(R+h)\right), \tag{3.18}$$

We note here a numerical consideration that the R, z coordinates of a particle are

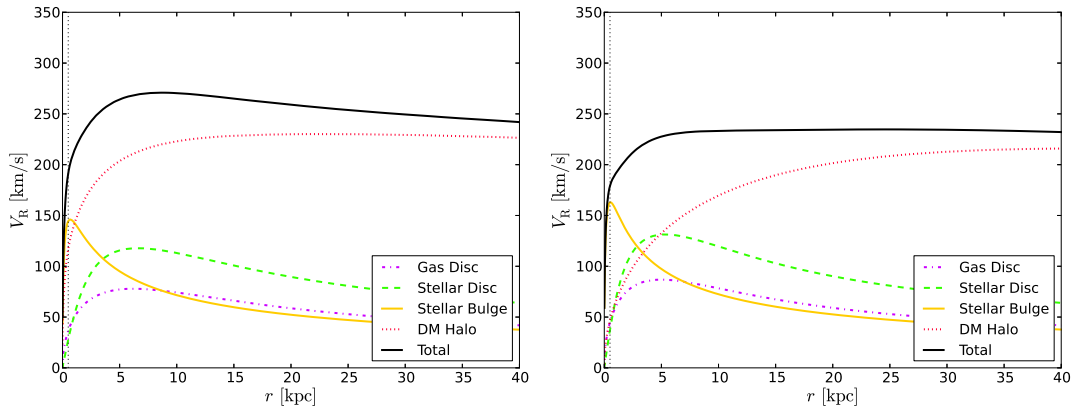

Figure 3.1: Rotation curves as derived with (left panel) and without (right panel) adiabatic contraction of the DM halo. Also shown as a vertical dotted line is $2.8\varepsilon_{\rm soft}$ where $\varepsilon_{\rm soft}$ is the Plummer equivalent softening length. Note that the two cases have differing disc scale-lengths, $h = 3.45\,{\rm kpc}$ and $2.78\,{\rm kpc}$ respectively, this is due to the dependence of the scale-length on the DM halo circular velocity and therefore its contraction.

independent, therefore any artificial correlation must be carefully avoided.

Halo contraction

As an optional feature we include the ability to approximate the DM halo contraction resulting from the formation of a galactic disc. Following the approach of Blumenthal et al. (1985) (also Mo et al. 1998) we assume that the matter which makes up the galaxy, both dark and otherwise, was initially distributed following a Hernquist profile (as employed in our calculations of the disc angular momentum) but as the baryonic matter began to cool and collapse the DM distribution responded by contracting adiabatically. We also assume that the halo remains spherically symmetric under the contraction, under these assumptions the angular momentum of individual DM particles is conserved. Considering a single particle at initial radius,$r_{\rm i}$, moving to a new position with radius, $r_{\rm f}$, we may write,

$$GM_{\rm f}(< r_{\rm f}) = GM_{\rm i}(< r_{\rm i}), \tag{3.19}$$

where $M_{\rm i}$ is the total initial mass enclosed within $r_{\rm i}$ as given by the Hernquist profile and $M_{\rm f}$ is the total final mass enclosed within $r_{\rm f}$. The final mass $M_{\rm f}$ is equal to the sum of the (now contracted) DM component of the mass initially within $r_{\rm i}$ ($= m_{\rm DM}M_{\rm i}(< r_{\rm i})$) and the baryonic matter within $r_{\rm f}$,

$$M_{\rm f}(< r_{\rm f}) = M_{\rm d}(< r_{\rm f}) + M_{\rm b}(< r_{\rm f}) + m_{\rm DM}M_{\rm i}(< r_{\rm i}), \tag{3.20}$$

where we analytically know $M_{\rm b}(< r)$ from Equation 3.4 and $M_{\rm d}(< r)$ is found similarly to Equation 3.18 whilst setting $R = z = r$,

$$M_{\rm d}(< r) = \frac{M_{\rm d}}{h} \tanh\left(\frac{r}{2z_0}\right)\left(h - e^{(-r/h)}(r+h)\right). \tag{3.21}$$

By iterating we then find a value of $r_{\rm f}$ which satisfies Equation 3.19. The problem is further complicated because the determinations of the disc scale-length, h, and the halo contraction are interdependent; we must therefore iterate over the two calculations from a first guess until the solutions converge. See Fig. 3.1 for an illustration of the effects of contraction on rotation curves.

Gaseous disc

The radial dependence of the gas distribution is set as for the stellar component in Section 3.1.1, and follows,

$$\Sigma_{\rm g}(R) = \frac{M_{\rm g}}{2\pi h^2} e^{(-R/h)}. \tag{3.22}$$

To ensure the gas is initially placed in a stable structure we assume hydrostatic equilibrium,

$$\frac{\partial P}{\partial z} = -\rho_{\rm g}\frac{\partial \Phi}{\partial z}, \tag{3.23}$$

where Φ is the total gravitational potential. Substituting in our EoS (Equation 2.69) we obtain,

$$\begin{aligned} \frac{\partial P}{\partial z} &= A\gamma\rho_{\rm g}^{\gamma-1}\frac{\partial \rho_{\rm g}}{\partial z}, \\ &= -\rho_{\rm g}\frac{\partial \Phi}{\partial z}. \end{aligned} \tag{3.24}$$

Rearranging we see,

$$\rho_{\rm g}^{\gamma-2}\frac{{\rm d}\rho_{\rm g}}{{\rm d}z} = -\frac{1}{A\gamma}\frac{{\rm d}\Phi}{{\rm d}z}, \tag{3.25}$$

separating variables then gives us the integrals,

$$\int_{\rho_0}^{\rho_{\rm g}} \rho_{\rm g}^{\gamma-2}{\rm d}\rho_{\rm g} = -\frac{1}{A\gamma}\int_{\Phi_0}^{\Phi}{\rm d}\Phi, \tag{3.26}$$

where ρ_0,Φ_0 are the respective mid-plane values. Performing the integrations and rearranging gives,

$$\rho_{\rm g}(z,R) = \left[\rho_0^{\gamma-1}(R) - \left(\frac{\gamma-1}{A\gamma}\right)\left[\Phi(z,R) - \Phi_0(R)\right]\right]^{\frac{1}{\gamma-1}}. \tag{3.27}$$

The mid-plane potential Φ_0 is known numerically; however we must determine the mid-plane density, ρ_0, by iteration demanding that the 3D density agrees with the surface density i.e. that it fulfils the constraint,

$$\Sigma_{\rm g}(R) = \int_{-\infty}^{\infty} \rho_{\rm g}(R, z, \Phi) {\rm d}z. \tag{3.28}$$

At a given radius we may then obtain a profile for $M_{\rm g}(< z)$ by numerically integrating Equation 3.27, we then interpolate this profile when vertically positioning the gas particles. The known density distribution is then used with Equation 2.69 and the ideal gas law to find the temperature of each particle.

At this stage we discuss an important numerical consideration in this method, many of the preceding derivations have required the use of spatial derivatives and we have begun to introduce the use of the potential, Φ, for both of these purposes we create a fine logarithmic mesh in R, z. It is at these mesh points which we calculate the gravitational potential due to the mass distribution using a parallelised 'Tree' method and define the density profiles. The mesh is also employed extensively when calculating the velocity distributions.

3.1.2 Particle velocities

Collisionless particle velocities

When considering the velocities of the particles representing collisionless components we follow Hernquist (1993) (see also Binney & Tremaine 1987) and calculate the distribution by considering the Collisionless Boltzmann Equation (CBE). In deriving our distribution we assume that it only depends on the energy, E, and the z-component of the angular momentum $L_{\rm Z}$ as well as assuming that the velocities are isotropic. In such a case the mixed second order moments vanish as do the radial and vertical first order moments ($\langle v_{\rm R} v_{\rm Z} \rangle = \langle v_{\rm R} v_\phi \rangle = \langle v_{\rm Z} v_\phi \rangle = 0$, $\langle v_{\rm R} \rangle = \langle v_{\rm Z} \rangle = 0$). The non-vanishing second order moments are then obtained from the Jeans equations as,

$$\langle v_{\rm Z}^2 \rangle = \langle v_{\rm R}^2 \rangle = \frac{1}{\rho} \int_{\rm Z}^{\infty} \rho(z', R) \frac{\partial \Phi}{\partial z} {\rm d}z', \tag{3.29}$$

$$\langle v_\phi^2 \rangle = \langle v_{\rm R}^2 \rangle + \frac{R}{\rho} \frac{\partial (\rho \langle v_{\rm R}^2 \rangle)}{\partial R} + v_{\rm c}^2, \tag{3.30}$$

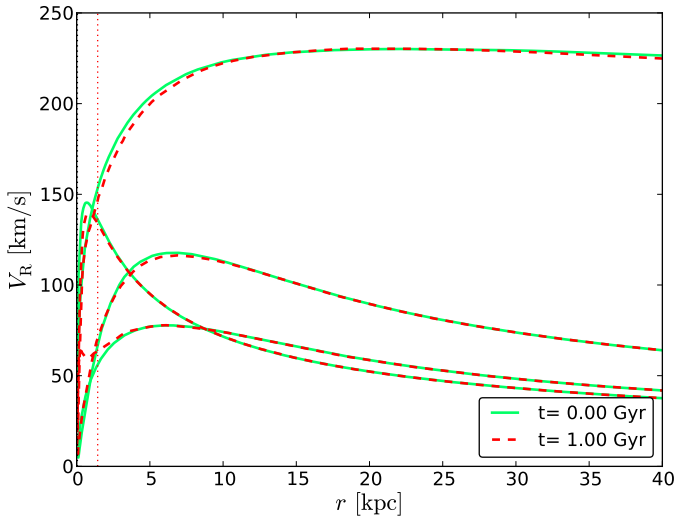

Figure 3.2: Evolution of galaxy rotation curves for an adiabatically contracted isolated model galaxy with 7×10^6 particles. Rotation curves are shown at $t = 0.0$ and $1.0\,\mathrm{Gyr}$ in a gravity and hydrodynamics only simulation for (top to bottom) dark matter, stellar disc, gas disc and stellar bulge. Also shown as a vertical dotted line is the estimated two-body relaxation radius at $1.0\,\mathrm{Gyr}$. A small level of contraction in the central region is seen, however for the most part the galaxies are extremely stable.

where ρ is the density of the currently considered mass component, Φ is the gravitational potential from all components and $v_{\rm c}$ is the circular velocity,

$$v_{\rm c}^2 = R\frac{\partial \Phi}{\partial R}. \tag{3.31}$$

We then require a suitable function to approximate the velocity distribution at any point, for this purpose we choose a triaxial Gaussian distribution with its axes coincident with the axisymmetric coordinate system,

$$F(v_X, R, z) = \frac{1}{\sqrt{(2\pi\sigma_X^2)}} \exp\left(-\frac{(v_X - \mu)^2}{2\sigma_X^2}\right), \tag{3.32}$$

where $X(= R, z, \phi)$, $\sigma_X^2(= \sigma_X^2(R, z))$ is the velocity variance along a general axis, X, and $\mu(= \mu(R, z) = \langle v_X \rangle)$ is the mean streaming velocity. The velocity dispersions and variances are related by

$$\begin{aligned} \sigma_{\rm R}^2 &= \langle v_{\rm R}^2 \rangle \\ \sigma_{\rm Z}^2 &= \langle v_{\rm Z}^2 \rangle \\ \sigma_\phi^2 &= \langle v_\phi^2 \rangle - \langle v_\phi \rangle^2 \end{aligned} \tag{3.33}$$

where we have used $\langle v_{\rm R} \rangle = \langle v_{\rm Z} \rangle = 0$.

For the stellar bulge we set the streaming velocity, μ, to zero as in Springel et al. (2005) however this is not true for the DM halo. For the halo we set the mean rotational velocity at any point to be a fixed fraction of the circular velocity (with a fiducial value of $\mu = 0.01 v_{\rm c}$), note however that this is of small importance when compared to the radial motions of the DM particles and it is the velocity dispersion which contributes the majority of support to the halo.

Once more we take the approach of Springel et al. (2005) and continue to employ the Gaussian approximation when describing the stellar disc with the assumption that

$$\langle v_{\rm R}^2 \rangle = f_{\rm R} \langle v_{\rm Z}^2 \rangle, \tag{3.34}$$

where it is assumed that $f_{\rm R} = 1$, this is justified as being well supported by observational evidence. In the case of the disc, unlike the halo and bulge, it is the rotational motions of the particles which is most important for providing support to the structure. When considering this mean azimuthal streaming of the disc we invoke the epicyclic approximation,

$$\sigma_\phi^2 = \sigma_{\rm R}^2 \frac{\kappa^2}{4\Omega}, \tag{3.35}$$

where the epicyclic frequency, κ is defined as,

$$\kappa^2 = \frac{3}{R}\frac{\partial \Phi}{\partial R} + \frac{\partial^2 \Phi}{\partial R^2}, \tag{3.36}$$

and,

$$\Omega = \frac{1}{R^2}\frac{\partial \Phi}{\partial R}. \tag{3.37}$$

We then define

$$\eta^2 = \frac{4\Omega^2}{\kappa^2} = \frac{4}{R}\frac{\partial \Phi}{\partial R}\left(\frac{3}{R}\frac{\partial \Phi}{\partial R} + \frac{\partial^2 \Phi}{\partial R^2}\right)^{-1}. \tag{3.38}$$

to obtain the simplified relation, $\sigma_\phi^2 = \sigma_{\rm R}^2/\eta^2$. Equations 3.30 and 3.33 then allow us to write the mean streaming velocity,

$$\langle v_\phi \rangle = \sqrt{\langle v_\phi^2 \rangle - \frac{\sigma_{\rm R}^2}{\eta^2}}. \tag{3.39}$$

Numerically, the velocity distributions are defined for the fixed spatial mesh described briefly in Section 3.1.1 once the matter distributions have been finalised. This is so that the full gravitational potential is then known in regularly distributed positions and then

may be integrated or differentiated as needed. When finding the velocity of any given particle, bilinear interpolation is used to find the approximate σ (and where appropriate μ) at the particle's position, the Gaussian distribution is then sampled using the so-called *accept-reject* method.

Gaseous disc velocities

The velocity structure of the gaseous disc is much simpler because the majority of its support is provided by its pressure, it is therefore assumed to undergo solid body rotation i.e. its velocity depends only on R and $v_{\rm z} = v_{\rm R} = 0$. Assuming balance between the gravitational pull and the centrifugal and pressure support on the disc we have,

$$\frac{\partial \Phi}{\partial R} = \frac{v_{\phi,\rm g}^2}{R} - \frac{1}{\rho_{\rm g}} \frac{\partial P}{\partial R}, \tag{3.40}$$

where P and $\rho_{\rm g}$ are the gas pressure and densities respectively. We then find the particle velocities to be

$$v_{\phi,\rm g} = \sqrt{R \left(\frac{\partial \Phi}{\partial R} + \frac{1}{\rho_{\rm g}} \frac{\partial P}{\partial R} \right)}. \tag{3.41}$$

The model galaxy is now fully specified and from the method and assumptions we have utilised we expect it to show very little evolution over multiple dynamical times, as shown in Fig. 3.2.

Galaxy parameters

Our galaxy parameters are as follows. The mass is $M_{200} = 1.360 \times 10^{12}\,{\rm M}_\odot$[1], with an NFW concentration parameter $c = 9$, yielding a total system mass $M = 1.913 \times 10^{12}\,{\rm M}_\odot$. The mass is split (stated as fractions of M_{200}) according to the disc fraction $f_{\rm d} = 0.04$, and bulge fraction $f_{\rm b} = 0.01$, with the remaining mass residing in the DM halo. The disc is split once more into gas and stars subject to the fraction in gas, $f_{\rm g} = 0.3$. The component masses are; DM halo mass $M_{\rm h} = 1.84 \times 10^{12}\,{\rm M}_\odot$, gaseous disc mass $M_{\rm g} = 1.63 \times 10^{10}\,{\rm M}_\odot$, stellar disc mass $M_\star = 3.81 \times 10^{10}\,{\rm M}_\odot$ and stellar bulge mass $M_{\rm b} = 1.36 \times 10^{10}\,{\rm M}_\odot$. We set the radial disc scale-length, $h = 3.45\,{\rm kpc}$, through angular momentum considerations, and use it to define the bulge scale-length and disc scale height $b = z_0 = 0.2\,h$. Our galaxy parameter choices are made to roughly describe a Milky Way like galaxy, with the details chosen to allow comparison with earlier work such as Springel et al. (2005); Schaye & Dalla Vecchia (2008) and Debuhr et al. (2010).

[1] M_{200} is the mass enclosed within R_{200}, the radius at which the density as given by the Hernquist profile is $200\rho_{cr}$, where ρ_{cr} is the critical density of the universe.

Table 3.1: Numerical parameters for our model galaxies, simulated with varying resolution. Columns 2-6 give the total particle number, as well as the number in the DM halo, gaseous disc, stellar disc and stellar bulge respectively. Columns 7 & 8 list the dark matter and baryonic particle masses (in $M_\odot$) while Column 9 gives the (equivalent Plummer) gravitational softening length used in our simulations. Values in parentheses correspond to a version of the low resolution run with modified softening (MS). All of our main results use the high resolution simulations; runs using the other resolution levels are investigated in Section 3.4.1.

Resolution	N	N_h	N_g	$N_\star$	N_b	m_DM	m_bar	$\varepsilon_\mathrm{soft}$ [kpc]
Very-Low	7E4	59109	2178	6099	2614	3.08E7	6.24E6	0.23
Low(MS)	7E5	591089	21780	60990	26138	3.08E6	6.24E5	0.05(0.11)
High	7E6	5910890	217800	609900	261380	3.08E5	6.24E4	0.05

The galaxies were constructed in high and low resolution realisations and simulated with a variety of baryonic physics models for $3\,\mathrm{Gyr}$. Tables 3.1 and 3.2 summarise the initial conditions and models run, respectively.

3.2 Isolated disc galaxies

We begin our investigation by performing tests of the feedback recipes in isolated disc galaxies. Performing simulations of an isolated disc galaxy provides us the opportunity to study the models in a regime where the black hole is typically expected to be in a phase of low activity and provides a comparison for the behaviour of black holes in violent mergers. Employing such high resolution 'toy models' also ensures any observed phenomena may be more easily disentangled because the systems themselves are simple and relatively well understood.

In the following sections we perform simulations that employ the methods for describing gas processes and feedback outlined in Section 2.2. Specifically, we simulate the Bondi accretion method with kernel-weighted feedback as set out by Springel et al. (2005), labelled here as K[ernel]AGN; the Bondi method with 'strong' feedback by Booth & Schaye (2009), labelled S[trong]AGN; and the disc accretion method based on Power et al. (2011) with 'strong' feedback (D[isc]AGN). We also consider a model with no feedback[2] (NFB) and a model with supernovae only (SN). Models run with both AGN and supernovae are denoted XAGN_SN, where X is (K, S, D) as discussed. Table 3.2 summarises the details of these runs and lists values for the main AGN feedback parameters.

[2]To clarify, NFB runs contain no macroscopic winds, however a pressure contribution from supernova feedback is implicit in the assumed EoS for all simulations.

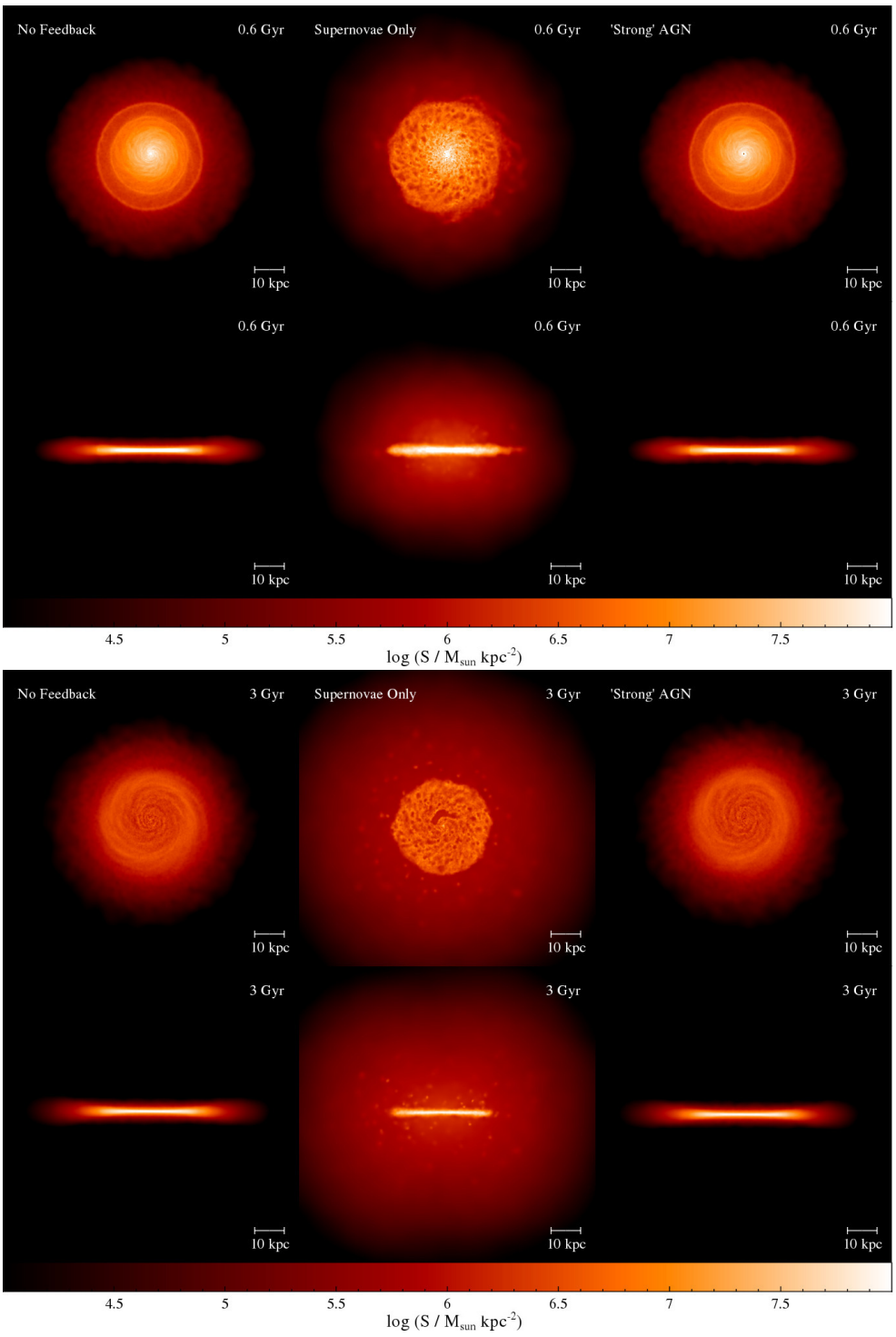

Figure 3.3: Projected face- and edge-on gas surface density plots for an isolated galaxy simulated with various feedback implementations, at $t = 0.6, 3.0\,\mathrm{Gyr}$. Each column shows results for the NFB, SN and SAGN models respectively. Each panel is $100\,\mathrm{kpc}$ on a side and density is coloured on a log scale. Reduction of density for all models occurs due to star formation, however overall the gas is very stable. A slight redistribution of gas is seen for the SAGN model but the most pronounced case is for supernova feedback (SN).

Table 3.2: Summary of our main runs and important parameter choices. Column 1 lists the label used to refer to each model, while columns 2 & 3 specify whether supernovae and AGN are included. Pertinent details of the run are given in column 4; columns 5-7 lists values of the appropriate BH accretion rate parameter; column 8 the number of particles heated by the BH in one event and column 9 the assumed value for the feedback coupling efficiency parameter. The value of $N_{\rm heat}$ for the KAGN runs is approximate.

Label	SN	AGN	Details	α	β	$\epsilon_{\rm ff}$	$N_{\rm heat}$	$\epsilon_{\rm f}$
NFB	N	N	No feedback	-	-	-	-	-
SN	Y	N	Supernovae only	-	-	-	-	-
KAGN	N	Y	Bondi accretion, kernel feedback	100	-	-	50	0.05
KAGN_SN	Y	Y	Bondi accretion, kernel feedback, supernovae	100	-	-	50	0.05
SAGN	N	Y	Boosted Bondi accretion, strong feedback	-	2	-	10	0.15
SAGN_SN	Y	Y	Boosted Bondi accretion, strong feedback, supernovae	-	2	-	10	0.15
DAGN	N	Y	Disc accretion, strong feedback	-	-	0.1	10	0.15
DAGN_SN	Y	Y	Disc accretion, strong feedback, supernovae	-	-	0.1	10	0.15

3.2.1 Simulations with and without supernova feedback

We first investigate the effect of supernovae on the host galaxy properties, neglecting the AGN for the time being. Fig. 3.3 shows projected gas surface density maps for the NFB and SN runs at $t = 0.6$ and $3\,\mathrm{Gyr}$. The maps illustrate qualitatively that supernovae quickly generate a gas halo that persists for the duration of the simulation. They also modify the disc structure, increasing the gas porosity. The reduction in density in the disc over time is predominantly due to star formation as this can be seen for the NFB case.

Fig. 3.4 shows the evolution of the global star formation rate for the NFB and SN simulations (solid and dashed lines respectively). We also show the star formation suppression factor, $S_{\rm X} = \dot{M}_\star({\rm NFB})/\dot{M}_\star({\rm SN})$, in the bottom panel. As expected, we see a reduction in the star formation rate when supernovae are included. This persists until $t \sim 1.5\,\mathrm{Gyr}$ when we see a relative *increase* due to low-level star formation from gas which would have otherwise already formed stars in the absence of supernovae[3].

The primary change seen in simulations with supernova feedback is a reduction in the stellar mass of the disc. This is clearly seen in Fig. 3.5, where both the mass in new stars and in a supernova-driven wind is shown as a fraction of initial gas mass, versus time for

[3] The suppression in the star formation rate is found to be consistent with that seen in Dalla Vecchia & Schaye (2012) under the appropriate parameter choices (see their Fig. 10).

the NFB and SN simulations. A reduction of ~ 10 per cent in stellar mass is seen by the end of the simulation, caused by the inclusion of supernovae. It is clear that the majority of supernova heated gas is returning to the equation of state on a short timescale, as the mass in the wind is considerably lower than in new stars.

3.2.2 Simulations with AGN feedback only

We now consider runs with AGN feedback only. Unlike the supernovae, the AGN feedback has no effect on the star formation rate for any model (an example is shown in the bottom panel of Fig. 3.4 for the SAGN run). This is likely due to the differing scales involved as the black hole typically only interacts with the central $\sim 0.1\,\mathrm{kpc}$ whereas the star formation takes places on kpc scales. Although the black holes do not change the large-scale galaxy properties they can be seen to drive a weak wind.

The growth in BH mass with time is shown in Fig. 3.6, where we plot both the smoothed accretion rate (in units of the Eddington rate; top panel) and the integrated mass (middle panel). Here we can see that the three models produce different accretion behaviour, leading to very different final masses. However, we note that the normalisation and therefore the final mass may easily be tuned through accretion rate parameter choices for any given model. We have chosen to employ the original values where appropriate (KAGN and SAGN) as these were tuned to recover the $M_{\mathrm{BH}} - M_{\mathrm{bulge}}$ relation in full cosmological simulations. For the Power et al. (2011) method (which was not tested on cosmological volumes) we adopted the original value for $t_{\mathrm{visc}} (= 10\,\mathrm{Myr})$ and tuned the free-fall efficiency parameter, $\epsilon_{\mathrm{ff}} = 0.1$, so as to bring the final mass roughly in line with the Booth & Schaye (2009) method as we adopted their feedback prescription for the DAGN model. The most significant factor affecting the final BH mass in isolated galaxy simulations is the resolution used (we investigate this in Section 3.4.1).

We also note that the models predict different BH histories. Bondi-based methods predict that the BH grows smoothly whereas in the DAGN method it undergoes an initial period of rapid growth followed by quasi-periodic accretion events. Unlike the spatially adaptive Bondi methods, the disc method employs a small and finite accretion radius which initially contains gas (an artefact of our initial conditions) but is quickly removed through accretion and feedback, shutting off the black hole growth. After this time, the net BH growth rate is similar in the SAGN and DAGN models despite the different accretion method, while the BH in the KAGN method continues to grow at a faster rate. This suggests that the choice of feedback plays an important role in determining the BH growth rate (we confirm this in Section 3.4.6).

It is also interesting to note that none of the black holes in these simulations reach

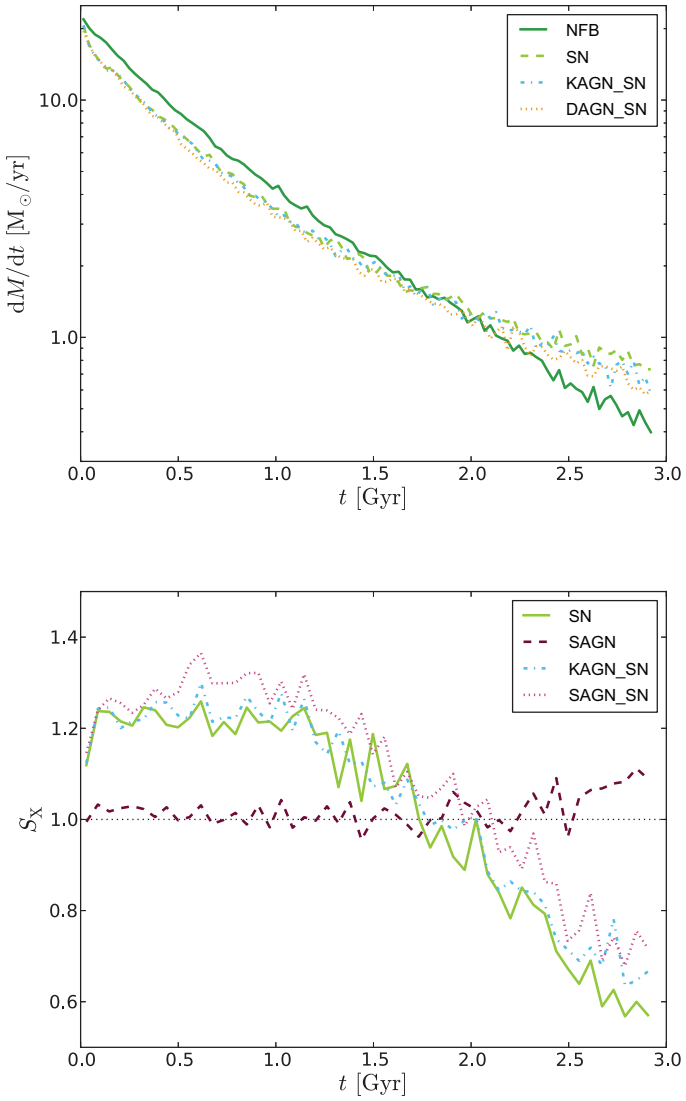

Figure 3.4: Star formation rate (top) and suppression factor (bottom) throughout simulations of an isolated high-resolution disc galaxy. Suppression is calculated as a ratio of instantaneous star formation rates, no-feedback case over feedback case. Supernova feedback causes the dominant suppression of the star formation rate, while the AGN wind is unable to interact with the majority of the galaxy, only having a minor influence when able to couple with the supernova-inflated hot halo.

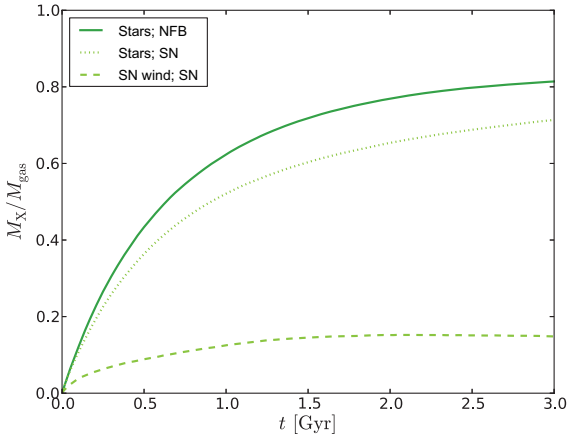

Figure 3.5: Fractional mass in new stars and particles tagged as being in a supernova wind versus time for the isolated high-resolution disc galaxy, with and without supernova feedback. All masses are shown as a fraction of the initial gas mass. Supernovae act to reduce the amount of gas on the equation of state and therefore the mass in stars.

the mass scales ($\sim 10^7 - 10^8\,\mathrm{M}_\odot$) predicted from the observations (e.g. Magorrian et al. 1998; Tremaine et al. 2002). There are some possible causes for this discrepancy, several of which are discussed later in this work, such as reduced accretion in the absence of mergers, low initial black hole mass, resolution effects and large-scale gas accretion. Investigating the final issue would require the inclusion of a hot gas halo (e.g. Sinha & Holley-Bockelmann 2009; Moster et al. 2011; Wurster & Thacker 2013) and/or the simulation of large-scale accretion onto the galaxy (e.g. Moster et al. 2012), and is beyond the scope of this work.

3.2.3 Simulations with supernova & AGN feedback

We now investigate the effect of combining both supernova and AGN feedback in our simulations. Fig. 3.4 shows a mild reduction in the star formation rate in the simulations including both strong AGN and supernovae (SAGN_SN), compared with the supernova only case (SN). This is due to AGN winds coupling to a supernova-fuelled hot gas halo reducing cooling and subsequent star formation (the effect is slightly more prominent in lower resolution simulations; not shown). This has been verified by examining the least dense particles in the simulations and it was found that gas driven out to large radii by strong AGN feedback is missing in simulations also including supernova feedback. The effect is not seen in the KAGN_SN models as there the AGN drives a much weaker wind due to the larger mass being heated.

Semi-analytic galaxy formation models commonly assume that the effects of super-

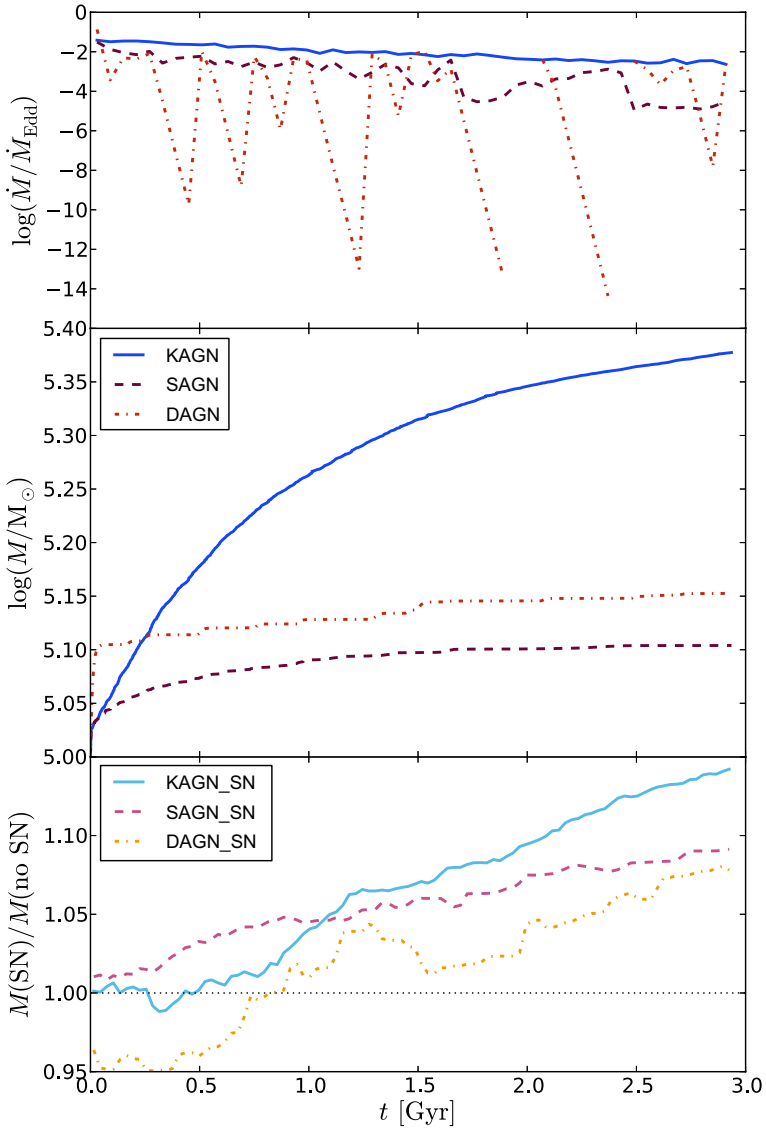

Figure 3.6: Evolution of BH mass with time, for the fiducial AGN models without supernovae in isolated galaxy simulations. The top panel shows the smoothed black hole accretion rate in units of the Eddington rate, while the central panel shows the integrated black hole mass in each of the three models. The bottom panel shows ratios of integrated masses found between these and corresponding simulations including supernovae. Supernovae increase the BH mass in all models by preventing gas depletion through star formation and driving gas towards the BH. However, this increase ($\sim$ 10 per cent) is much smaller than the differences between the AGN feedback models themselves (which can be tuned if necessary).

nova and AGN feedback affect galaxy properties independently of one another (e.g. Bower et al. 2006; Croton et al. 2006; Guo et al. 2011). This approach has recently been brought into question by the work of Booth & Schaye (2013), who found that the two feedback processes suppressed the star formation rate less than if they were assumed independent. For a more quantitative analysis we calculated the feedback suppression 'χ' parameter as used in Booth & Schaye (2013), where χ is defined as

$$\chi = \frac{S_{\rm AGN+SN}}{S_{\rm AGN} \times S_{\rm SN}}, \tag{3.42}$$

and $S_{\rm X}$ is the suppression in the star formation rate due to process X. The value of χ quantifies the level of interaction of AGN and supernova feedback which results in the suppression of star formation. A value of $\chi > 1$ ($\chi < 1$) shows that the two feedback processes have amplified (weakened) each others' ability to reduce the star formation rate and $\chi = 1$ indicates that the two processes are independent. We find $\chi \approx 1$ at all times for KAGN runs and $\chi \simeq 1$ rising to $\chi \simeq 1.15$ at late times for the SAGN and DAGN runs. This indicates that the interaction between the two feedback processes is of minimal importance, even for the strong feedback simulations where a coupling is observed. This weak amplification disagrees with the value of $\chi \sim 0.3$ found by Booth & Schaye (2013) for systems of $M \sim 10^{12}\,M_{\odot}$ such as this. However as this work considers one high resolution object in detail whereas Booth & Schaye (2013) perform a cosmological simulation, this finding is not necessarily a direct contradiction. Both the environment of the galaxy and how well the outflow is resolved are likely to be important in determining the strength of this effect.

The lower panel of Fig. 3.6 shows the ratio of BH masses for the main AGN models with and without supernovae over the course of the simulations. Regardless of model, the black hole mass is mildly enhanced by the action of supernovae after $1\,{\rm Gyr}$. We have verified that this effect is due to a combination of reduced star formation leaving more gas to accrete and winds from the star-forming disc feeding the central BH.

In addition to the primary investigations, we analysed the effect the various baryonic processes had on the resulting dark matter distribution. It has been shown (by e.g. Navarro et al. 1996a; Read & Gilmore 2005; Ogiya & Mori 2012) that an oscillating baryonic system in dwarf galaxies (e.g. driven by the duty-cycle of an AGN) can in turn cause an oscillation in the background gravitational potential, smoothing out dark matter cores, however this is not seen.

We note that the high gas fraction and IMF chosen for the initial conditions and model lead initially to an artificially high star formation rate which is unlikely to exist in reality but provides a higher baryonic content for our investigations. The higer gas con-

tent is shown in Fig. 3.3, where we can see that the gas surface density at early times is $\sim 10\,\mathrm{M}_{\odot}\mathrm{pc}^{-2}$ compared to the Milky Way's $\sim 1\,\mathrm{M}_{\odot}\mathrm{pc}^{-2}$; for comparison, Ultra-Luminious Infra-Red Galaxies (ULIRGs) typically have $\sim 2-4\,\mathrm{M}_{\odot}\mathrm{pc}^{-2}$ (Kennicutt & Evans 2012). This in turn leads to a higher initial star formation rate of $\sim 20\,\mathrm{M}_{\odot}\mathrm{yr}^{-1}$ (Fig. 3.4), however this quickly drops. Chomiuk & Povich (2011) have recently found a current star formation rate for the Milky Way by reviewing all available methods and found that they are consistent with $M_{\mathrm{star}} = 1.9\pm0.4\,\mathrm{M}_{\odot}\mathrm{yr}^{-1}$, however taking into account resolution effects Kennicutt & Evans (2012) give an estimated average star formation rate of $8.25\,\mathrm{M}_{\odot}\mathrm{yr}^{-1}$. We therefore find that the star formation and gas content of our isolated galaxies proceed from a higher to lower gas densities and star formation rates when compared to the Milky Way, independent of feedback model, as the gas is consumed from the disk without being replenished.

In summary, the reduction in star formation rate in our isolated galaxy is dominated by the effect of supernovae, whilst AGN have very little impact regardless of whether the feedback processes are simulated in isolation or in tandem. The final black hole mass is found to differ between models and consistently shows a mild increase as a result of the inclusion of supernovae.

3.3 Merging disc galaxies

Having investigated the influence of supernova and AGN feedback processes on isolated systems, we now turn our attention to how they interact through a major merger. It is important to consider merging systems as they are thought to be a critical phase in galaxy evolution, driving both periods of high AGN activity and starbursts. It has been shown previously by Springel et al. (2005) that the inclusion of AGN feedback significantly reduces star formation during the starburst. Here we re-investigate this result to establish whether this is a generic feature seen in our runs.

3.3.1 The merger scenario

We have chosen to simulate a 1:1 major merger between identical disc galaxies as described in Section 3.1. This extreme choice was made primarily to allow for easier comparison with the isolated galaxy simulations and with previous work. We start the merger with an initial separation of $150\,\mathrm{kpc}$, and a perpendicular impact parameter of $25\,\mathrm{kpc}$. The galaxies initially have approximately zero total energy, corresponding to a net velocity for each galaxy of $185\,\mathrm{kms}^{-1}$ in the centre of mass frame, directed parallel to the separation

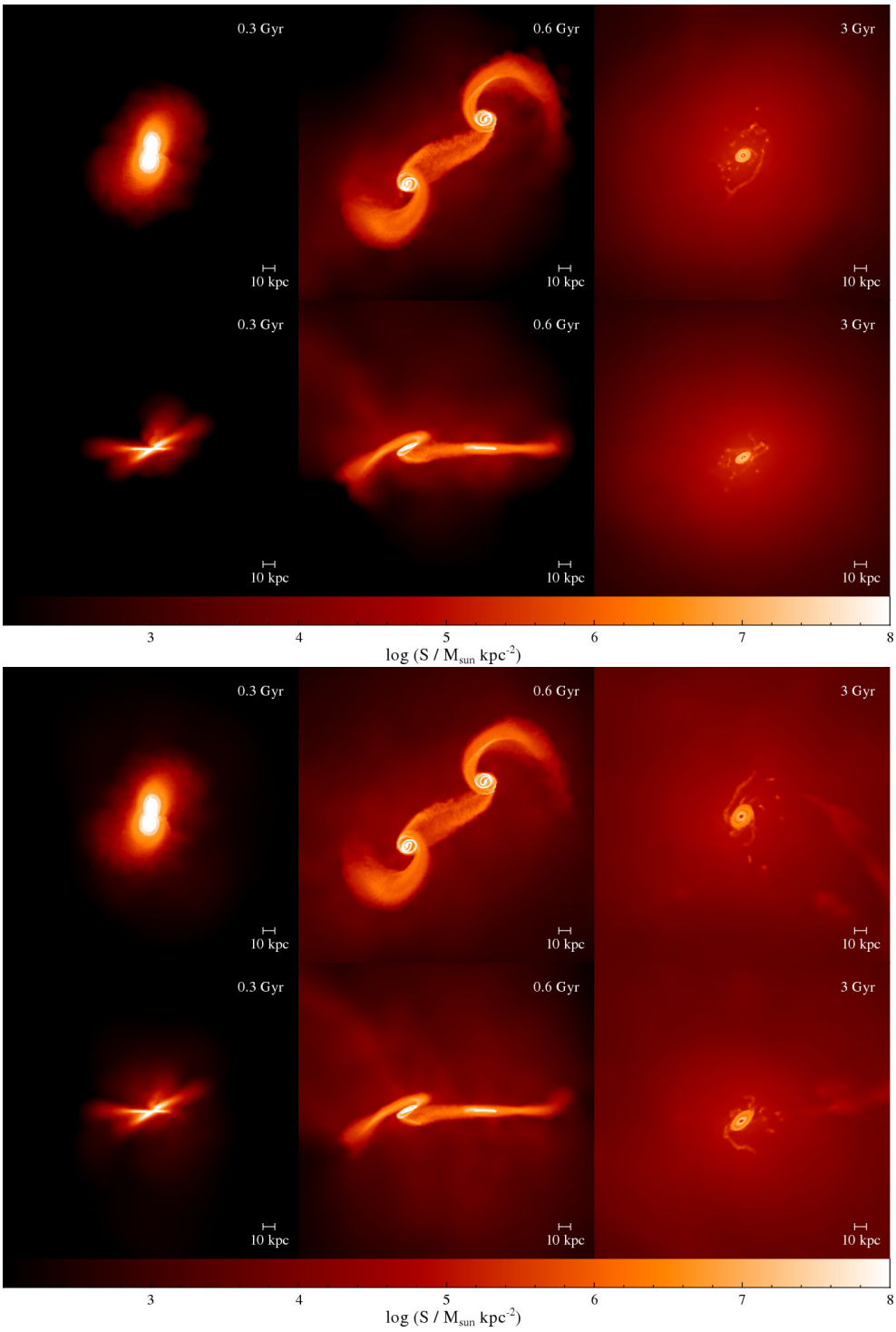

Figure 3.7: Projected face- and edge-on gas surface density plots for merging galaxies in the NFB (top panels) and DAGN simulations (bottom panels). Columns show snapshots taken at times, $t = 0.3, 0.6, 3.0\,\mathrm{Gyr}$, panels are $250\,\mathrm{kpc}$ on a side and density is shown on a log scale in units $\mathrm{M}_\odot\,\mathrm{kpc}^{-2}$. Viewed face-on at $t = 0.3\,\mathrm{Gyr}$, the upper (lower) galaxy has entered from the right (left) with its rotation axis tilted (parallel) with respect to the line-of-sight and swings around to appear as the lower (upper) galaxy at $t = 0.6\,\mathrm{Gyr}$ producing tidal tails and bridges, before finally coalescing. Including strong AGN feedback causes gas outflows from early on and heats gas, resulting in reduced star formation more gas surviving until the end of the simulation.

axis. One of the galaxies is rotated by 30° with respect to both the axis of symmetry and the plane of the merger. This merger geometry is intentionally similar to earlier work (e.g. Springel et al. 2005; Debuhr et al. 2010). Our choice of merger set-up results in the galaxy centres experiencing two passes, coalescing on the second, and merging at around $t \sim 1.5\,\mathrm{Gyr}$. Three key phases of the merger are illustrated in Fig. 3.7, which shows the column density of gas for the first pass, largest subsequent separation and final state, for the NFB and DAGN simulations.

At $t = 3\,\mathrm{Gyr}$ the merging system has had time to relax back into an equilibrium state. The stellar population of the remnant is a slowly rotating oblate ellipsoid with sphericity, $s(= c/a) = 0.49$; elongation, $e(= b/a) = 0.86$; and triaxiality, $T[= (a^2-b^2)/(a^2-c^2)] = 0.33$ where $a > b > c$ are the square roots of diagonal elements in the mass distribution tensor (see Bryan et al. 2013). The abundance of gas at late times is model-dependent, but takes the form of a slowly rotating extended halo with a rotating ($v_\mathrm{c} \sim 200\,\mathrm{kms}^{-1}$) dense gas disc at its very centre. The central disc is formed at a small angle to the plane of the merger due to the initial tilt applied to one of the galaxies (Fig. 3.7).

All merger remnants have similar λ_R values, a proxy for the stellar angular momentum,

$$\lambda_\mathrm{R} = \frac{\langle R|V|\rangle}{\langle R\sqrt{V^2+\sigma^2}\rangle}, \tag{3.43}$$

as applied to ATLAS 3D galaxies (e.g. Emsellem et al. 2007; Bois et al. 2011), of $\lambda_\mathrm{R} \sim 0.01$ meaning that our merger initial conditions form 'slow rotators' independent of any feedback processes.

Mergers, in general, redistribute the dark matter to give a larger $R_{200} = 135\,\mathrm{kpc}$, resulting in a more diffuse halo than in the isolated galaxy initial conditions. This increases the baryon fraction within R_{200} to 0.08.

3.3.2 Mergers with supernova feedback only

We begin, as with our investigation into isolated galaxies, by evaluating the effect of the supernovae. The evolution of the star formation rates for the main simulations are shown in Fig. 3.8 as well as the suppression factor relative to the no-feedback case. For the NFB and SN models, an increase in the rate is seen for both passes ($t \sim 0.3$ and $1.3\,\mathrm{Gyr}$), however the burst at the time of second passage is substantially more significant, as found in previous studies when the galaxies contain a bulge (e.g. Mihos & Hernquist 1996; Springel et al. 2005; Debuhr et al. 2010). The primary burst takes place just as the galaxies coalesce, when the gas discs collide most strongly. As in the isolated case, we find that supernovae reduce the star formation rate throughout the majority of the

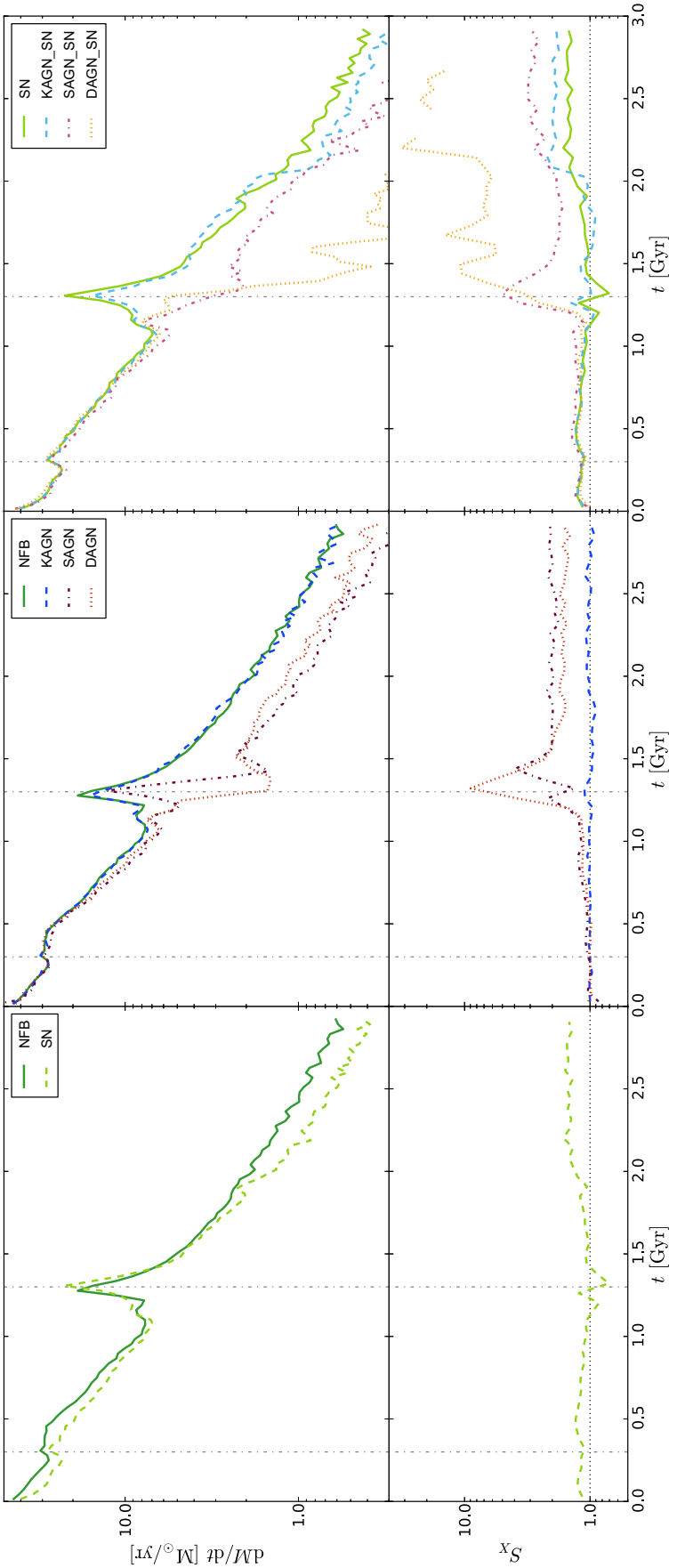

Figure 3.8: Star formation rates and suppression factors for merging galaxy simulations with supernova feedback (left panels); AGN feedback (middle panels); and both (right panels). Vertical lines indicate the times of first and second passage. The suppression factor is the ratio of the feedback case to the no-feedback case. Strong AGN feedback has the largest impact on the star formation rate, eliminating the main starburst.

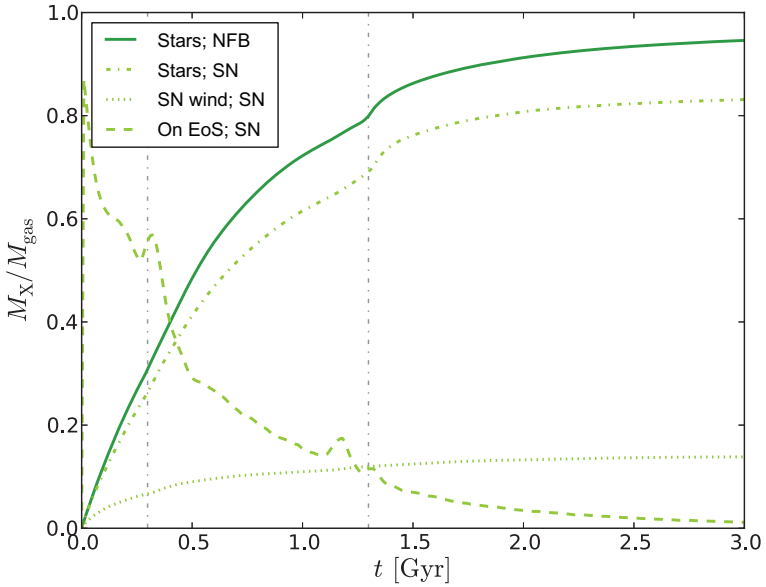

Figure 3.9: Fractional mass in new stars and gas in various phases for simulations of high-resolution disc galaxy mergers with and without supernova feedback. For the NFB case only the stellar mass is shown, while for SN we additionally plot the supernova-heated particles and gas on the equation of state. All masses are shown as a fraction of the initial gas mass. As in the isolated case, supernovae reduce the amount of gas on the equation of state and stellar mass formed.

simulation. However, star formation through the starburst is unchanged, suggesting that the supernova-heated gas is largely confined during this period.

Fig. 3.9 shows the fraction of initial gas mass turned into stars versus time for the NFB and SN simulations. We also plot the fraction heated by supernovae and gas currently on the equation of state for the latter case. Almost all of the gas is converted into stars by the end of the simulation in the NFB run while supernovae reduce this fraction by ~ 13 per cent, similar to that seen in the isolated galaxy simulations. Supernovae cause an additional reduction of mass on the equation of state early on, reducing star formation and preserving gas. The amount of gas on the equation of state temporarily increases twice, coinciding with the timing of the galaxy passages that cause an increase in gas density during the collision. This leads to the enhanced star formation rate that acts to reduce the amount of gas on the equation of state once more. The amount of gas previously heated by supernovae shows only a weak change at the times of the merger passages as it has escaped to areas of lower density. The number of particles tagged as heated is, as in the isolated simulation, only a small fraction of the number of stars formed because the majority quickly rejoins the equation of state without escaping the disc.

We present in Fig. 3.10, the final temperature distributions of gas particles for the NFB, KAGN_SN and SAGN_SN simulations (left to right). Here we discuss the effect

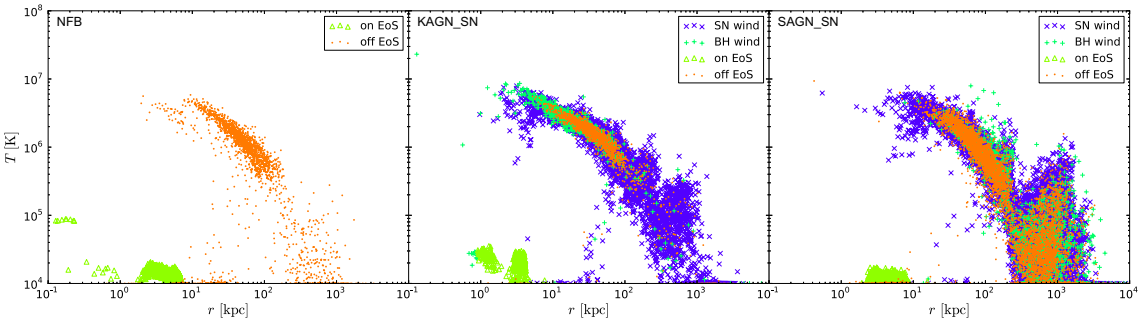

Figure 3.10: Final temperature distributions versus radius for gas particles in the NFB, KAGN_SN and SAGN_SN (left to right) simulations, calculated at $t = 3\,\mathrm{Gyr}$. Symbols indicate the 'tags' applied to gas particles. The predominant trend in all panels is the same, indicating that the dynamical effects of the merger cause much of the heating and redistribution of the gas. However, the runs with strong AGN feedback (SAGN_SN is shown here) produce a larger amount of hot gas ($T > 10^5\,\mathrm{K}$) at large radii ($r > 100\,\mathrm{kpc}$).

of supernovae using the KAGN_SN particle temperature distribution as a proxy for SN, to avoid duplication as they are remarkably alike. The distributions for NFB and SN are very similar, producing a halo of diffuse, hot gas that extends to $\sim 1\,\mathrm{Mpc}$ from the halo centre. This indicates that the dominant cause of heating is gravitational in origin and a consequence of the merger. The importance of dynamical effects in the formation of the hot halo is corroborated by the increase in gas fraction in the halo. This is 53 per cent at the end of the simulation when feedback is omitted compared to 0.02 per cent for the isolated galaxy (fractions with supernovae increase to 90 and 48 per cent respectively).

The final gas density profiles are shown in Fig. 3.11. Profiles are shown at $t = 3\,\mathrm{Gyr}$ and centred on the centre of stellar mass; also shown are the ratios of the density profiles compared to the NFB simulation. The SN profile shows only a small increase in gas density beyond $10\,\mathrm{kpc}$ due to a reduction in star formation.

3.3.3 Mergers with AGN feedback only

In stark contrast to the isolated galaxy case we find that in merging systems, the AGN can have the dominant effect on the star formation rate when the feedback is strong (SAGN and DAGN; Fig. 3.8). While the KAGN model has no impact on the star formation rate, the SAGN and DAGN models significantly reduce the amount of stars formed during and after the merger. In the DAGN case, the AGN also eliminates the starburst; if generic (and not just for our particular merger configuration) it contradicts observational evidence linking mergers with starburst activity (see e.g. Alexander & Hickox 2012 and references therein). Over the whole simulation, the weaker kernel feedback (KAGN) reduces the final mass in stars by only 5 per cent, by reducing the starburst duration and strong feedback

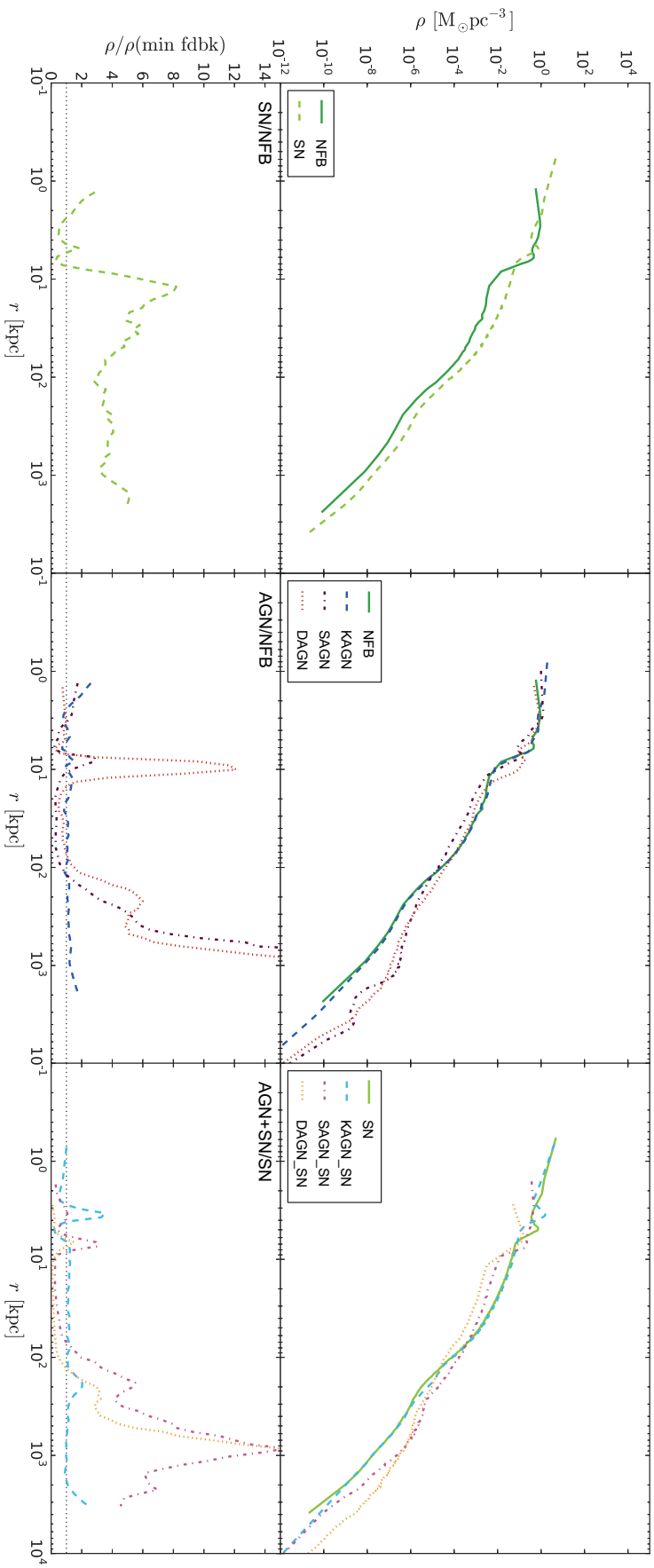

Figure 3.11: Final gas density profiles for the main set of simulations, grouped into runs with no AGN (left panels), AGN only (centre panels) and supernovae plus AGN (right panels). The lower sub-panels show the ratio for each model relative to the NFB run in the left and centre panels, and the SN run in the right panel. Both supernovae and strong AGN feedback affect the gas distribution, with the latter pushing gas out to larger radii.

by ~ 25 per cent. We investigate this further in Section 3.4.6.

The wide disparity in the power of the AGN to influence its environment is likely due to the differing temperatures which gas is heated to. At 10^8 K (the strong feedback heating temperature) radiative cooling has less of an effect, as the cooling time increases as $\sqrt{T}$ when the emission is dominated by thermal Bremsstrahlung. Therefore, by spreading the available feedback energy over many particles neighbouring the black hole and depositing any available energy promptly, the kernel-weighted method heats more gas to lower temperatures where it can cool more easily. The centre and right panels of Fig. 3.10 show that whilst kernel feedback removes gas from the equation of state and up to temperatures of $\sim 10^5$ K, strong feedback heats much more gas to higher temperatures and larger radii (up to 10^6 K at 10^3 kpc), resulting in less gas on the equation of state.

Final gas density profiles (middle panels of Fig. 3.11) show a redistribution of gas out to large radii in the case of the strong feedback models. The kernel-weighted feedback method makes very little difference to the gas distribution, causing only a slight increase in gas at $r \lesssim 10\,\mathrm{kpc}$. The strong feedback methods however redistribute gas out to much larger radii, $r > 10^2\,\mathrm{kpc}$, with an order of magnitude larger density than stars at that radius, increasing the mass of gas at $r > 10^3\,\mathrm{kpc}$ by two orders of magnitude from 2×10^7 to $2.5 \times 10^9\,\mathrm{M}_\odot$. This does not, however, significantly change the baryon fraction within R_{200} compared to the NFB case. AGN have little effect on stellar density profiles, as found for isolated galaxies, due to the sub-dominant mass in new stars and the large amount of stellar mixing which occurs though a merger. Furthermore, gas removed to lower densities by strong AGN feedback is less likely to return and will never form stars over the course of the simulation.

Evolution of the black holes with time for the three main AGN models are shown in Fig. 3.12. The top panels show the average mass accretion rates (in units of the Eddington rate), while the middle panels show the integrated masses of the two black holes as well as their sum. The black holes undergo a spike of growth at the times of the first and second passes, forming a tight binary system during the latter which has not coalesced by the end of the simulation (black holes are found to merge more readily in low resolution simulations). Correspondingly there is a large increase in the net amount of feedback energy deposited compared to the isolated case, which in itself suggests the AGN will influence its environment more strongly. The AGN activity peaks are coincidental with merger passes, as the latter drives an inflow of gas, increasing the density around the black hole, and thus boosting the accretion rate.

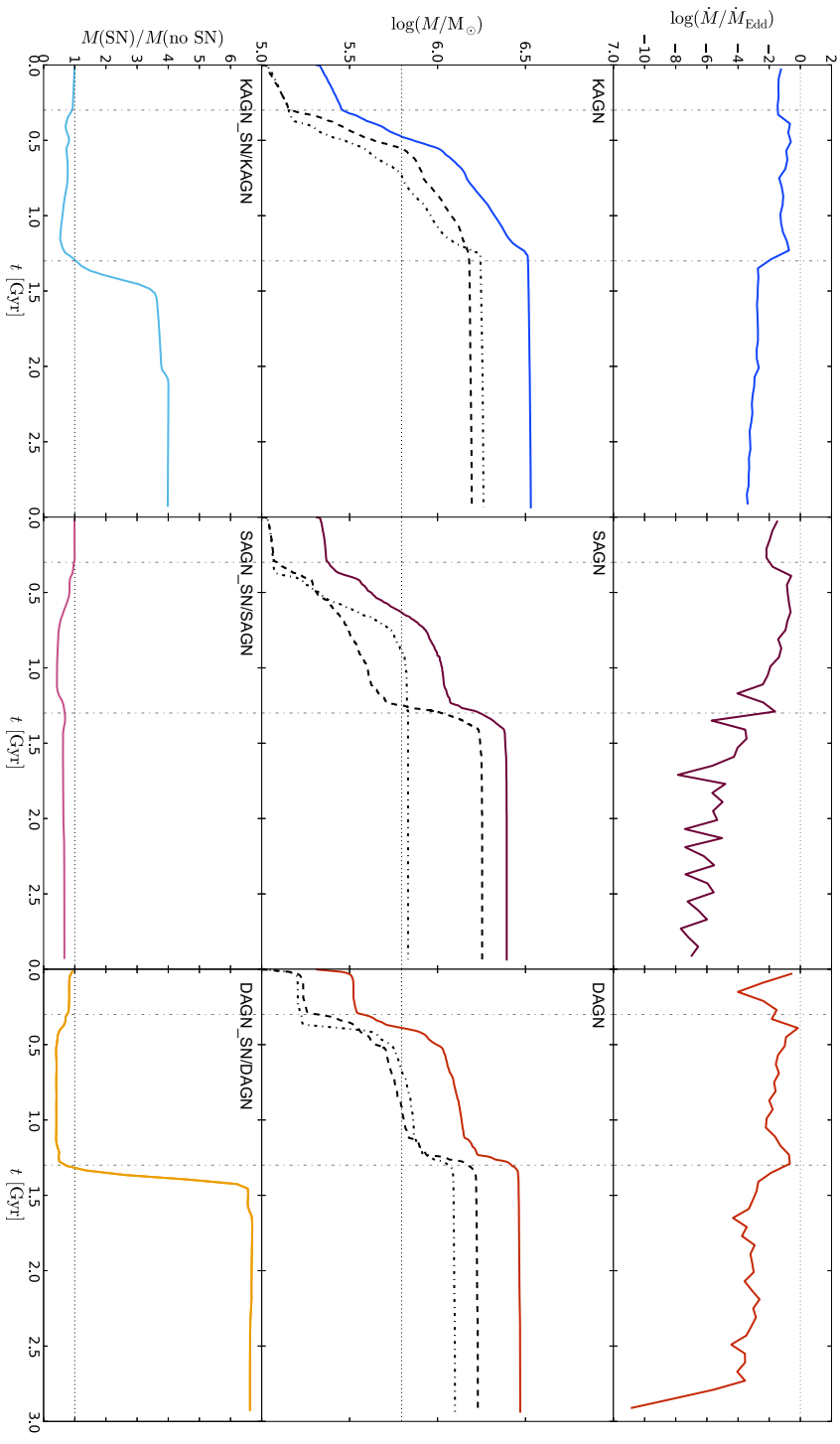

Figure 3.12: Evolution of the black holes with time through a merger for the fiducial AGN models; left to right, KAGN, SAGN and DAGN respectively. The top panels show the binned total mass accretion rate in units of the Eddington rate, onto both of the black holes, for models without supernovae. In the middle panels, the integrated 'internal' black hole masses are shown (dotted and dashed lines), with the solid line representing the sum of the two. Lower panels show the total black hole mass for each AGN model with supernovae relative to the no-supernovae equivalent. The horizontal black dotted line in the central panel shows the threshold mass above which black hole re-centring is halted, whilst elsewhere it denotes a value of unity. Boosted growth rates can be seen at the times of first passage and coalescence of the merger. The inclusion of supernovae increases the final black hole mass when the two black holes do not merge (as is the case with KAGN and DAGN).

3.3.4 Mergers with supernova & AGN feedback

The previous sections have shown that AGN can play a more significant role than supernovae in determining the star formation rate during a merger. We can see from the star formation rates and ratios in Fig. 3.8 that strong AGN feedback (SAGN and DAGN models) is even more effective at reducing star formation for the majority of the simulation with the starburst now being terminated in both cases. The SN and AGN both provide additional thermal energy to hot halo gas, increasing its cooling time and thus reducing the amount of material joining the equation of state.

For a more quantifiable measure of the combined suppression effects of the feedback processes, we again calculate the χ parameter. We find, as in the isolated galaxy simulations, χ values consistent with unity prior to coalescence but rising to $\sim 3\,(1.4)$ at late times for the strong (kernel-weighted) models respectively. This, as discussed in the context of isolated galaxies, is a departure from the findings of Booth & Schaye (2013). However, we note that χ values calculated after the merger are prone to noise due to the low-level of star formation at this time.

The coupling of the AGN outflow to the supernova-fuelled hot gas halo, observed in both our isolated and merging galaxy simulations, raises the question of whether such a halo ought to have been included in our initial conditions. Such an approach has been adopted by recent galaxy merger studies (e.g. Sinha & Holley-Bockelmann 2009; Moster et al. 2011) and may have affected our findings through the influence of feedback on late-time gas accretion from the halo. However, since we compare our galaxy models primarily to each other rather than observations any effect should be reduced, and simulations including supernovae quickly generate a halo in any case. Furthermore, omitting this component has allowed a high resolution study on the role of feedback processes which is more easily compared with preceding studies.

Supernovae have a stronger effect on black hole mass in mergers compared to the isolated galaxy simulations. In the KAGN_SN and DAGN_SN simulations the reduction in star formation resulting from the inclusion of supernovae results in more gas in the galaxy after coalescence to feed the black hole (Figs. 3.11 and 3.12). The heating from supernovae therefore acts to increase growth by reducing star formation and leaving more surrounding gas at late times to be accreted by the black hole. This trend is not seen in the SAGN_SN simulation because the black holes merge promptly at coalescence, resulting in a comparatively reduced total accretion rate as the merged black hole stablilises at the centre of the system.

In this section we have shown that, in contrast to simulations of isolated galaxies, it

is possible for AGN to play the dominant role in suppressing star formation in a merger scenario. The method by which feedback energy is deposited is crucial in determining the strength of suppression; whilst models incorporating strong feedback eliminate the starburst, the weaker kernel-weighted mode merely reduces its duration. Supernovae still play a role in suppressing the star formation during the majority of the simulation, but are found to be incapable of reducing the strength of the starburst by themselves.

3.4 A closer look at the models

Our main simulations have allowed us to analyse the role feedback processes play in disc galaxies for a range of existing models. We now go on to look into numerical effects and the impact of our chosen parameters. As the high resolution achieved in these simulations is currently out of reach of typical cosmological simulations, we begin by investigating the impact of employing a lower mass resolution in Section 3.4.1. The effect of increasing the galaxy gas fraction to better represent the high redshift systems in which most quasar growth and mergers are believed to occur is examined in Section 3.4.2. To analyse the consequence of choosing an initial black hole mass of $10^5\,\mathrm{M}_\odot$, we perform tests in which we set this to a larger value in Section 3.4.3.

We also discuss issues raised whilst performing this work and further investigate aspects of the feedback models. Simulations of isolated galaxies showed that black holes appear to self regulate, slowing their growth as found by Di Matteo et al. (2005). However this may equally be caused by star formation consuming the gas which would otherwise feed the black holes; we study this further by artificially turning off star formation in Section 3.4.4. A further investigation provoked by the main body of this work originated in the finding that the temperature to which we heat gas in AGN feedback is critical. We extend our investigation to varying supernova temperature in Section 3.4.5. Finally, we disentangle the accretion and feedback elements of the Di Matteo et al. (2005) and Booth & Schaye (2009) models incorporated in the main investigation to confirm that the AGN feedback temperature is the main feature driving the change in the star formation rate in Section 3.4.6.

3.4.1 Numerical resolution

In order to evaluate the effect of changing the simulation mass resolution, we re-run the main suite of simulations with one tenth of the number of particles but with all other galaxy parameters held constant (see Table 3.1, comparing Low versus High resolution).

We begin by probing the differences in the star formation rate for simulations run at lower resolution.

The star formation rates in simulations of isolated galaxies show a small decrease in star formation due to a reduced ability to resolve high-density clumps where stars form. However the dependence on resolution is slight, with around a ~ 10 per cent reduction, so we do not discuss this further. The resolution dependence of simulated mergers is more complex. Fig. 3.13 shows the ratio (low resolution/high resolution) of stellar mass formed against time for the NFB, SN, KAGN_SN and SAGN_SN simulations (simulations without supernovae show identical trends). As found in isolated galaxies, low-resolution simulations generally under-produce stars, leaving more gas. However, they show an *increase* in star formation during starbursts as this gas is compressed during the merger. The NFB, KAGN, SAGN and DAGN simulations produce $1, 5, 15$ and 17 per cent less stellar mass over the course of the simulations respectively[4]. The larger reduction in stellar mass for the strong feedback AGN models (DAGN and SAGN are very similar at lower resolution) is due to the powerful outflows interacting with more gas, as a result of the larger smoothing lengths in low resolution simulations.

The black hole mass in low resolution simulations, plotted as a fraction of the high resolution mass is shown in Fig. 3.14 for isolated galaxies (top panel) and mergers (bottom panel), for the main AGN simulations. All AGN models produce a larger black hole mass in low resolution simulations. This resolution dependence is largely due to more poorly resolved accretion, meaning that in low resolution simulations a black hole can accrete much more mass before capturing a particle and lowering the local density. The effect is even more severe in the KAGN model, where the typical heating temperature decreases in the low resolution case as the kernel mass increases.

For the low and high resolution simulation sets we chose to vary the particle number whilst holding the gravitational softening length constant. As the softening length is linked with the minimum smoothing length ($h_{\rm min} = 2.8\,\varepsilon_{\rm soft}$) and DAGN accretion radius ($r_{\rm acc} = \varepsilon_{\rm soft}$) this fixes the typical physical scale for the AGN methods regardless of resolution (we note both methods therefore have an undesirable dependence on spatial resolution). It is, however, more common in cosmological simulations to vary the softening length to avoid numerical effects such as two-body relaxation (Power et al. 2003). Additionally it is unclear whether the resolution effects on the star formation and black hole mass are a generic trend.

In order to address these issues we perform two additional simulation sets (see Ta-

[4]We note that changing the simulation mass resolution does not directly modify the time interval or mass loading of feedback events for a given accretion rate in the strong feedback method because we decrease $N_{\rm heat}$ by the same factor by which we decrease the resolution (to $N_{\rm heat} = 1$).

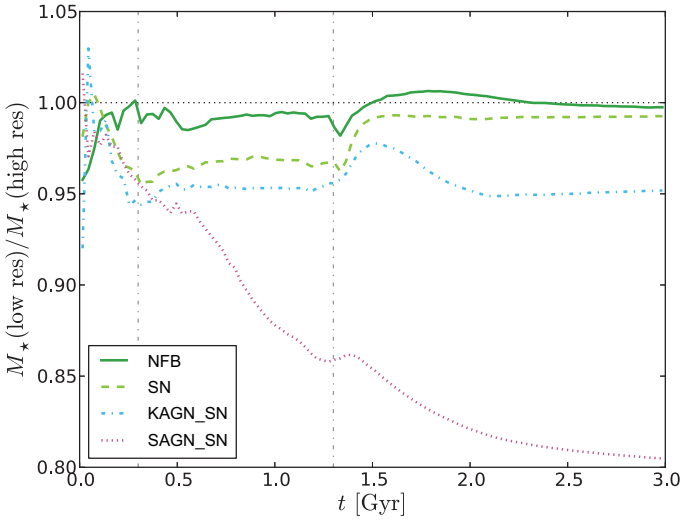

Figure 3.13: Ratio of stellar mass formed during simulations performed at high and low resolution for NFB, SN, KAGN_SN and SAGN_SN models in merging galaxies. The SAGN_SN simulation exhibits the strongest resolution dependency due to the difficulty in resolving a columnated energetic outflow at low resolution. Under-resolving the outflows increases the amount of gas with which they interact with and heat.

ble 3.1) with particle number equal to the Low resolution and a factor of ten lower (Very-Low; $N = 7 \times 10^4$, $N_{\rm heat} = 0.1$ where applicable) respectively. The additional simulations are performed with softening lengths scaled with respect to the High resolution runs as $\varepsilon_2 = (N_1/N_2)^{1/3}\varepsilon_1$; yielding softening lengths of 0.05, 0.11, $0.23\,{\rm kpc}$ for the High, Low and Very-Low runs respectively.

We present in Fig. 3.15 the total mass of black holes and stars formed against total particle number for the extended simulation set performed with the fiducial AGN models (omitting supernova feedback). We find that performing an additional simulation at Very-Low resolution confirms the trends previously seen. Across models, lowering the resolution means more poorly resolved accretion, cold gas-clumps and AGN outflows which results in lower star formation rates and increased black hole masses as previously discussed. Increasing the softening length (in the $N = 7 \times 10^5$ simulations) makes negligible difference in the NFB simulation where the reduction in stellar mass formed is very slight, however simulations including feedback generally exhibit a slightly reduced final black hole mass. This is due to the increased minimum smoothing length resulting in larger outflows which lower the accretion rate more effectively. The lower accreted mass leads to less feedback energy deposited into the gas in total and allows for a minor increase in star formation. It is interesting to note that the black hole masses obtained using different methods appear to be converging, however verifying this would require

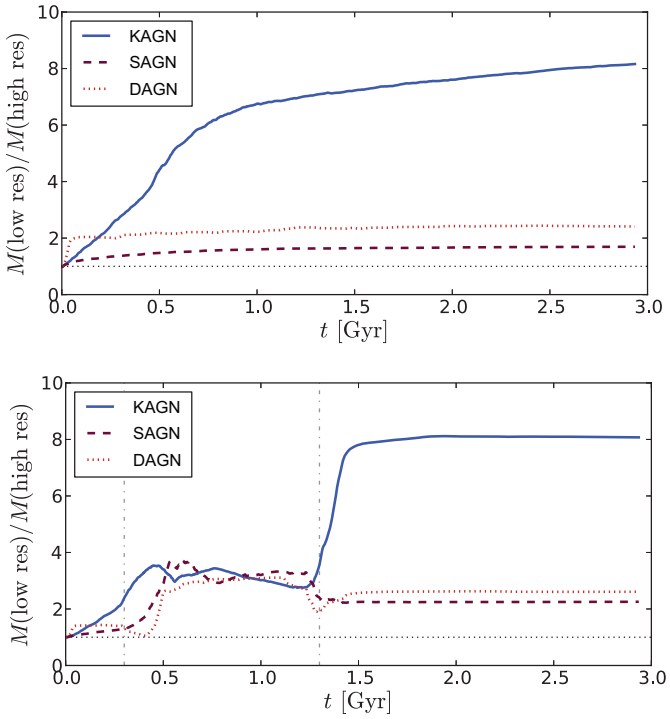

Figure 3.14: Total black hole mass ratio in low resolution over high resolution simulations in isolated (top) and merging (bottom) galaxies. For all models, black holes grow significantly more in low resolution simulations.

even higher resolution simulations, which we leave for further study. We also note that varying the number of SPH neighbours (e.g. to keep the weighted mass within the kernel constant) between resolutions may give a better scaling for the KAGN model, however such a change would also modify the hydrodynamical behaviour of the gas.

A more direct comparison with the black hole masses found in the work of Springel et al. (2005) and Di Matteo et al. (2005) is made possible using our Very-Low resolution simulations, as their runs used 8×10^4 particles. In isolated galaxy simulations we find a black hole mass of $7.2 \times 10^6\,\mathrm{M}_\odot$ which is broadly consistent with Springel et al. ($\sim 2 \times 10^6\,\mathrm{M}_\odot$). However it is not surprising to find a discrepancy as our differing resolution, star formation routine, ISM model and disc gas fraction will all affect the black hole mass. In merging systems we again find a final black hole mass higher ($6.7 \times 10^7\,\mathrm{M}_\odot$) than the value obtained in previous studies ($\sim 1 - 3 \times 10^7\,\mathrm{M}_\odot$; Springel et al. 2005; Johansson et al. 2009). The simulations with an irregular merger geometry such as our own are at the lower end of this range, therefore the deviation is slightly larger in merging systems than isolated.

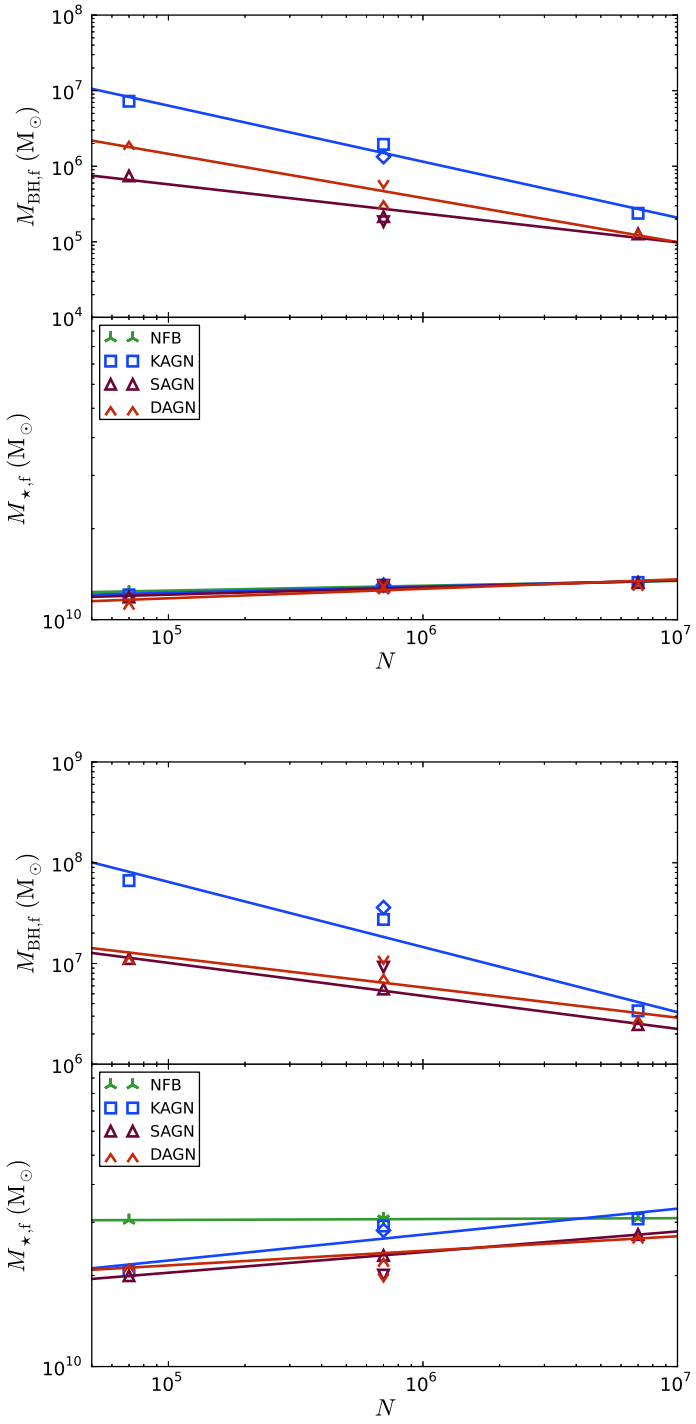

Figure 3.15: Total mass of black holes and stars formed (upper and lower sub-panels respectively) against total number of particles at the end of isolated (top) and merging (bottom) galaxy simulations for the fiducial AGN models. Variant symbols denote the standard Low resolution simulations whereas the others have scaled softening lengths; lines are fits to the scaled-softening simulations. A Very-Low resolution simulation confirms the trends of decreasing black hole mass and increasing stellar mass with higher resolution AGN simulations.

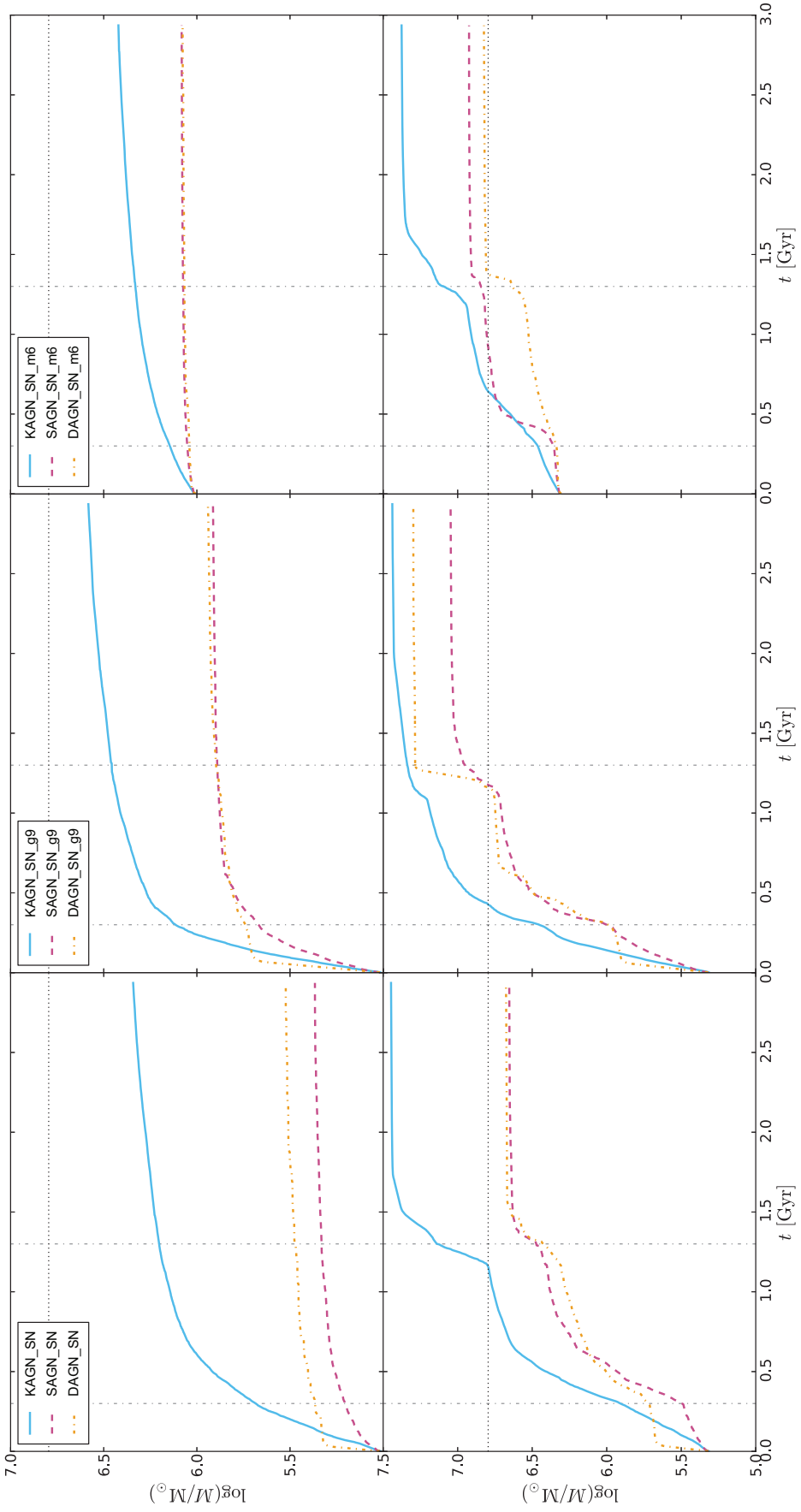

Figure 3.16: Black hole mass throughout low resolution, isolated (top) and merging (bottom) galaxy simulations including the three primary AGN models. Columns (left to right) show: standard initial black hole mass and disc gas fraction ($M_{\rm BH,i} = 10^5\,{\rm M}_\odot$, $f_{\rm g} = 0.3$); increased disc gas fraction ($M_{\rm BH,i} = 10^5\,{\rm M}_\odot$, $f_{\rm g} = 0.9$); and increased initial black hole mass ($M_{\rm BH,i} = 10^6\,{\rm M}_\odot$, $f_{\rm g} = 0.3$). The final black hole mass is relatively unaffected (to within a factor of 2-3) by changing either the disc gas fraction or initial mass.

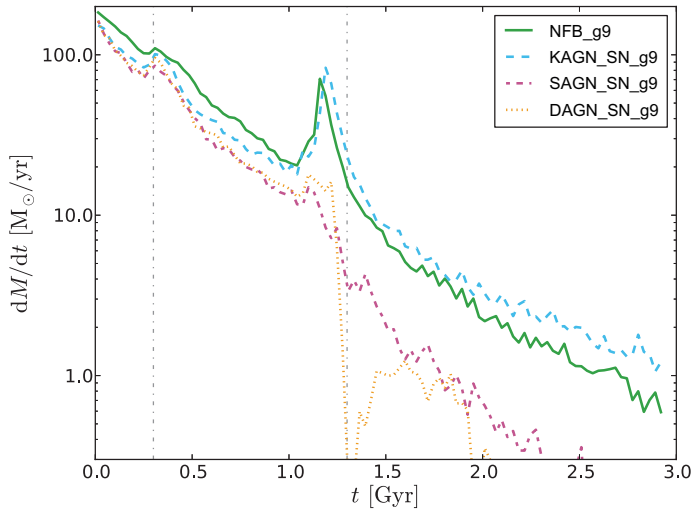

Figure 3.17: Star formation rate throughout simulations of low resolution merging galaxies with an increased disc gas fraction $f_{\rm g} = 0.9$ including the three primary AGN models and supernovae (KAGN_SN_g9, SAGN_SN_g9, DAGN_SN_g9). The shape and trends are the same as seen with the fiducial gas fraction, however the absolute rate is almost an order of magnitude larger.

3.4.2 Initial gas fraction

We now investigate how the supernova and AGN feedback processes interact in gas-rich discs with a gas fraction $f_{\rm g} = 0.9$, more appropriate for a high redshift system. (The simulations are performed at low resolution for the standard AGN models to minimise CPU time consumption.) Fig. 3.16 shows the black hole mass evolution for the low resolution fiducial models (left panels) and increased gas fraction (centre panels) for the three AGN models simulated with supernovae in isolated (top row) and merging (bottom row) galaxies. This change has the effect of accelerating the coalescence of the galaxies/black holes. However, we find that the black holes in gas-rich systems cease growth at broadly similar masses to the fiducial simulations for all AGN models. This is perhaps surprising as we have shown that the black hole growth is very sensitive to the amount of gas available in its surroundings (Section 3.3.4). This is explained by the increased level of star formation observed in the gas-rich galaxies (Fig. 3.17) consuming the gas on the same timescale as in the fiducial galaxy and terminating black hole growth. Aside from the higher star formation rates seen across all times, the feedback models show the same trends in the star formation rate as in the case of the models with lower gas fraction. Supernovae dominate the star formation suppression in the isolated galaxies and through mergers the AGN model with weak feedback suppresses the star formation slightly, but it is shut off completely by the strong feedback models.

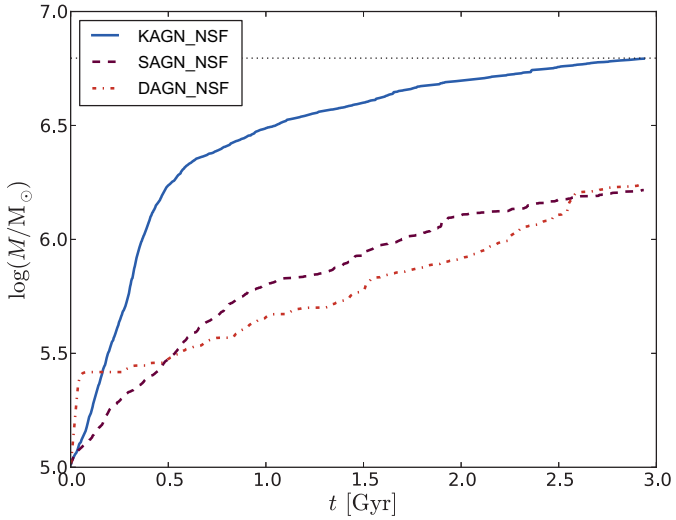

Figure 3.18: Black hole mass evolution for isolated galaxies simulated with the fiducial AGN models and no star formation. This shows that the black holes have not self-regulated their own growth through feedback within 3 Gyr.

3.4.3 Initial black hole mass

The initial black hole mass used in our main simulation runs is motivated by the approximate mass scale of primordial 'seed' black holes formed through the direct collapse of zero metallicity gas (see e.g. Bellovary et al. 2011 and references therein) and the desire for compatibility with previous studies. This value is poorly constrained and well below the mass of a black hole predicted by observational relations for this galaxy, $M_{\rm BH} \sim 10^7\,M_\odot$ (Magorrian et al. 1998; Tremaine et al. 2002; Häring & Rix 2004). Here we investigate the sensitivity of the black hole mass evolution to the initial mass chosen. We perform additional low resolution simulations for the KAGN, SAGN and DAGN models with an initial mass of $M_{\rm BH,i} = 10^6\,{\rm M}_\odot$. While this mass is substantially larger (10 times the fiducial mass) it is still lower than the predicted value and therefore still requires significant growth to reach this relation.

We find that changing the initial mass in this way (Fig. 3.16) does not greatly affect the final mass of the black holes. Growth ceases at similar values to the fiducial low resolution runs provided that the initial mass does not exceed the final mass in the standard case. The star formation rate is similarly independent of initial black hole mass (not shown).

Table 3.3: Parameters for supplementary simulations investigating supernova feedback. Columns detail the simulation label, supernova feedback efficiency, number of gas particles heated by each star particle and the temperature by which gas is heated through a feedback event. Note that KAGN_SN_N1T1 is our fiducial choice.

Label	$\epsilon_{\rm SN}$	SN $N_{\rm heat}$	$T_{\rm heat}$ [K]
KAGN_SN_N1T1	0.37	1	1×10^7
KAGN_SN_N10T0.1	0.37	10	1×10^6
KAGN_SN_N3T1	1.1	3	1×10^7
KAGN_SN_N1T3	1.1	1	3×10^7

3.4.4 No star formation

We showed previously (Section 3.2.2) that in isolated galaxies the growth of the central black hole slows over time. This may be interpreted as evidence that the black hole has self-regulated its growth through feedback, however we noted that this 'self regulation' occurs on a similar timescale as gas is depleted from the galaxy. As a means of modifying the timescale over which gas is consumed in the galaxy systems, we perform additional simulations in which we artificially turn off star formation.

Fig. 3.18 shows black hole mass versus time for models with no star formation. All models yield substantially larger final black hole masses and the slowing of black hole growth towards the end of the simulation is less clear. This shows that, at least in artificially isolated galaxies without an external gas source, black hole growth is halted due to external gas consumption through star formation. Although a galaxy would normally be fed with cooling gas from a halo or accretion along a filament, it is possible that the regulation of black hole growth through star formation is important in low redshift galaxies for which filamentary structures have been disrupted and/or the gas becomes too diffuse to cool efficiently onto the galaxy.

3.4.5 Supernova feedback parameters

As a probe of the numerical sensitivity of our supernova feedback implementation we also present additional low resolution simulations performed with varying mass loading factors and supernova heating temperatures. In the fiducial model, each star formed causes one neighbouring gas particle to be heated to $10^7\,\mathrm{K}$, coupling the supernova energy with an efficiency, $\epsilon_{\rm SN} = 0.37$. Here we additionally simulate this feedback with several different parameter choices (Table 3.3), namely heating 10 particles to $10^6\,\mathrm{K}$, thereby keeping the total energy output constant, a case where we deposit all the energy available (see Chapter 2 Section 2.2.2 for a derivation) into 3 particles heated to $10^7\,\mathrm{K}$; and a maximal

case where we heat 1 particle to $3 \times 10^7\,\mathrm{K}$.

Fig. 3.19 shows projected gas density plots for the range of supernova parameters. Increasing the strength of the feedback, and particularly the temperature, increases the porosity in the gas disc and redistributes more gas into the hot halo. Note that the simulations were performed with the KAGN method in conjunction with supernova feedback as this model allows an investigation of the effect on the black hole during a merger, without the AGN terminating star formation.

Fig. 3.20 shows the evolution of the star formation rate in isolated (left panel) and merging (right panel) idealised disc galaxies. Star formation is barely suppressed in the KAGN_SN_N10T0.1 simulation, whilst the fiducial model KAGN_SN_N1T1 is only marginally less powerful than the KAGN_SN_N3T1 variant, despite the latter having three times as much energy available per supernova. Finally, the KAGN_SN_N1T3 model causes by far the most suppression of star formation at all times, even delaying the timing of the starburst. The delay does not have a dynamical origin as the black holes are dynamically bound/merged by $t = 1.37\,\mathrm{Gyr}$. It is caused by the longer time it takes for the gas to condense out of the hotter and more diffuse halo created by the supernovae.

In summary, the level of star formation suppression due to supernovae is most sensitive to the choice of heating temperature, a finding in agreement with the results from our AGN feedback simulations.

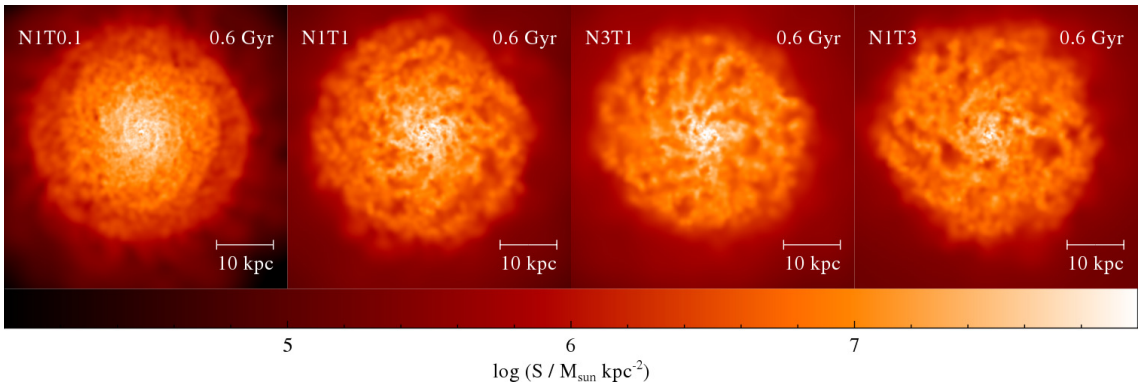

Figure 3.19: Projected logarithmic face-on gas surface density maps for isolated galaxies simulated with different supernova feedback parameters at $t = 0.6\,\mathrm{Gyr}$ (all simulations include Bondi-type kernel-weighted AGN feedback). Models shown have increasing (left to right) feedback strength: (KAGN_SN_)N10T0.1, N1T1, N3T1, N1T3. A larger heating temperature leads to an increased porosity of the gas disc.

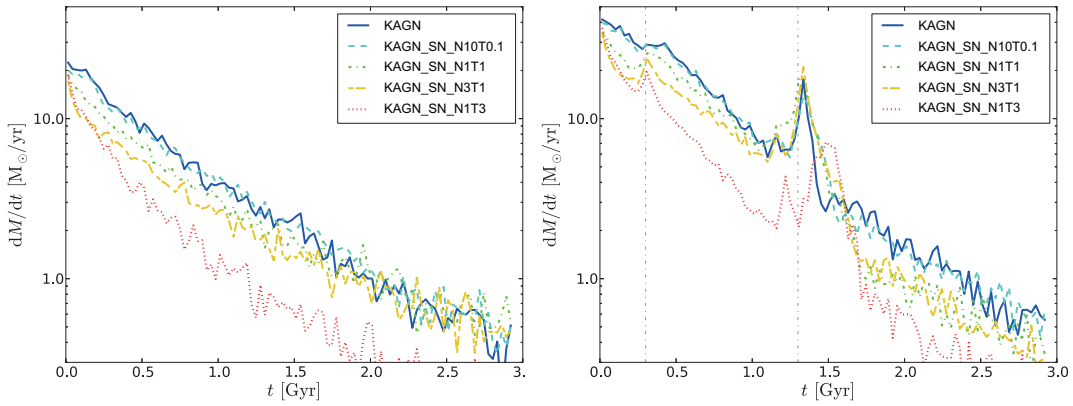

Figure 3.20: Evolution of the star formation rate with varying supernova feedback strength for low resolution simulations employing kernel-weighted, Bondi-type AGN feedback in isolated (left panel) and merging (right panel) disc galaxies. The low resolution fiducial model (KAGN) is shown for comparison. The N1T3 model causes by far the most suppression of star formation.

3.4.6 AGN feedback parameters

The findings of our main investigation indicate that the most important aspect of an AGN model, in terms of the effect on the host galaxy, are the details of how the feedback energy is deposited. Specifically, the temperature reached by heated gas is shown to be critically important. Striking differences were found between the Bondi-based AGN models of Di Matteo et al. (2005) and Booth & Schaye (2009) which differ primarily by employing kernel-weighted and strong feedback respectively. However, the details of the two methods have additional variations; the values of the feedback coupling efficiency ($\epsilon_{\rm f} = 0.05$ versus 0.15) and accretion rate boost, $\alpha = 100$ or $\propto \rho^2$ (see Chapter 2 Section 2.2.3 for details) both change between the models. In order to disentangle the effects of these choices we have performed two extra simulations, changing each of the parameters one at a time. Table 3.4 summarises the extra simulations performed.

In Fig. 3.21, we compare the star formation rate (top panel) and total black hole mass (bottom panel) between the fiducial Bondi models and the additional merger simulations at low resolution. This shows conclusively that the heating method is the dominant factor in determining the star formation suppression by AGN feedback in these systems. Changing the accretion rate density dependence does have a small effect on the star formation at early times, but the dominant trend of declining and terminating star formation still occurs at the same time. Modifying the available feedback energy by a factor of three through the $\epsilon_{\rm f}$ parameter has no discernible impact upon the star formation rate (a result similar to that found by Debuhr et al. 2011).

The black hole mass evolution is also sensitive to changes made to the heating effi-

Table 3.4: Additional simulation parameters probing the AGN feedback method. Columns detail the simulation label, Bondi accretion rate boost factor, number of feedback-heated particles, feedback distribution type and AGN feedback efficiency.

Label	Acc.	α	$N_{\rm heat}$	Type	$\epsilon_{\rm f}$
KAGN_SN_α_05	Bondi	100	50	kernel	0.05
SAGN_SN_α_05	Bondi	100	1	strong	0.05
SAGN_SN_α_15	Bondi	100	1	strong	0.15
SAGN_SN_β_15	Bondi	$\propto n_{\rm H}^2$	1	strong	0.15

ciency parameters, showing a trend for reducing mass with increasing feedback strength as would be expected. These findings show that the black hole feedback efficiency can be used to tune the black hole mass without affecting the host galaxy, as long as the feedback method is constant, in agreement with Booth & Schaye (2009).

3.5 Discussion and conclusions

AGN feedback models are becoming a standard component in both large scale *N*-body hydrodynamical simulations and semi-analytic modelling, but the full implications of incorporating even the current simplistic models are not yet fully understood. One particular uncertainty is how the combination of AGN and supernova feedback processes change the star formation rate in a galaxy. We performed and compared a series of identical high resolution disc galaxy simulations with a range of sub-grid model combinations including a variety of AGN models and supernova feedback strengths. Changing only the feedback models allowed us to perform a clean comparison between competing parametrisations, as well as probing the details of the processes involved and how the models interact. Beginning with an isolated disc galaxy we investigated how feedback processes change the star formation rate and where appropriate the black hole growth. Building on this understanding we simulated the galaxies undergoing major mergers and analysed the effects of AGN and supernova feedback on the galaxy through an active phase in its evolution. Our main conclusions may be summarised as follows:

- In isolated Milky-Way-mass model disc galaxies supernova feedback dominates the star formation suppression, whereas AGN feedback has no impact for any of the tested models. This is due to the disparity in scales upon which the processes act; AGN activity is (eponymously) confined to the central region whereas supernovae occur throughout the galactic disc.

- AGN feedback plays a much larger role in mergers and may completely eliminate

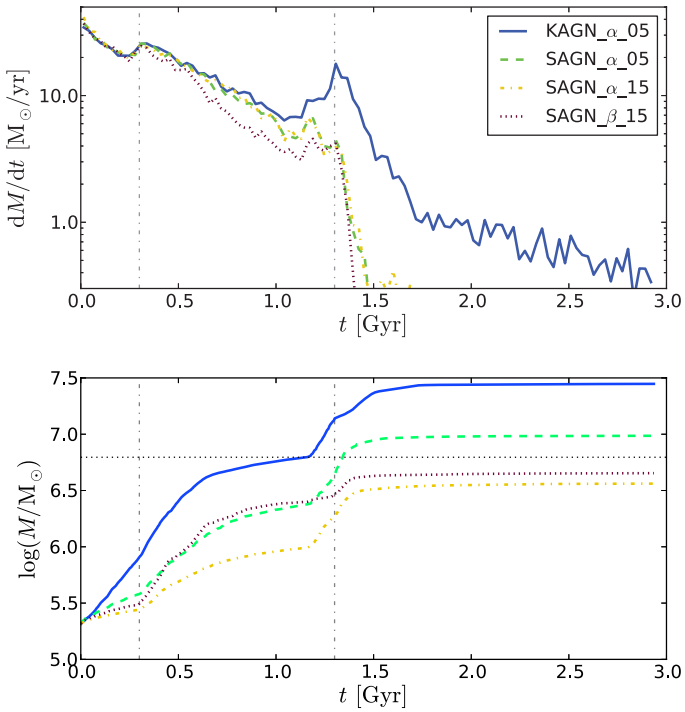

Figure 3.21: Effect of varying AGN feedback parameters on the star formation rate (top panel) and total black hole mass (bottom panel) in low resolution merger simulations. The star formation rate through a merger is dominated by the choice of feedback model, while the final black hole mass also shows a strong dependence on the efficiency parameter $\epsilon_{\rm f}$.

the starburst when the heating is strong. The most important factor determining the strength of AGN feedback on the host galaxy is the temperature to which gas is heated and correspondingly the feedback mass loading. A higher temperature allows (fewer) gas particles to escape from high density regions without suffering from significant radiative losses.

- Supernova and AGN feedback are largely independent, with only a slightly stronger suppression of the star formation rate when acting together than if they acted independently. This finding is in contradiction to the findings of Dalla Vecchia & Schaye (2012) and supports the approach taken in semi-analytic modelling, (Bower et al. 2006; Croton et al. 2006; Guo et al. 2011). However, our simulations are a restricted set of conditions and ignore complex effects such as external gas accretion.

- Numerical resolution strongly affects the black hole mass due to under-resolved feedback and accretion. The problem is more severe for the kernel-weighted model where lower resolution simulations result in lower heating temperatures due to the increase in mass within the kernel. However, the stellar mass appears to converge

less quickly with resolution in strong feedback models.

- The black hole mass is sensitive to the choice of both the feedback and accretion models, however the parameters may be tuned to obtain desired masses with little effect on the galaxy. The mass is strongly affected by gas consumption through star formation in these model systems which neglect an external gas source such as a hot halo or minor mergers. Gas fraction and initial black hole mass do not affect the final black hole mass by a large factor.

- The level of star formation suppression due to supernovae is (as for AGN feedback) strongly linked to the temperature of heated gas with higher temperatures causing a larger reduction. The number of heated particles (mass loading) is of secondary importance. However, even the maximally strong supernova feedback model was unable to prevent a starburst occurring in the galaxy merger when AGN feedback was weak.

The main outcomes of this study will be of use for informing future theoretical works simulating/modelling AGN and SN feedback. Future N-body methods incorporating AGN in galaxy formation simulations should consider that the (thermal) feedback strength is the key factor in determining the effect on its host galaxy. Additionally we find that AGN and SN feedback processes are largely independent across models in these systems, supporting the approach taken in semi-analytic modelling. Our findings may indicate that it may be premature to attempt to probe the detailed features of AGN (e.g. durations of feedback episodes, luminosities) for comparison with observations using the current generation of models designed for studying galaxy formation.

While we have gone some way towards disentangling the role of feedback processes across multiple models for the same systems, further work is required to make progress with many aspects of our understanding of AGN feedback in galaxies. Due to our need to perform multiple high resolution simulations, we were only able to study two identical systems. Future work, taking advantage of advances in computational power, may investigate these processes in cosmological zoom simulations (Tormen et al. 1997) of multiple galaxy masses and environments. A possible shortcoming of this work is that the IMF employed (Salpeter) is currently in question, with alternatives e.g. Chabrier and Kroupa IMFs arguably giving better fits to data. An alternative IMF alters the star formation history of a galaxy as well as the energy available from supernovae. However the trends outlined in this study are unlikely to change substantially with an alternative IMF for a given supernova model.

Chapter 4

Simulations of groups and clusters with AGN feedback

Gravity is a habit that is hard to shake off.

SIR TERENCE "TERRY" PRATCHETT

As discussed in Chapter 1 (Section 1.2.1), AGN activity in groups and clusters of galaxies is commonly linked to observations of hot, radio-emitting plasma lobes embedded in cavities within the X-ray-emitting ICM (see e.g. McNamara & Nulsen 2007; Alexander & Hickox 2012 and references therein). Due to the extreme temperatures and sizes of these objects, it has been estimated that their total power output may to be in excess of $10^{43}\,\mathrm{ergs}^{-1}$, with associated energy outputs of the order $10^{61}\,\mathrm{erg}$ (e.g. McNamara & Nulsen 2007; Cavagnolo et al. 2010; Alexander & Hickox 2012).

Observationally there is a dichotomy between cool core and none-cool core clusters they are observationally distinguished by their central entropies and temperatures. The technical distinction between the two classes varies, however a cool core cluster typically has a lower central temperature/entropy, a shorter central cooling time and higher mass deposition rates (Hudson et al. 2010). However, despite these distinctions, all galaxy clusters have cooling times shorter than the age of the Universe. Therefore, without a substantial source of heat, these clusters would be expected to form catastrophic cooling flows, depositing $> 100\,\mathrm{M}_{\odot}$ of gas onto the central galaxy and forming large numbers of stars. Due to the large amount of energy required to offset cooling, AGN are thought to be the source of this feedback (see Chapter 1 Section 1.2.1; e.g. Fabian 2012).

Previous work simulating these objects has been somewhat successful in modelling AGN in the radio regime (see Chapter 1 Section 1.2.4). For example, using thermal feedback in model clusters (Dalla Vecchia et al. 2004; Sijacki & Springel 2006) successfully

prevented the over-cooling catastrophe using AMR and SPH simulations respectively. Likewise, simulating AGN jets with kinetically-driven (anisotropic) winds has been reasonably successful in grid-based codes. For example, Cattaneo & Teyssier (2007) reproduced the observed BH accretion rate and X-ray luminosity in a model object based upon the Virgo cluster, reversing the effect of a cooling flow. Also using AMR, Gaspari et al. (2011) and Gaspari et al. (2013) have had success in matching observations for a selection of groups and clusters by simulating kinetic AGN outflows. Furthermore, incorporating a dual-mode scheme in cosmological simulations has been shown by Sijacki et al. (2007) and Vogelsberger et al. (2013) to prevent an over-production of stars in high mass galaxy systems. However, a potential shortcoming of this work is the need for the AGN heating efficiency to be tuned 'by hand' across the range of cluster masses to prevent under/over-heating the ICM.

Despite numerous studies; how the existing models perform in different environments, the phenomena driving their effects and the sensitivity of the models to their parameters remain unknown. Furthermore, it remains unclear whether it is possible for SPH simulations incorporating a single AGN feedback model to match observational constraints across a range of objects and masses. We therefore now go on to perform a range of simulations in a selection of group and cluster objects using the models utilised in Chapter 3. In order to model AGN on cluster scales we also incorporate an anisotropic, jet-like, AGN feedback model based upon that of Booth & Schaye (2009); this is discussed in detail in Section 4.2.

Previous studies have used various tests for their AGN models; we adopt the following constraints for our own investigation:

- In the first instance, objects should be maintained in an equilibrium state by the AGN.
- Correspondingly, there should be a low level of star formation, if any.
- Object profiles for density, entropy and X-ray luminosity must agree with observational (REXCESS; see Böhringer et al. 2007) data.
- AGN heating should not produce negative entropy gradients in the core (i.e. 'entropy inversions').
- Phenomenological features of the ICM such as X-ray cavities, radio lobes, jets, shells etc. should be observed

We begin by outlining our procedure for creating equilibrium group and cluster objects in Section 4.1 before discussing specific parameter choices for our initial conditions in

Section 4.1.3. In order to begin our study, in Section 4.1.3 we perform simulations with the standard galactic-scale AGN models (from Chapter 3) before incorporating and testing a bipolar radio-mode AGN model in Section 4.2.

4.1 Creating equilibrium groups and clusters

For the purposes of this investigation, we represent groups and clusters of galaxies by a simplified approximation with properties motivated by observational studies; the simplifications used allow for higher resolution simulations and more straightforward analysis than other methods e.g. cosmological zoom simulations. We represent our simulated objects as equilibrium spherically symmetric groups/clusters consisting of a dark matter halo, central stellar spheroid (both described by Hernquist profiles following the method outlined in Chapter 3 Section 3.1 for particle positions and velocities) and an Inter-Galactic Medium (IGM) or ICM (as appropriate) initially in hydrostatic equilibrium.

4.1.1 Collisionless particles

When defining the positions of the collisionless components we follow the method given in Chapter 3 Section 3.1; briefly we assume that the DM component and stellar spheroid follow the (un-contracted) Hernquist mass profile (Hernquist 1990) with observationally-motivated scale-lengths, and that their velocity field are described locally as multivariate Gaussian distributions.

4.1.2 Gaseous halo particles

The positions of the population of gaseous particles are defined by specifying an input entropy profile and assuming hydrostatic equilibrium. All gas particles initially have zero velocity as they are supported by pressure forces alone.

We begin by defining the entropy,

$$K = \frac{k_{\rm B}T}{n_{\rm e}^{2/3}}, \tag{4.1}$$

which is related to the classical thermodynamic entropy by a logarithm and an additive constant where $n_{\rm e}$ is the electron number density. The gas is described by the ideal gas equation,

$$P = \frac{\rho_{\rm g} k_{\rm B} T}{\mu m_{\rm H}}, \tag{4.2}$$

where we relate the gas density to the electron number density by,

$$\rho_{\rm g} = n_{\rm e}\mu_{\rm e}m_{\rm H}, \tag{4.3}$$

where $\mu_{\rm e}(= 1.16)$ is the mean molecular weight per electron. We then combine Equations 4.1 and 4.3 to obtain,

$$k_{\rm B}T = \frac{\rho_{\rm g}^{2/3}}{\mu_{\rm e}^{2/3}m_{\rm H}^{2/3}}K, \tag{4.4}$$

and substitute in Equation 4.2 before rearranging to give an expression for the gas density defined in terms of entropy and pressure,

$$\rho_{\rm g} = \mu^{3/5}\mu_{\rm e}^{2/5}m_{\rm H}P^{3/5}K^{-3/5}. \tag{4.5}$$

Turning now to the gaseous halo; we begin by demanding hydrostatic equilibrium, thereby assuming that the gravitational and pressure support forces are balanced,

$$\frac{{\rm d}P}{{\rm d}r} = -\rho_{\rm g}\frac{{\rm d}\Phi}{{\rm d}r}. \tag{4.6}$$

Therefore, for a spherically symmetric system utilising Newton's shell theorem,

$$\frac{{\rm d}P}{{\rm d}r} = -\frac{GM(<r)}{r^2}\rho_{\rm g}, \tag{4.7}$$

and substituting in our expression of the ideal gas equation (Equation 4.5) before rearranging gives,

$$P^{-3/5}\,{\rm d}P = -G\mu^{3/5}\mu_{\rm e}^{2/5}m_{\rm H}\frac{M(<r)}{r^2}K^{-3/5}\,{\rm d}r. \tag{4.8}$$

We then perform the integrals from r to the surface, $r_{\rm s}$, where we define $P(r_{\rm s}) = P_{\rm s}$, obtaining

$$P(r) = \left[P_{\rm s}^{2/5} + G\mu^{3/5}\mu_{\rm e}^{2/5}m_{\rm H}\int_r^{r_{\rm s}}\frac{M(<r)}{r^2}K^{-3/5}(r)\,{\rm d}r\right]^{5/2} \tag{4.9}$$

In practice we demand $P_{\rm s} = 0$ and iterate to solve for $r_{\rm s}$ under the condition that the gas fraction within r_{500} is equal to a predetermined value. We may then trivially obtain the gas temperature and density profiles using Equations 4.4 and 4.5 respectively for a given entropy profile.

Table 4.1: Parameters for describing the matter distribution of the simulated group and clusters. Column 1 lists the object labels, columns 2 and 3 define the DM NFW and Hernquist profile scale radii, while columns 4-7 give total masses and radii at $\Delta = 200$ and 500 respectively. Columns 8 and 9 specify the baryonic and gas mass fractions within r_{500} respectively and the final column states the initial BH mass. All masses and radii stated in $10^{13}\,\mathrm{M}_\odot$ and kpc units respectively except for $M_{\rm BH}$ $[10^9\,\mathrm{M}_\odot]$.

Object	c	a	M_{200}	r_{200}	M_{500}	r_{500}	$f_{500}^{\rm star}$	$f_{500}^{\rm gas}$	$M_{\rm BH}$
GG	4.74	127	0.668	241.6	0.498	177.6	0.016	0.046	0.85
LC	3.79	314	7.13	545.98	5.31	388.1	0.005	0.073	2.51
HC	3.03	770	70.5	1206.9	50.5	843.6	0.002	0.090	7.37

4.1.3 Defining the group & cluster properties

Since the observed effects are likely to change in objects with differing escape velocities, it is important to probe the influence of AGN and supernovae across a range of masses. We therefore choose to simulate three objects defined roughly by $M_{200} = 10^{13}$, 10^{14} and $10^{15}\,\mathrm{M}_\odot$, corresponding to a galaxy group (GG) as well as low and high mass clusters (LC, HC). In order to keep our analysis as simple as possible across the range of masses, we simulate realistic, but roughly self-similar, objects. We now outline the motivation for the object parameters which are summarised in Table 4.1.

To completely specify the dark matter halos we must define their masses and concentrations. All component masses are defined by the mass fraction within r_{200}; for the dark matter this may be expressed as $M_{\rm DM}(r_{200}) = (1 - f_{\rm b})M_{200}$ (where $f_{\rm b} = f_{\rm star} + f_{\rm gas}$ is the baryon fraction) and the total mass may be obtained using Equation 3.2 for a known scale-length, a. The halo concentration fitting formula from Duffy et al. (2008),

$$c_{200} = 5.74 \times \left(\frac{M_{200}}{2 \times 10^{12} h^{-1}\mathrm{M}_\odot}\right)^{-0.097}, \tag{4.10}$$

is used to obtain the concentrations for the dark matter halos before conversion to scale-lengths using Equation 3.3. The stellar spheroid has a scale-length proportional to the dark matter halo ($b = 0.1a$) and mass normalised by $M_\star(r_{500}) = f_{500}^{\rm star} M_{500}$. The values of $f_{500}^{\rm star}$ are calculated using the Moster et al. (2010) fit to simulations

$$M_\star = 2M \left(\frac{M_\star}{M}\right)_0 \left[\left(\frac{M}{M_1}\right)^{-\beta} + \left(\frac{M}{M_1}\right)^{\gamma}\right]^{-1}, \tag{4.11}$$

where $M_1 = 79.25\,\mathrm{M}_\odot$, $(M_\star/M)_0 = 0.2817$, $\beta = 1.068$ and $\gamma = 0.611$ are the fitting parameters, under the assumption that all stellar mass belongs to the central galaxy.

Table 4.2: Median values of entropy profile fitting parameters as well as characteristic mass and radius values. The first column gives the core classification group while the following four state the mean values of the groups taken directly from the observational data of Pratt et al. (2010) and the final two are properties derived from these means. All entropy values stated in $\mathrm{keV\,cm^2}$.

Core type	$\widetilde{K}_0$	$\widetilde{K}_{100}$	$\widetilde{\alpha}$	$\widetilde{M}_{500}\,[\mathrm{M}_\odot]$	$\widetilde{r}_{500}\,[\mathrm{kpc}]$	$\widetilde{K}_{500}$
Non-cool core	88.33	145.40	0.82	2.7×10^{14}	946.51	701.59
Cool core	3.16	137.26	0.99	3.1×10^{14}	975.70	754.69

The mass within r_{500} may then be calculated analytically, however the fraction must be specified before M_{500} is known accurately. We must therefore calculate the value approximately, assuming the total mass follows a Hernquist profile (e.g. Equation 3.1).

Defining the gaseous halo properties requires a normalisation of the mass profile and a description of the entropy profile. For the mass normalisation we choose to define the gas fraction within r_{500}, $M_{\mathrm{gas}}(r_{500}) = f_{500}^{\mathrm{gas}} M_{500}$, adopting values derived from the fit of Giodini et al. (2009),

$$f_{500}^{\mathrm{gas}}(h/0.7)^{3/2} = 9.3^{+0.2}_{-0.2}\left(\frac{M_{500}}{2\times10^{14}\,\mathrm{M}_\odot}\right). \tag{4.12}$$

In order to define the entropy profile, we utilise the median fit to REXCESS data from Pratt et al. (2010) for both non-cool and cool core undisturbed clusters as a basis for our self-similar entropy profiles. The fitted profiles take the form,

$$K(R) = K_0 + K_{100}\left(\frac{R}{70h^{-1}\mathrm{kpc}}\right)^{\alpha}, \tag{4.13}$$

for which we calculate the median values of each fitting parameter as well as physical properties to allow scaling of profiles, the values are listed in Table 4.2. It is convenient to define a characteristic entropy scale for groups and clusters; for this we follow Pratt et al. (2010) (and Voit et al. 2005). We calculate an entropy from the equivalent thermal energy for virial equilibrium at the radius at which the enclosed density is $(\Delta =)500$ times the critical density of the Universe (ρ_{cr}). Therefore, using Equation 4.1 with the virial theorem ($E = -W$),

$$k_{\mathrm{B}}T = \frac{GM_{500}\mu m_{\mathrm{H}}}{2r_{500}}, \tag{4.14}$$

(an exact result for an isothermal sphere) gives a characteristic entropy value for a group

Table 4.3: Prescribed group/cluster entropy profile values and core type. All entropy values are obtained by scaling the median observational data of Pratt et al. (2010) using the self-similar scaling of K_{500} and are stated in $\mathrm{keV\,cm^2}$.

Object	Core Type	K_0	K_{100}	K_{500}
GG	None cool	8.65	35.82	55.64
LC	None cool	39.47	87.75	248.56
HC	None cool	180.11	214.71	1121.02

or cluster,

$$K_{500} = 106\,\mathrm{keV\,cm^{-2}} \left(\frac{M_{500}}{0.7\times10^{14}h^{-1}\mathrm{M}_\odot}\right)^{2/3} \left(\frac{1}{f_\mathrm{b}}\right)^{2/3} E(z)^{-2/3} \left(\frac{h}{0.7}\right)^{-4/3}. \quad (4.15)$$

The median entropy profile is then scaled for the different mass objects self-similarly (assuming $K_{500} \propto M_{500}^{2/3}$) for a constant α. In order to perform the scaling, we first calculate the median characteristic radii ($\widetilde{r}_{500}$), masses ($\widetilde{M}_{500}$) and entropy profile fitting parameters ($\widetilde{K}_0,\ \widetilde{K}_{100},\ \widetilde{\alpha}$), for the observed cool core and non-cool core clusters. We then define the scaled properties $\mathcal{K} = K/K_{500}$ and $\mathcal{R} = r/r_{500}$ and substitute into Equation 4.13 to obtain

$$\begin{aligned}\mathcal{K}(\mathcal{R}) &= \frac{1}{\widetilde{K}_{500}}\left(\widetilde{K}_0 + \widetilde{K}_{100}(\mathcal{R}r_{500})^{\widetilde{\alpha}}\right) \\ &= \frac{1}{K_{500}}\left(K_0 + K_{100}(\mathcal{R}r_{500})^{\alpha}\right).\end{aligned} \quad (4.16)$$

we may then re-arrange to find

$$K_0 = \left(\frac{M_{500}}{\widetilde{M}_{500}}\right)^{2/3} \widetilde{K}_0, \quad (4.17)$$

and

$$K_{100} = \left(\frac{M_{500}}{\widetilde{M}_{500}}\right)^{2/3} \left(\frac{r_{500}}{\widetilde{r}_{500}}\right)^{-\alpha} \widetilde{K}_{100}. \quad (4.18)$$

The entropy profile parameters are illustrated in Fig. 4.1, which shows the entropy profiles of the idealised groups and clusters both unscaled and scaled to highlight their self-similar nature. This and all entropy, density and temperature profiles presented for the group and cluster objects are calculated by taking the mean value within a series of spherical shells, each containing 500 particles, centred on the gas; profile parameters are listed in Table 4.3.

Adopting the parameters we have chosen produces realistic, stable (explicitly tested for $10\,\mathrm{Gyr}$ and shown for the GG in Fig. 4.3) non-cool core groups and clusters. Fig. 4.2

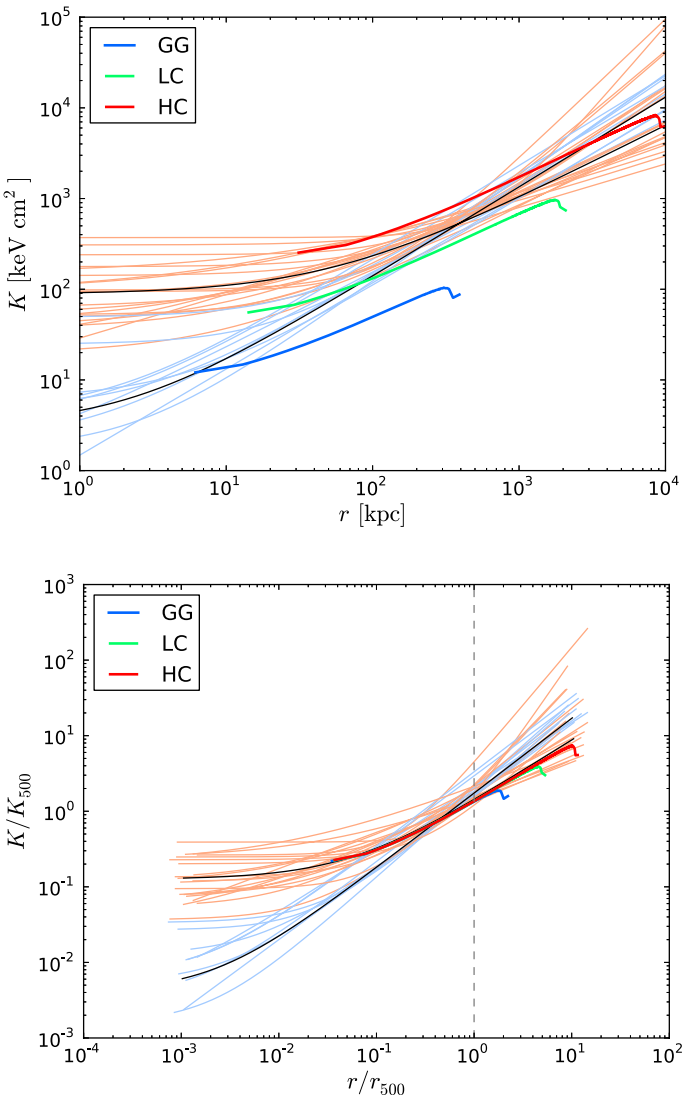

Figure 4.1: Initial group/cluster entropy profiles for the GG, LC and HC objects shown unscaled (top panel) and scaled (bottom panel) with respect to the characteristic radius and entropy (see Equation 4.15). REXCESS observational data for non-cool core and cool-core clusters (Pratt et al. (2010)) are shown in pink and pale blue for comparison. The median observational non-cool core and cool-core profiles are over-plotted in black.

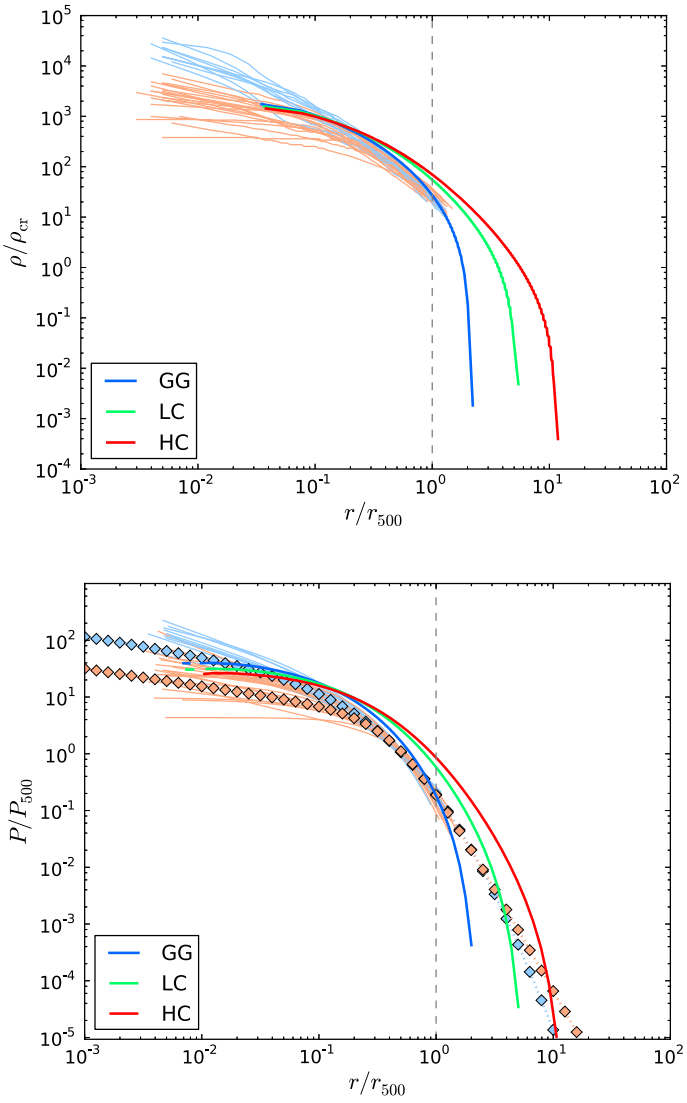

Figure 4.2: Initial group/cluster density (top) and pressure (bottom) profiles obtained from enforcing hydrostatic equilibrium on our specified systems. REXCESS observational data of non-cool core and cool-core clusters are shown in pink and pale blue for comparison, profiles taken from Croston et al. (2008) and diamonds show best-fit profiles from PLANCK (Planck Collaboration et al. 2013c).

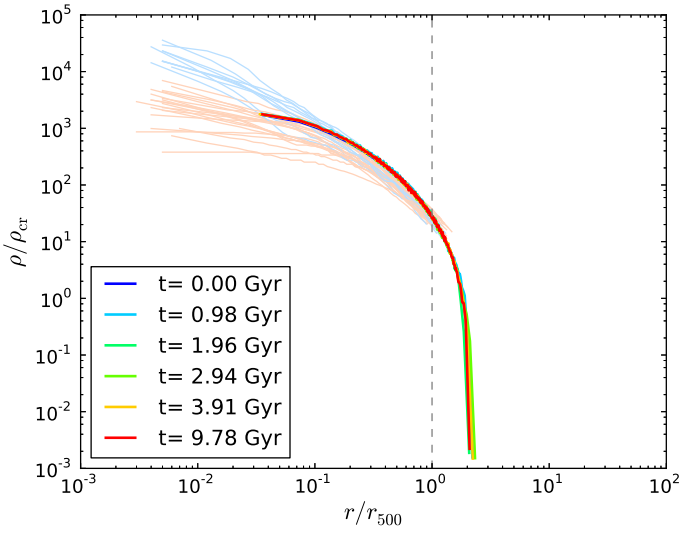

Figure 4.3: Galaxy group density profile (scaled as a ratio of the critical density) stability demonstrated for evolving the system with gravitational and hydrodynamical forces only. The simulation shown simulates a GG object with 10^6 DM particles for $10\,\mathrm{Gyr}$. REXCESS observational data of non-cool core and cool-core clusters are shown in pink and pale blue for comparison.

shows density and pressure profiles obtained under the assumption of hydrostatic equilibrium and the previously defined parameters as well as comparisons to relevant observational data from the REXCESS survey. The pressure profile is somewhat higher at all points than the idealised mean fit to data. This deviation is due to the lack of a complete dataset which fully characterises each aspect of a group or cluster. This makes the combination of different datasets necessary, which may not be self-consistent. Additionally, the idealised gas properties are in hydrostatic equilibrium by construction, an assumption which is unlikely to hold on the periphery of clusters at the interface with the cosmic web. Each central galaxy is assumed to host a super-massive black hole at its centre with a mass chosen to lie on the observed $M_\star - M_{\rm BH}$ relation (from Bennert et al. 2011),

$$\log M_{\rm BH} - 8 = \alpha(\log M_\star - 10) + \beta \log(1+z) + \gamma + \sigma,\, M_{\rm BH} = 1.905 \times 10^{-4} M_\star^{1.12} \quad (4.19)$$

where α is the slope of the relations at $z = 0$, γ is the intercept of the relations at $z = 0$, σ is the intrinsic scatter which is assumed to be non-evolving, β describes the evolution of the scaling relation and all masses are in $\mathrm{M}_\odot$ units. Here, we have used the combined dataset (with Merloni et al. 2010) with the fitting parameters $\alpha = 1.12$, $\beta = 1.15$, $\gamma = -0.68$, $\sigma = 0.16$. The black hole masses obtained for our objects are listed in Table 4.1.

The numerical parameters of the initial conditions generated for groups and clusters at our chosen resolutions are listed in Table 4.4. We perform all simulations for $10\,\mathrm{Gyr}$

Table 4.4: Numerical parameters for groups and clusters initial conditions. We simulate three objects fiducially at an intermediate resolution, but investigate the effects of utilising low and high resolutions for a subset of models in Chapter 5 Section 5.5. Column 1 indicates the unique initial conditions file label, column 2 gives the total number of particles in use and columns 3-5 list the numbers in each species. Columns 6 & 7 give the DM and baryonic particle masses in $\mathrm{M}_{\odot}$ and the final column details the gravitational softening length in kpc units.

IC Label	N	N_{DM}	N_{gas}	$N_{\star}$	m_{DM}	m_{b}	$\varepsilon_{\mathrm{soft}}$
GG5	1.13E5	1E5	9.94E3	3.30E3	1.7E8	3.1E7	5.3
LC5	1.60E5	1E5	5.85E4	1.19E3	1.6E9	2.9E8	11.1
HC5	2.56E6	1E5	2.46E6	3.31E2	1.6E10	2.9E8	23.1
GG6	1.13E6	1E6	9.94E4	3.30E4	1.7E7	3.1E6	1.7
LC6	1.60E6	1E6	5.85E5	1.19E4	1.6E8	2.9E7	3.5
HC6	2.56E7	1E6	2.46E7	3.31E3	1.6E9	2.9E7	7.3
GG7	1.13E7	1E7	9.94E5	3.30E5	1.7E6	3.1E5	0.2
LC7	1.60E7	1E7	5.85E6	1.19E5	1.6E7	2.9E6	0.4
HC7	2.56E8	1E7	2.46E8	3.31E4	1.6E8	2.9E6	0.3

at a fiducial resolution (with 10^6 DM particles) and a lower resolution with one tenth the number of particles to check for resolution effects; simulations are optionally performed at a higher resolution, however this is computationally demanding and so reserved only for a subset. Included in the table is the gravitational softening length $\varepsilon_{\mathrm{soft}}$ of our simulations; we set this value by following the optimal choice as defined by Power et al. (2003),

$$\varepsilon_{\mathrm{soft}} = \frac{4r_{200}}{\sqrt{N_{200}}}, \tag{4.20}$$

where we set $N_{200} = M_{200}/m_{\mathrm{b}}$ in order to ensure even baryon dominated systems are well resolved.

In order to establish a baseline for our future work modifying AGN models, we begin by studying the effect of incorporating the standard AGN methods from Chapter 3 (detailed in Table 3.2) in galaxy groups and clusters (see Table 4.4). The models studied consist of the kernel-weighted (KAGN; Di Matteo et al. 2005; Springel et al. 2005) and 'strong' (SAGN; Booth & Schaye 2009) heating models which utilise Bondi accretion (Hoyle & Lyttleton 1939; Bondi & Hoyle 1944; Bondi 1952) and the modified disc accretion model (DAGN; Power et al. 2011, see Chapter 2 Section 2.2.3) which also utilises 'strong' heating.

Utilising and analysing the behaviour of the existing AGN models in each object allows us to understand their behaviour more thoroughly and find avenues for possible improvements. As in the first investigation, we varied the AGN accretion and feedback models as well as optionally including supernova feedback. In order to reduce dupli-

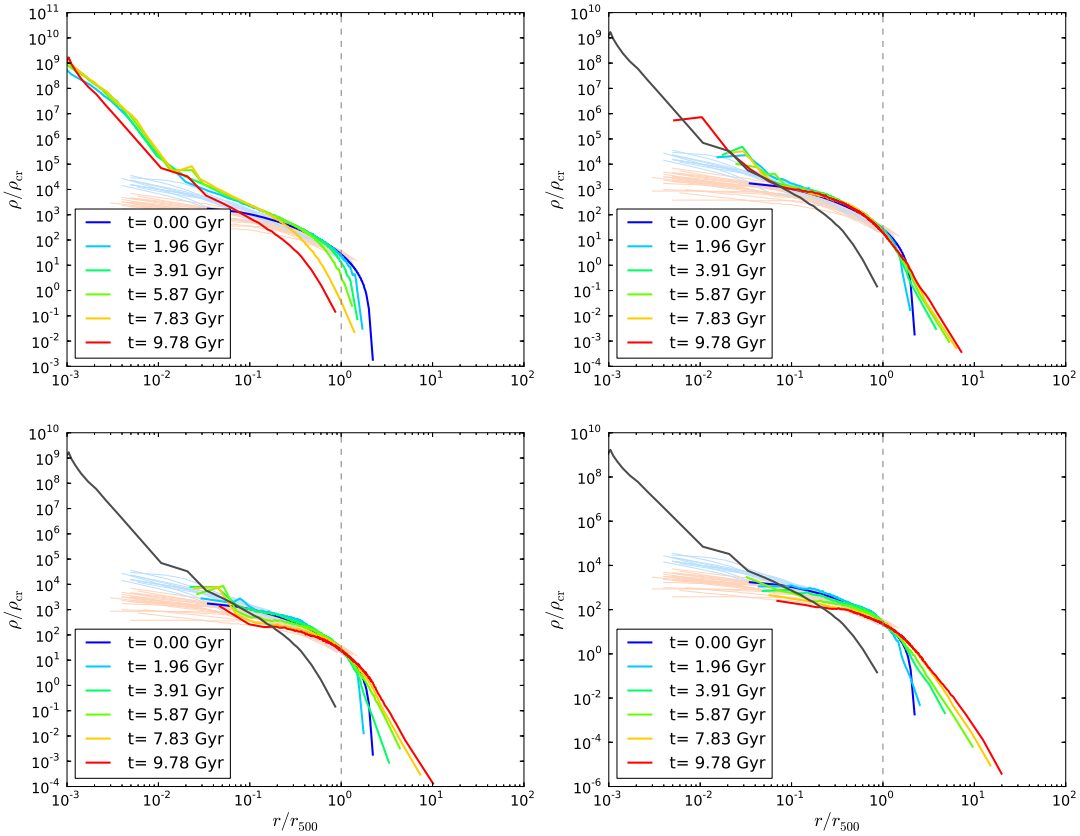

Figure 4.4: Gas density profile evolution for the GG object simulated with different AGN models. Clockwise from top left we show the resulting NFB, KAGN, DAGN and SAGN model profiles over the course of the simulation. Density and radius are shown scaled in terms of the critical density ($\rho_{\rm cr}$) and r_{500} respectively, with the latter value indicated by a vertical dashed grey line. The final NFB profile is over-plotted in dark grey for comparison.

cation and remove ambiguities, we omit results with SNe and strong feedback models with $N_{\rm heat} = 1$ as they are remarkably similar to the results presented here (no SNe, $N_{\rm heat} = 10$).

4.1.4 Results for galaxy groups

Fig. 4.4 shows the density profiles computed at different snapshots across the $10\,\mathrm{Gyr}$ simulation time for models with no AGN and the three standard models; for the AGN simulations we over-plot the final NFB simulation profile for comparison. In the galaxy group (GG) simulations including no AGN the IGM quickly undergoes a substantial contraction as gas falls unopposed towards the centre, leading to a $6\,\mathrm{dex}$ central density increase. The strong AGN models are able to prevent this extreme density increase, however the KAGN model still ends the simulation with gas in the central $\sim 0.1 r_{500}$ which is approximately

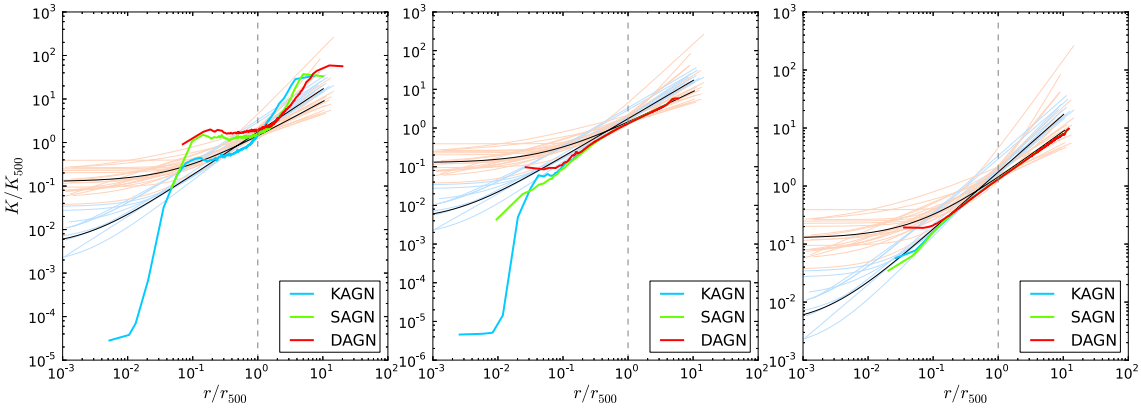

Figure 4.5: Final ($t = 10\,\mathrm{Gyr}$) scaled entropy profiles for the GG (left panel), LC (centre panel) and HC (right panel) objects, simulated with the standard AGN models. Radius and entropy are shown scaled in terms of r_{500} and the characteristic entropy at that radius (as given by Equation 4.15) respectively, with the former value indicated by a vertical dashed grey line.

100 times more dense than the initial value. Therefore only the strong AGN feedback models are able to prevent the cooling catastrophe. We present in Fig. 4.5 the final scaled entropy profiles for the GG, LC and HC objects (left to right) for simulations using the different AGN models. The entropy profiles show that the strong feedback models are successful in retaining a non-cool core profile reasonably in line with observations where the KAGN model is not.

Fig. 4.6 shows the black hole mass (left panel) and luminosity (right panel) evolution for the three AGN models across time. The left panel shows in the upper section the BH accretion rate as a ratio of the limiting Eddington rate (the top bar indicates if the accretion is Eddington limited on a time-step with a check; this does not occur for these runs) and the integrated BH mass in the lower sub-panel; whilst the right panel shows the integrated BH (dotted/dashed lines) and gas (solid lines) luminosities. The total energy radiated by the gas is calculated by utilising the tabulated cooling functions employed by GADGETX (see Chapter 2 Section 2.2.1) to give instantaneous cooling rates which are then integrated between snapshots (all 500 snapshots are typically used, however the results are not sensitive to this choice); the AGN luminosities, however, are calculated from logged values at each timestep. For the KAGN model the central gas is colder and more dense for the majority of the simulation, leading to a higher accretion rate onto the BH and a (26 per cent) higher final mass. The increased density also means that the group simulated with the KAGN model radiates ~ 10 times as much energy compared to SAGN over the course of the simulation, despite having similar BH integrated luminosities. This difference is due to the higher heating temperature in the SAGN model and its higher feedback efficiency providing a high AGN luminosity at early times, which prevents an immediate density

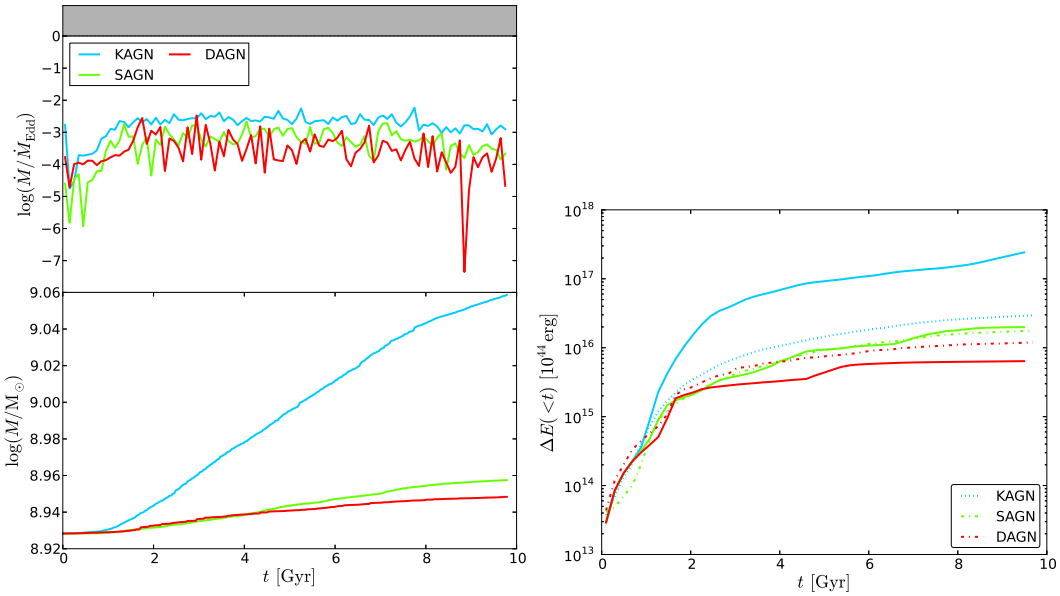

Figure 4.6: BH mass (left panel) and luminosity (right panel) evolution for simulations of the GG object incorporating different AGN models. The left panel is subdivided into a plot indicating when a time-step is Eddington limited, the binned BH accretion rate in Eddington units and the integrated mass, top to bottom. The right panel shows the integrated energy emitted from the BH in feedback and radiated by the gas halo as dotted/dashed and solid lines respectively.

increase leading to a corresponding jump in cooling. Therefore, despite having a strong impact on the majority of the gas in the group, the SAGN model is not effective at heating the core. This is due to the hot feedback-heated particles escaping to larger radii, typically clearing the core region, lowering the central density and doing work outside of the core region where their impact is diluted. However, the density profile evolution slows over time and the observed BH mass plateau suggest that the AGN is slowing further accretion onto the core.

Now considering the DAGN model, we find an almost identical BH mass evolution to SAGN; as these models share the same feedback algorithm, this indicates that the dominant mechanism controlling the AGN evolution in GGs is the effect of AGN feedback on large-scale gas flows onto the core. The BH luminosity, mass and feedback wind behaviour are all very similar to SAGN, however Fig. 4.4 shows that BH feedback has a larger impact on the GG gas density profile for the DAGN model, lowering the central gas density by an order of magnitude. The relative strength is due to the sporadic accretion onto the BH creating more episodic feedback events which deposit more energy at once, creating winds and thereby strongly reducing the central density of the GG. This effect also lowers the group's instantaneous X-ray luminosity by a factor of a few, slowing future cooling.

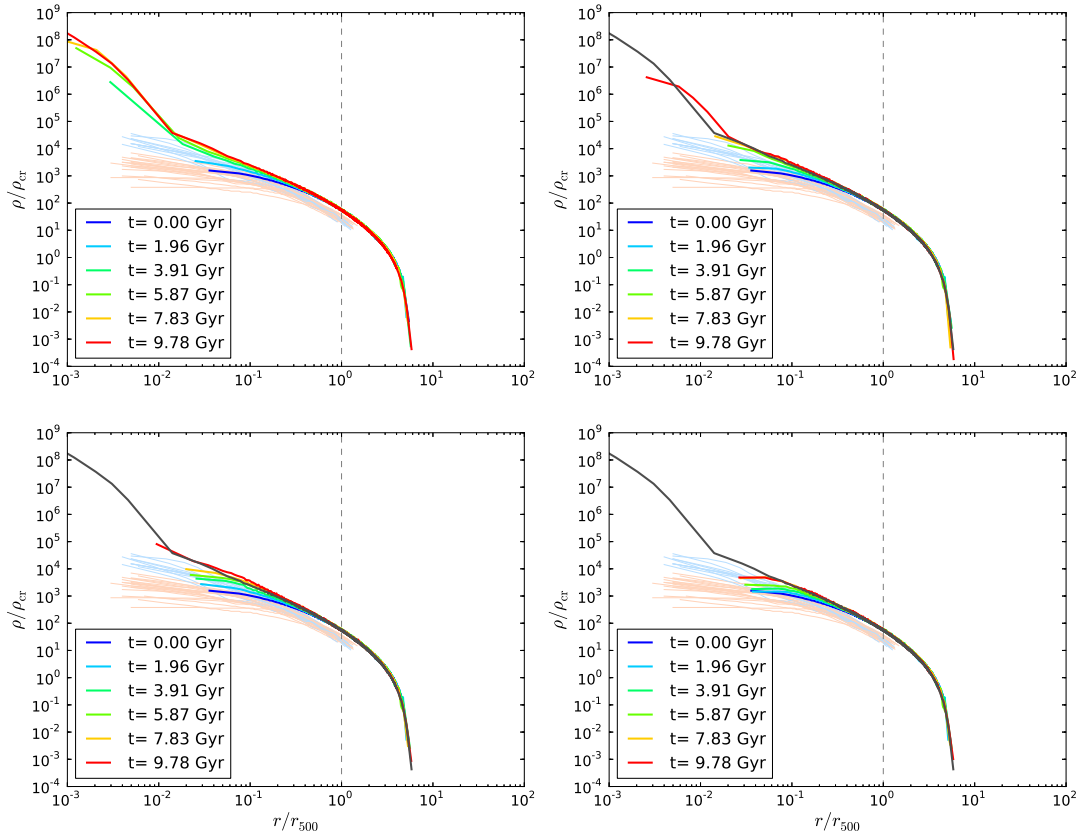

Figure 4.7: Density evolution for the LC object simulated with different AGN models. Clockwise from top left we show the resulting NFB, KAGN, DAGN and SAGN model profiles over the course of the simulation. Density and radius are shown scaled in terms of the critical density ($\rho_{\rm cr}$) and r_{500} respectively, with the latter value indicated by a vertical dashed grey line. The final NFB profile is over-plotted in dark grey for comparison.

4.1.5 Results for low mass clusters

Moving up in object mass, we now look at the performance of the AGN models in the low-mass cluster (LC). Fig. 4.7 shows the density profiles computed at different snapshots across the $10\,\mathrm{Gyr}$ simulation time for models with no AGN and the three standard models; again for the AGN simulations we over-plot the final NFB profile for comparison. In the NFB simulation we see a central density-increase / temperature-drop below $\sim 0.5r_{500}$, with more extreme deviations seen within $\sim 0.01r_{500}$. No AGN model completely prevents these trends; they do however eliminate the more pronounced changes in the very centre. Unlike in GG, each AGN model yields a different BH mass evolution which we now discuss, beginning with the KAGN model.

Fig. 4.8 shows the black hole mass and integrated luminosity evolution for the three AGN models in the LC object across time (details are as in Fig. 4.6). The KAGN black

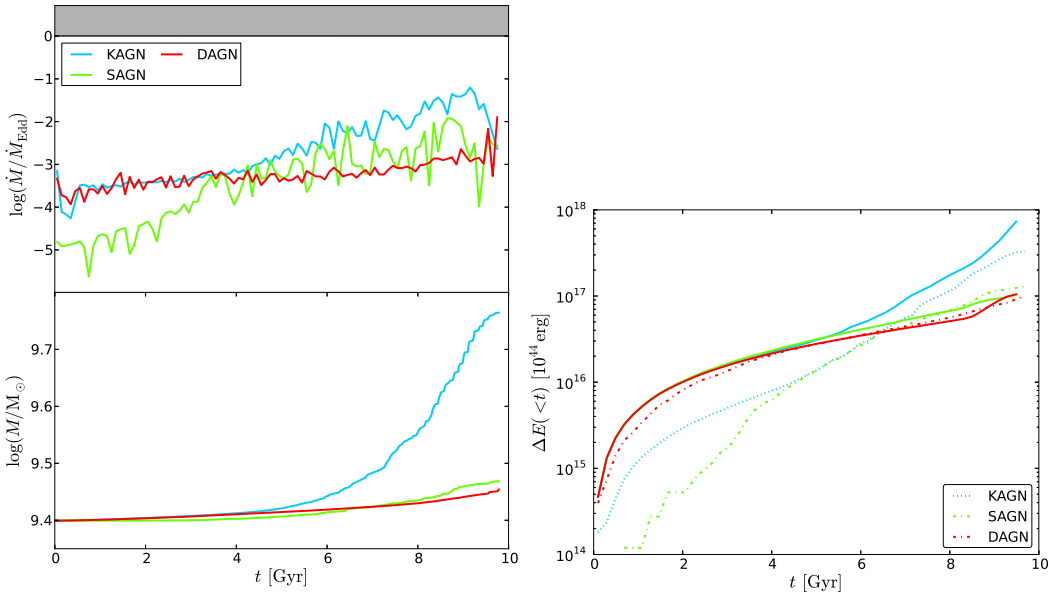

Figure 4.8: BH mass (left panel) and luminosity (right panel) evolution for simulations of the LC object incorporating different AGN models. The left panel is subdivided into a plot indicating when a time-step is Eddington limited, the binned BH accretion rate in Eddington units and the integrated mass, top to bottom. The right panel shows the integrated energy emitted from the BH in feedback and radiated by the gas halo as dotted/dashed and solid lines respectively.

hole experiences a low level of growth which increases at around $5\,\mathrm{Gyr}$, when the majority of accretion occurs and the BH more than doubles in mass by the end of the simulation. The kernel-weighted feedback therefore is not powerful enough to stop the accumulation of dense, cold (and low entropy) gas in the central $\sim 0.5 r_{500}$, leading to a final (central) density increase of almost a factor of 10^5. This later growth is likely linked to the longer cooling time compared to GG, meaning that the majority of gas takes more time to cool and fall into the cluster centre. At this time the AGN feedback is unable to halt the inflow although it is successful in lessening the dramatic changes seen when no AGN is included.

The SAGN model gives rise to similar final density, entropy and temperature profiles as for the KAGN model outside $0.1\,r_{500}$, despite its different BH mass evolution. The SAGN BH grows more slowly before rising similarly to the KAGN model, however the rise is less sudden and the rate lower, resulting in a BH mass which is a few times lower by the end. The growth of the DAGN BH is near-constant, rising slightly towards the end of the simulation, giving a final BH mass almost identical to SAGN run. We note that early in the simulation the accretion rate is very similar to the other models, despite utilising a different accretion rate model. The near-constant level of heating from the start of the simulation keeps the cooling rate low until around $3\,\mathrm{Gyr}$ later than in the KAGN and SAGN models (showing an increase at $t \simeq 8\,\mathrm{Gyr}$). Despite reducing the level of

radiative cooling from the ICM, the DAGN model is still unable to prevent the contraction of the cluster increasing the core density; performing only slightly better than the Bondi methods. From Fig. 4.5 we can see that the DAGN model is, however, more successful in maintaining the core density and entropy, leading to less of a central entropy drop, although it exhibits a small central entropy inversion which is ruled out observationally.

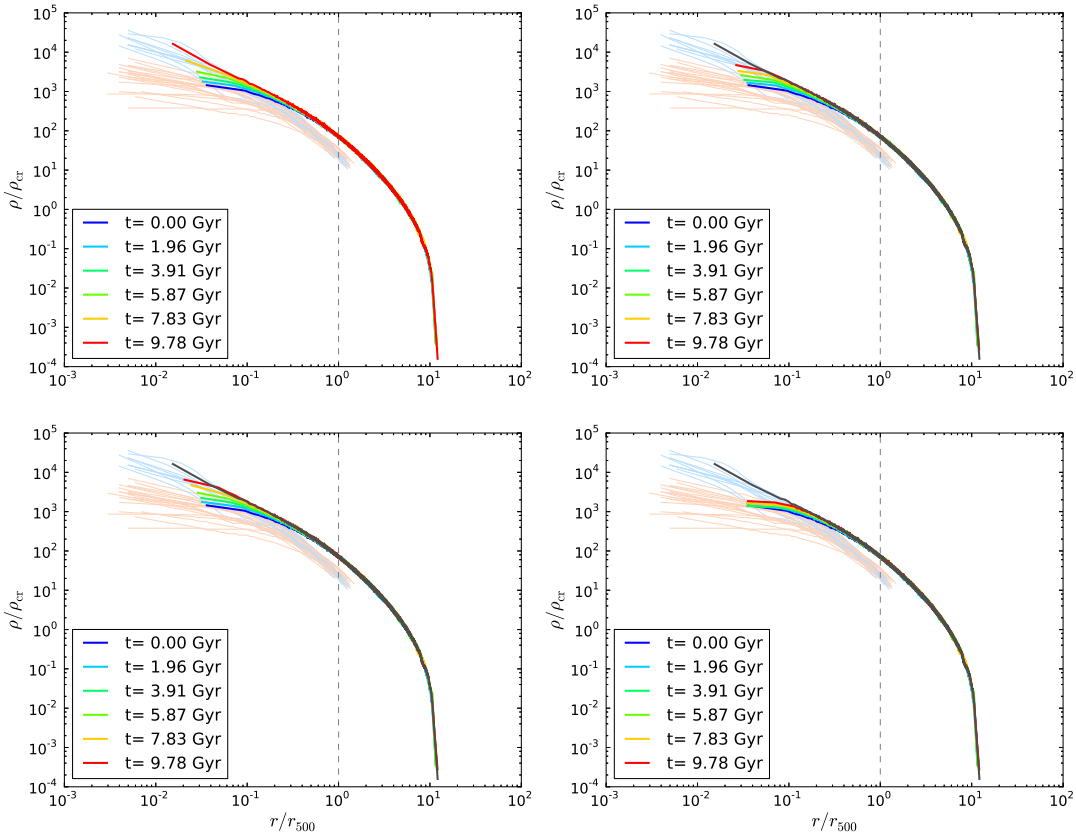

Figure 4.9: Density evolution for the HC object simulated with different AGN models. Clockwise from top left we show the resulting NFB, KAGN, DAGN and SAGN model profiles over the course of the simulation. Density and radius are shown scaled in terms of the critical density ($\rho_{\rm cr}$) and r_{500} respectively, with the latter value indicated by a vertical dashed grey line. The final NFB profile is over-plotted in dark grey for comparison.

4.1.6 Results for high mass clusters

Finally, we analyse the effects of existing AGN models in the HC object. We present in Fig. 4.9 the density profiles computed at different snapshots across the $10\,\mathrm{Gyr}$ simulation time for the main AGN feedback models. It is apparent that the NFB simulation with unchecked cooling again gives rise to an increase in central density. Correspondingly we find a drop in the core temperature and entropy (not shown), each undergoing around an

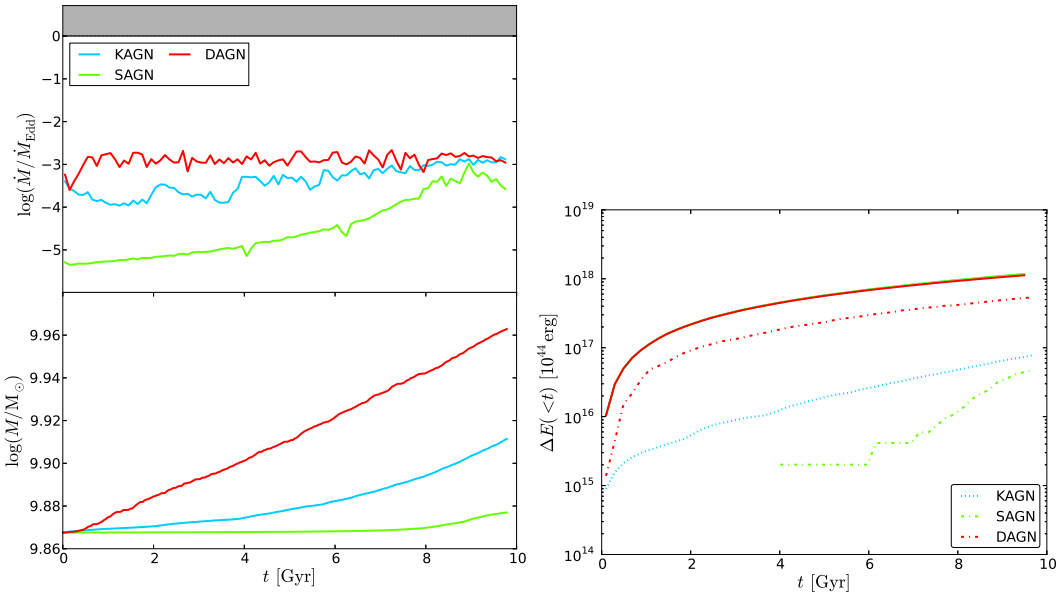

Figure 4.10: BH mass (left panel) and luminosity (right panel) evolution for simulations of the HC object incorporating different AGN models. The left panel is subdivided into a plot indicating when a time-step is Eddington limited, the binned BH accretion rate in Eddington units and the integrated mass, top to bottom. The right panel shows the integrated energy emitted from the BH in feedback and radiated by the gas halo as dotted/dashed and solid lines respectively.

order of magnitude change. The drop in entropy is much less severe than is seen in the lower mass objects and the changes take longer to occur due to the longer cooling time of the hot ICM. All AGN models reduce the increase in core density, with the DAGN model being most successful. At the end of the simulation, the central density in the DAGN model is two times higher than at the start, whereas in the other AGN models, it undergoes an order of magnitude increase. Fig. 4.5 shows that the DAGN model also successfully maintains the initial entropy (and temperature; not shown) profiles through feedback, albeit with a slight central entropy inversion.

Fig. 4.10 shows the BH mass (left panel) and integrated luminosity evolution (right panel) for the three AGN models in the HC object (otherwise as Figs. 4.6 and 4.8) across time. The SAGN black hole only begins growth (and feedback) at $t \sim 4\,{\rm Gyr}$ (due to its low level of accretion), with a luminosity rising to $10^{44}\,{\rm erg\,s^{-1}}$ by the end of the simulation. We can also see that the unique accretion method for the DAGN model means that it now has the most massive BH, with the black holes growing by a factor of ~ 1.23, 1.07, 1.02 for the DAGN, KAGN and SAGN models respectively, this results in a higher integrated energy output for the DAGN model. The initial low level of growth and late increase seen in the SAGN model (and not seen for the KAGN model) is due to the density dependence of the accretion rate suppressing early growth combined with the longer cen-

tral ($r < 100\,\mathrm{kpc}$) cooling time in this object ($\sim 200\,\mathrm{Gyr}$ compared to 20, $10\,\mathrm{Gyr}$) for the LC and GG respectively. Despite the similar effect on the cluster profiles, the smoothed AGN luminosities are quite dissimilar across models; DAGN radiates at constant rate of $2 \times 10^{44}\,\mathrm{erg\,s^{-1}}$, almost matching the ICM luminosity. The KAGN model BH luminosity is too low to balance cooling despite it growing from 0.1 to $1 \times 10^{44}\,\mathrm{erg\,s^{-1}}$ over the course of the simulation; this is a relatively low level of growth compared to the deficit in global energies and is due to the kernel feedback heating locally and slowing BH accretion. The cluster X-ray luminosities are unaffected by any AGN activity; the DAGN, KAGN and SAGN model BHs offset ~ 50, 8 and 5 per cent of the energy lost to cooling respectively. Once again the DAGN model AGN has outflows spread over larger radii from early times, with the same absolute values across models as in the LC object (not shown).

4.1.7 Summary of results

In summary, out of the models tested the DAGN model performs best across the whole mass range. In the absence of AGN, the central temperature/entropy drops, density increases and the central X-ray luminosity increases by orders of magnitude in all objects. The strong AGN methods are over-powerful and moderately reduce the central densities in the GG, but cannot completely stabilise the clusters against cooling. AGN do not balance the amount of energy lost through cooling over the course of simulation in any object, but this varies greatly between models, they do however succeed in reducing SF rate from around $100, 100, 10$ to $\sim 1, 5, 0\,\mathrm{M_\odot\,yr^{-1}}$ (in GG, LC, HC respectively; resolution dependent).

4.2 Simulations with a bipolar AGN model

In the previous section we found that our stock models tend to over-heat low mass objects and under-heat the larger structures. In an attempt to solve this we introduce anisotropic heating which better reflects the assumed geometry of observed radio jets. Previous work using grid-based codes has shown that the pressurised ICM keeps jets columnated (e.g. Cattaneo & Teyssier 2007) meaning that they penetrate farther into the ICM before spreading out and interacting substantially with their environment. This may mean heated particles leave the GG object entirely and so reduce the over-heating so far encountered, whilst heating more of the larger objects and slowing cooling onto the core. We therefore modify the SAGN method to heat in a bipolar fashion, in an attempt to model (thermally) the effects of jet heating.

In order to simulate feedback in the fashion of a bipolar jet, we adopt the following

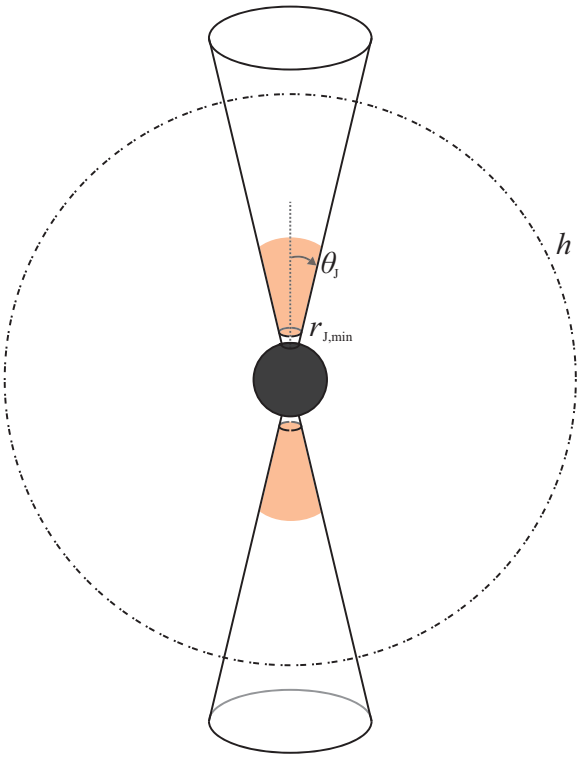

Figure 4.11: Schematic diagram of the anisotropic AGN feedback model geometry. The BH particle is assigned a vector representing the jet axis, about which gas may be heated; the standard SPH smoothing length, h, (within which gas may be accreted) is not used for defining the heating geometry. The jet volume is described by an opening angle, $\theta_{\rm J}$, and minimum radius, $r_{\rm J,min}$, to define a volume within which (normally the nearest) gas may be heated.

routine. A BH particle is assigned a vector representing the jet axis, the nearest $N_{\rm heat}$ particles to the BH which lie within an angle $\theta_{\rm J}$ of the axis will be heated in a heating event if they are outside a fixed minimum radius ($r_{\rm J,min}$; see Fig. 4.11 for a schematic). The minimum radius is incorporated to represent the inflation of bubbles by sub-grid jets and to ensure that the preferred direction for the buoyant rise of the hot bubbles is that of the jet axis.

It is commonly thought that the jet and spin axes of an AGN are aligned (Blandford & Znajek 1977), however there is currently uncertainty about the amount of movement this axis undergoes and the timescales involved. Classic Fanaroff-Riley (Fanaroff & Riley 1974) AGN show little or no signs of re-orientation and produce long, ordered jets; however theoretical arguments and some observations support a case for rapid re-orientation (e.g. Ekers et al. 1978; Merritt & Ekers 2002; Campanelli et al. 2007; Babul et al. 2013). We therefore model two extreme cases; one where the jet axis is fixed parallel to the z-axis (FV model) and another where the axis is randomly changed each time-step (RV model). We adopt $\theta_{\rm J} = 10\,^{\circ}, r_{\rm J,min} = 0$ as our fiducial parameters and initially investigate

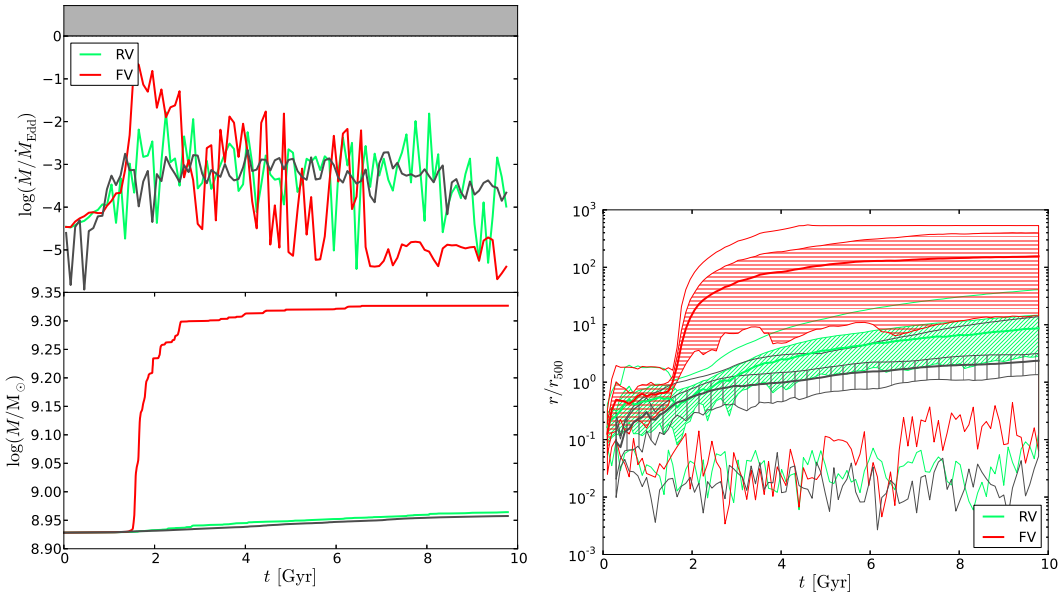

Figure 4.12: BH mass (left panel) and wind position (right panel) evolution for simulations of the GG object simulated with the fiducial RV and FV anisotropic AGN feedback models. The left panel is subdivided into a plot indicating when a time-step is Eddington limited, the binned BH accretion rate in Eddington units and the integrated mass (top to bottom). The right panel shows the mean position of heated particles (thick line), one standard deviation around it (shaded area) and bounding values across simulation time. The data plotted in grey is taken from the corresponding isotropic feedback simulation.

the differences between this and isotropic SAGN feedback.

Consistency checks

Before performing the investigation, we ensured that the modifications to the code had been incorporated correctly by performing consistency checks on the method. The novel anisotropic method and algorithms should be degenerate with the original strong AGN Bondi model under the choice of $\theta_{\rm J} = 180\,^\circ, r_{\rm J,min} = 0$; we therefore explicitly checked this expectation for a range of $N_{\rm heat}$ values and group/cluster objects and found no discrepancies.

4.2.1 Simulation results

We choose to evaluate the impact of simulating jet-heating with the RV model first as it simulates feedback via concentrated 'bubbles' but is still isotropic in a time-averaged sense which will make comparisons with the isotropic SAGN model easier to interpret. We will then go on to investigate a fixed jet model in the second part of this section.

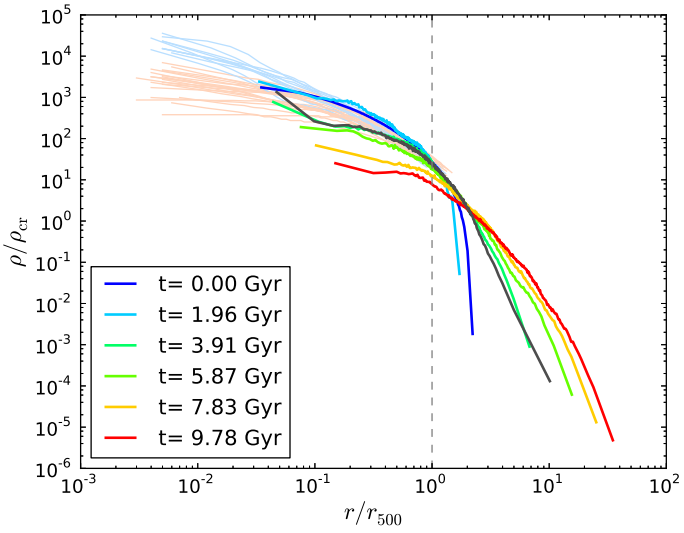

Figure 4.13: Density evolution for the GG object simulated with the fiducial RV anisotropic AGN feedback model. Density and radius are shown scaled in terms of the critical density and r_{500} respectively, with the latter value indicated by a vertical dashed grey line. The final corresponding isotropic feedback simulation profile is over-plotted in dark grey for comparison.

Randomly re-orienting jet axis

We begin by investigating bipolar feedback in the GG object with a randomly re-orienting jet axis. Fig. 4.12 shows the BH mass (left panel) and distribution of wind particles (right panel) over the course of the simulation with the corresponding isotropic data shown in dark grey for comparison. The left hand panel is sub-divided into plots indicating if the accretion is Eddington limited, the BH growth rate and integrated mass in the top, middle and bottom panels respectively. The right hand panel shows the position of the wind particles via the mean (thick line), one standard deviation (hatched area) and the upper/lower values as thin lines. The BH mass evolves similarly to the isotropic model, showing only a slight increase. This means that their energy budgets are the same and any differences are as a result of the different feedback geometries. We can also see that the anisotropic wind travels to larger radii than the isotropic simulation, as is expected. The winds in the anisotropic model immediately penetrate the gas more efficiently, with a mean radius of $10r_{500}$ at the end of the simulation, 5 times higher than the isotropic simulation. The gas travels farther because the feedback is produced in defined bubbles rather than being released in a diffuse fashion.

We present in Fig. 4.13 the evolution of the GG density profile when simulated with the fiducial bipolar model, also shown for comparison in dark grey is the final state of the SAGN model. The RV jet heating clearly has a much stronger effect on the gas, lowering

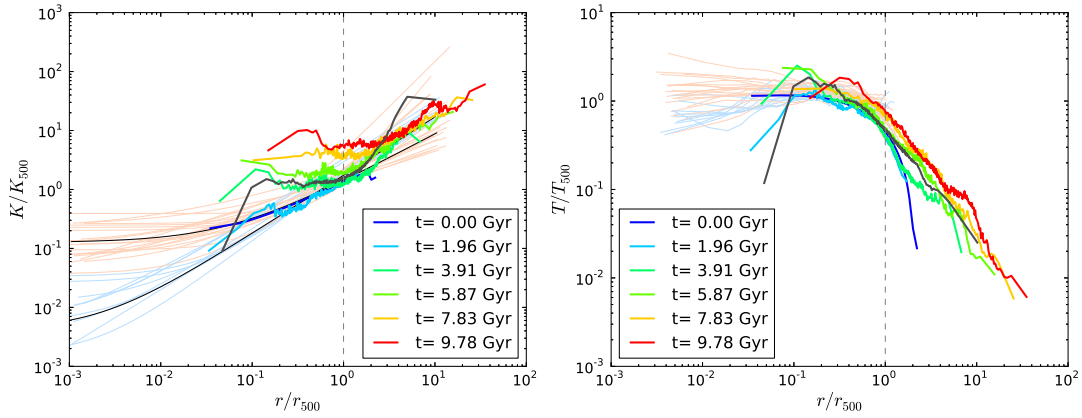

Figure 4.14: Entropy and temperature evolution (left and right panels respectively) for the GG object simulated with the fiducial RV anisotropic AGN feedback model. Density and radius are shown scaled in terms of the critical density and r_{500} respectively, with the latter value indicated by a vertical dashed grey line. The final corresponding isotropic feedback simulation profile is over-plotted in dark grey for comparison.

the final core density by a factor of 10 and increasing the maximum gas radius to four times its original value. This also eliminates the central density spike seen in the isotropic simulation as gas is blown out.

Fig. 4.14 shows the evolution of the GG entropy (left panel) and temperature profiles (right panel) for the fiducial RV anisotropic feedback simulation, with the final SAGN profiles again shown for comparison. The entropy profiles show that the further-reaching feedback-heated particles are successful in maintaining the original profile before $\sim 2\,\mathrm{Gyr}$. Afterwards, the overly-powerful outflows raise the entropy at all radii and prevent the formation of a cool-core at all times in the simulation. The temperature plots (right) show clearly that a small-scale core of cold gas is present at all times which also lowers the central entropy profile.

We now move on to analyse the impact of jet-like feedback on the LC object. Fig. 4.15 shows the evolution of the density profile for the fiducial feedback model with the final isotropic (SAGN) profile plotted for comparison. Over the course of the simulation the effects of cooling increase the central density as in the SAGN simulation. The action of the BH is moderately more effective in this object however and leads to a density plateau and a lower final density within $0.1\,r_{500}$. We present in Fig. 4.16 the binned entropy and temperature profiles for the LC object (otherwise as Fig. 4.14) at several times in the simulation. The entropy and temperature evolution show the same gradual decrease over time due to cooling which is expected to coincide with the observed density increase. At some time between ~ 8 and $10\,\mathrm{Gyr}$ however, the pattern changes and the core appears to

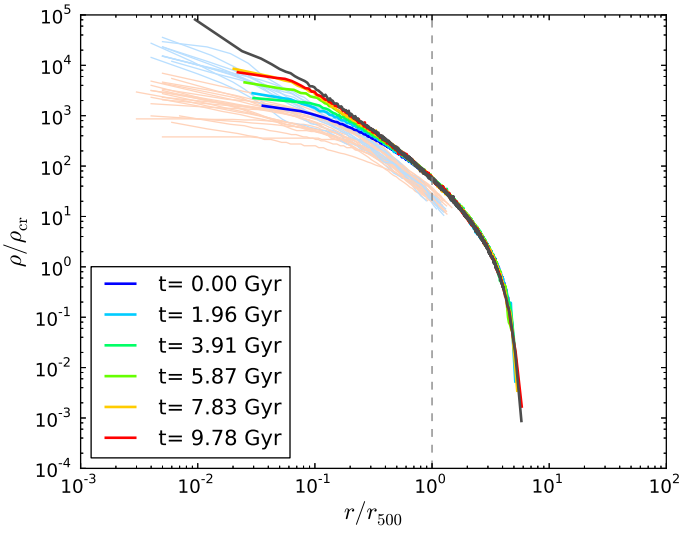

Figure 4.15: Density evolution for the LC object simulated with the fiducial RV anisotropic AGN feedback model. Density and radius are shown scaled in terms of the critical density and r_{500} respectively, with the latter value indicated by a vertical dashed grey line. The final corresponding isotropic feedback simulation profile is over-plotted in dark grey for comparison.

grow warmer due to feedback. There are also signs of AGN heating at the periphery of the object showing that the winds can penetrate the ICM effectively.

Fig. 4.17 shows the BH mass and wind position evolution over the course of the simulation for the LC object (otherwise as Fig. 4.12). The BH mass evolves almost identically to the isotropic simulation, giving it the same available feedback energy, but despite this the wind propagates much further (as indicated in the temperature profiles) whilst still heating the core.

Finally, we now go on to discuss the effect of the fiducial jet-like feedback model on the most massive object in the sample, HC. We show in Fig. 4.18 the evolution of the density (left panel) and entropy (right panel) profiles for the fiducial feedback model with the final isotropic (SAGN) profile plotted for comparison in dark grey. The central density rises steadily over the course of the simulation, halting only at $t \sim 8\,\mathrm{Gyr}$, and staying slightly lower than that of the isotropic feedback. The radiative cooling over the course of the simulation results in a corresponding drop in entropy (and temperature, not shown) which results in the cluster taking on the characteristic shape of a cool core within r_{500}.

We present in Fig. 4.19 the BH mass (upper panel) and growth rate (lower panel) over the course of the simulation with the corresponding isotropic data shown in dark grey for comparison. We find very little growth until $t \sim 8\,\mathrm{Gyr}$ when the BH begins a period of accelerated growth which has not ended by the end of the simulation. We note that

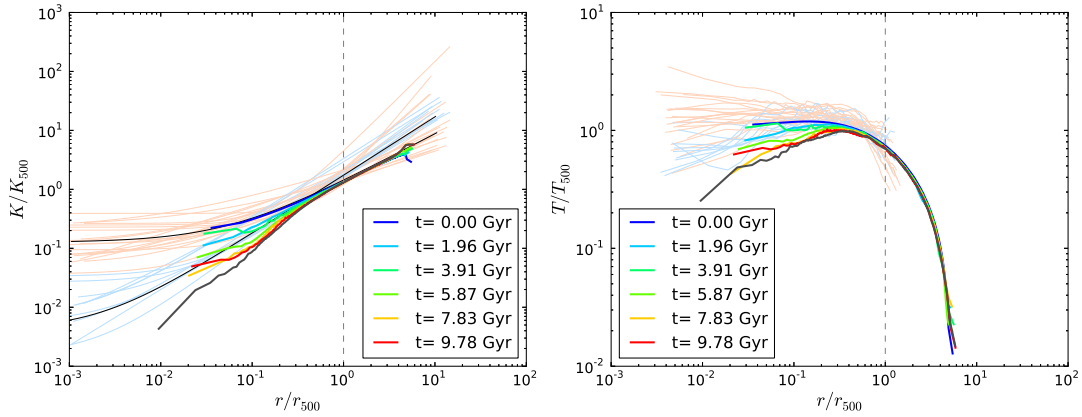

Figure 4.16: Entropy and temperature evolution (left and right panels respectively) for the LC object simulated with the fiducial RV anisotropic AGN feedback model. Density and radius are shown scaled in terms of the critical density and r_{500} respectively, with the latter value indicated by a vertical dashed grey line. The final corresponding isotropic feedback simulation profile is over-plotted in dark grey for comparison.

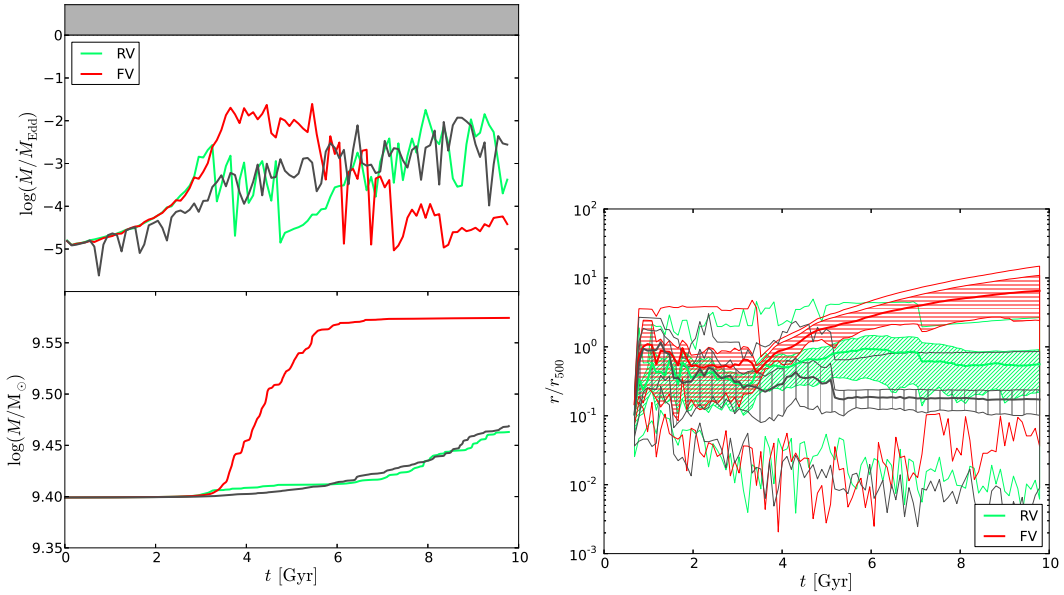

Figure 4.17: BH mass (left panel) and wind position (right panel) evolution for simulations of the LC object simulated with the fiducial anisotropic AGN feedback model. The left panel is subdivided into a plot indicating when a time-step is Eddington limited, the binned BH accretion rate in Eddington units and the integrated mass, top to bottom. The right panel shows the mean position of heated particles (thick line), a standard deviation around it (shaded area) and bounding values across simulation time. The data plotted in grey is taken from the corresponding isotropic feedback simulation.

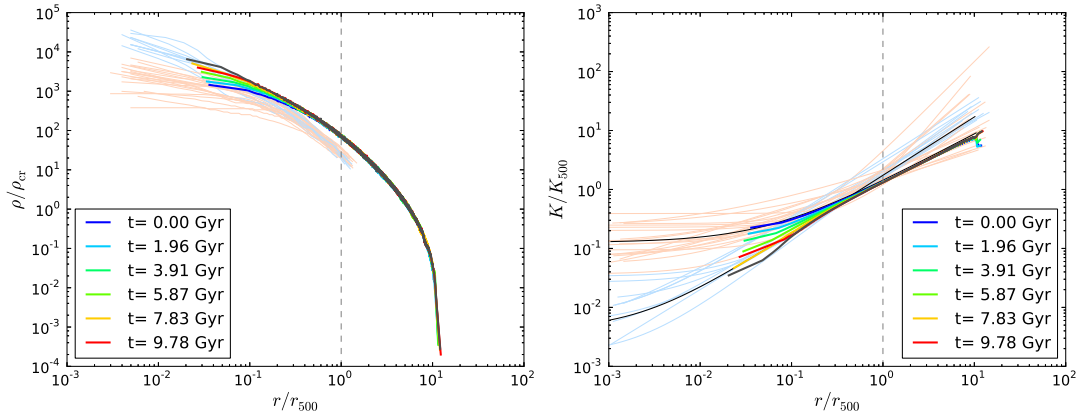

Figure 4.18: Density and entropy evolution (left and right panels respectively) for the HC object simulated with the fiducial RV anisotropic AGN feedback model. Density and radius are shown scaled in terms of the critical density and r_{500} respectively, with the latter value indicated by a vertical dashed grey line. The final corresponding isotropic feedback simulation profile is overplotted in dark grey for comparison.

whilst the growth in mass is very low in comparison to the initial mass in this object, on an absolute scale the accreted mass is large at around $1 \times 10^9\,\mathrm{M}_\odot$.

The position of the AGN-heated winds is not shown for this object because the spread in position of heated particles is far smaller than the lower mass objects (the majority are confined to the core). Upon closer examination, the wind is largely restricted to the same physical scale ($\sim 1000\,\mathrm{kpc}$) as in the LC object however this region now corresponds to only $\sim r_{500}$.

In summary, utilising the anisotropic heating leads to higher entropies and lower densities than the isotropic SAGN model in all simulated objects. This is because the AGN winds rise more effectively through the ICM and interact with the gas more strongly.

Fixed jet axis

We now go on to investigate the effect of a fixed BH jet axis in the low mass GG system; we otherwise use the fiducial parameter set as previously discussed. Fig. 4.20 shows the final density (left column) and entropy (right column) profiles for the GG (top row), LC (centre row) and HC (bottom row) objects, simulated with both the FV and RV anisotropic AGN feedback models. We show, for comparison, the initial profiles as dark grey lines.

We first discuss the effect of using a FV in the context of the GG object simulations. The density profile (left) for the FV simulation is broadly similar to that of the RV model, largely disrupting the GG object; however small details show that differences do exist. The relative under-density throughout the majority of the group and extended distribution

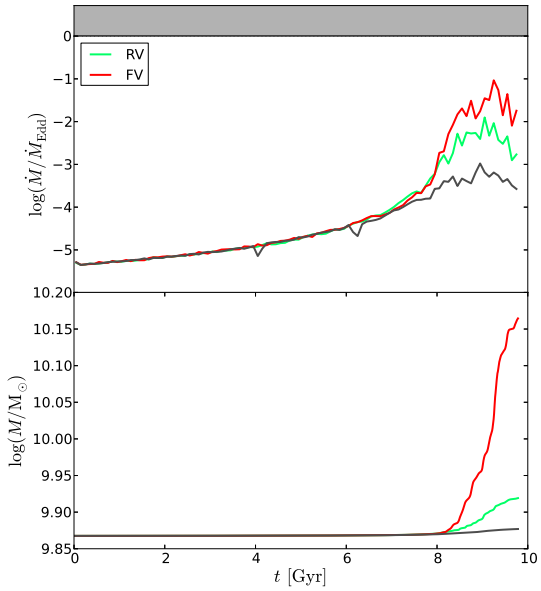

Figure 4.19: BH mass (left panel) and wind position (right panel) evolution for simulations of the HC object simulated with the fiducial anisotropic AGN feedback model. The panel is subdivided into a plot indicating when a time-step is Eddington limited, the binned BH accretion rate in Eddington units and the integrated mass, top to bottom.

of gas at large radii indicates that the fixed-vector jet is more effective at redistributing gas in the GG (see below). Considering now the final entropy profile (middle panel) we find that the entropy has increased throughout the group, just as in the RV model. The increase is, however slightly stronger than in the RV simulation. The final temperature profile (not shown) follows the same pattern as the entropy profile, being broadly similar to the RV case.

The BH mass evolution (Fig. 4.12) shows little growth initially, evolving almost identically to the RV and isotropic feedback models before $t \sim 1.5\,\mathrm{Gyr}$. However, after this time the growth undergoes a spike, increasing the total mass by more than a factor of two within $1\,\mathrm{Gyr}$ and accounts for 90 per cent of the growth in the simulation. The feedback released as a result of this outburst far outweighs the X-ray luminosity of the group and leads to the structure being completely disrupted; we now go on to discuss this in more detail.

Examination of the evolution of the GG density shows that prior to the strong outflow at $t \sim 2\,\mathrm{Gyr}$ the profile is very stable within r_{500}, the only changes being an increase in gas at large radii due to the far-reaching jet. After the outflow, the density falls by a factor of 10 within r_{500} as gas is thrown out to ~ 40 times the original extent of the group before finding a new equilibrium configuration. However, the binned density and temperature profiles at this time (not shown) do not indicate why this growth should occur

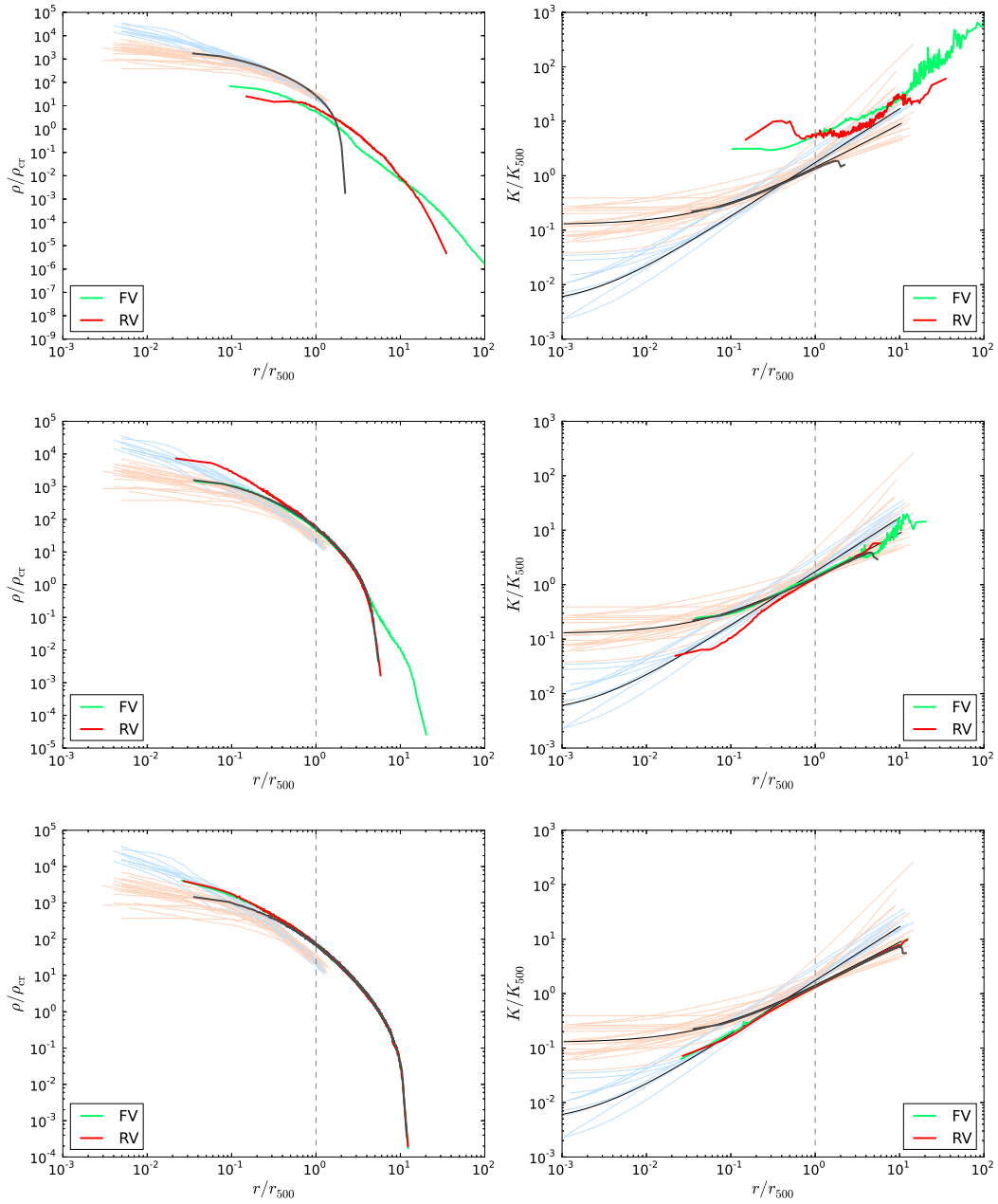

Figure 4.20: Final density (left column) and entropy (right column) profiles for the GG (top row), LC (centre row) and HC (bottom row) objects simulated with the anisotropic AGN feedback model. Simulations performed with fixed and random BH vectors are shown in each panel as well as the initial group/cluster profiles in dark grey for comparison. The FV model drives more powerful winds than the RV model, however the differences and impact on the cluster reduces for higher object mass.

as there is no substantial cool core. Examination of rendered plots reveals that the growth is due to a dense knot of gas forming within the central $\sim 1\,\mathrm{kpc}\,(\sim 10^{-2}r_{500})$ which is undisturbed by feedback. This is likely because it lies within $\varepsilon_{\mathrm{soft}}$, meaning that the strong AGN heating is no longer able to guarantee the heating of the particles closest to the BH particle due to the minimum smoothing length (see Chapter 2 Section 2.3). The BH in the RV model does not undergo the surge in growth because the central knot of gas is jostled away from the BH as the bubbles are inserted at changing positions around it.

Comparing the positions of AGN-heated particles for fixed and randomly orienting jets in the GG object (Fig. 4.12) shows that the fixed jet penetrates further into the ICM. This is because changing the axis removes the preferred direction, whereas a constant vector means that preceding bubbles carve a 'chimney' out of the ICM meaning that successive bubbles encounter less resistance from the ICM. The strong outburst at $t \sim 2\,\mathrm{Gyr}$ creates a jet which completely escapes the group (before reaching an artificial boundary and halting).

Continuing on to discuss the intermediate and higher mass objects (LC, HC), we begin by discussing the final profiles shown in Fig. 4.20. Overall, the density, entropy and temperature (not shown) profiles are very similar to the RV simulations. The deviations from the main profiles are the same as those noted for the GG profile, however the level of discrepancy between FV and RV models decreases with increasing object mass. One notable change is that the increased strength of the AGN feedback for the fiducial FV model in the LC object means that the model is now successful in maintaining the initial profiles against the effects of cooling, preventing the formation of high-density cold-cores.

For the LC object, there is remarkably little variation within $4r_{500}$ over the course of the simulation showing that the modified feedback method has balanced radiative cooling in the core. The *total* energy radiated is, however an order of magnitude larger than this value. A slight increase in density is seen in the central region prior to the total AGN energy surpassing the total radiated energy at $t \sim 3.3\,\mathrm{Gyr}$, however this is reversed by $t \sim 6\,\mathrm{Gyr}$ (not shown) whereas in the isotropic heating case it continues to grow (see Fig. 4.7).

The BH mass evolution (Fig. 4.17) for the LC (HC) object continues the trend seen for the GG object in that it shows little growth until $t \sim 4\,\mathrm{Gyr}$ ($t \sim 8\,\mathrm{Gyr}$), evolving almost identically to the RV model. However, after this time the mass increases rapidly, ending the simulation with a much larger final mass. This is due, as in the GG object, to a combination of hot gas efficiently escaping the central region and gas cooling onto the core along a direction perpendicular to the jets. The later time at which growth begins to accelerate compared to the GG simulation is due to the longer cooling time for these objects.

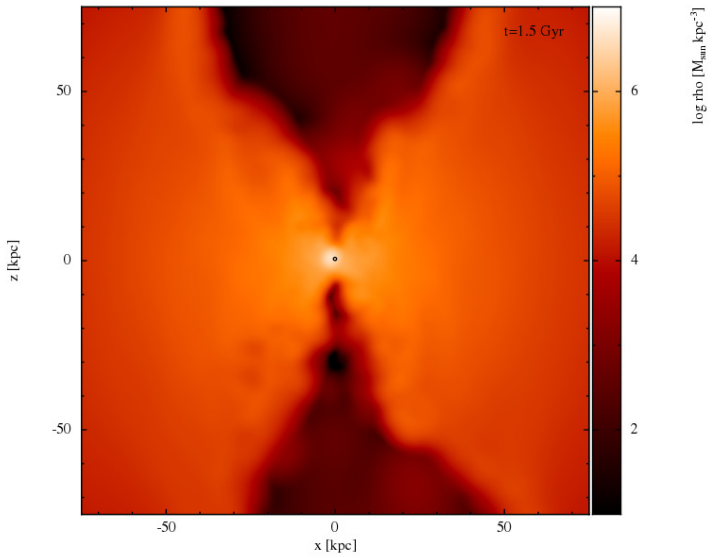

Figure 4.21: Zoomed density slice of the GG for the fiducial FV jet model at $t = 1.5\,\mathrm{Gyr}$ with the BH position indicated by a black circle. The images are made by taking $100\,\mathrm{kpc}$ deep slices through the centre of the cluster, each frame is $100\,\mathrm{kpc}$ on a side and colours indicate the mean density on a log scale.

4.2.2 Spurious cold knots

Whilst performing the fiducial simulations and preliminary investigations into the effect of varying feedback geometry, it was realised that the cold 'knots' of gas observed in the simulations had a significant effect on the BH accretion and feedback. Fig. 4.21 shows a density slice for the inner region of the fiducial FV jet simulation at $t = 1.5\,\mathrm{Gyr}$ with the BH position indicated by a black circle. A central dense sphere of gas of radius $\sim 4\,\mathrm{kpc}$ is clearly observed at this time and the BH particle lies within it; also immediately apparent is the large cavity caused by overly-strong AGN feedback along the jet axis. Over the course of the FV simulation the knot (composed of tens of particles) is remarkably stable and shows only minor oscillations in its position, the timing of which are linked to the large BH accretion/feedback events (such as that seen at $t \sim 2\,\mathrm{Gyr}$ and briefly discussed in Section 4.2.1).

Figs. 4.22 and 4.23 show rendered gas density (top row), entropy (upper middle), temperature (lower middle) and ram over thermal pressure ($0.5\rho v^2/P$; bottom row) at $t = 0.5$, 1.5, 5, $10\,\mathrm{Gyr}$ (left to right) for the GG object simulated with the fiducial FV and RV fiducial jet models respectively. The images are made by taking $100\,\mathrm{kpc}$ deep slices through the centre of the cluster at various times in the simulation and each frame is $500\,\mathrm{kpc}$ on a side. Close examination of Figs. 4.22 and 4.23 shows the knot is composed of cold, dense, low entropy gas residing in the central region. It is clear that the properties

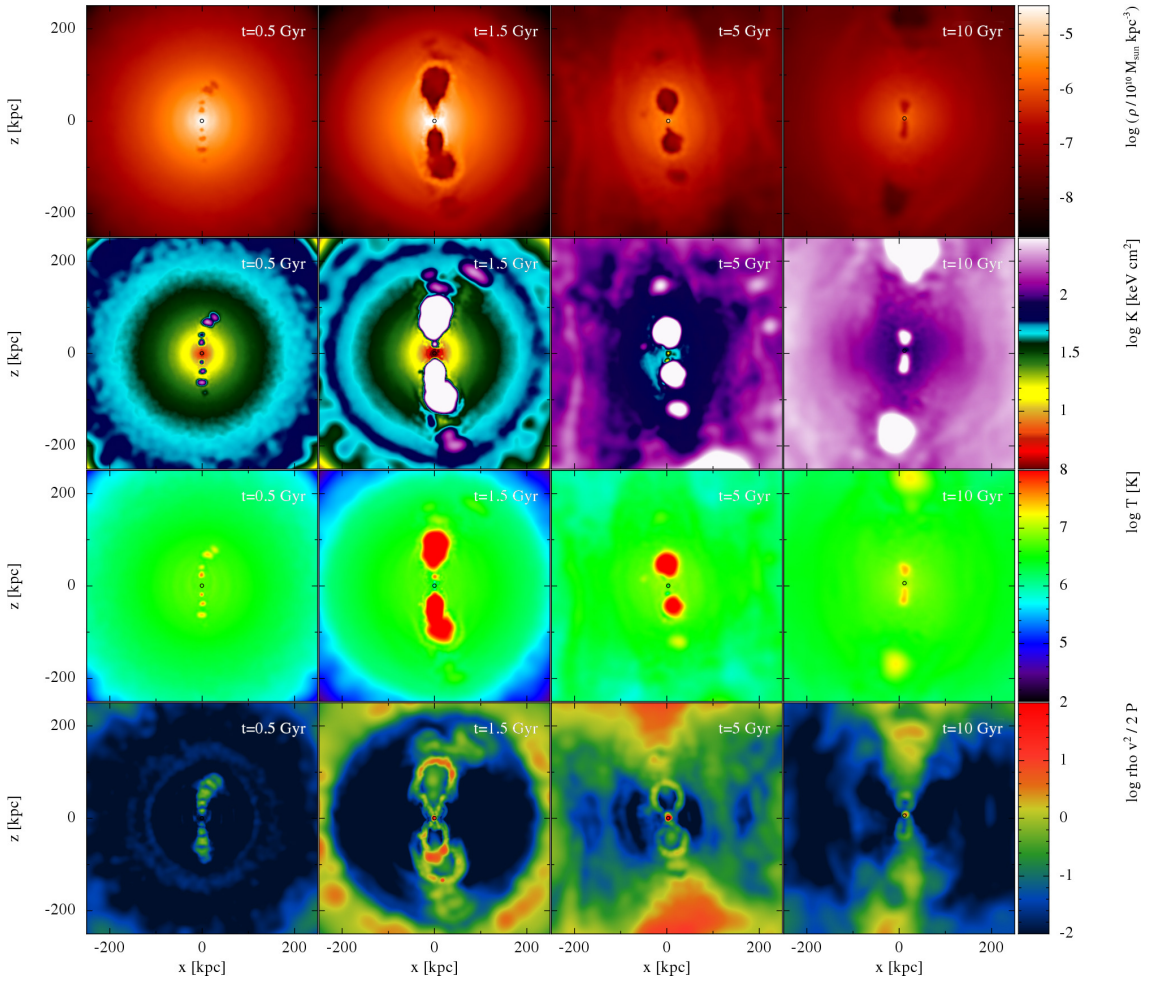

Figure 4.22: Rendered gas density (top row), entropy (upper middle), temperature (lower middle) and ratio of ram to thermal pressure (bottom row) at $t = 0.5, 1.5, 5, 10\,\mathrm{Gyr}$ (left to right) for the GG object simulated with the fiducial FV jet model. Images show projected properties within slices of dimensions $500\mathrm{kpc} \times 500\mathrm{kpc} \times 100\mathrm{kpc}$. The BH position is indicated by a black circle.

within this region are very different to those outside of the core and therefore the BH accretion rate is determined by an unrepresentative region of the group.

The temperatures and densities of the individual particles in the knot (not shown) reveal that the gas is typically at $T \sim 10^4\,\mathrm{K}$ and has a density too low to lie on the equation of state although some particles do join the EoS and form stars. The ratio of ram pressure plots (bottom row Figs. 4.22 and 4.23) reveal the presence of fast-moving, low-pressure clumps of gas. These small ($\sim 4\,\mathrm{kpc}$ across) clumps typically form near the out-flowing jets and rapidly fall into the central region as they cool before merging with the central knot. Once in the central region the cold and dense gas then causes the BH to have a high accretion (and therefore heating rate).

Examining now the rendered gas properties for the RV simulation in Fig. 4.23 we

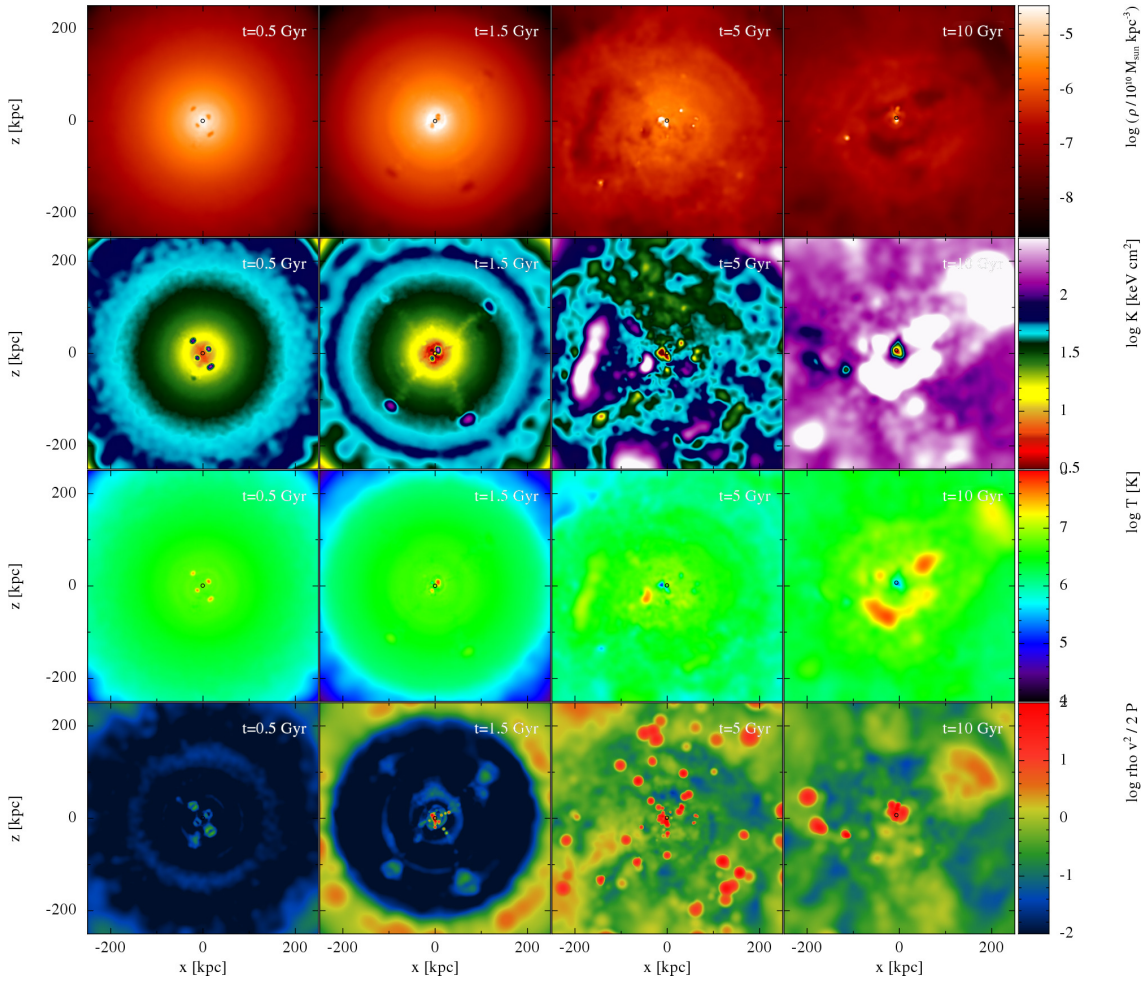

Figure 4.23: Rendered gas density , entropy, temperature and ratio of ram to thermal pressure for the GG object simulated with the fiducial RV jet model (otherwise as Fig. 4.22).

see a more disturbed cold core in the GG. The rotating vector means that the gas does not simply escape in one jet and cool perpendicular to it, but instead infalling material is continually interacting with the jet in a complex fashion. The resulting disturbance of the core means lower BH growth as the cold knot is disrupted and moved away from the BH by the chaotic movements of the IGM. However the knot is still being formed by infalling low-entropy clumps. In fact the entropy, temperature and pressure ratio plots all show more of the cold clumps of gas. This is because more of the ICM is compressed by outflows, increasing its density and increasing its cooling rate.

At this stage it is unknown if the low entropy clumps we observe are physical or not, but their persistence is unlikely to be. Recent work into SPH methods (see e.g. Ritchie & Thomas 2001; Agertz et al. 2007; Read et al. 2010; Read & Hayfield 2012; Sijacki et al. 2012; Saitoh & Makino 2013) has shown that the density-entropy formulation of SPH as utilised here, has shortcomings which lead to numerical artefacts. Most relevant to the

cold blobs seen here is an artificial surface tension at contact discontinuities which acts to separate gas particles and reduce mixing even when the pressure ought to be constant as discussed (see Chapter 2 Section 2.1.2 Equation 2.41). The tension acts to stabilise low-entropy gas clumps and prevent their ablation, leading to reduced mixing.

Power et al. (2013) show that in non-radiative cosmological simulations of cluster growth, the cold clumps collect at the centre of the potential well leading to the well-known (e.g. Frenk et al. 1999) low entropy core found in SPH simulations. The clumps found by Power et al. (2013) are seeded by the accretion of cold gas and substructures, whereas in these simulations they are produced by powerful outflows, however the outcome remains the same. As we begin with very smooth initial conditions this issue affects the standard SAGN model discussed in Section 4.1.3 to a much lesser extent, as the AGN-driven outflows are randomly oriented meaning strong compressions in the ICM are less likely; the KAGN simulations are even less affected as they produce a weaker isotropic feedback.

4.3 Discussion and conclusions

Beginning with the standard AGN models first discussed in Chapter 3, we now summarise the effects of simulating galaxy groups and clusters with central AGN heating.

Simulations without AGN form classic cooling flows resulting in star formation rates of the order $100 - 1000\,\mathrm{M}_{\odot}\,\mathrm{yr}^{-1}$ as the gas radiates energy and loses thermal support. Each of the three objects (of different mass) we simulated cools and forms a cold, dense core of gas where the majority of star formation occurs in the absence of AGN feedback.

The main outcomes from simulations including the KAGN, SAGN and DAGN models are as follows:

- We find that both of the strong feedback models (SAGN and DAGN) lower (raise) the central density (entropy) by an order of magnitude in the GG object, but provide insufficient energy to completely halt cooling in the higher mass objects.

- Strong AGN do mitigate the level of cooling within the ICM, but not to a large enough degree to stabilise the energy losses. The influence of the hot AGN winds are also seen in the entropy profiles, where they prevent the formation of the extreme low-entropy cores at the cost of producing a small entropy inversion.

- Changing the accretion rate calculation between the Bondi and disc models (in SAGN and DAGN) does lead to some differences in the final ICM profiles, notably leading to the DAGN model successfully maintaining the initial HC profiles.

However, the level of differences are low overall and the SAGN model arguably performs better in the GG object.

- The weaker and localised kernel-weighted feedback (KAGN model) is unable to halt cooling and has an even less significant impact on the cluster gas profiles. In the GG object this results in a better match to the original profiles as the strong feedback models are too powerful. However, it lacks the power to stabilise large-scale gas halos in clusters, as shown by the severe drop in the central entropy by several orders of magnitude in each object.

- Broadly, the stock AGN models do not balance the amount of energy lost through cooling over the course of the simulation in any object. Despite this they succeed in reducing the star formation rate, bringing it more in line with observations by warming the core.

Therefore, we find that none of the existing methods tested here are able to effectively offset cooling in the higher mass clusters and that the behaviour of the GG object is highly sensitive to the AGN model. This may suggest that other physical processes are important in offsetting cooling losses from galaxy clusters such as e.g. thermal conduction (see e.g. Bertschinger & Meiksin 1986; Smith et al. 2013). The sensitivity of galaxy groups to the details of the AGN model and therefore possibly to any actual AGN activity may also cast doubt on the suitability of these objects for cosmological parameter estimation (e.g. via the baryon fraction; Laganá et al. 2013) in the near term. We do, however, note that no effort has been made to tune the models in use and that is situation may be improved for any single model.

Having found that the stock models cannot successfully influence the majority of the gas in the cluster objects, we went on to simulate a bipolar variation of the SAGN model so that the winds may better escape the central region and lower cooling throughout the cluster. Additionally, such models may produce winds that escape more easily from lower mass objects without having as large an impact on the IGM, a feature which would improve on our previous models.

We perform simulations that show the bipolar models succeed in creating outflows that penetrate the ICM and slow cooling, although the outflows continue to interact with and heat large amounts of gas. The outflows are often over-powered and deposit too much heat into the group/cluster objects. Phenomenologically, the bipolar AGN feedback reproduces better the jet/cavity structures found in observations of the ICM.

Detailed analysis finds that a large fraction of the accretion is chaotic and of a numerical origin. The high level of accretion is due to cold clumps of gas, formed by out-flowing

winds compressing gas and/or lifting it to larger radii causing it to cool rapidly, falling back into the central region. Whilst the accretion of gas cooled through such mechanisms is a real effect, the clumps of gas are made artificially stable by a spurious pressure force across density discontinuities. This force is inherent in the formulation of SPH employed by GADGET-2, and although current work is ongoing to improve the SPH method, this is beyond the scope of the current work.

Therefore the BHs in our fiducial anisotropic heating simulations are growing artificially quickly due to spurious cold clumps of gas which fall to centre and persist due to a numerical cause. We now go on to present a more physically-motivated novel AGN feedback model which reduces this effect.

Chapter 5

A hybrid scheme for AGN feedback

Please excuse the crudity of this model,
I didn't have time to build it to scale or to paint it.

DR. EMMETT "DOC" BROWN

We now present a novel 'hybrid' AGN feedback model which represents both the quasar and radio modes within one framework. In this aspect it is similar to the Sijacki et al. (2007; also Vogelsberger et al. 2013) model, however they differ in a few key areas. The AGN simulated by this scheme is assumed to produce a low-power jet as it accretes (irrespective of the rate) and produces an additional isotropic quasar radiation field at high accretion rates. Concurrent feedback acting in two separate modes is therefore possible in this model, an aspect which is supported by observations of quasars with jet features (see e.g. Bridle & Perley 1984). Additionally, the timescales upon which it is expected that the AGN will switch modes is typically shorter than that which we can resolve effectively (e.g. for stellar mass BHs, Fender & Belloni 2012).

Numerically, the heating is performed using the modified and optionally anisotropic jet heating described in Chapter 2 Section 4.2 with an additional quasar mode represented using the Springel et al. (2005) kernel-weighted mode (see Fig. 5.1 for a schematic). The jet therefore uses the critical heating temperature method whereas the quasar mode deposits its energy instantaneously. Whilst the radio mode is designed to be effective at escaping its local environment (achieved by the use of the minimum heating temperature requirement, see Section 2.2.3) the quasar heating component is local and isotropic, mimicking an obscured AGN.

The energy is divided between the two modes by utilising a cut in accretion rate as motivated by observations of X-ray binaries which are thought to occupy either a low or high feedback state (Churazov et al. 2005). However, whereas previous models explicitly

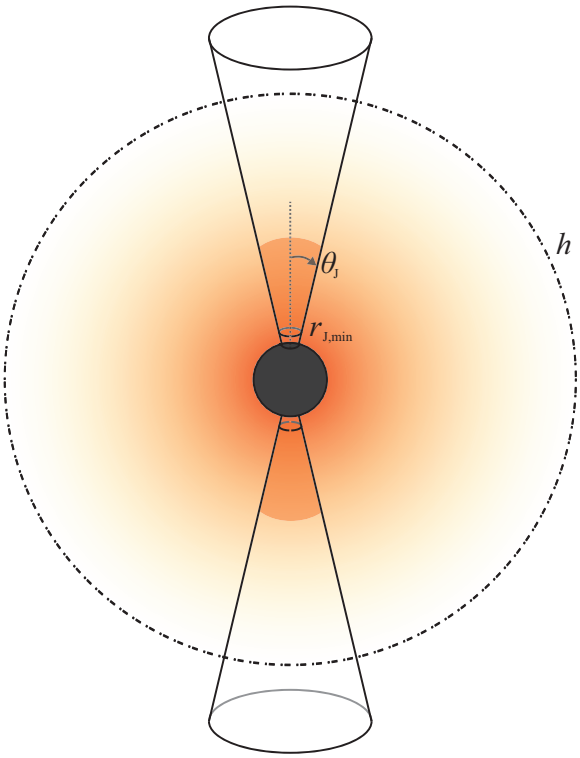

Figure 5.1: Schematic diagram of hybrid AGN feedback model. Gas is heated within the bipolar conical jets by set temperature jumps ($T_{\rm crit}$) to represent radio mode feedback. The usual SPH kernel (with smoothing length h) is used at high accretion rates to deposit excess energy instantaneously, representing the quasar mode.

switch between active modes, this model effectively smooths over the switches in a time-averaged fashion. Below the cut, energy goes into the radio-mode reservoir for SAGN-like (anisotropic) heating; whereas any mass accreted above this rate provides energy to be deposited immediately, distributed spatially according to the SPH kernel as in KAGN.

The energy budget for the quasar and radio modes are then given by

$$\Delta E_{\rm radio} = \min(\dot{M}, \dot{M}_{\rm crit})\, \epsilon_{\rm m} \epsilon_{\rm r}\, \delta t\, c^2, \tag{5.1}$$

$$\Delta E_{\rm quasar} = \begin{cases} \min(\dot{M} - \dot{M}_{\rm crit}, \dot{M}_{\rm Edd} - \dot{M}_{\rm crit})\, \epsilon_{\rm f} \epsilon_{\rm r}\, \delta t\, c^2 & \text{if } \dot{M} > \dot{M}_{\rm crit}, \\ 0 & \text{otherwise,} \end{cases} \tag{5.2}$$

where $\Delta E_{\rm radio}$ and $\Delta E_{\rm quasar}$ are the amounts of energy to be deposited via the radio and quasar modes respectively, δt is the duration of the time step, $\lambda_{\rm Edd}$ ($= \dot{M}/\dot{M}_{\rm Edd}$) is the accretion rate in Eddington units and $\dot{M}_{\rm crit}$ ($= \lambda_{\rm Edd,c} \dot{M}_{\rm Edd}$) is the critical accretion rate at which the feedback energy is split. The efficiency parameters $\epsilon_{\rm r}$, $\epsilon_{\rm m}$ and $\epsilon_{\rm f}$ correspond to the efficiency with which accreted matter is radiated, the mechanical coupling efficiency and the radiative coupling efficiencies respectively.

Other than the feedback model, all other simulation parameters are held as in Section 4.1.3. We do not consider SNe in the following simulations as their impact is inherently limited for a group/cluster object in equilibrium due to the low star formation rates.

This chapter will be structured as follows. After introducing and testing the model in Section 5.1, we go on to investigate the effect of varying some of the model parameters and assumptions on the BH mass and the group/cluster properties. Section 5.2 investigates the outcomes of simulations performed with alternate jet geometries, whilst in Section 5.3 we impose a minimum time interval between radio feedback events. In Section 5.4 we perform simulations varying the assumed feedback coupling efficiencies in the model before performing a short resolution study in Section 5.5.

5.1 The fiducial bipolar hybrid AGN model

We begin by performing simulations with the same fiducial bipolar geometry as in Chapter 4 Section 4.2.1 with the hybrid heating model.

In order to assess the impact of utilising this model (not simply changing the feedback energy available), the efficiency parameters for both modes are set equal to that used for the SAGN simulations ($\epsilon_{\rm m} = \epsilon_{\rm f} = 0.15$; $\epsilon_{\rm r} = 0.10$) for the following tests. We opt for a value slightly lower than previous works for the $\lambda_{\rm Edd,c}$ parameter (e.g. 10^{-2}; Sijacki et al. 2007), initially choosing a value of $\lambda_{\rm Edd,c} = 10^{-3}$ for the following. This value is chosen after inspection of preliminary tests, and tuned so that both modes can be active in the objects we simulate. Due to the large degree of uncertainty in both the value this parameter may take physically and the high numerical sensitivity of the accretion rate (through the BH time-step) we argue this is a reasonable value.

Fig. 5.2 shows rendered gas properties for the GG (top two rows), LC (centre rows) and HC (bottom two rows) objects with fiducial RV and FV hybrid jet AGN in the left and right columns respectively. We present the rendered density (upper panel of each pair) and entropy (lower of each pair) for each object at $t = 5$ and $10\,{\rm Gyr}$. The images are made by taking $100\,{\rm kpc}$ deep slices through the centre of the cluster at various times in the simulation and each frame is $500\,{\rm kpc}$ on a side. The images illustrate how the FV simulations form jets with preferential directions (even clearing-out the gas along the axis in the GG object) whereas RV simulations create bubbles; the impact on the group/cluster is lower for higher masses. The GG and LC objects already show reduced signs of the spurious low-entropy dense knots of gas.

We now analyse the effect of anisotropic feedback models on our group/cluster objects

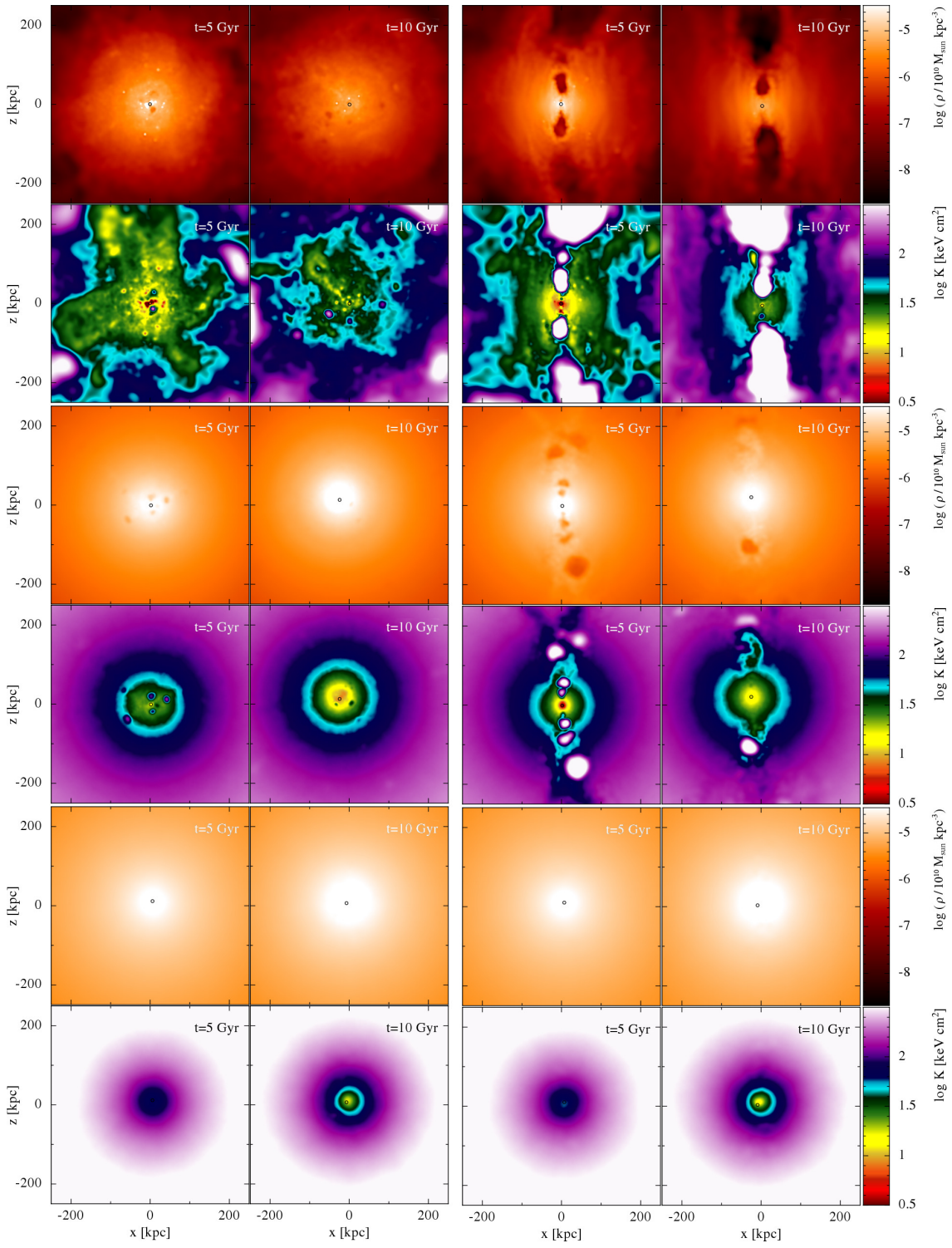

Figure 5.2: Rendered gas properties for the GG (top two rows), LC (centre rows) and HC (bottom two rows) objects with fiducial RV and FV hybrid jet AGN in the left and right columns respectively. We present the rendered density (upper of each pair) and entropy (lower panel of each pair) for each object at $t = 5$ and $10\,\mathrm{Gyr}$. Images show projected properties within slices of dimensions $500\mathrm{kpc} \times 500\mathrm{kpc} \times 100\mathrm{kpc}$, the BH position is indicated by a black circle.

in detail.

5.1.1 Randomly re-orienting jet axis

First considering the RV simulations, it is striking that the hybrid mode yields final density profiles which are very similar to the standard isotropic simulation[1], with less deviation seen with increasing mass. This is shown in Fig. 5.3, which plots the evolution of the GG, LC and HC objects density profiles (top to bottom) with the final corresponding isotropic profile shown as a dark grey line. The final entropy and temperature profiles are also remarkably similar. This contrasts with the pure-jet (i.e. non-hybrid) model simulations which were very different from the isotropic model, especially in the lower mass objects. Therefore, the spurious (now reduced by including the quasar mode) accretion was a large cause of the differences seen in Chapter 4 Section 4.2.

As the models now produce similar final gas profiles we take the ratios between them in order to highlight the relative differences. Fig. 5.4 shows the final density (top), entropy (middle) and temperature (bottom) profiles as a ratio of the fiducial (non-hybrid) isotropic feedback for the GG, LC and HC objects in order to highlight the small differences. Increased central densities arise due in part to the weaker quasar-mode feedback being unable to completely stop the low-entropy gas from collecting in the centre. As discussed in Chapter 4 Section 4.2.2, a source of low entropy gas in these simulations is the bubbles themselves. As the (high entropy) bubbles or jets rise through the ICM they compress gas on their leading edge which then cools faster (due to the n^2 dependence of Bremsstrahlung) and sinks to the centre of the group/cluster. This effect is not seen in the isotropic feedback models as the heating is more diffuse and therefore causes less significant compressions in the gas. This low entropy gas gives a corresponding increase in star formation; the hybrid mode produces 2.65×10^{10}, 4.64×10^{10}, $0.15 \times 10^{10}\,\mathrm{M}_{\odot}$ of stars for the GG, LC and HC objects respectively compared to 0.85×10^{10}, 0.72×10^{10} and $0.00 \times 10^{10}\,\mathrm{M}_{\odot}$ for the corresponding isotropic simulations; this is therefore the action of *positive* AGN feedback. We do, however, note that at some level this effect is still likely affected by the spurious numerical issues discussed previously.

We however note that the majority of the central deviation occurs within the softening length for these simulations (see Table 4.4) and is therefore susceptible to numerical effects. At the edges of the GG (and to some extent LC) object there is an increase in density as gas is redistributed from the core. This gas has a lower entropy than appears in the isotropic simulation at this radius however this is merely as a result of the redistribution

[1]For clarity, we now refer to the isotropic hybrid model as the 'standard' isotropic or isotropic model. Comparing the isotropic hybrid and isotropic models (not shown) are remarkably similar in any case.

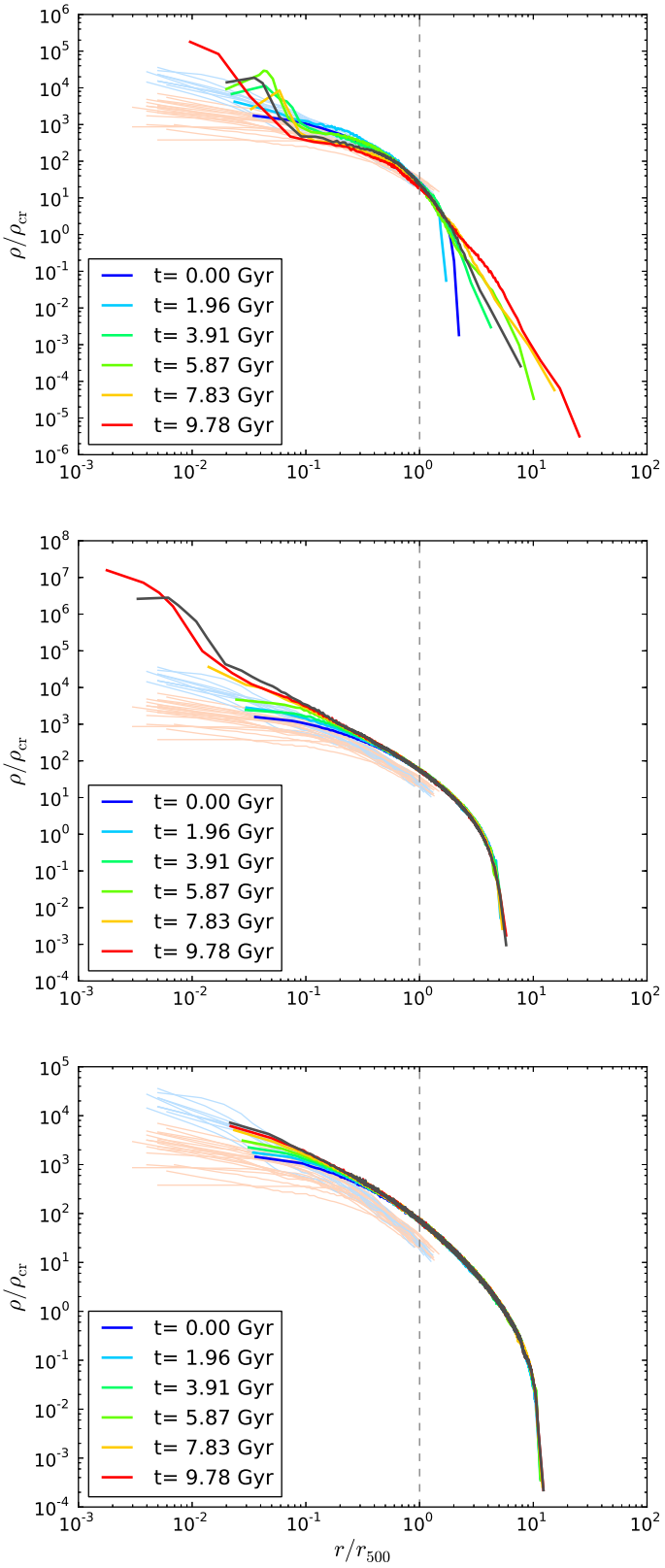

Figure 5.3: Density evolution for the GG (top), LC (centre) and HC (bottom) objects simulated with the hybrid (fiducial) anisotropic feedback model with a randomly-reorienting jet vector. Shown over-plotted in dark grey is the final density profile for the corresponding isotropic model.

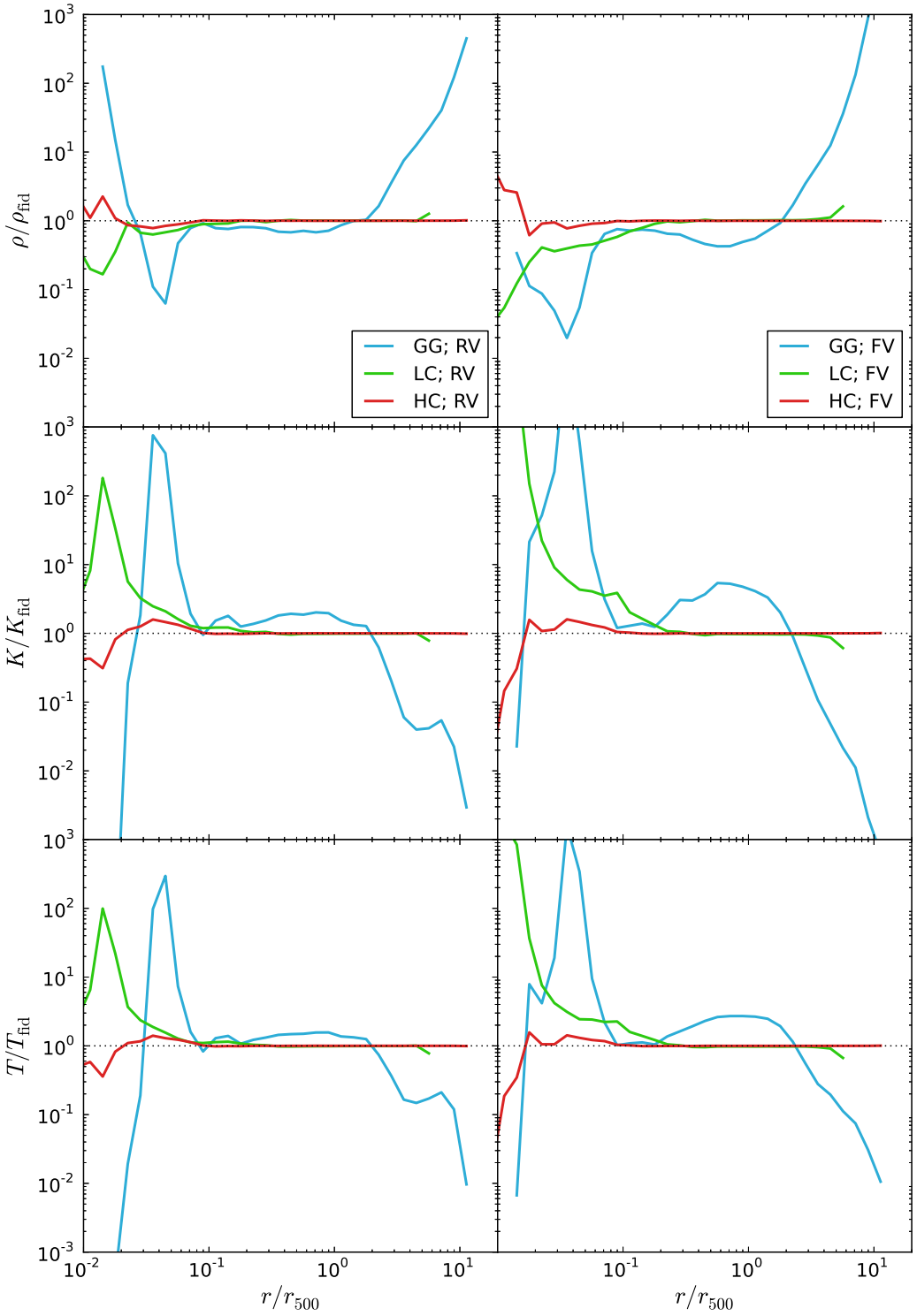

Figure 5.4: Final density (top), entropy (middle) and temperature (bottom) profiles as a ratio of the fiducial (hybrid) isotropic feedback for the GG, LC and HC objects. We show simulations with randomly-reorienting and fixed jet vectors in the left and right columns respectively.

of gas. As the hot gas rises to the periphery of the cluster which is at much larger radii in this simulation ($\sim 200 r_{500}$ for the GG object) than the corresponding isotropic simulation ($\sim 10 r_{500}$), cooler gas settles in its wake.

The BH growth history and wind position evolution are shown in Fig. 5.5 (top and bottom rows respectively) for the fiducial hybrid model simulated in each object (left to right GG, LC, HC). The upper figures are subdivided into three panels, the upper sub-panel indicates, for an individual time-step, when the BH accretes above the critical value and turns on quasar-like feedback. The central panel shows the BH accretion rate, with the horizontal dotted line indicating the critical accretion rate at which the feedback mode switches ($\dot{M}_{\rm crit}$). The lower panel shows the integrated BH mass. The lower row shows the position of the wind particles via the mean (thick line), one standard deviation (hatched area) and the upper/lower values as thin lines.

The RV hybrid BH mass in the GG object evolves similarly to the isotropic model until $t = 4\,{\rm Gyr}$ at which time it experiences the first of two drops in growth lasting $\sim 2\,{\rm Gyr}$, leading to a slightly reduced final BH mass[2]. Therefore, despite the lower total energy output from the BH, strong bubble feedback leads to more gas at larger radii ($r \geq 4\,r_{500}$) in the GG. Fig. 5.5 shows the position of the AGN-heated particles against time for the fiducial hybrid heating models. The majority of heated particles in the RV simulation settle at $r \approx 4\,r_{500}$ causing an increase in density (Fig. 5.4), whereas in the pure-jet simulation (Fig. 4.12) the heated particles reach $r \approx 10\,r_{500}$. The lowering gas densities and increasing entropy can be seen in the rendered gas images (Fig. 5.2).

The LC and HC objects each show the same trend towards increased central gas densities in the hybrid mode, however the discrepancy reduces for increasing object mass as the BH has less impact on its host in all cases. Fig. 5.2 shows empirically that the level of change is lower in these objects. The increase in gas density observed at the periphery of the GG object are no longer present (Fig. 5.4) as the outflows are more confined and remain within r_{500} for all models in these objects (Fig. 5.5). The BH mass evolution in the LC object is very similar for the RV and isotropic models until $t \sim 9\,{\rm Gyr}$ when the isotropic simulation experiences a surge in growth that is absent in the RV simulation. This is because the bubble heating lowers the density and cooling rates throughout the ICM. The HC simulation, however yields a 20 per cent *larger* final BH mass. This is due to the feedback-seeded over-dense gas which cools and 'rains' on to the central region and subsequently feeds BH growth. Although at a low level, this is significant as the ICM has a long cooling time and would otherwise condense onto the core at a very low rate

[2]The non-hybrid isotropic model yields a slightly different accretion rate and oscillates around approximately $10^{-3}\,\dot{\rm M}_{\rm Edd}$

5.1.2 Fixed jet axis

We now move on to discuss the effect of simulating the fiducial hybrid AGN model with a FV in the group and cluster objects. Generally, the final galaxy profiles (Fig. 5.4) exhibit the same trends as the equivalent RV simulations, albeit with some minor differences which we now discuss.

The final density, entropy and temperature ratios for the FV simulations are shown in the right-hand column of Fig. 5.4. As in the RV GG simulation, there is an increase in gas at large radii which is not present in the LC or HC simulations. This is significantly enhanced compared to the RV simulation, with gas reaching as far as $100\,r_{500}$ (where it is limited by an artificial boundary). In the GG and LC objects, the strong feature of the cold and dense central region is reduced, now having a lower density core bounded by high entropy gas.

The BH mass evolution for the FV simulations (Fig. 5.5) are very similar to the RV simulations in the LC and HC objects and more massive in the GG object. The pattern of growth is also different, with the FV BHs undergoing more steady accretion at or around $\dot{M}_{\rm crit}$. This is due to the cold gas accumulating primarily in a steady cooling flow perpendicular to the jet rather than in cold-dense blobs as in the RV simulation. The quasar mode is therefore more effective at opposing the gradual flow and regulating accretion.

Fig. 5.2 shows in the right hand column the rendered gas densities and entropies for the objects simulated with FV AGN. It shows that the FV heating is more effective at warming and dispersing the core in the GG and LC objects (no change is visible for the HC object). The larger amount of quasar mode feedback (Fig. 5.5) and the accompanying increase in AGN luminosity therefore heats the area around the BH, raising the entropy and lowering the density as previously discussed.

The reduced impact of spurious accretion driven by artificial cold blobs cooling onto the group/cluster core in the hybrid model shows that they were primarily responsible for the differences between the RV and FV models observed in the previous chapter.

5.1.3 Conclusions on the fiducial hybrid model

As a result of incorporating the hybrid feedback model the BH mass growth rate in all simulations reaches an effective maximum at or just above the critical value. This is due to the quasar mode 'switching on' and lowering the accretion rate by heating and dispersing the cold knot of gas close to the BH particle (rather than halting large-scale cooling) in a way which was not possible for the pure jet model.

We find that wind particles travel farther in the anisotropic feedback simulations for

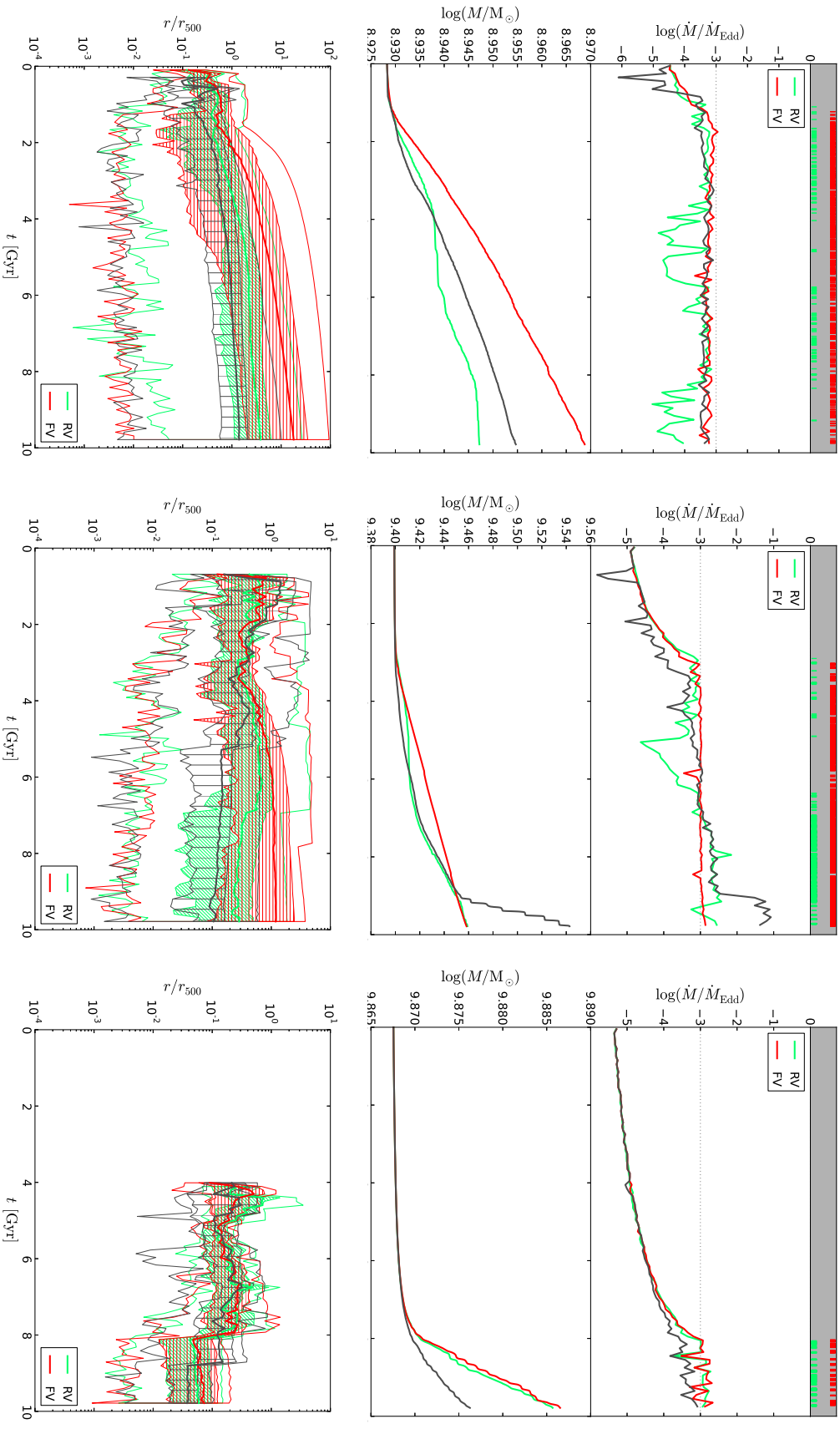

Figure 5.5: BH mass (top row) and wind position (bottom row) evolution for the hybrid AGN model in GG, LC and HC objects (left to right). Upper panels are subdivided into plots showing when a time-step is in the quasar mode, the BH accretion rate and the mass, top to bottom. The wind position is shown via the mean (thick line), standard deviation (hatched area) and the limiting values (thin lines). Grey lines show isotropic feedback results.

both RV and FV jets than in the isotropic feedback model as heated gas interacts with less of the stationary ICM. The FV simulation in particular leads to winds which travel significantly farther as successive heated particles lower the density and sweep up gas along the jet axis. In the GG object, the FV simulation blows gas out to such large radii that they completely escape the IGM. (We note that winds do not travel as far as in the non-hybrid jet models as less energy is deposited.) Whilst the GG object produces the expected bubble and cavity phenomenology as is expected from observations (e.g. Bîrzan et al. 2004), we see relatively little evidence in the LC object and none in the HC. Compared to the AMR simulations of Heinz et al. (2006) who simulated a $M \sim 7 \times 10^{14}\,\mathrm{M}_{\odot}$ cluster with an idealised AGN wind, we find significantly less structure. This may be linked to the better treatment of mixing in the grid-based code and the mixing introduced by the non-static ICM. The spurious surface tension in this formulation of SPH inhibiting mixing via the Rayleigh-Taylor instability.

As the hybrid model succeeds in driving winds which escape to larger radii, the AGN leads to more heating in the GG object as the winds interact with a large part of the ICM rather than leaving the group unchanged as was hoped. This leads to final GG gas density profiles which are disrupted compared to the initial case but which remain within observational bounds. Despite heating the low mass (GG) object more effectively than isotropic feedback, the fiducial hybrid model does not succeed in preventing the cluster objects from cooling and increasing their central densities.

The concentrated jet feedback is responsible for an *increase* in star formation (compared to the isotropic heating simulation) through positive feedback as the outflows shock gas leading to increased cooling. Although the quasar mode heats gas as it settles into the centre mitigating this effect, it cannot prevent the resulting formation of cores in all cases. Generically, the increase in star formation through positive feedback affects the RV simulation more severely due to the larger solid angle of gas which is compressed. Accordingly, the FV simulations form many less stars than RV simulations in all objects except for the HC; the warming of the ICM out to larger radii for the FV models is also responsible for reducing the star formation through slowing the cooling rates onto the core.

We note that the RV and FV simulations give similar results to the isotropic feedback model (SAGN) in the hybrid simulations, in contrast to the non-hybrid model for which there were large differences in behaviour. This shows once more that the spurious accretion onto the BH which is reduced in the hybrid model was introducing significant errors.

Whilst the formation of the blobs is not prevented in this method, their effect on the BH growth and star formation (not shown) is greatly reduced. We therefore now proceed

Table 5.1: Model parameters for hybrid anisotropic simulations investigating varying jet geometry, where we indicate fiducial simulations in bold. The first column gives the BH vector type where F stands for fixed vector and R for randomly re-orienting. Columns 2-4 give the AGN feedback efficiencies whilst columns 5-7 define the minimum number of particles heated and the geometry of the jet. The final column lists the minimum radio feedback duty cycle (not applicable here).

BH vector	$\epsilon_{\rm r}$	$\epsilon_{\rm f}$	$\epsilon_{\rm m}$	$N_{\rm heat}$	$r_{\rm J,min}$ [kpc]	$\theta_{\rm J}$	$\delta t_{\rm J,min}$ [yr]
F	0.10	0.15	0.15	10	0	05 °	–
F	**0.10**	**0.15**	**0.15**	**10**	**0**	**10** °	–
F	0.10	0.15	0.15	10	0	30 °	–
F	0.10	0.15	0.15	10	5	10 °	–
F	0.10	0.15	0.15	10	10	10 °	–
R	0.10	0.15	0.15	10	0	05 °	–
R	**0.10**	**0.15**	**0.15**	**10**	**0**	**10** °	–
R	0.10	0.15	0.15	10	0	30 °	–
R	0.10	0.15	0.15	10	5	10 °	–
R	0.10	0.15	0.15	10	10	10 °	–

to investigate the parameters of the hybrid model.

5.2 The effect of varying feedback geometry

Having investigated the effect of implementing a novel hybrid AGN model on the fiducial models and verifying that the problem of cold clumps has been mitigated, we now begin an investigation into the effects of varying the jet geometry. The effect of modifying the both the opening angle and minimum radius of the jets is investigated for each of the different mass objects; see Table 5.1 for a full listing of the models simulated. Varying the jet opening angle is interesting as it will alter the amount of gas which the wind interacts with and may affect the mixing and range of heated particles. It also affects the way thermal energy is deposited into the gas; narrowing the jet increases the radius at which gas is heated and can create jets extending for tens of $\rm kpc$. Additionally, narrowing the jet opening angle increases the temperature to which gas is heated by making it more likely that the same gas is heated in multiple iterations of the heating routine on a single time-step. Changing the minimum heating radius is interesting as offset jets simulate the presence of a sub-grid narrow jet which escapes the BH's local environment without interacting with it.

The results of varying the jet geometry are illustrated qualitatively in Fig. 5.6, which shows the rendered gas density for the GG object at $t = 5\,\rm Gyr$ for simulations with varying jet opening angle (top panels) and minimum heating radius (lower panels); upper

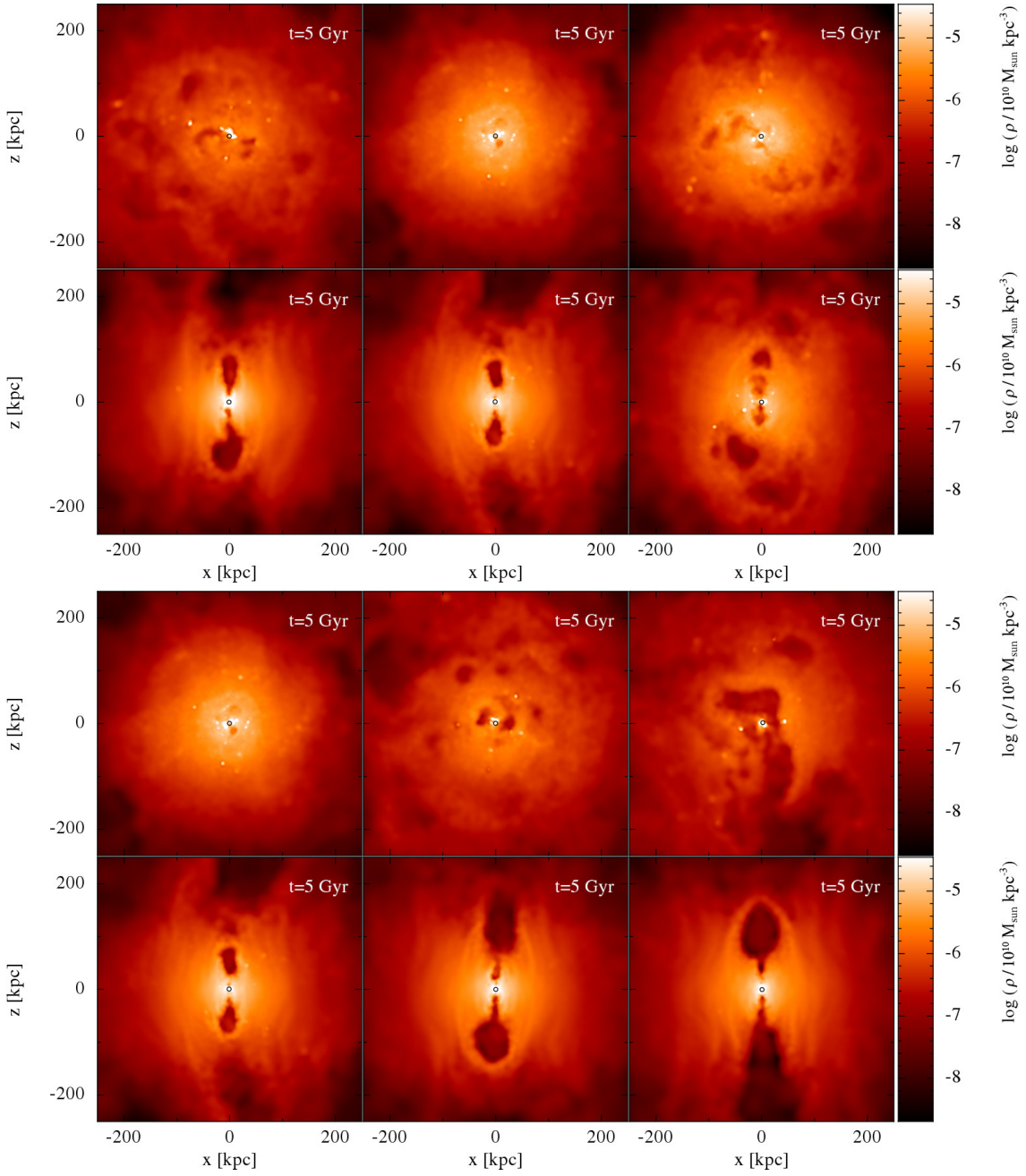

Figure 5.6: Rendered gas density for the GG object at $t = 5\,\mathrm{Gyr}$ for simulations with varying jet opening angle (top panel) and minimum heating radius (lower panel); upper and lower rows show simulations with RV and FV jets respectively. Left to right, columns show simulations with $\theta_{\mathrm{J}} = 5\,^{\circ}$, $10\,^{\circ}$ and $30\,^{\circ}$ in the top panel and $r_{\mathrm{J,min}} = 0\,\mathrm{kpc}$, $5\,\mathrm{kpc}$ and $10\,\mathrm{kpc}$ in the lower panel. Images show projected properties within slices of dimensions $500\mathrm{kpc} \times 500\mathrm{kpc} \times 100\mathrm{kpc}$, the BH position is indicated by a black circle.

and lower rows show simulations with RV and FV jets respectively. Left to right, columns show simulations with $\theta_{\rm J} = 5\,^\circ$, $10\,^\circ$ and $30\,^\circ$ in the top panels and $r_{\rm J,min} = 0$, 5 and $10\,{\rm kpc}$ in the lower panels. The images are otherwise made as in Fig. 4.23. The GG object alone is shown because it experiences the most prominent changes (as in previous sections), however the trends are similar for the LC object. Broadly, we see stronger outflows for narrower jets and larger minimum radii, however all of the bimodal AGN simulations show similar cavity structures. We now investigate the detailed changes for different geometries on each object in turn, first for the RV and later FV simulations.

5.2.1 Random BH vector

Jet opening angle

Fig. 5.7 shows the final density, entropy and temperature profiles (top to bottom) for simulations using the hybrid AGN model with different jet geometries as a ratio of the corresponding $\theta_{\rm J} = 10\,^\circ$, $r_{\rm J,min} = 0\,{\rm kpc}$ simulation. Both the RV (left panels) and FV (right panels) simulations for the GG, LC and HC objects are shown as solid, dashed and dotted lines respectively.

Concentrating on the left panels only, by far the largest variation is seen for the GG object where we see that narrowing the jet opening angle dramatically increases the effect on the gas profiles. This is due to the hotter gas forming bubbles which rise quickly and redistribute the ICM before creating a hot diffuse and outer layer. Accordingly, a larger opening angle results in a final density profile which is less extended than either the fiducial or the narrower jet. As the heated gas will travel along the pressure gradient away from the cluster core, the wider jet grows more dispersed (perpendicular to the direction of travel) and results in less directional outflows as the bubble is disrupted and redirected by the anisotropic ICM. The wider opening angle therefore reduces the range of the feedback; increasing its effectiveness slightly in the centre whilst lowering it further out. Accordingly, a narrower opening angle leads to more, hotter gas at the edges of the group as gas escapes more effectively.

Similar trends are seen for the corresponding LC simulations, however the variation in parameters causes less severe differences and the profiles converge at $0.2\,r_{500}$. (We note that the deviation at a given scaled radius is expected to be smaller in the higher mass objects as it corresponds to a larger physical radius.) This is due to a combination of effects, firstly the longer cooling time in this object means that BH accretion and feedback becomes less important. Secondly, the more pressurised ICM prevents the formation of a jet cavity (Fig. 5.6) and so the winds form bubbles which slow before they reach the edge

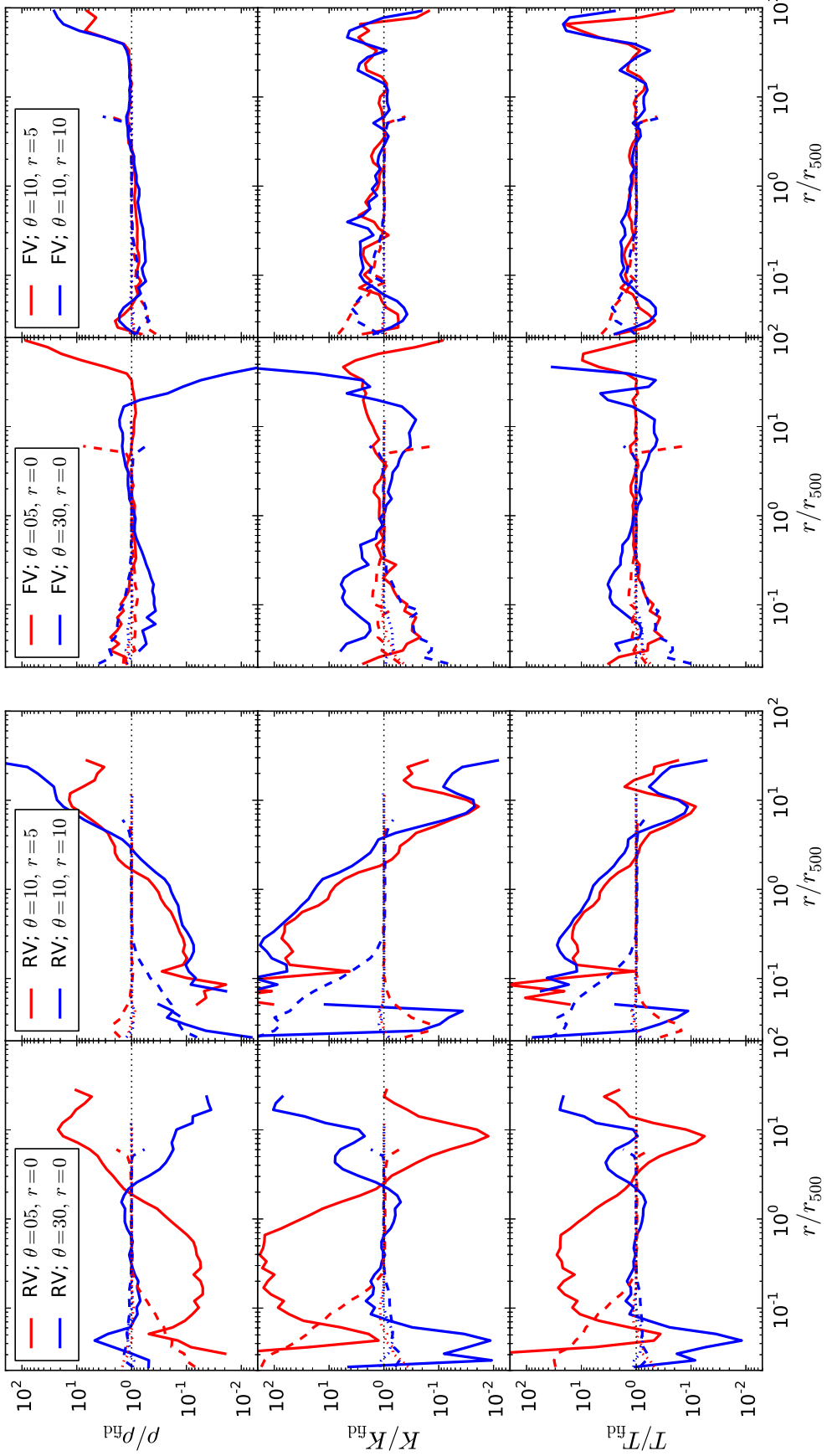

Figure 5.7: Final density profile (top row), entropy (middle row) and temperature (bottom row) profiles as a ratio of the respective fiducial model profile for different fixed (left panel) and random (right panel) jet geometries. Profiles for the GG, LC and HC object are shown as solid, dashed and dotted lines respectively.

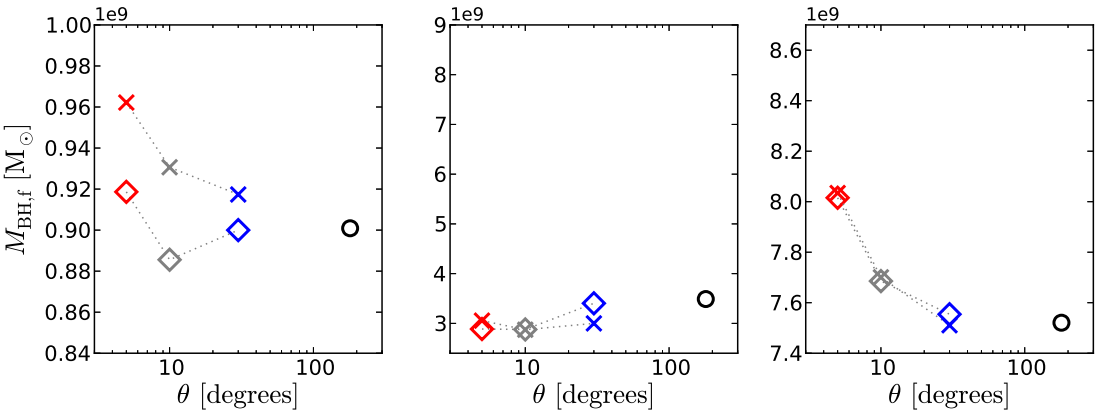

Figure 5.8: Final BH mass for simulations of anisotropic hybrid feedback with different opening angles in the GG (left panel), LC (centre panel) and HC (right panel) objects. Diamonds and crosses indicate simulations with randomly re-orienting and fixed BH jet vectors respectively whilst circles indicate isotropic feedback.

of the cluster. The HC object shows no significant difference in profiles for variations in this parameter and therefore we do not discuss it further.

Fig. 5.8 shows the final BH mass for GG, LC and HC (left to right) simulations performed with different jet opening angles, where diamonds denote RV simulations, crosses FV and circles isotropic feedback. For the FV simulations, varying the opening angle does not have a strong impact on the BH mass in any of the simulated objects as the largest variation from the fiducial model is merely a 5 per cent effect (in the GG simulation). What small variations are seen for the GG and LC objects do not show a consistent trend, due to the complex behaviour of the jets. Depending on the details of the simulation, jets may escape the central region, heat gas or compress it leading to increased cooling rates. However, a pattern does emerge in HC object due to its longer cooling time which allows us to isolate the trend of decreasing BH mass with increasing jet width. This is due to the lower opening angle forming more powerful jets which escape the central region, leaving only cooler gas which yields a higher accretion rate.

We plot in Fig. 5.9 the final stellar masses for the GG, LC and HC (left to right) simulations performed with different jet opening angles. The GG and LC objects each show less star formation in simulations with $\theta_{\rm J} = 5\,^\circ$. This is due to less gas cooling out of the more diffuse and higher-entropy gas shown in Fig. 5.7. This scenario does not apply to the HC object which shows a decrease in star formation when the jet opening angle is increased from $\theta_{\rm J} = 5\,^\circ$ to $10\,^\circ$. Fig. 5.10 shows the median BH wind position for simulations of anisotropic hybrid feedback with different opening angles in the all group/cluster objects for RV, FV and isotropic feedback simulations. We can see that

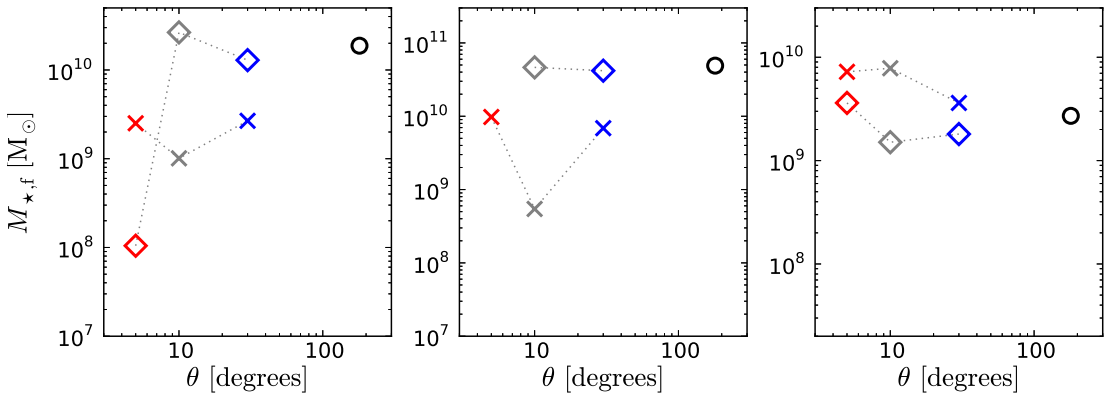

Figure 5.9: Total stellar mass formed for simulations of anisotropic hybrid feedback with different opening angles in the GG (left panel), LC (centre panel) and HC (right panel) objects. Diamonds and crosses indicate simulations with randomly re-orienting and fixed BH jet vectors respectively whilst circles indicate isotropic feedback.

increasing the opening angle means that the wind is less effective at escaping the central region. Therefore, the difference in stellar mass formed occurs because the longer cooling time means that only the central, dense gas cools within the simulation time and heating gas locally to the BH is then more effective at reducing the star formation.

Minimum jet radius

We now move on to investigate the effect of imposing a minimum radius criterion within the feedback routine on the cluster profiles. The right panels of the RV column in Fig. 5.7 show the density, entropy and temperature profiles as a ratio of the fiducial AGN model for different $r_{\mathrm{J,min}}$ values. The GG object (solid) shows a severely reduced central density with a corresponding entropy/temperature increase for minimum radii of both 5 and $10\,\mathrm{kpc}$ with very little difference shown between them. Either non-zero radius therefore leads to more gas being heated within and expelled from r_{500} for the GG object. Fig. 5.11 shows the total stellar mass formed for simulations with different minimum radii (otherwise as in Fig. 5.9), and it shows that this heating of the central gas also leads to a reduction in star formation. The increase in feedback effectiveness may be partially explained by the higher BH masses obtained for simulations with larger minimum heating radii (Fig. 5.12). This occurs due to the larger minimum radius allowing more cool gas to settle around the BH giving higher accretion rates.

The mass does not, however, explain the non-linear impact upon the profiles; therefore the dynamics of the heated gas also plays a part as winds are more directional and travel further. Fig. 5.13 shows the median BH wind position for simulations of anisotropic

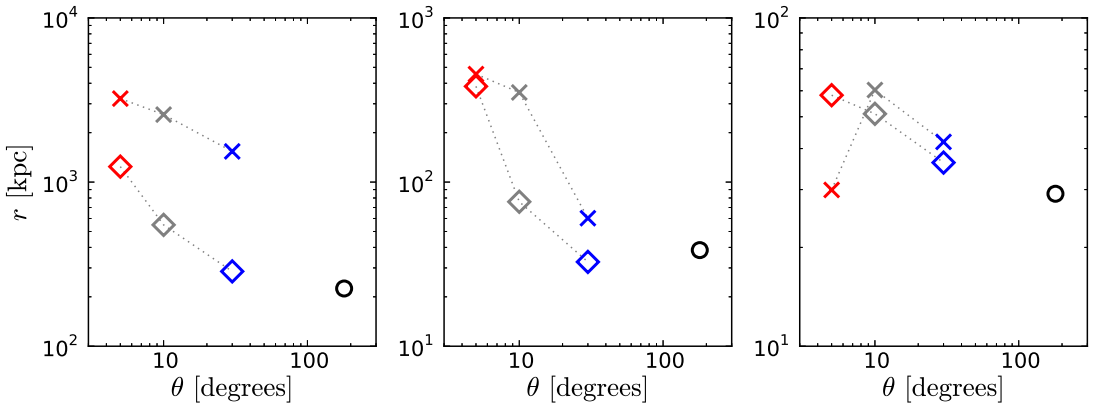

Figure 5.10: Median BH wind position for simulations of anisotropic hybrid feedback with different opening angles in the GG (left panel), LC (centre panel) and HC (right panel) objects. Diamonds and crosses indicate simulations with randomly re-orienting and fixed BH jet vectors respectively whilst circles indicate isotropic feedback.

hybrid feedback with different minimum jet radii in the group/cluster objects for RV, FV and isotropic feedback simulations. In the galaxy group the BH winds do indeed travel farther from the BH with increasing minimum heating radius, increasing exponentially with median radii of $\sim$ 500, $\sim$ 1000 and $\sim$ 2000 kpc for $r_{\rm J,min} = 0$, 5 and 10 kpc respectively. This then explains why the final profiles for the non-zero minimum radii are similar as the $r_{\rm J,min} = 5\,{\rm kpc}$ winds efficiently escape out of the GG ($r_{500} = 177.6\,{\rm kpc}$; see Table 4.1) and so the additional effective wind power from further increasing the minimum radius is lost to the group without affecting the IGM.

The LC object does, however, exhibit differences in central density and entropy (Fig. 5.7; dashed lines) for the two minimum heating radius values, showing opposite responses about the fiducial model. In this higher mass object, the $r_{\rm J,min} = 10\,{\rm kpc}$ model alone is powerful enough to heat gas, lower the central ($< 0.2\,r_{500}$) density and increase the entropy; whilst using $r_{\rm J,min} = 5\,{\rm kpc}$ appears to *weaken* the influence on the cluster gas when compared to the $r_{\rm J,min} = 0$ model. The final BH masses (Fig. 5.12) and wind positions (Fig. 5.13) exhibit the same pattern of variations with increasing minimum radius. They each show a slight decrease compared to the fiducial simulation when $r_{\rm J,min} = 5\,{\rm kpc}$, followed by a net increase for $r_{\rm J,min} = 10\,{\rm kpc}$, whereas the stellar masses progressively decrease with increasing minimum radius (Fig. 5.9; no stars form for $r_{\rm J,min} = 10\,{\rm kpc}$). Therefore the relatively weak influence on the cluster for the lower minimum radius occurs because the BH winds cannot escape the central region to influence the ICM. Instead, the additional thermal energy lowers the central star formation by preventing cool gas from forming stars, resulting in a larger gas density.

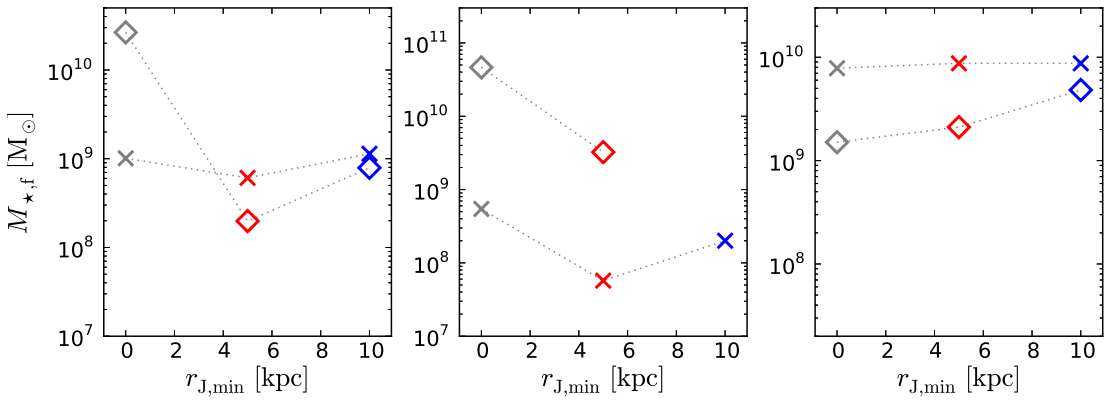

Figure 5.11: Total stellar mass formed for simulations of anisotropic hybrid feedback with different minimum jet radii in the GG (left panel), LC (centre panel) and HC (right panel) objects. Diamonds and crosses indicate simulations with randomly re-orienting and fixed BH jet vectors respectively.

The highest mass cluster does not show any variation in density or entropy profiles when simulated with hybrid jets of any geometry (Fig. 5.7; dotted lines). Similarly there is very little variation in final BH mass (Fig. 5.12) and wind position (Fig. 5.13); the total stellar mass, however, does show a weak trend for increasing with $r_{\mathrm{J,min}}$, rising by around a factor of three.

5.2.2 Fixed BH vector

We now go on to discuss the effect of varying the jet parameters for simulations of hybrid model AGN with a fixed jet axis. It is immediately apparent from inspection of the final group/cluster profiles (Fig. 5.7; right panel) that they are less affected by variations in the jet geometry than the RV models. Rendered gas density images (Fig. 5.6) reveal that the directional FV outflows carve out a chimney/cavity from the GG object, indicating why the differences are less prominent in the azimuthally averaged profiles. We now discuss the detailed impact on each object in turn, first discussing the effect of varying the jet opening angle and secondly of imposing a minimum heating radius.

Jet opening angle

The final density profile for the GG object (Fig. 5.7) shows that a narrower opening angle ($5\,^\circ$) than the fiducial value ($10\,^\circ$) redistributes more gas to larger radii; and correspondingly a wider angle ($30\,^\circ$) blows out much less. Compared to the RV simulations the gas is cast to much larger radii; this is in agreement with the final wind positions (Fig. 5.10)

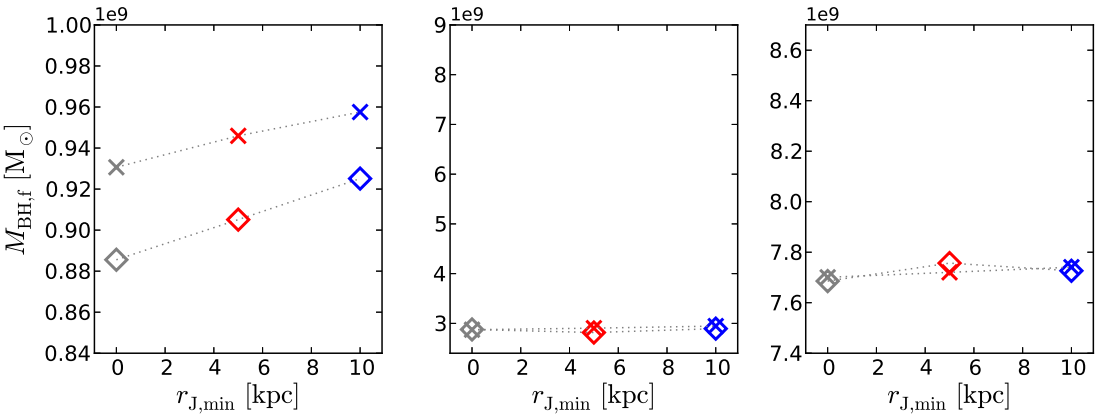

Figure 5.12: Final BH mass for simulations of anisotropic hybrid feedback with different minimum jet radii in the GG (left panel), LC (centre panel) and HC (right panel) objects. Diamonds and crosses indicate simulations with randomly re-orienting and fixed BH jet vectors respectively.

which generally travel farther than the RV simulations and stop sooner for wider jets. The central density is higher (lower) for narrower (wider) jets (compensated by a small reverse change outside of r_{500}) and the opposite pattern is seen for the entropy/temperature with the same cross-over point. This trend in the profiles is in agreement with the final BH wind particle positions, as wide jets interact with and sweep-out gas from the centre more effectively, whereas narrow jets escape more readily. The increase in cool gas at the core of the group for the $\theta_{\rm J} = 5\,^\circ$ simulation is due to the gas perpendicular to the jet axis which cools onto the cluster core as it is not heated. The final BH mass is also affected by this and drops monotonically with increasing jet opening angle in line with the central density and temperature trends (Fig. 5.8). The total stellar mass formed (Fig. 5.9) does not, however, follow such a clear-cut trend. The final stellar mass is at a minimum for the intermediate opening angle simulated (the fiducial model), being approximately equal for the other values. There are two distinct sources of star formation in these simulations; the wide jet model gives higher star formation because it offsets cooling less well and allows cooling onto the core, whereas the narrow jet simulation forms more (than the fiducial model) due to stronger positive feedback as the bubbles are hotter and more defined. This causes the increase in star formation for both narrower and wider jets. It also shows the delicate balance between the two effects which increase star formation in these simulations and the heating which lowers it.

The effects of modifying the FV jet opening angle upon the gas profiles (Fig. 5.7; dashed lines) of the LC object are now discussed. Generally, the trends observed at the outer edge are a weaker analogue of those observed for the corresponding GG object simulations; i.e. the narrower jet opening angle blows out more gas to higher radii (Fig. 5.10).

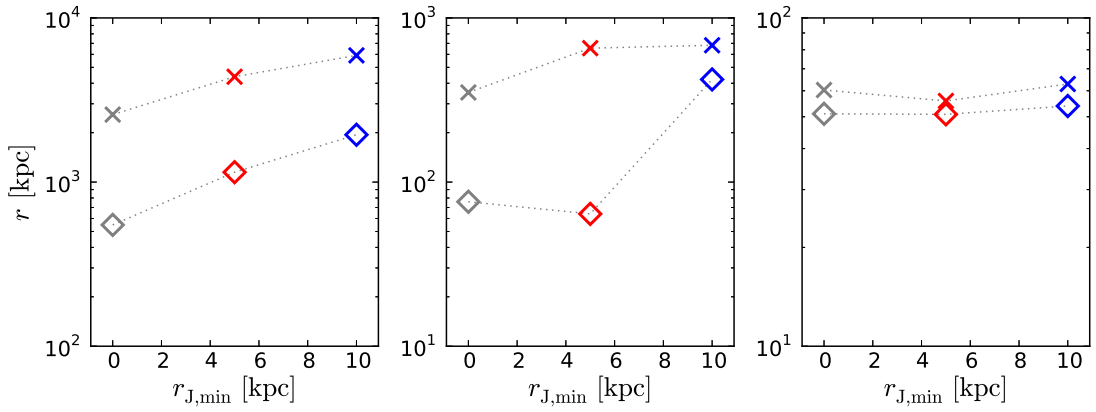

Figure 5.13: Median BH wind position for simulations of anisotropic hybrid feedback with different jet minimum radii in the GG (left panel), LC (centre panel) and HC (right panel) objects. Diamonds and crosses indicate simulations with randomly re-orienting and fixed BH jet vectors respectively.

The central region does not share this similarity, here the gas density is very weakly reduced in the centre for the narrow jet simulation and increased for the wide simulation. This is linked to the distance travelled by the wind particles, which are similar for the fiducial and narrow jet simulations and an order of magnitude larger than in the wide angle jet simulation. This means that the wide angle jet is unable to prevent gas cooling onto the core and increasing the density. The final BH mass (Fig. 5.8) and total stellar mass (Fig. 5.9) both show a trend for increasing with $\theta_{\rm J}$ (which is further strengthened if the isotropic data are included), except for an artificially high value for the narrow jet model. This is due to the narrower jet forming hotter and more defined bubbles and causing clumps of gas to form which later cool onto the core. We note that whilst in the GG object, the narrow jet simulation does not form bubbles however it does in the LC object. this is due to the higher ambient pressure and increased time between feedback events.

The HC object, as in the RV simulations, does not show any variation in density, entropy or temperature profiles when simulated with different jet geometries (Fig. 5.7; dotted lines). The small changes in final BH mass observed also agree well with the randomly re-orienting vector simulations (Fig. 5.8), whereas the BH wind position (Fig. 5.13) deviates slightly for the narrow angle jet simulation at a factor of two lower. The reduction in radial range of the wind particles is explained by the late activation of the quasar mode in the narrow jet simulation which creates a population of wind gas around the BH, lowering the median position. Finally, the stellar masses formed show only very small changes (< 10 per cent difference), but do show a trend for decreasing with increasing opening angle.

Minimum jet radius

The fiducial FV model is now compared with simulations in which we vary the minimum jet heating radius, $r_{\rm J,min}$. The group/cluster gas property profiles (Fig. 5.7; right panel) show clearly that, in general, altering the minimum jet heating radius also has very little impact upon the fixed vector simulations regardless of object. This supports the view formed during the analysis of the RV simulations that increasing this parameter above zero primarily acts to columnate the outflow; this does not make a difference in the already highly ordered FV jets.

The density, entropy and temperature profiles for the $r_{\rm J,min} = 5$ and $10\,{\rm kpc}$ simulations are strikingly similar to one another for all objects. The HC object shows no differences in the profiles and so is not discussed. Compared to the fiducial model, the GG (and to a lesser extent LC) object simulations show an increase in gas at large radii as it is efficiently redistributed from the centre. Additionally, the GG object shows a small ($< 0.1\,r_{500}$) increase in central density caused by cold gas, due to in-falling cold blobs which do not occur as readily in the LC object.

The stellar mass formed (Fig. 5.11) in the GG and LC objects shows a relatively small deviation between models, however it again shows the characteristic minimum for the $r_{\rm J,min} = 5\,{\rm kpc}$ model due to the balance between maintaining the ICM temperature and seeding cold blobs through forming high density shells. The difference between simulations is reduced compared to the RV models because less gas is impacted by the outflows and gas becomes entrained by the ordered outflow, reducing the creation of dense shells. The HC object shows no substantial variation in star formation with minimum jet radius.

The Final BH masses (Fig. 5.12) follow broadly the same trends as outlined for the RV simulations, independent of object the final BH mass increases with larger $r_{\rm J,min}$. The GG object follows a pattern identical to the RV simulations with systematically ~ 10 per cent higher masses whereas the LC and HC objects show only a weak trend.

5.2.3 Summary from varying the jet geometry

Beginning with the RV simulations, we find that simulations incorporating narrower jets have a larger impact on the gas in the GG and LC objects as the AGN-heated gas is hotter and more confined, causing the gas to rise further in the ICM. Similarly, introducing a non-zero minimum heating radius increases the impact on the gas, but each of the values modelled here give very similar results. This is because the enhancement in effectiveness is primarily due to the increased directionality of the jet/bubbles as the heated particles

rise along similar paths rather than dispersing; this too allows the wind particles to reach larger radii.

Changing the jet geometry varies the star formation by a large degree, although there is less variation for increasing object mass. This is primarily tied to the level of strong feedback and the amount of star formation caused by winds compressing gas, causing it to cool. Neither the jet opening angle or minimum radius, however, have a large impact on the BH mass.

Considering now the impact on simulations performed with different FV jet geometries, we find that parameter variations have much less influence compared to the RV models as the jet impacts on a small solid angle. This results in the powerful winds clearing an area of gas in the GG object forming a 'chimney', and saturating the influence on the small amount of gas heated in the LC/HC objects. On a smaller level, varying the opening angle does affect the outer density as narrower jets reach farther, however we do not find the large-scale outflows present in observations of some clusters (Heinz et al. 2006).

For both random and fixed jet vectors we find that in the LC object only a narrowed or substantially-centrally offset jet is powerful enough to affect the cluster significantly. Additionally, although the jet geometry does not impact on the ICM, it does affect the levels of star formation and the final BH mass. The nature of the influence is non-trivial as winds can either boost star formation and the BH mass by increasing cooling or suppress it by heating the gas.

Generally, we note that increasing the opening angle increases the convergence between the fixed and random vector models as they each tend towards isotropic feedback. A broad finding is that the radius to which AGN-heated gas escapes is an important factor in determining the fate both of the IGM/ICM but also the levels of star formation and growth of the BH.

5.3 Imposing a minimum radio duty-cycle

We now perform simulations with minimum time intervals imposed between heating events in order to study how the timing and power of the feedback episodes affects the cluster and BH properties. The feedback mechanism will act exactly as in previous hybrid AGN model investigations except that the BH particle cannot deposit its (radio-mode) energy until a set time period has elapsed since the previous heating event. With the timing of heating effectively fixed (assuming the BH accretes sufficient mass to heat the particles to the critical temperature, see Chapter 2 Section 2.2.3), the property varying at each heat-

Table 5.2: Model parameters for hybrid anisotropic simulations investigating varying the minimum jet feedback duty-cycle where we indicate simulations using the fiducial assumed efficiencies in bold. The first column gives the BH vector type where F stands for fixed vector and R for randomly re-orienting. Columns 2-4 give the AGN feedback efficiencies whilst columns 5-7 define the minimum number of particles heated and the geometry of the jet and the final column lists the minimum radio feedback duty cycle (where applicable).

BH vector	$\epsilon_{\rm r}$	$\epsilon_{\rm f}$	$\epsilon_{\rm m}$	$N_{\rm heat}$	$r_{\rm J,min}\,[{\rm kpc}]$	$\theta_{\rm J}$	$\delta t_{\rm J,min}\,[{\rm yr}]$
R	0.10	0.15	0.15	10	0	10°	1×10^6
R	0.10	0.15	0.15	10	0	10°	3×10^6
R	0.10	0.15	0.15	10	0	10°	1×10^7
R	0.10	0.15	0.15	10	0	10°	3×10^7
R	0.10	0.15	0.15	10	0	10°	1×10^8
F	0.10	0.15	0.15	10	0	10°	1×10^6
F	0.10	0.15	0.15	10	0	10°	3×10^6
F	0.10	0.15	0.15	10	0	10°	1×10^7
F	0.10	0.15	0.15	10	0	10°	3×10^7
F	0.10	0.15	0.15	10	0	10°	1×10^8

ing event now becomes the amount of energy deposited. All simulations are performed using the hybrid AGN model and therefore the quasar mode is still free to deposit energy instantaneously and continuously as in previous sections.

By varying the timing of heating events we are able to investigate the effect of a BH feeding-back into its environment through trickle-heating which is linked to a quiescent 'maintenance mode', as well as more bursty bubble heating, which is associated with phenomenological features such as X-ray cavities. Although imposing an ad-hoc timescale externally onto the BH particle may be undesirable from a modelling point-of-view, it allows us to probe an important feedback parameter in a more controlled fashion which may inform future modelling considerations.

The models simulated with different imposed minimum time intervals are described in Table 5.2. We perform all simulations with the fiducial anisotropic jet geometry for each of the group and cluster objects (GG, LC, HC) with both fixed and randomly re-orienting jet vectors.

Fig. 5.14 shows the rendered gas density for the GG (top panel) and LC (lower panel) objects at $t = 5\,{\rm Gyr}$ for simulations with varying minimum jet duty-cycle; upper and lower rows show simulations with RV and FV jets respectively. Left to right, columns show simulations with $\delta t_{\rm J,min} = 10^6,\ 10^7,\ 10^8\,{\rm Gyr}$. The images are made by taking $100\,{\rm kpc}$ deep slices through the centre of the cluster at various times in the simulation and each frame is $500\,{\rm kpc}$ on a side. It is immediately apparent that lengthening the duty-cycle increases the impact on the GG object.

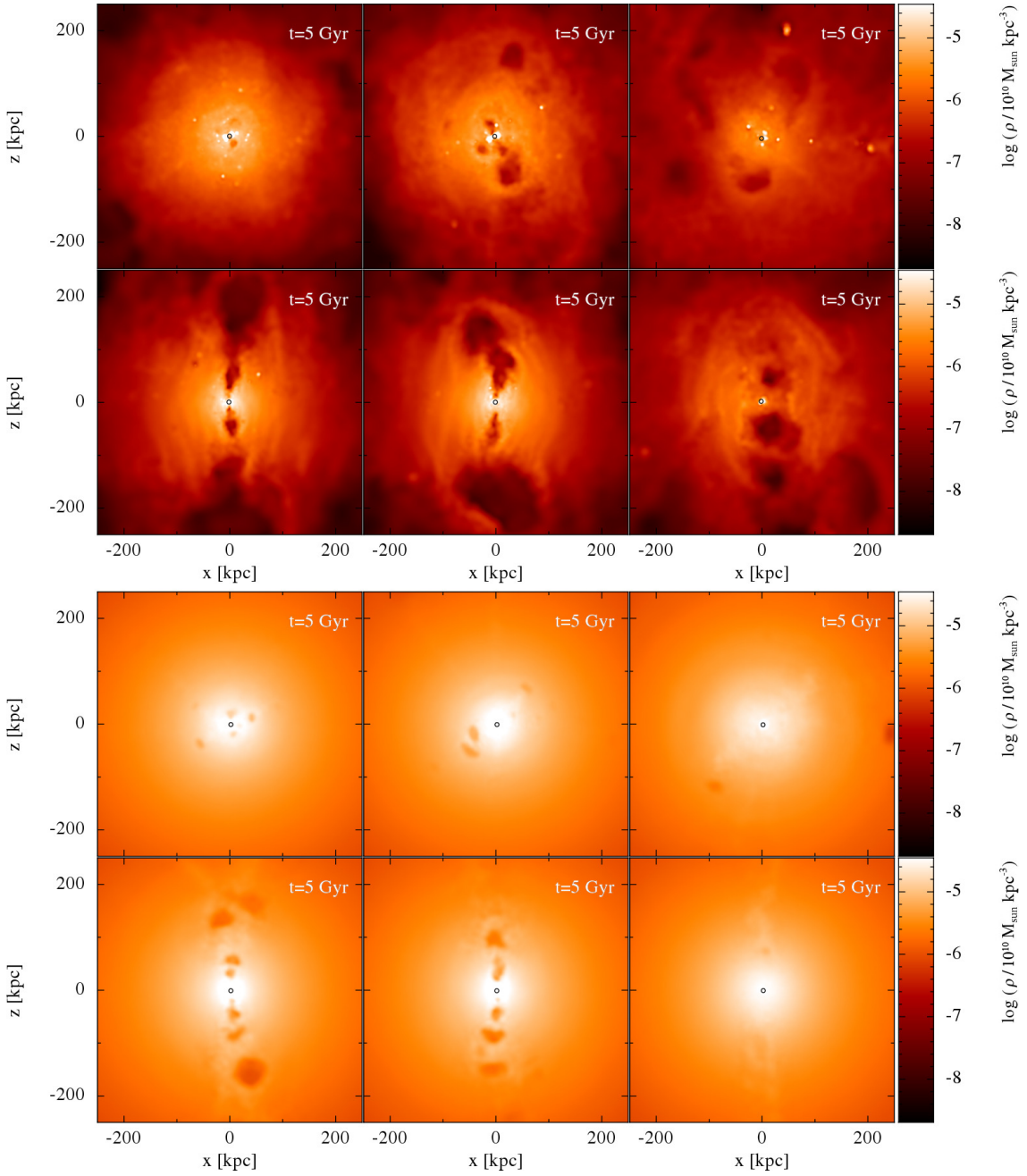

Figure 5.14: Rendered gas density for the GG (top panel) and LC (lower panel) objects at $t = 5\,\mathrm{Gyr}$ for simulations with varying minimum jet duty-cycle; upper and lower rows show simulations with RV and FV jets respectively. Left to right, columns show simulations with $\delta t_{\mathrm{J,min}} = 10^6\,\mathrm{Gyr}$, $10^7\,\mathrm{Gyr}$, $10^8\,\mathrm{Gyr}$. Images show projected properties within slices of dimensions $500\mathrm{kpc} \times 500\mathrm{kpc} \times 100\mathrm{kpc}$, the BH position is indicated by a black circle.

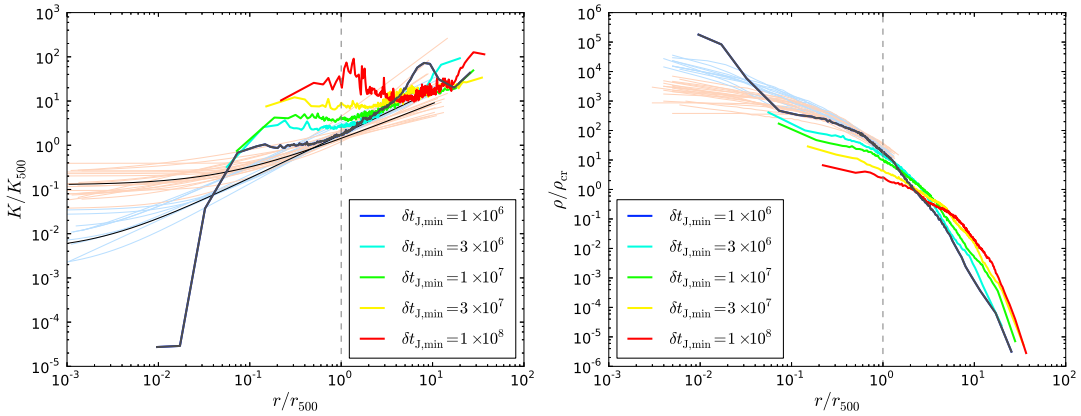

Figure 5.15: Final density (left) and entropy (right) profiles for the GG object simulated with the fiducial anisotropic hybrid RV AGN feedback model. The corresponding final profile for a simulation without a BH duty-cycle is over-plotted in dark grey for comparison.

5.3.1 Random vector

We begin by discussing the effect of varying the BH feedback duty-cycle on our lowest mass object (GG). Fig. 5.15 shows the final density and entropy profiles for the GG object when simulated with the hybrid AGN model with a range of $\delta t_{\rm J,min}$ values imposed. Increasing the time between outbursts enhances the effect of feedback on the group's density profile, leading to progressively lower central densities and higher entropies as well as less radiated energy (not shown). Fig. 5.16 shows (as diamonds) the total number of stars formed (top row), final BH mass (bottom row) and median radial position of AGN-heated gas (bottom row) for the GG, LC and HC (columns, left to right) objects simulated with the different $\delta t_{\rm J,min}$ values. Generically, the total stellar mass decreases with increasing heating interval. This is in agreement with the profiles, as the progressively lower gas densities and higher entropies slow the rate at which gas cools onto the core and becomes dense enough to join the effective equation of state and so become eligible for star formation. The centre-left panel of Fig. 5.16 shows that the AGN wind escapes to larger distances as $\delta t_{\rm J,min}$ increases. This allows the bubbles to influence more gas and slow cooling throughout the group. Furthermore, as Fig. 5.14 shows, increasing the time between outflows forms larger bubbles which interact with a larger solid angle as they rise, increasing their effect further.

Considering the BH masses, we can see that the final mass (Fig. 5.16) vary significantly with $\delta t_{\rm J,min}$. Increasing the time between heating events raises the final BH mass until $\delta t_{\rm J,min} = 3 \times 10^7\,{\rm Gyr}$ when the trend reverses. This shows two effects at tension, where initially the increased interval means that heated particles more effectively leave the

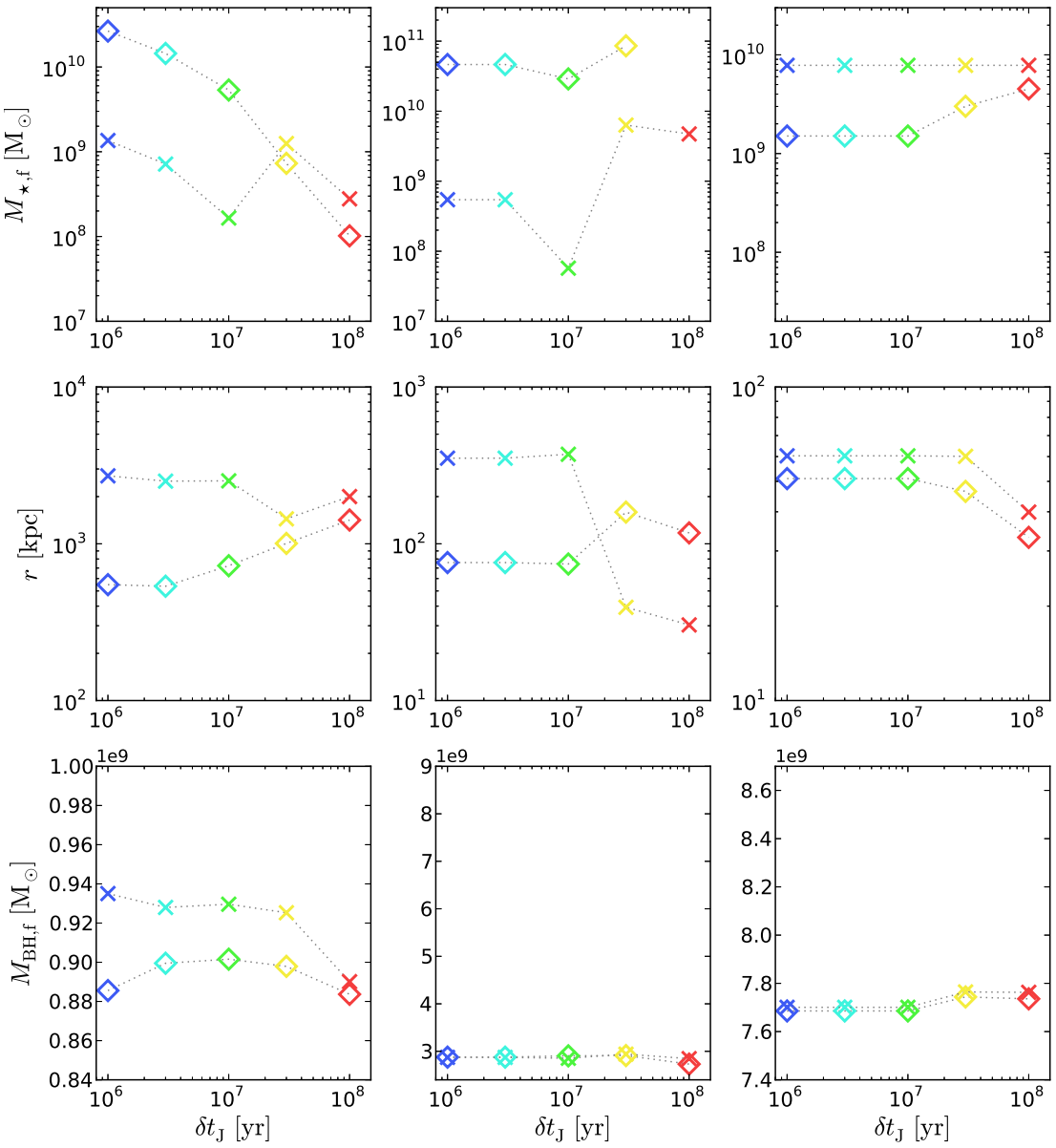

Figure 5.16: Total stellar mass formed (top row), median position of AGN wind particles (centre row) and final BH mass for simulations of anisotropic hybrid feedback and different radio jet duty-cycles in the GG (left panel), LC (centre panel) and HC (right panel) objects. Diamonds and crosses indicate simulations with randomly re-orienting and fixed BH jet vectors respectively, whilst circles indicate isotropic feedback.

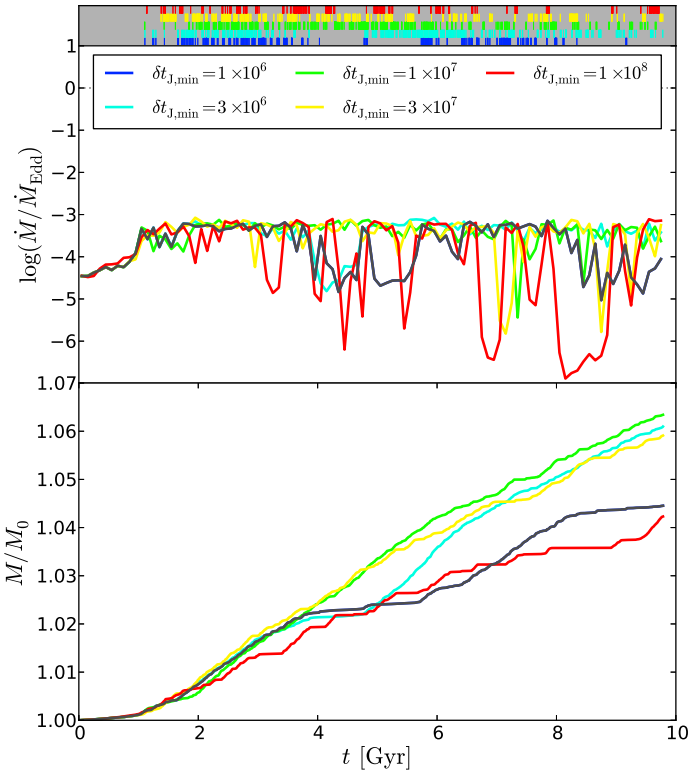

Figure 5.17: BH mass evolution for the GG object simulated with the fiducial anisotropic hybrid RV AGN feedback model. The top panel indicates if the BH is depositing feedback in the quasar mode on an individual time-step, the centre panel shows the accretion rate in Eddington units and the bottom panel shows the normalised integrated mass. The corresponding data for a simulation without a BH duty-cycle is over-plotted in dark grey for comparison.

central region and allow the BH to grow more, however at still-higher interval values the strengthened heating means that less gas cools onto the core fuelling BH growth. The corresponding BH mass evolution is shown in Fig. 5.17 where the top panel indicates if the BH is depositing feedback in the quasar mode on an individual time-step, the centre panel shows the accretion rate in Eddington units and the bottom panel shows the normalised integrated mass. Although the final BH masses differ and the accretion is slightly more 'bursty' for the longer time interval simulations, the BH mass increases fairly smoothly and similarly in all models, varying by only a few per cent (this is generally the case and so we will plot only the final masses in the future). The total radiated energy is also lower for the longer imposed time intervals (~ 100 times lower for the $\delta t_{\rm J,min} = 1 \times 10^8\,{\rm Gyr}$ model when compared to the $\delta t_{\rm J,min} = 1 \times 10^6\,{\rm Gyr}$ simulation).

Moving on to discuss the LC object, we can see that the increase in cooling time and its larger size means that (as in the previous sections) the object is less affected by the parameter changes. The final entropy and density profiles are shown in Fig. 5.18 and it

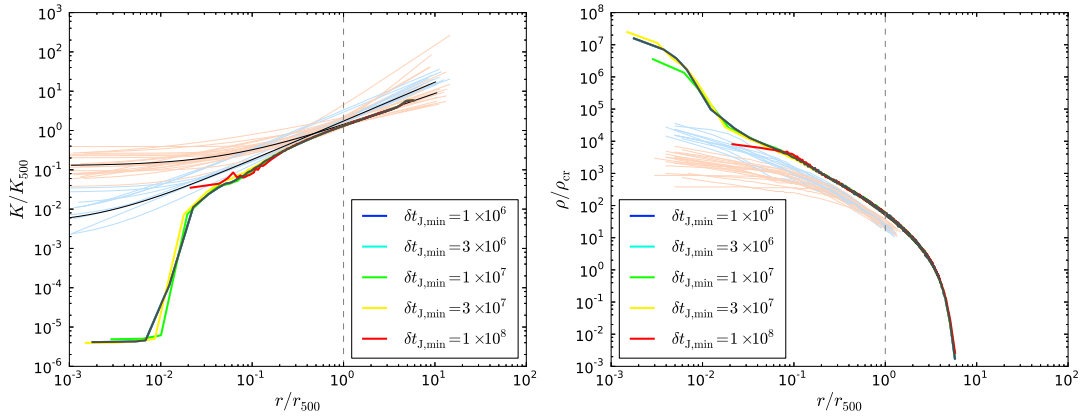

Figure 5.18: Final density (left) and entropy (right) profiles for the LC object simulated with the fiducial anisotropic hybrid RV AGN feedback model. The corresponding final profile for a simulation without a BH duty-cycle is over-plotted in dark grey for comparison.

is clear that only the longest intervals between heating have any discernible effect on the final profiles, causing a heating of the core. This core heating leads to lower accretion rates and accordingly a lower final BH mass (Fig. 5.16). Interestingly, despite having no impact on the profiles, the timing of the heating events does affect the star formation. Initially, the star formation decreases with increasing time interval as in the GG object, however there is a break in this pattern for the $\delta t_{\rm J,min} = 3 \times 10^7$ yr simulation. This model forms more stars than any other time interval tested for RV feedback in this object. It is also the model for which the AGN wind travels farthest from the core showing that as the winds escape the core more effectively, the central gas can cool freely to form stars. This effect is also enhanced by an increase in the amount of gas condensing onto the core, due to the bubbles compressing and disrupting more of the ICM as they rise.

In the HC object, the minimum feedback interval has even less effect on the ICM; the density, entropy and temperature profiles (not shown) are identical for all time intervals. The star formation in this object (in contrast to in the GG object) *increases* with $\delta t_{\rm J,min}$. This is due to the larger and hotter bubbles generating stronger compressions in the ICM and more positive feedback. We note that the star formation is of a very low level, however, and susceptible to numerical noise. The stronger interaction with the ICM for larger bubbles is evident by the reduction in the winds' final distance from the BH.

5.3.2 Fixed vector

Having discussed the impact of varying the time interval between heating events for all objects simulated with a RV anisotropic jet, we now discuss the effects when the BH jet

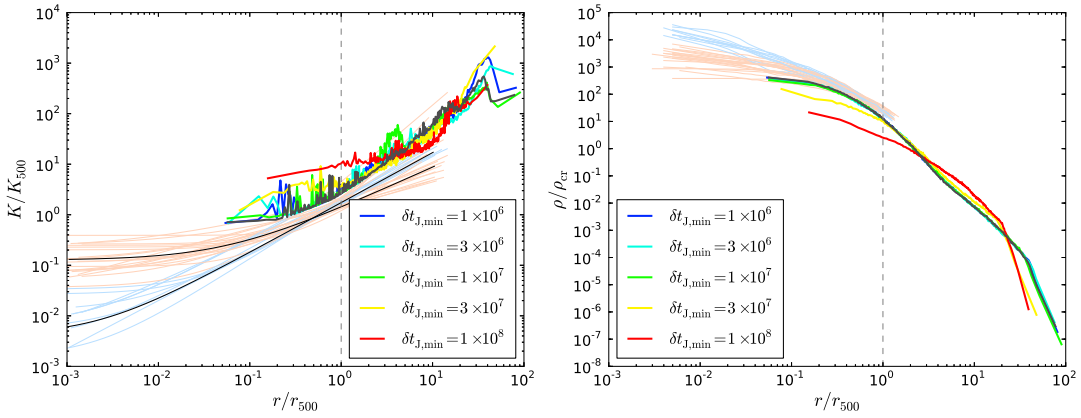

Figure 5.19: Final density (left) and entropy (right) profiles for the GG object simulated with the fiducial anisotropic hybrid FV AGN feedback model. The corresponding final profile for a simulation without a BH duty-cycle is over-plotted in dark grey for comparison.

vector is instead fixed (FV).

Fig. 5.19 shows the final entropy and density (left and right panels respectively) profiles for the GG object simulated with FV jets of different length AGN duty-cycles. The profiles show an increase in entropy and decrease in density throughout the object with increasing time interval as was found for RV jets. The level of the entropy (density) increase (decrease) is not, however, gradual. The profiles appear very similar as the interval is increased until $\delta t_{\rm J,min} = 3 \times 10^7\,{\rm yr}$ when the profiles begin to show more significant changes. This is similar to the $r_{\rm J,min}$ investigation (Section 5.2.1) which found that the profiles were similar when the winds escaped the group efficiently, without doing additional work. Fig. 5.16 (bottom row; indicated as crosses) shows the final median AGN wind positions. We can see that the jets from the lower time interval AGN are escaping the GG object and so have a similar effect on the profiles. Once the jets are confined, increasing the time interval further strengthens the effect on the profiles and the distance which the winds travel. Therefore, increasing the heating interval has more of an effect on the group as jets become more intermittent and the flow is less well defined, meaning that the trajectories of the heated particles are wider; this is confirmed by visual inspection of the rendered images (Fig. 5.14).

Now analysing the final BH masses (Fig. 5.16; bottom row), we find progressively lower values as the feedback time interval is increased. Due to the fixed anisotropic feedback heating only part of the cluster, cooling perpendicular to the jet axis is important in these simulations. More-frequently-active 'trickle' jets are more narrow and therefore allow more mass to accrete onto the BH unopposed. The $\delta t_{\rm J,min} = 1 \times 10^6\,{\rm yr}$ simulation BH is more massive than that in the RV simulation because the FV jets are still able

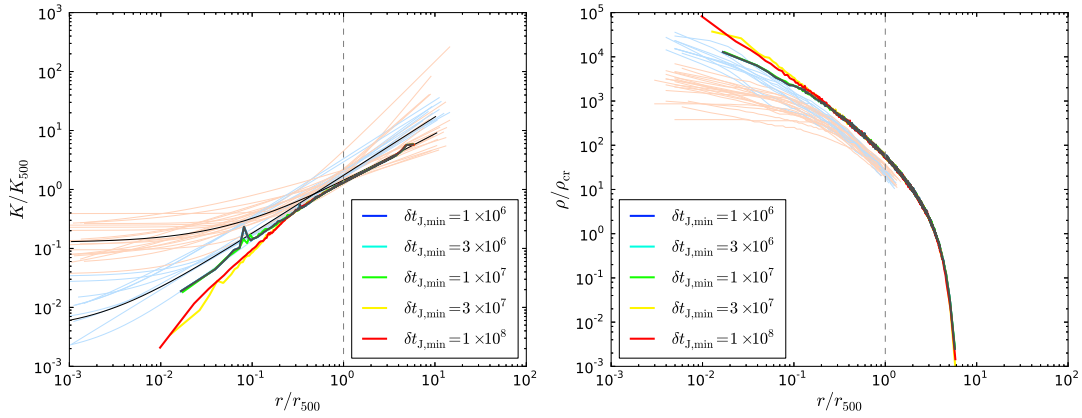

Figure 5.20: Final density (left) and entropy (right) profiles for the LC object simulated with the fiducial anisotropic hybrid RV AGN feedback model. The corresponding final profile for a simulation without a BH duty-cycle is over-plotted in dark grey for comparison.

to escape the central region, unlike in the RV simulation, where no stable flow can be created. The joint effects of jet widening for increasing time interval and the dichotomy in wind range also impacts upon the total stellar mass formed. The stellar mass decreases with increasing time interval as more gas is heated, with a break at $\delta t_{\rm J,min} = 3 \times 10^7\,{\rm yr}$. As the jets fragment to form bubbles within the IGM and no longer escape the group, they interact with and compress more gas, colling it, and resulting in star formation through positive feedback. Interestingly, with longer time intervals the wind radius, BH mass and total stellar mass come into close agreement with RV simulations as jets act more like bubbles and the wind particles cease establishing flows within the gas.

Moving on to the intermediate mass LC object, the gas also shows a bunching of profiles (Fig. 5.20) rather than a gradual variation for all duty-cycle values, except for the two largest which show very similar variations. In this object, increasing the duty-cycle *decreases* the entropy of the cluster within $0.2\,r_{500}$ and shows a corresponding density increase. This can be explained with the aid of the rendered image, which shows that in the LC object does not clear out a chimney for any time interval value (Fig. 5.14). Therefore, only the BH wind in the lower duty-cycle simulations is able to escape the cluster core, whilst the less frequent (larger $\delta t_{\rm J,min}$) winds travel less far with median final ranges of $\sim 0.10\,r_{500}$ for $\delta t_{\rm J,min} = 3 \times 10^7, 1 \times 10^8\,{\rm yr}$ compared to r_{500} for the others (Fig. 5.16). Since the wind cannot influence the majority of the ICM, the total energy radiated from the clusters (not shown) is two to three times higher for the longer time interval simulations than the others (which radiate $3 \times 10^{61}\,{\rm erg}$). Therefore, as the BH mass stays roughly constant for varying time interval, the energy loss is not balanced and so the reduced radius of the wind (combined with the effect of positive feedback) causes

the increased central density. The star formation does not directly reflect the effects of this cooling, instead following the same pattern as the GG object; the total stellar mass decreases with increasing time interval with a break at $\delta t_{\rm J,min} = 3 \times 10^7$ yr as jets become confined. This shows that the level of central heating is important for determining the level of star formation in the cluster.

Finally we discuss the effects of varying the jet duty-cycle in the most massive object, HC. We do not show the final entropy or density profiles for this object as they show no variation. The total star formation (Fig. 5.16) is similarly unaffected, however the BH mass shows a low-level effect similar to that seen in the RV simulations with a very slight systematic increase. The higher star formation in the longer time interval simulations is again due to the effect of positive AGN feedback.

5.3.3 Summary from feedback time intervals

Beginning with the RV simulations, we find that increasing the time interval between jet heating events means that the feedback winds interact with more gas as the bubbles are larger and hotter. This particularly enhances the effectiveness of feedback on the GG IGM, resulting in significantly higher entropies and lower densities which slows the star formation in the group. The gas in the LC object shows the same patterns with increasing time interval, however the HC object shows no variation.

The impact of varying the time interval on the BH mass is less straight-forward to interpret, however each object is affected by a balance of the AGN warming the central gas and the creation of in-falling dense clumps seeded by more powerful outflows. This balance is particularly important in the GG object which has the shortest cooling time. For the LC object, only the longest feedback time intervals impact on the profiles and the HC object does not show any changes, although the star formation and BH growth in both are influenced by the length of the duty-cycle. The LC object is particularly sensitive to how far the feedback winds travel within the ICM and how much gas is disturbed as they travel. Due to the dual effects of the feedback heating and causing the gas to cool, stronger feedback can in some cases result in *higher* star formation through positive AGN feedback. This phenomenon is a main cause of star formation in the HC object as the cooling time is otherwise too long for meaningful star formation.

We now move on to consider the FV jet simulations with varying AGN radio duty-cycles. The GG/LC objects show the same pattern in gas property profiles as for the RV models, but the variation with increasing interval length is less gradual. Rather than seeing an increasing degree of influence with successive values, no changes in the profiles are seen except for the longest interval lengths (although the HC object still shows no

changes). As found in Section 5.2 for narrow jets, this is because the more frequent time intervals form stable flows which escape the cluster without depositing all their energy whereas the intermittent feedback bubbles mix up and interact with more gas as they follow less well-defined paths.

As for the RV simulations, we find less massive GG BHs in simulations with longer time intervals. This is because the gas local to the BH (from which it accretes) gathers predominantly through the smooth accretion of gas, which narrower jets interact with less and allow more gas to cool. The same trend is seen for stellar mass until long duty-cycle feedback forms bubbles and drive positive feedback. This again becomes the predominant source of star formation in the higher mass (LC and HC) objects.

For longer time intervals, the wind can no longer form a steady flow through the ambient gas away from the AGN and the jets break up into bubbles. In the GG object this typically results in more effective heating as the power output is higher, however in the higher mass objects, the AGN winds travel less far and heat less effectively. The growing similarity to bubbles with increasing duty-cycle is also shown by the similar levels of star formation and BH growth in the FV and RV simulations.

5.4 Varying the feedback efficiencies

The final aspects of the model we investigate are the assumed feedback efficiencies. For simplicity we have so far chosen to set the feedback coupling efficiencies for both the quasar and radio modes at the plausible values $\epsilon_{\rm f} = \epsilon_{\rm m} = 0.15$ (Sijacki et al. 2007 and Booth & Schaye 2009) in our fiducial model. However, the appropriate values of these parameters are not known, due to both physical and numerical uncertainty. For example, energy may be lost to radiation at an artificially high rate in simulations, due to poor resolution. Observations show that mechanical jets are highly efficient, and that a low (Cavagnolo et al. 2010) or negligible (McNamara & Nulsen 2007) fraction of energy is lost to radiation. It is therefore plausible that the mechanical coupling efficiency can be as high as 100 per cent. The radiative coupling efficiency is also constrained by models, and is thought have values in the range 10 to 20 percent (e.g. Shakura & Sunyaev 1973; Yu & Tremaine 2002).

We therefore perform simulations in each of our group and cluster objects with different assumed efficiencies, see Table 5.3 for a full listing of the models simulated in each of the GG, LC and HC objects. Simulations are performed using both isotropic heating and the fiducial jet geometry for models in which we vary one efficiency parameter at a time from the standard set.

Table 5.3: Model parameters for hybrid anisotropic simulations investigating varying the feedback efficiency parameters where we indicate simulations using the fiducial assumed efficiencies in bold. The first column gives the BH vector type where F stands for fixed vector and R for randomly re-orienting. Columns 2-4 give the AGN feedback efficiencies whilst columns 5-7 define the minimum number of particles heated and the geometry of the jet and the final column lists the minimum radio feedback duty cycle (where applicable).

BH vector	$\epsilon_{\rm r}$	$\epsilon_{\rm f}$	$\epsilon_{\rm m}$	$N_{\rm heat}$	$r_{\rm J,min}$ [kpc]	$\theta_{\rm J}$	$\delta t_{\rm J,min}$ [yr]
F	0.10	0.05	0.15	10	0	180°	–
F	**0.10**	**0.15**	**0.15**	**10**	**0**	**180°**	–
F	0.10	0.25	0.15	10	0	180°	–
F	0.10	0.15	0.25	10	0	180°	–
F	0.10	0.15	0.50	10	0	180°	–
F	0.10	0.15	1.00	10	0	180°	–
R	0.10	0.05	0.15	10	0	10°	–
R	**0.10**	**0.15**	**0.15**	**10**	**0**	**10°**	–
R	0.10	0.25	0.15	10	0	10°	–
R	0.10	0.15	0.25	10	0	10°	–
R	0.10	0.15	0.50	10	0	10°	–
R	0.10	0.15	1.00	10	0	10°	–
F	0.10	0.05	0.15	10	0	10°	–
F	**0.10**	**0.15**	**0.15**	**10**	**0**	**10°**	–
F	0.10	0.25	0.15	10	0	10°	–
F	0.10	0.15	0.25	10	0	10°	–
F	0.10	0.15	0.50	10	0	10°	–
F	0.10	0.15	1.00	10	0	10°	–

We begin by performing simulations with isotropic feedback in order to provide the most straightforward comparison with earlier work.

5.4.1 Isotropic hybrid feedback

Each simulated group/cluster object will be discussed in turn, beginning with the analysis of the GG object simulations.

The final entropy (top row) and density (bottom row) profiles of the GG object simulated with different mechanical (left) and radiative (right) coupling efficiencies are shown in Fig. 5.21. The entropy increases and density decreases throughout the object for increasing $\epsilon_{\rm m}$, as the AGN outflows deposit more energy and redistribute more gas. However, varying the quasar mode efficiency ($\epsilon_{\rm f}$) does not have as pronounced an affect on the group as this mode accounts for only ~ 10 per cent of the energy emitted from the AGN (for fixed $\epsilon_{\rm m}$). Increasing its value slightly *lowers* the entropy between 0.1 and $1\,r_{500}$, warms the core and *increases* the core density. We now go on to investigate the cause of

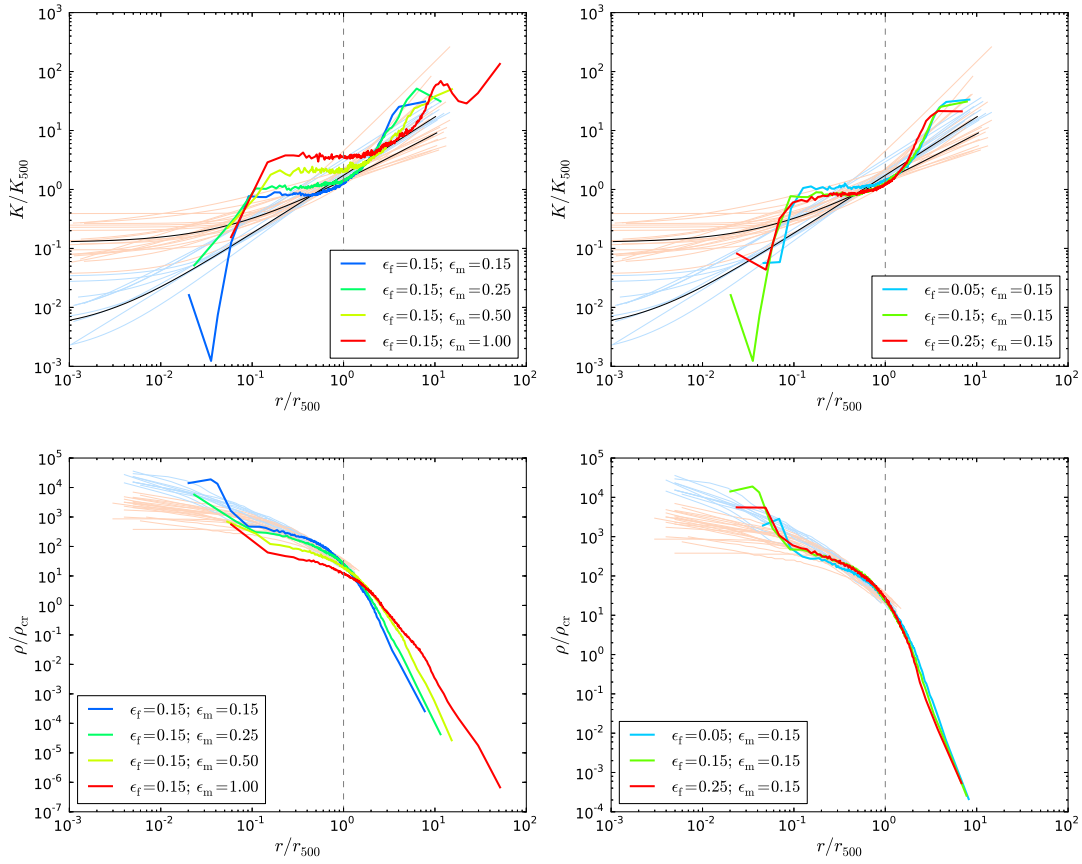

Figure 5.21: Final entropy (top row) and density (bottom row) profiles for the GG object simulated with the isotropic hybrid AGN feedback model with different mechanical (left) and feedback coupling (right) efficiencies.

this effect.

We present in Fig. 5.22, the final BH masses for simulations of hybrid feedback with different mechanical (top) and radiative feedback coupling (bottom) efficiencies in the GG (left panel), LC (centre panel) and HC (right panel) objects. Increasing ϵ_m gives the expected trend for higher entropy gas which results in lower accretion leading to lower final BH masses. Closer inspection of the BH mass evolution is given in Fig. 5.23 which indicates if an individual time-step is depositing feedback in the quasar mode in the top panels, the centre panels show the accretion rate in Eddington units and the bottom panels show the normalised integrated mass for simulations of the isotropic hybrid AGN feedback model using different mechanical (left) and radiative feedback (right) coupling efficiencies. As in the IGM profiles, very little effect is seen for varying ϵ_f. This is despite the AGN often depositing energy via the quasar mode. Similarly, the star formation shows a strong dependence on ϵ_m and almost none on ϵ_f; the total stellar masses are shown for different feedback efficiencies in Fig. 5.24 (otherwise plotted as in Fig. 5.22). Increasing

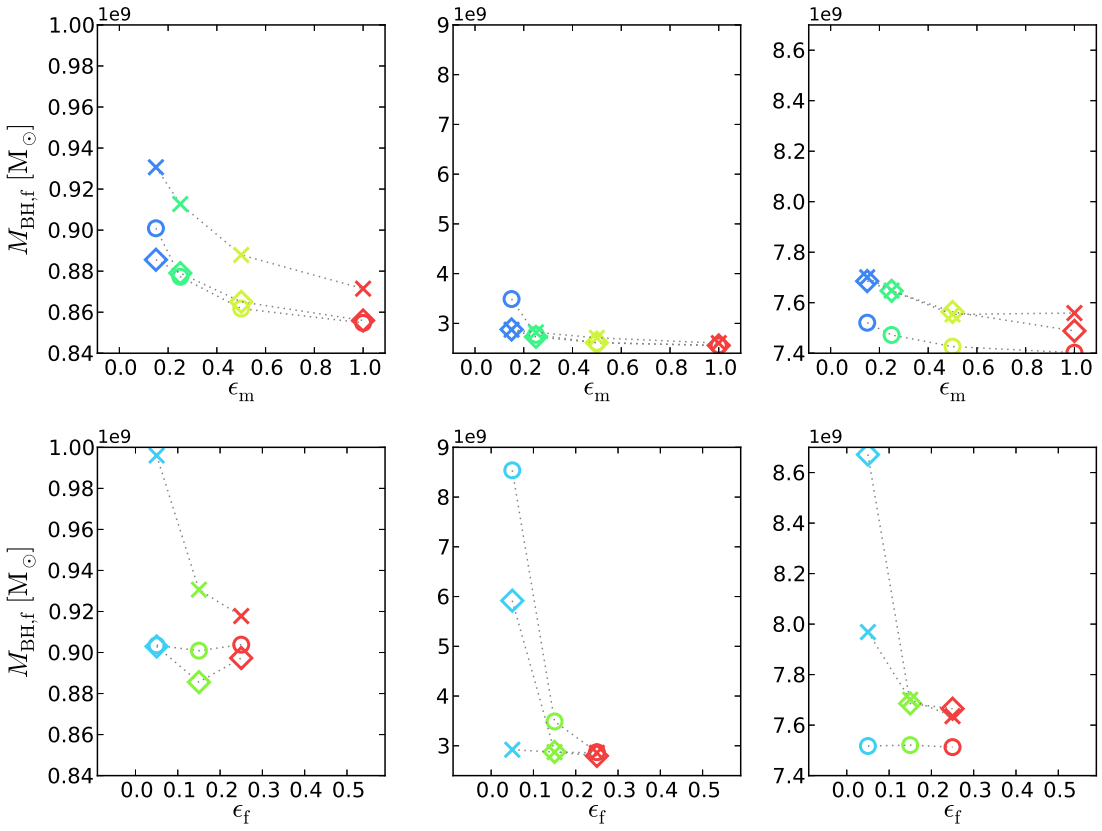

Figure 5.22: Final BH mass for simulations of hybrid feedback with different mechanical (top) and radiative feedback coupling (bottom) efficiencies in the GG (left panel), LC (centre panel) and HC (right panel) objects. Diamonds and crosses indicate simulations with randomly re-orienting and fixed BH jet vectors respectively whilst circles indicate isotropic feedback.

the mechanical efficiency gives a clear trend towards decreasing stellar mass as the more powerful AGN heats the gas. However, we find a weak increase for varying $\epsilon_{\rm f}$.

Therefore increasing the radiative feedback efficiency in this object produces the opposite to the expected outcome, slightly cooling the gas and forming more stars whilst not affecting the BH mass.

The integrated energy emitted from the group/cluster gas (solid lines) and the AGN via the quasar (dotted) and radio (dot-dashed) modes (the sum as a dashed line) is shown in Fig. 5.25 for the GG and LC objects in the left and right panels respectively. The weaker quasar mode at early times for the $\epsilon_{\rm f} = 0.05$ GG simulation allows a slight increase in energy emitted via the radio mode at $t \approx 1\,{\rm Gyr}$ which lowers the energy radiated from the cluster by a large degree for several $\rm Gyr$. This then is the cause of the lowest efficiency quasar-mode having the largest affect over the gas, causing the reduction (increase) in density (entropy) over the majority of the group as less gas cools into the central region.

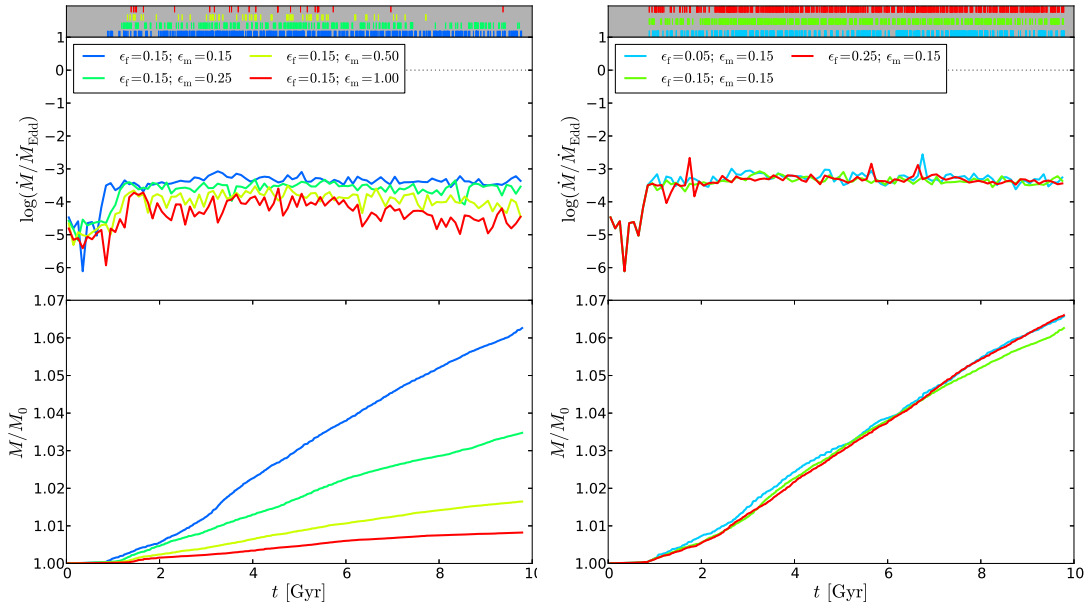

Figure 5.23: BH mass evolution for the GG object simulated with the isotropic hybrid AGN feedback model with different mechanical (left) and feedback coupling (right) efficiencies. The top panels indicate if an individual time-step is depositing feedback in the quasar mode, the centre panels show the accretion rate in Eddington units and the bottom panels show the normalised integrated mass.

Although this effect does not explain the deviation in the core, this is a very small-scale effect which is highly sensitive to numerical noise and centring errors.

We now analyse the effect of varying the feedback efficiencies in the intermediate mass, LC, object beginning with the impact on the cluster gas as shown in Fig. 5.26; the final entropy (top row) and density (bottom row) profiles. It is apparent that the LC object shows much less variation than the group, as was found when investigating the other model parameters. Varying the mechanical efficiency introduces changes to the final central entropy profiles within $0.05\,r_{500}$, where we find an entropy increase for larger $\epsilon_{\rm m}$ values. The final density shows corresponding changes, where the higher entropy cores also have lower gas densities, leading to associated drops in star formation (Fig. 5.24). Varying $\epsilon_{\rm f}$ (relating to the quasar mode) affects the entropy in the same core area, however in a much weaker fashion and does not impact on the density in any significant way. Although this parameter does affect the entropy profiles, they do not show a clear progression with increasing radiative feedback efficiency. Despite this, the star formation shows a weak trend for reducing for larger values of this parameter as the small-scale cold knot is warmed more effectively by the more powerful quasar.

We now consider the BH mass evolution in this (the LC) object, as shown in Fig. 5.27,

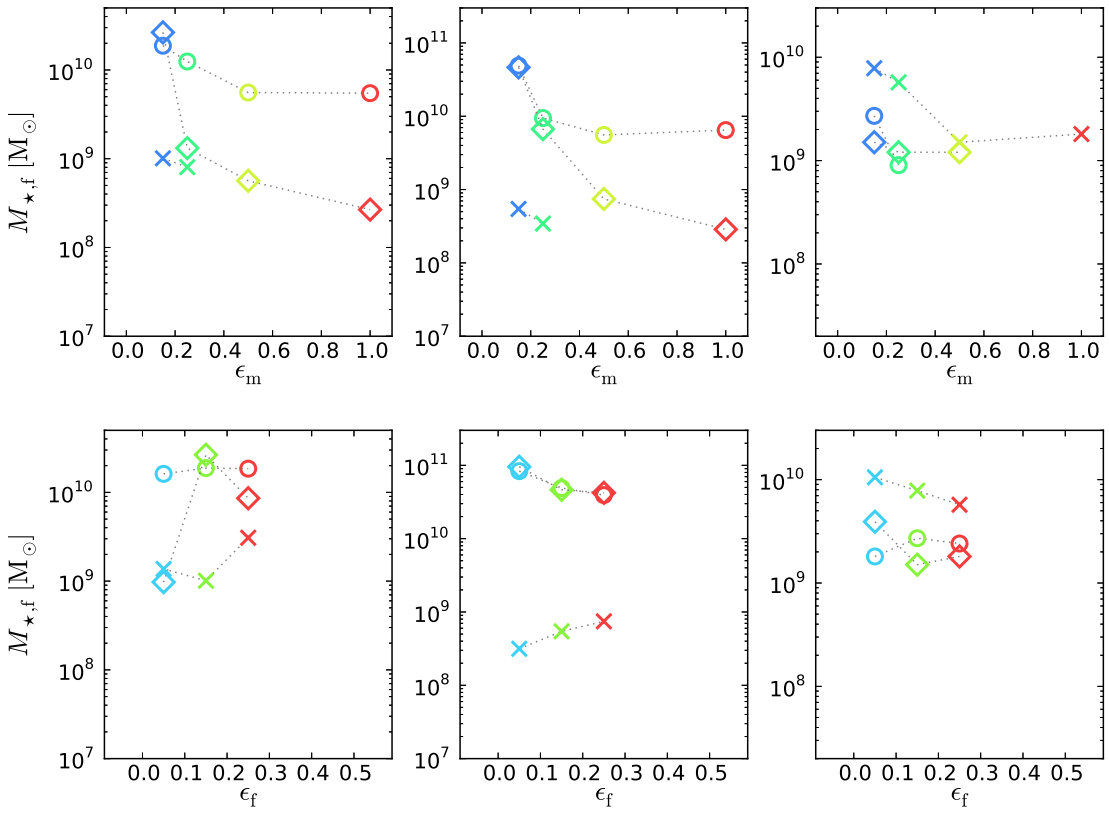

Figure 5.24: Total stellar mass formed for simulations of hybrid feedback with different mechanical (top) and radiative feedback coupling (bottom) efficiencies in the GG (left panel), LC (centre panel) and HC (right panel) objects. Diamonds and crosses indicate simulations with randomly re-orienting and fixed BH jet vectors respectively whilst circles indicate isotropic feedback.

where we indicate if an individual time-step is depositing feedback in the quasar mode in the top panels, the centre panels show the accretion rate in Eddington units and the bottom panels show the normalised integrated mass for simulations varying ϵ_m and ϵ_f (in the left and right panels respectively). Models with larger mechanical coupling efficiencies give progressively lower final BH masses (see also Fig. 5.22), with the largest change seen when increasing the parameter from $\epsilon_\mathrm{m} = 0.15$ to 0.25; the same simulations which show the largest change in entropy. Correspondingly, this results in less quasar-mode accretion which begins progressively later for larger mechanical efficiencies. We note that, in a departure from the usually steady accretion, the BH in the $\epsilon_\mathrm{m} = 0.15$ simulation undergoes a burst of growth at late times which results in the AGN spending nearly $2\,\mathrm{Gyr}$ in the quasar mode. This shows that the lower amount of feedback energy released in this model was unable to prevent the density building and catastrophic cooling occurring. Now considering the efficiency of feedback released via the quasar mode, we find that increasing ϵ_f also

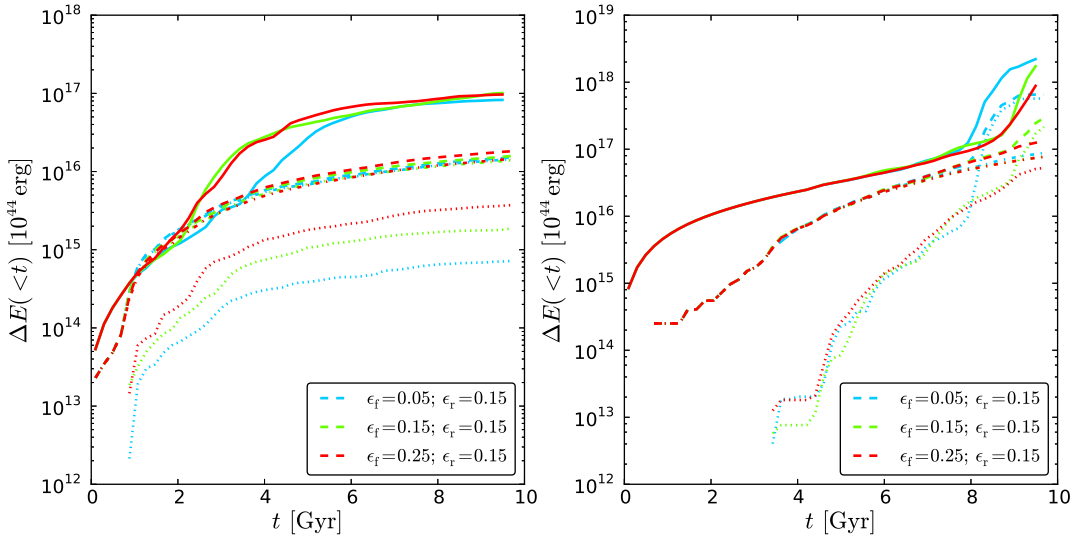

Figure 5.25: Integrated energy emitted from the group/cluster gas (solid lines) and the AGN via the quasar (dotted) and radio (dot-dashed) modes (the sum is shown dashed) for the GG and LC objects in the left and right panels respectively.

reduces the BH mass but without significantly modifying the accretion mode. The burst seen at late times is stronger (suppressed) for less (more) efficient feedback. Therefore the BH mass shows no clear evidence for the unusual trend for these simulations seen in the ICM profiles.

In an attempt to understand the response of the cluster gas to increased radiative efficiency, we (as for the GG object) turn to analysis of the gas and AGN radiated energies. We find that the integrated energy emitted by the AGN in these simulations too shows an unusual trend, as the $\epsilon_{\rm f} = 0.05$ simulation radiates the most followed by the $\epsilon_{\rm f} = 0.15$ and 0.25 simulations. This occurs as the more powerful quasar mode feedback is able to prevent a late-time cooling flow from establishing until later in the simulation. The higher (lower) core entropy (density) for the $\epsilon_{\rm f} = 0.05$ simulation is then due to the simulation ending (and the profiles being observed) shortly after a powerful episode of AGN feedback occurs, brought on by the surge in BH growth as gas cools rapidly. Likewise, the LC simulation has the lowest entropy as the gas luminosity has only just begun to spike due to the gas cooling on to the core, and feedback has not yet responded. However, we again caution that the changes in the core region are highly sensitive to noise and so this change may not be representative.

As in previous investigations, the HC object gas profiles are largely unaffected by modifying the feedback parameters and so are not shown. There is, however, a small effect whereby increasing the mechanical efficiency gives a factor of ~ 2 increase in central

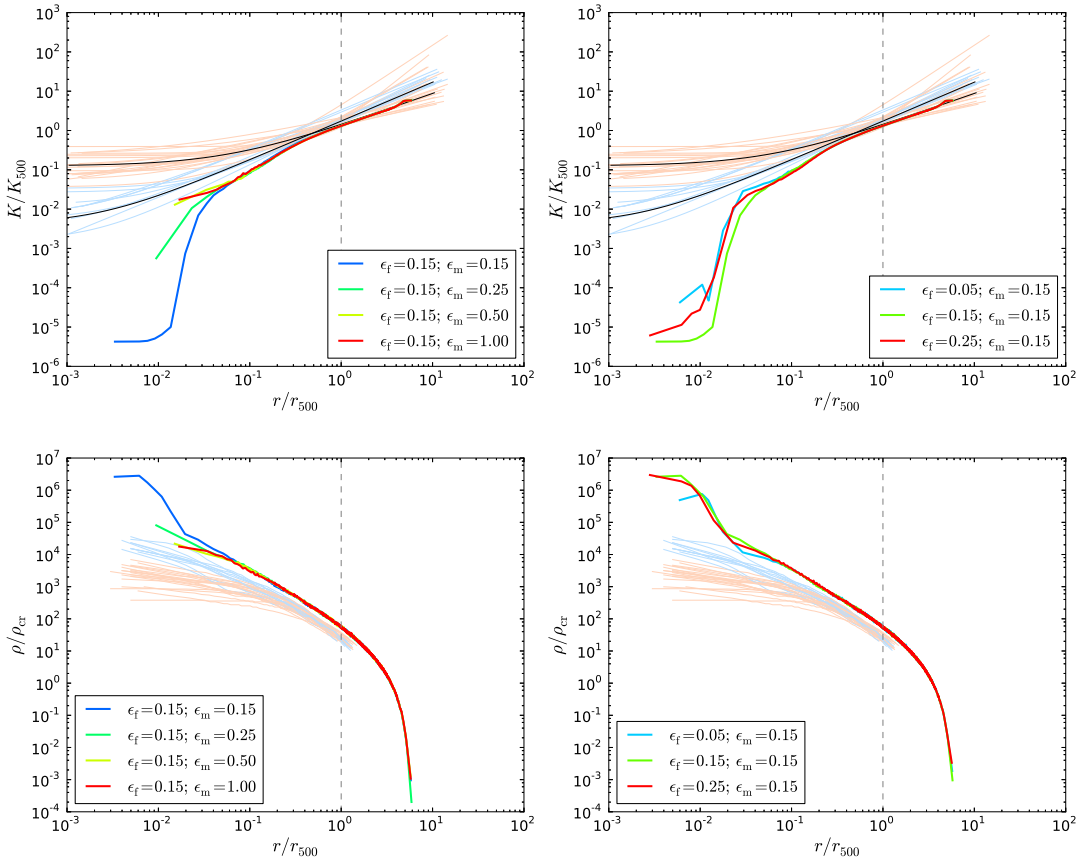

Figure 5.26: Final entropy (top row) and density (bottom row) profiles for the LC object simulated with the isotropic hybrid AGN feedback model with different mechanical (left) and feedback coupling (right) efficiencies.

entropy between the extreme values. Likewise, we do not show detailed BH evolution plots because the small differences are captured by the final mass, Fig. 5.22. We find that increasing the mechanical efficiency, $\epsilon_{\rm m}$, between the extreme values lowers the final BH mass by only $\sim$ 1 per cent and changing $\epsilon_{\rm f}$ has no effect whatsoever. Varying the mechanical and feedback efficiencies can vary the final stellar masses by factors of a few (Fig. 5.24), and although there are insufficient data points to make a strong statement due to the level of scatter, they are consistent with a reduced mass for larger values of either efficiency. The integrated energy emitted from the BHs and ICM in the HC (not shown) are also near-identical for different efficiency parameters, further showing that varying this model choice does not significantly impact on the cluster.

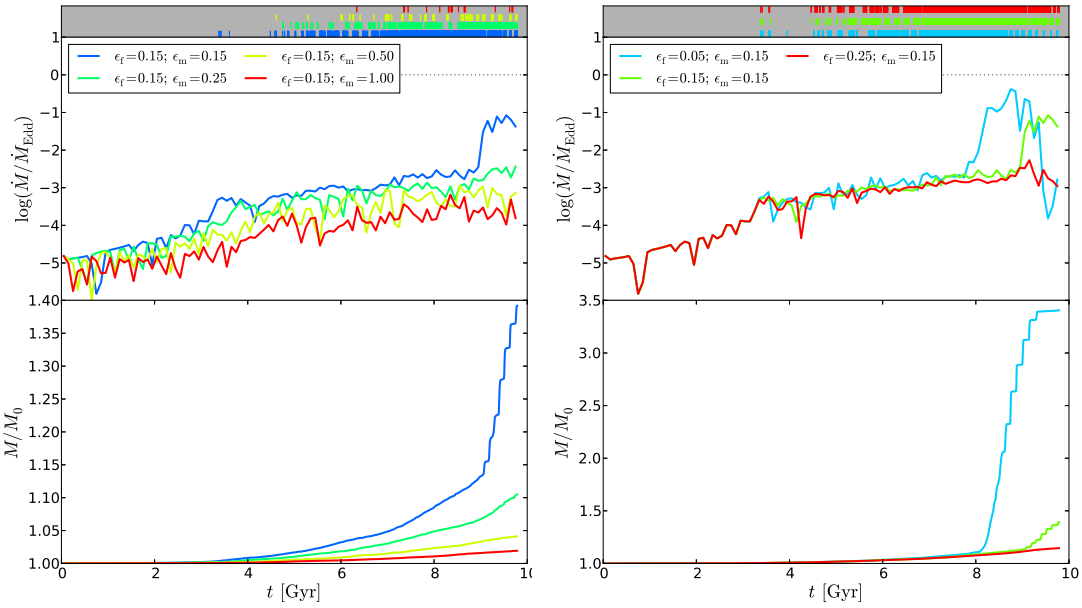

Figure 5.27: BH mass evolution for the LC object simulated with the isotropic hybrid AGN feedback model with different mechanical (left) and feedback coupling (right) efficiencies. The top panels indicate if an individual time-step is depositing feedback in the quasar mode, the centre panels show the accretion rate in Eddington units and the bottom panels show the normalised integrated mass.

5.4.2 Anisotropic hybrid feedback

Having investigated the effects of varying the efficiency parameters in the most simple assumed geometry, we may now go on to perform an analysis for anisotropic heating. We again utilise the fiducial jet geometry, for which we perform simulations with both a randomly re-orienting and fixed jet in each of the group and cluster objects (see Table 5.3).

Random jet vector

We show in Fig. 5.28 the final entropy (top row) and density (bottom row) profiles for the GG object simulated with the fiducial anisotropic hybrid RV AGN feedback model with different mechanical (left column) and radiative (right column) feedback efficiencies. As in the isotropic feedback models, we see an entropy increase and density decrease in the central regions for higher $\epsilon_{\rm m}$ values; overall redistributing more gas than the isotropic feedback models. Similarly, the entropy increase is stronger in these simulations and the variation between profiles less predictable; the $\epsilon_{\rm m} = 0.50$ and 1.00 simulations have very similar final profiles. Broadly, the increase in gas entropy results in lower star formation (Fig. 5.24), and an identical trend for reducing final BH mass as in isotropic simulations (Fig. 5.22). The similarity between the largest value simulations may be linked to the

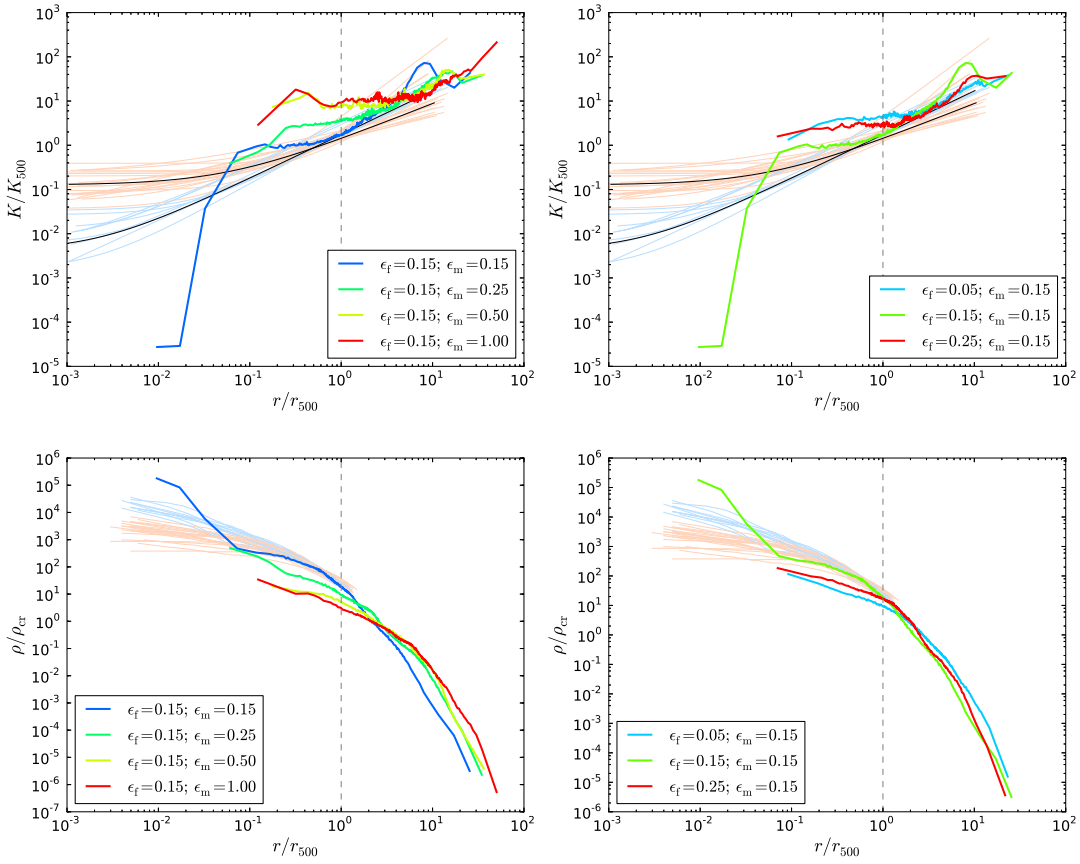

Figure 5.28: Final entropy (top row) and density (bottom row) profiles for the GG object simulated with the fiducial anisotropic hybrid RV AGN feedback model with different mechanical (left column) and radiative (right column) feedback efficiencies.

saturation of deposited energy we first discussed in Section 5.3.

Varying the quasar-mode efficiency, ϵ_f, too has more of an impact on gas profiles (Fig. 5.28) than in the isotropic feedback case. Counter-intuitively, both increasing *and* decreasing the efficiency from the fiducial value gives a higher entropy core and redistributes more gas. Correspondingly, the star formation peaks in the fiducial simulation as its gas is more dense and cooler. The final BH mass shows little variation for different radiative coupling efficiencies, however it is also lowest for the fiducial model. Therefore the fiducial model has the smallest impact on its environment for varying ϵ_f.

We found in Section 5.4.1 that the final cluster profiles can be highly susceptible to apparently small changes in the amount of jet feedback deposited at early times in the simulation, and inspection of the deposited energies (not shown) for the GG object shows that this explains the unusual final gas profiles for the fiducial ($\epsilon_f = 0.15$) simulation. Depositing slightly more (two times) energy via the quasar mode at $t \sim 1.3\,\mathrm{Gyr}$ (the equivalent of enough energy to heat 100 extra particles to T_{crit}) lowers the cooling rate

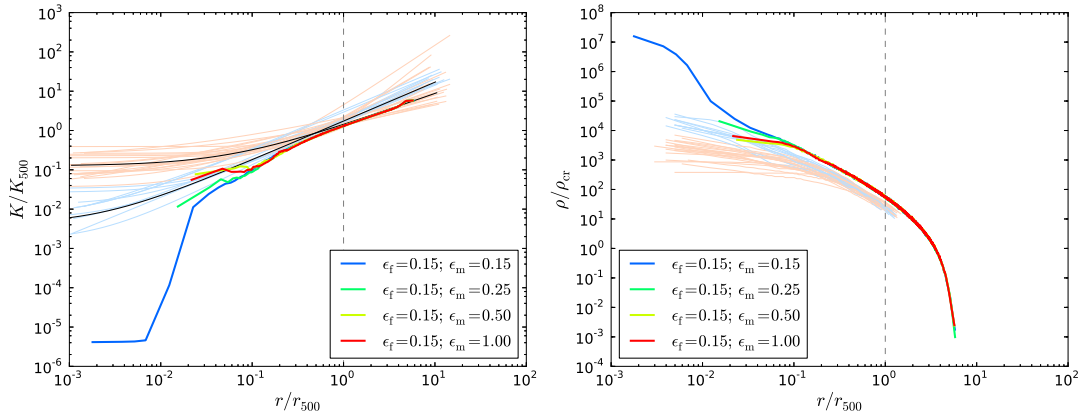

Figure 5.29: Final entropy (left panel) and density (right panel) profiles for the LC object simulated with the fiducial anisotropic hybrid RV AGN feedback model with different mechanical efficiencies.

onto the BH and accordingly the radio luminosity which then becomes the lowest by $t \sim 4\,\mathrm{Gyr}$; this allows the cluster to radiate more energy ($1.6 \times 10^{61}\,\mathrm{erg}$ compared to $4.0 \times 10^{59}\,\mathrm{erg}$ and $3.7 \times 10^{60}\,\mathrm{erg}$ for the $\epsilon_\mathrm{f} = 0.05$ and $\epsilon_\mathrm{f} = 0.25$ simulations respectively) and become more dense at late-times.

Fig. 5.29 shows the final entropy (left panel) and density (right panel) profiles for the LC object simulated with the fiducial anisotropic hybrid RV AGN feedback model utilising different mechanical feedback efficiencies. We do not show the profiles for the simulations varying the radiative feedback efficiency as they exhibit very little variation in this object. However, as we have previously found, the ICM entropy has higher and reduced density profiles for larger ϵ_m values as the radio jets are more powerful. The variation between simulations is, as for the GG object, less linear than for isotropic feedback, as the simulations using the largest efficiencies ($\epsilon_\mathrm{m} = 0.50$ and 1.00) are similar to one another but unlike the other simulations.

Increasing the mechanical feedback shows a clear trend for lowering the stellar mass formed, more effectively than for the isotropic case, causing a reduction of two orders of magnitude (Fig. 5.24). Although the binned gas profiles are unaffected by the choice of (ϵ_f) value, the star formation is slightly reduced with increasing radiative feedback coupling efficiency. This behaviour in stellar mass is identical to the trend and values found for the equivalent isotropic feedback simulations. This is because both the quasar mode feedback and the star formation are centrally concentrated.

Increasing the mechanical feedback coupling efficiency, ϵ_m, gives lower final BH masses (Fig. 5.22) with a trend identical to the isotropic simulations (as in the GG object) although the fiducial simulation deviates from this, giving a slightly reduced final

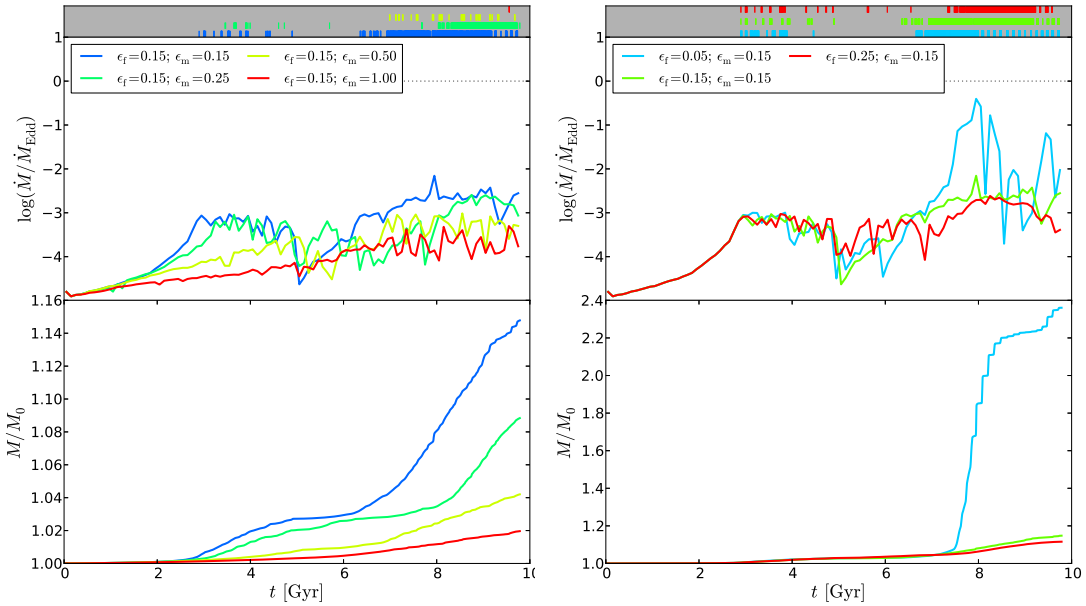

Figure 5.30: BH mass evolution for the LC object simulated with the fiducial anisotropic hybrid RV AGN feedback model with different mechanical (left) and feedback coupling (right) efficiencies. The top panels indicate if an individual time-step is depositing feedback in the quasar mode, the centre panels show the accretion rate in Eddington units and the bottom panels show the normalised integrated mass.

mass. For the radiative feedback efficiency, $\epsilon_{\rm f}$, we find a large discrepancy in final BH mass for the lowest efficiency simulation. The BH in this model has a greatly increased mass despite remarkably similar density and entropy profiles; we therefore examine this in more detail.

Fig. 5.30 shows the BH mass evolution in the LC object for varying mechanical (left) and radiative (right) feedback efficiencies. The mass evolution for the $\epsilon_{\rm f} = 0.05$ simulation shows that the large difference between the final mass is caused by a late surge in accretion due to an influx of cooling gas; the same feature as was found in the isotropic feedback simulations. This, combined with the relative inability of the weaker quasar-mode feedback to disrupt the cold knot, gives rise to a significantly larger final BH mass.

The final RV models we discuss in this section concern the high mass cluster (HC) simulated with different feedback efficiencies. We present in Fig. 5.31 the final entropy (left panel) and density (right panel) profiles for the HC object simulated with the fiducial anisotropic hybrid RV AGN feedback model with different mechanical feedback efficiencies. We do not show the profiles for the simulations varying the radiative feedback efficiency as they show very little variation. However, increasing the mechanical efficiency does have a weak effect within $0.1\,r_{500}$ where it increases the entropy and lowers the den-

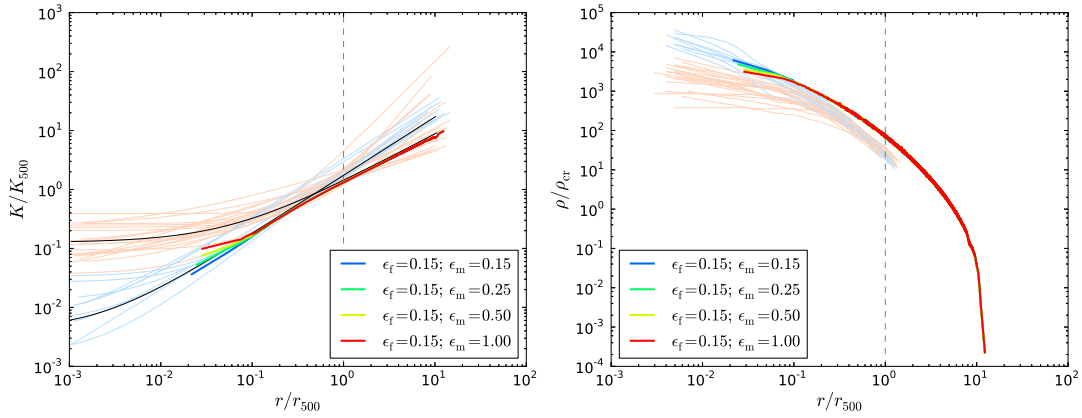

Figure 5.31: Final entropy (left panel) and density (right panel) profiles for the HC object simulated with the fiducial anisotropic hybrid RV AGN feedback model with different mechanical efficiencies.

sity; this is in contrast to the isotropic model which showed only a very slight difference. Accordingly, the impact on the cluster results in a weak trend for reducing stellar mass with increasing $\epsilon_{\rm m}$ value (Fig. 5.24). The radiative feedback efficiency, $\epsilon_{\rm f}$, shows no clear trend in stellar mass as the highest efficiency simulation yields a similar (slightly larger) stellar mass to the fiducial model; however it is clear that the lowest efficiency model results in significantly more stars forming, which is due to the lower level of central heating in this simulation.

The final BH mass (Fig. 5.22) shows the same trends with varying mechanical efficiency as the isotropic feedback simulations but with a systematically slightly higher mass. Increasing $\epsilon_{\rm f}$ leads to a decrease in BH mass in this object as it warms the local area of the ICM. The combination of systematically higher masses in anisotropic feedback simulations, and the above shows that the BH is still accreting from spurious cold blobs despite the quasar feedback, but also that they are disrupted with increasing success by the quasar mode with higher efficiencies.

Fixed jet vector

We now move on to discuss simulations of the FV hybrid AGN feedback model performed with varying feedback efficiencies in each of the simulated objects.

Beginning with the GG object, we present the final entropy (top row) and density (bottom row) profiles for the GG object simulated with the fiducial anisotropic hybrid FV AGN feedback model with different mechanical (left) and feedback coupling (right) efficiencies in Fig. 5.32. Raising the mechanical feedback coupling efficiency, $\epsilon_{\rm m}$, continues

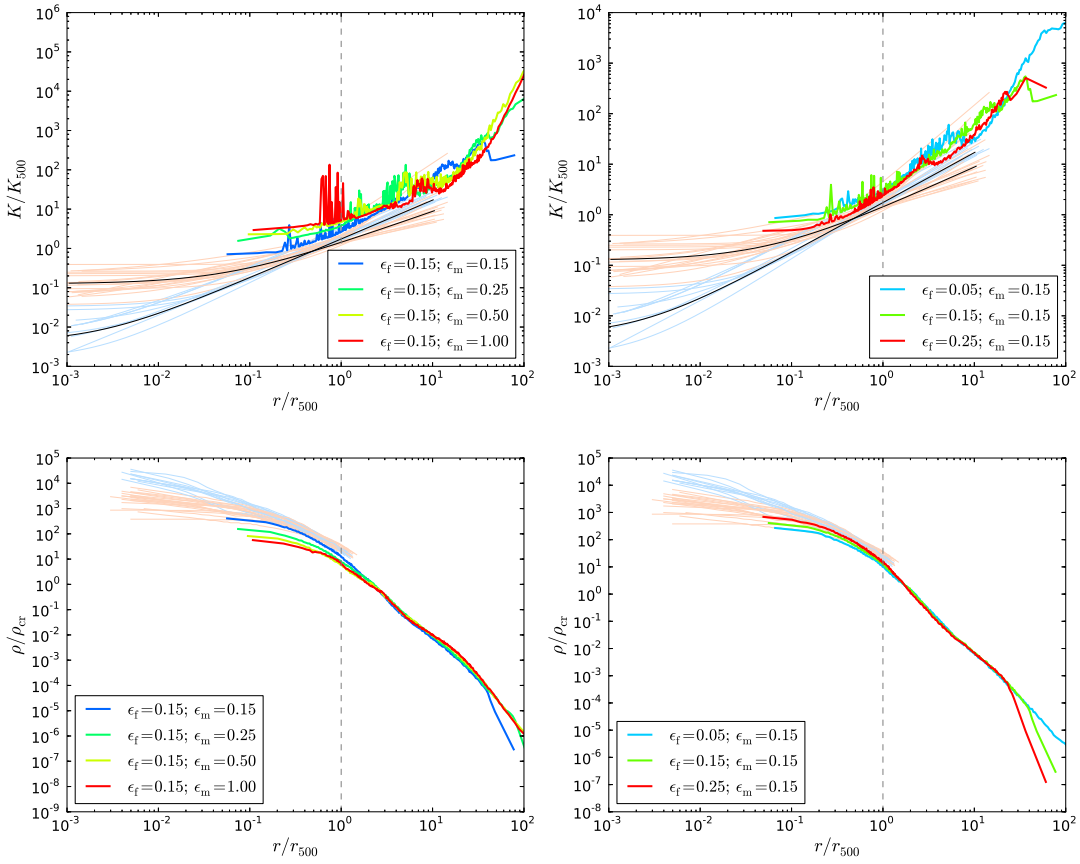

Figure 5.32: Final entropy (top row) and density (bottom row) profiles for the GG object simulated with the fiducial anisotropic hybrid FV AGN feedback model with different mechanical (left) and feedback coupling (right) efficiencies.

to result in a higher entropy as in the RV and isotropic feedback simulations. However in this case the trend is much weaker, causing an increase by only a factor of a few. Additionally, all of the profiles are similar except for lowest efficiency value, which is a factor of two lower and does not have as high entropy at the periphery. The decrease in density as a result of more effective feedback is also weaker, lowering by around an order of magnitude in the core. This in turn leads to a decrease in star formation (Fig. 5.24) which does not occur for high efficiencies as the feedback is very effective. In addition to the larger impact on the IGM, AGN with higher ϵ_m values give rise to more noisy entropy profiles, such is the contrast in temperatures with the concentrated wind particles.

As in the isotropic feedback simulation, increasing the ϵ_f value leads to *lower* central entropy values and allows for a higher final density, with less gas ejected out of the group (Fig. 5.32). The increase in low entropy gas in the group gives some evidence of a trend for a trend towards a slightly higher level of star formation, for larger radiative feedback coupling efficiencies, however the mass is slightly lower for the intermediate simulation

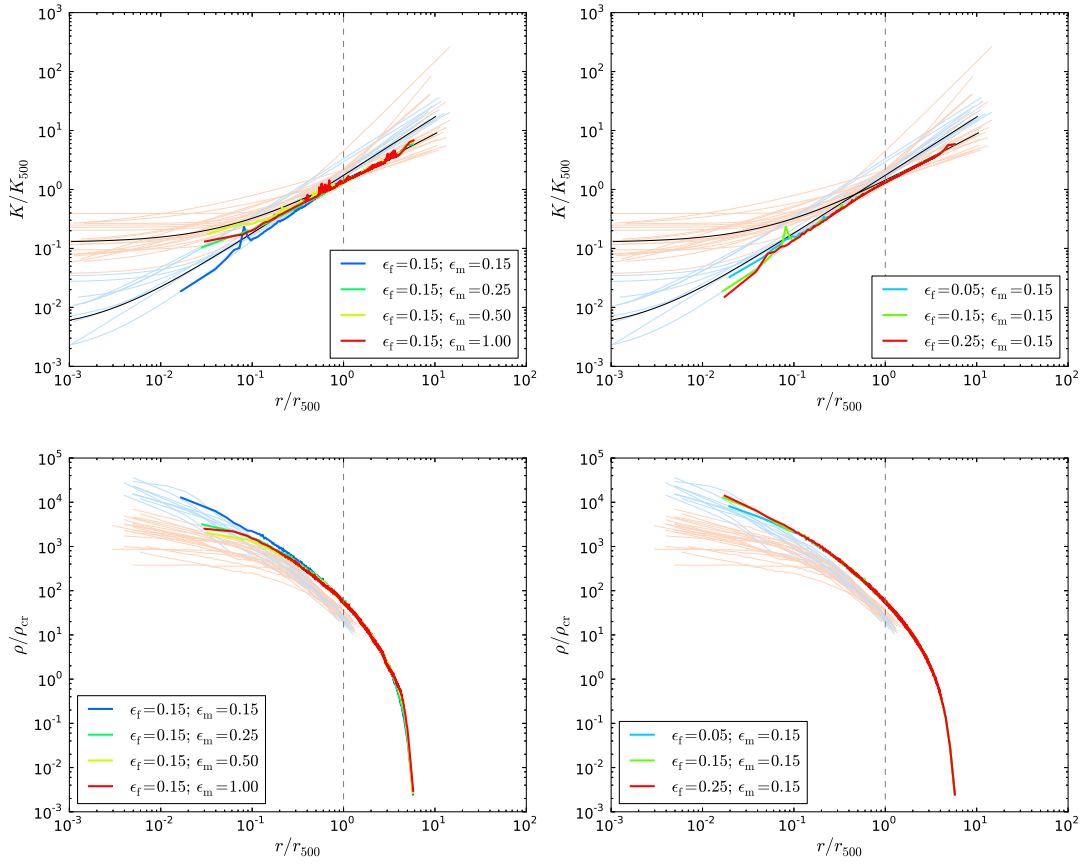

Figure 5.33: Final entropy (top row) and density (bottom row) profiles for the LC object simulated with the fiducial anisotropic hybrid FV AGN feedback model with different mechanical (left) and feedback coupling (right) efficiencies.

(Fig. 5.24).

The final BH masses reduce for increasing both feedback coupling efficiencies, this is illustrated in Fig. 5.22 by the cross symbols in the left column. The BH grows less in simulations with higher mechanical efficiency because the more powerful jets heats the IGM, lowers cooling onto the core, and accordingly the BH accretion rate. This yields masses very similar to the corresponding RV simulations. For increasing radiative coupling efficiency, the lower BH masses cannot also be due to the reduced large-scale cooling rates because the core is cooler (Fig. 5.32); therefore the reduction in BH mass is due to its influence on the localised cold blob around the BH. The smoothed accretion rates (not shown) are effectively capped at the critical rate (at which the quasar mode activates) for medium and high efficiency simulations showing that they warm and rarefy the blob, reducing the impact of spurious growth.

The effect of varying the radiative and mechanical feedback coupling efficiencies on the final entropy (top row) and density (bottom row) profiles, is shown in the left and right

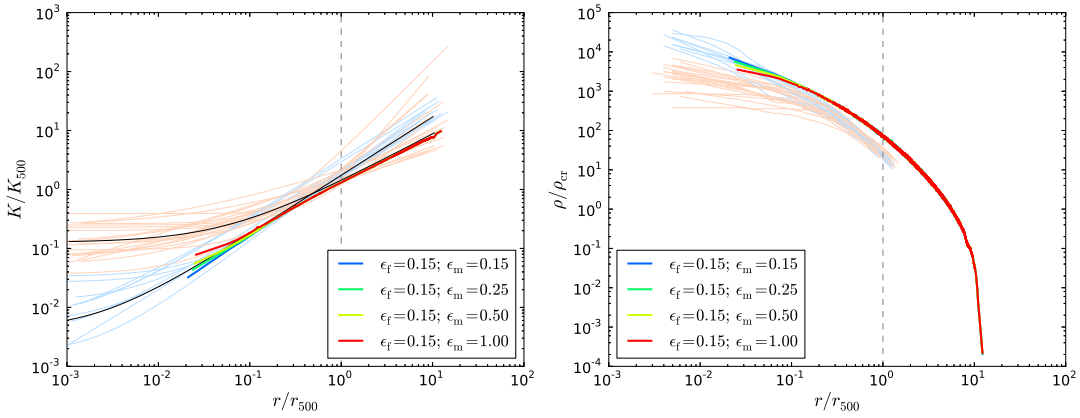

Figure 5.34: Final entropy (left) and density (right) profiles for the HC object simulated with the fiducial anisotropic hybrid FV AGN feedback model with different mechanical efficiencies.

columns of Fig. 5.33 respectively for the LC object simulated with the fiducial anisotropic hybrid FV AGN feedback model. Unlike in the RV and isotropic simulations, increasing the mechanical efficiency ($\epsilon_{\rm m}$) does not result in a simple trend in the entropy and density profiles when applied to a FV AGN. All parameter values give higher final entropy and lower density values than the fiducial set within $\sim 0.3\,r_{500}$ as expected for higher efficiencies, however we note that unusually the $\epsilon_{\rm m} = 0.5$ model (not 1.0) is marginally the most effective. The total star formation (Fig. 5.24) follows the same established trend and drops with increasing efficiency, resulting in neither of the two largest $\epsilon_{\rm m}$ simulations forming stars.

The final entropy density profiles for varying radiative coupling efficiency, $\epsilon_{\rm f}$, (Fig. 5.33; right column) show only a small impact. However, we find as in the lower mass object that increased quasar feedback efficiency acts to cool the core ($< 0.03\,r_{500}$) and increase the density with the fiducial and highest values giving very similar profiles. The total stellar masses formed during simulation (Fig. 5.24) does not show much variation, but shows a small increase with $\epsilon_{\rm f}$. The ~ 2 times higher energy input into the core region by the $\epsilon_{\rm r} = 0.25$ simulation AGN via the quasar mode cannot oppose this, as it provides a low absolute energy output (the radio mode supplies at least 10 times more energy).

The final BH masses (Fig. 5.22) in the LC object are reduced for larger values of either efficiency. The final masses themselves are similar to those in the corresponding RV simulations, except for the minimum $\epsilon_{\rm f}$ simulation which is three times lower and is now more in line with other data.

Therefore, we find that the choice of efficiency values are less important in the FV simulations for this object. This is because to the jet influences the cluster strongly, but only within a small solid angle. Most accretion, therefore, comes perpendicular to the

jet due to steady, gradual cooling as the gas has not been compressed by out-flowing winds. This means that the quasar mode is less important and accordingly so too is the radiative coupling efficiency. The mechanical efficiency too is of limited importance, because the gas which is affected by the jet is saturated by the powerful winds at relatively low efficiencies.

We present in Fig. 5.34 the final entropy (left panel) and density (right panel) profiles for the HC object simulated with the fiducial anisotropic hybrid FV AGN feedback model with different mechanical feedback efficiencies. Although the influence is not strong, we can see that increasing the mechanical coupling efficiency, $\epsilon_{\rm m}$, raises the entropy and lowers the density within $0.1\,r_{500}$. Correspondingly, the warmer and diffuse core forms less stars, leading to lower final stellar masses (Fig. 5.24). We note that this parameter is the first to significantly affect the HC gas. We do not plot the profiles for the simulations varying the radiative feedback efficiency as they show no variation. Despite showing no impact on the binned gas profiles, changing the radiative feedback efficiency follows the same trend in stellar mass formed as for $\epsilon_{\rm m}$, albeit to a less pronounced degree. Within these trends, the $\epsilon_{\rm m} = 0.50$ simulation stands out as it produces significantly less stars than would be expected. This is due to a spike in accretion at $t \sim 8\,{\rm Gyr}$ giving rise to a strong feedback episode, after which the cooling rate of the ICM is decreased.

The final BH masses, shown in Fig. 5.22, are lower for higher $\epsilon_{\rm m}$ values and yield values very similar to those found in the equivalent RV simulations. The masses are again similar to RV for the simulations varying $\epsilon_{\rm f}$, except for the minimum efficiency simulation which is now lower and more in line with other data.

5.4.3 Summary from varying feedback efficiencies

Varying the mechanical coupling efficiency, $\epsilon_{\rm m}$, follows the trends established in previous sections for increasingly powerful 'radio' AGN impacting on the group and cluster profiles; higher efficiency gives more powerful outflows which raise the entropy and lower the density. The effects are most prominent in the GG object, changing the profiles on all scales, whereas they only affect the LC core and do not influence the HC gas whatsoever. Similarly, we find for all objects that increasing this efficiency lowers the BH mass and star formation independent of the choice of isotropic or FV/RV jet geometries. This shows again that the 'strong' feedback has the largest effect on the gas in objects hosting an AGN. The degree of variation in the profiles is lower in the FV simulations where the excess energy escapes the GG more efficiently and interacts with less gas in the cluster objects, saturating its influence on the cluster. We also find striking agreement in the final BH masses obtained for different values of the mechanical efficiency for the RV and

isotropic feedback simulations.

Considering now the radiative feedback coupling efficiency, $\epsilon_{\rm f}$, we do not find trends which are so trivially understood. Counter-intuitively, raising the efficiency with which energy is liberated from matter accreted onto the BH heats its surroundings can *lower* the entropy and increase the density of the GG object. This is due to the high sensitivity of the group's cooling to the early radio feedback episodes which can be delayed and weakened by the more powerful quasar feedback. Such a delay then leads to higher levels of cooling overall as the gas becomes more dense and radiates more powerfully. In the LC object, the quasar-mode feedback is less important and varying the $\epsilon_{\rm f}$ produces only small changes which do not follow a simple pattern. The HC object, having a significantly deeper potential well and longer cooling time shows no changes. The quasar-mode efficiency in this model then has a relatively low impact on the group/cluster gas; however it is important for the BH mass. For larger efficiencies, the BH is more able to disperse the cold knot of gas which forms around the BH particle which reduces the impact of the spurious accretion.

We note more generally that the energy radiated by the cluster is highly sensitive to small changes in heating at early times, where small amounts of accreted mass can determine if the gas loses pressure support and collapses. We also note that due to the highly variable nature of the AGN, the final profiles can be sensitive to fluctuations in accretion and feedback rates leading to non-general conclusions. A study over a large cosmological volume would provide the statistics necessary to marginalise over this uncertainty.

5.5 Resolution study

In order to better understand the reliability of our findings, we now investigate the affect of simulating the hybrid AGN model at different resolution levels. To this end we perform additional low and high resolution simulations (as outlined in Table 4.4) for the isotropic feedback ($\theta_{\rm J} = 180\,^{\circ}$; $r_{\rm J,min} = 0$) as well as both the RV and FV fiducial jet ($\theta_{\rm J} = 10\,^{\circ}$; $r_{\rm J,min} = 0$) models. Furthermore, so as to understand whether or not the adopted fiducial resolution influenced the investigation into varying jet opening angle, we also simulated the ($\theta_{\rm J} = 5\,^{\circ}$; $r_{\rm J,min} = 0$) model at both higher and lower resolution.[3]

Fig. 5.35 shows the rendered gas density and entropy at $t = 5\,{\rm Gyr}$ for the GG and LC objects simulated at low (left panels) and high (right panels) resolutions for isotropic, RV and FV feedback top to bottom. Images show the projected density within slices of

[3]We keep the number of AGN-heated particles in a single feedback event ($N_{\rm heat}$) constant when varying the resolution. This in principle changes the mass-loading of the AGN winds, however as several heating events typically occur on a given time-step in these objects we do not expect the effect to be significant.

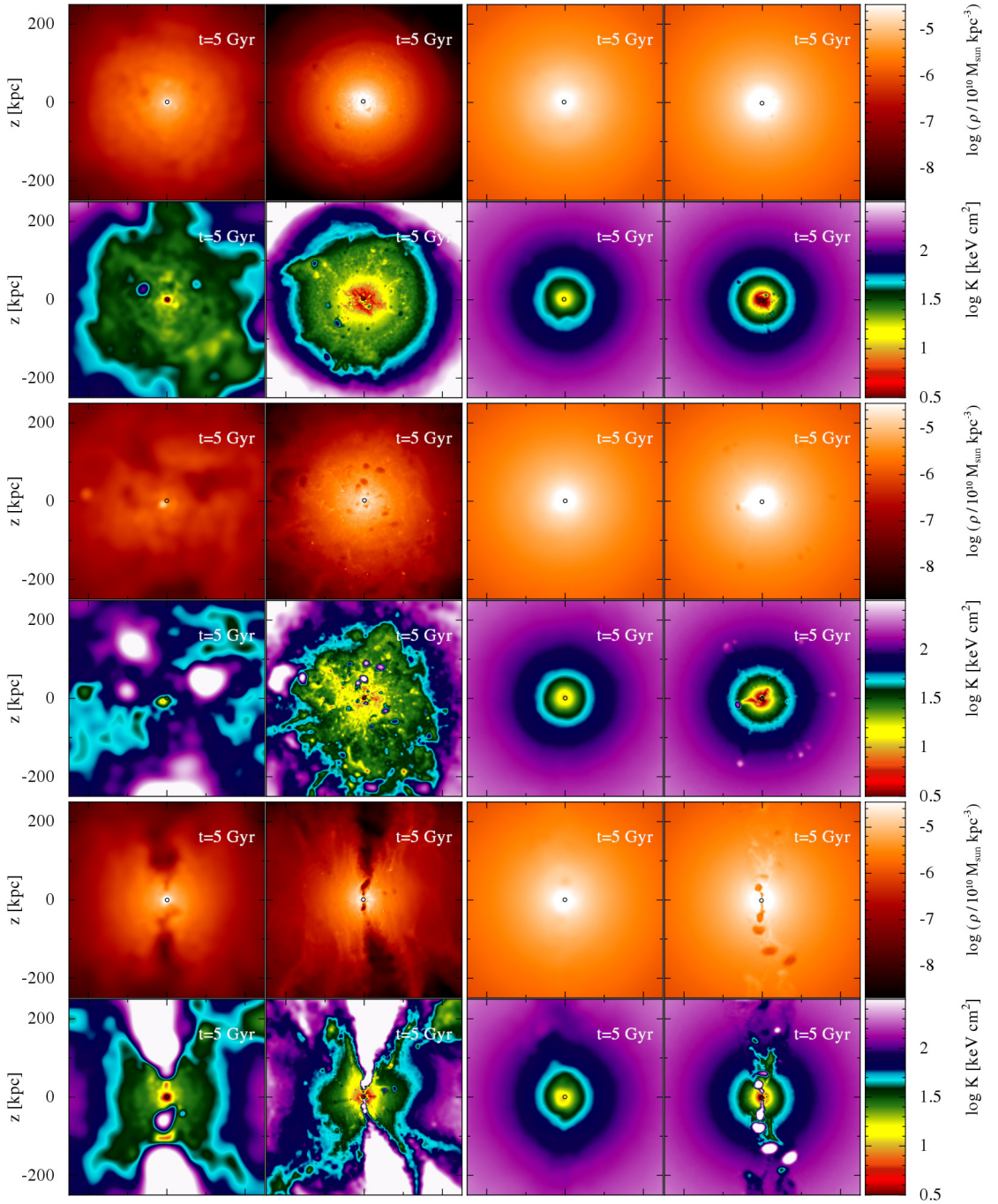

Figure 5.35: Rendered gas density (upper panels) and entropy (lower panels) at $t = 5\,\mathrm{Gyr}$ for the GG and LC objects (left and right columns respectively) simulated at low (left panels) and high (right panels) resolutions for isotropic, RV and FV feedback top to bottom. Images show the projected density within slices of dimensions $500\mathrm{kpc} \times 500\mathrm{kpc} \times 100\mathrm{kpc}$, the BH position is indicated by a black circle.

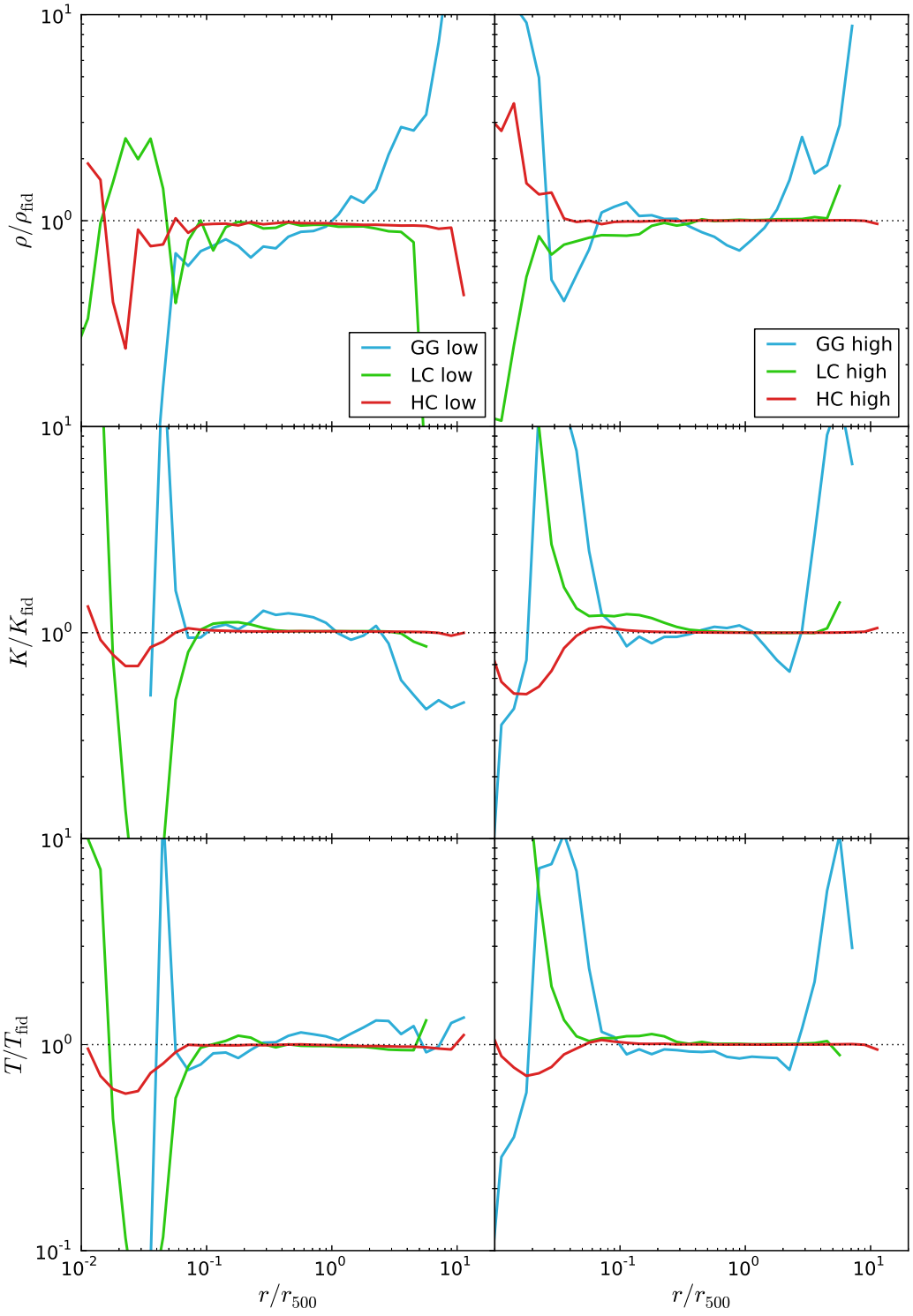

Figure 5.36: Final density (top), entropy (middle) and temperature (bottom) profiles for the isotropic hybrid feedback model at low (left column) and high (right column) resolution as a ratio of the fiducial isotropic feedback for the GG, LC and HC objects evaluated at $t = 10\,\mathrm{Gyr}$.

dimensions $500\mathrm{kpc}\times500\mathrm{kpc}\times100\mathrm{kpc}$, the BH position is indicated by a black circle. The increased level of detail in the high resolution simulations is apparent, although the key features such as aligned jets, bubbles and cleared-out chimneys are found at all simulation levels.

5.5.1 Isotropic hybrid feedback

We begin by analysing the impact of changing the resolution in the isotropic hybrid AGN model simulation. Fig. 5.36 shows the final density (top), entropy (middle) and temperature (bottom) profiles for low and high resolutions as a ratio of the fiducial resolution simulation in the left and right columns respectively, for the GG, LC and HC objects.

It is apparent that the resolution effects are largest for the GG models, having a decreasing impact with larger cluster mass. However, for the GG object there is an effect for the majority of the gas, as the change in resolution introduces significant changes in the core region ($r < 0.5\,r_{500}$) and the periphery of the group ($r > 2\,r_{500}$). The centre of the GG object is cleared more effectively in the low resolution simulation, leading to a low density void bounded by hot gas. As the gas profiles at all resolution levels are similar we find that the gas properties in the isotropic simulations are fairly converged.

Considering now the stellar mass formed during the simulation (not shown) we find in the lower mass (GG and LC) objects that increasing the number of particles leads to higher star formation rates. This follows the trend for increased star formation in the higher resolution simulations due to better simulation of over-densities in the gas (as discussed in Chapter 3 Section 3.4.1). The HC object, however produces less stars in the higher resolution simulation as the winds are confined to lower radii (not shown).

Generically, the final BH mass and wind radii exhibit more complex patterns which we do not investigate fully, however the variations are small and therefore do not significantly alter our conclusions. One exception to this is the final BH mass in the LC object which falls consistently for increasing resolution (with a factor of two change from low to high resolution) as the cold core is smaller and the majority of the central gas is therefore warmer and more diffuse.

5.5.2 Anisotropic hybrid feedback

The star formation and BH mass for the anisotropic models are not discussed in detail as the combination of competing effects is highly complex, however we note that the variations with resolution are typically not severe. One exception to this generalisation is that the FV simulations are more strongly resolution dependent in terms of the level of star

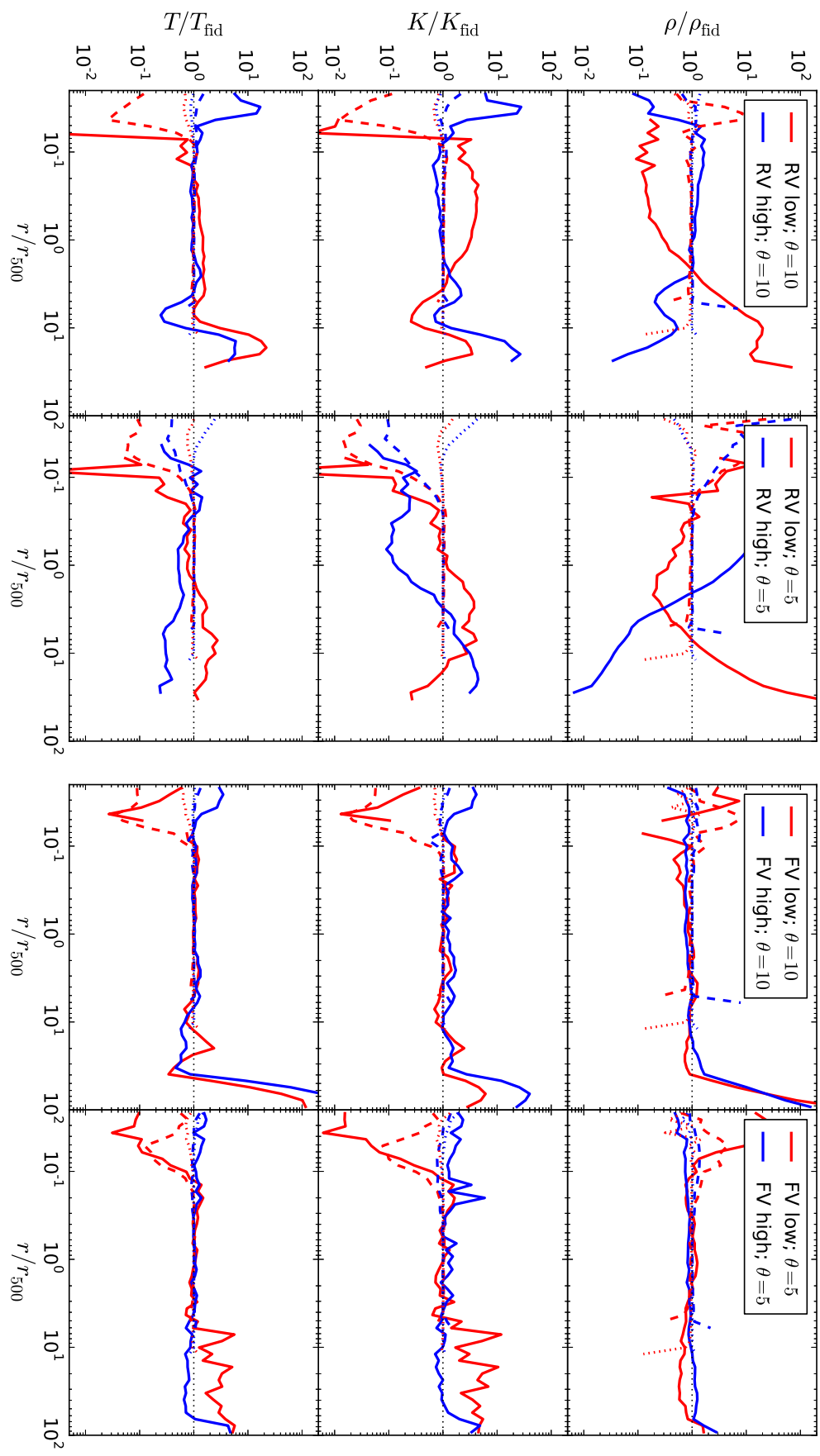

Figure 5.37: Final density profile (top row), entropy (middle row) and temperature (bottom row) profiles for different resolutions as a ratio of the respective fiducial model profile for fixed (left panel) and random (right panel) jet geometries. The left (right) column of each panel shows results for the low (high) density simulations. Profiles for the GG, LC and HC object are shown as solid, dashed and dotted lines respectively.

formation and final BH mass obtained which can vary as much as an order of magnitude.

Fiducial jet geometry

Fig. 5.37 shows the final density profile (top row), entropy (middle row) and temperature (bottom row) profiles for each group and cluster object at different resolutions as a ratio of the respective fiducial model profile for random (left panel) and fixed (right panel) jet geometries. The left (right) column of each panel shows results for the low (high) density simulations. As found for the isotropic feedback models, the gas in each of the fiducial anisotropic simulations is fairly well resolved as the majority of the cluster profiles are converged at most radii.

An interesting deviation from the similarity in profiles is the large discrepancy between the low and intermediate (fiducial) resolution GG RV simulations. Despite this large variation, the intermediate and higher resolution simulations appear well converged indicating that our previous results are sound. The under-resolved feedback presents itself in this model as a reduced (increased) gas density at low (high) radii as the AGN outflows interact with and blow out more gas. The high resolution simulation has the opposite effect at large radii as it interacts less with the IGM. Another feature of note is that the low resolution LC object has a lower entropy core in both the RV and FV simulations.

We note that the majority of deviations again occur at the core and outer edges where the profiles are most sensitive and the least gas is located; we therefore conclude that the gas is broadly converged in these simulations. However, as previously discussed this is not the case for the BH and stellar masses which are not converged. Due to the complexity involved in this analysis we leave the investigation of the detailed processes at play for further study.

Narrow jet opening angle

In order to gauge the level at which the resolution of our fiducial simulations may have influenced our findings, we perform additional simulations at high and low resolution of the narrow jet hybrid AGN model ($\theta_{\rm J} = 5\,^{\circ}$; $r_{\rm J,min} = 0$) as it poses a strong test for the spatial resolution. The gas property profiles for these simulations are shown in the right columns of each panel in Fig. 5.37.

The higher resolution simulations form narrower bubbles which escape the group more efficiently, causing less disruption and heating to the IGM. Correspondingly, the low resolution simulations result in more gas redistributing to higher radii. The RV simulations are far less well resolved than the corresponding fiducial opening angle simulations for every (GG, LC, HC) object, showing that the numerical resolution was preventing

the narrower jets and their interaction with ambient gas from being properly represented in the fiducial simulations. The inadequate resolution may be one reason for the poor agreement with similar grid-based simulations of AGN jets.

The high resolution FV simulations are very similar to the fiducial jet geometry findings. This is in agreement with our earlier results which found that the models with fixed jets are less sensitive to parameter variations.

5.6 Discussion and conclusions

Simulations of the fiducial hybrid AGN model were studied and we found them to be successful in forming winds which travelled further in the ICM and reduced the rate at which the gas in the GG and cluster objects cooled. By including the central quasar-mode heating component, the spurious accretion encountered in Chapter 4 was reduced significantly, if not eliminated, leading to a more stable model. Despite these improvements, the hybrid AGN method gives few substantial improvements over the simpler isotropic heating (SAGN) model aside from the improved morphological characteristics (bubble features).

Through varying parameters of the hybrid AGN model, we find several key results

- The ICM in the HC object is insensitive to changes in the majority of model parameters, however the levels of star formation and BH mass can be significantly affected.

- The distance to which AGN winds reach has a large impact on the group/cluster gas profiles as well as the star formation and level of accretion on to the BH

- Winds with larger ranges increase the strength of AGN feedback as the particles cluster and travel farther through the group; this may be achieved either by narrowing the jet opening angle or increasing the minimum radius.

- Increasing the length of the AGN duty cycle means that the winds interact with more gas as outflows are larger and hotter. This effect is also linked to the winds on short time intervals forming trickle jets whilst the longer time intervals fragment into bubbles which follow less defined paths.

- Longer time interval jets behave similarly to bubbles, therefore their effect is similar in the FV and RV simulations and travel less far through the ICM due to increased interaction with the gas.

- Strong AGN winds which interact with more gas form more stars through positive feedback as they compress more of the ambient gas. RV simulations therefore cause higher star formation than similar FV simulations, whilst wider jets and longer time interval jets likewise form more stars.

- Due to the interplay between winds heating the gas halo (slowing cooling) and compressing it to form stars, varying many of the moel properties do not result in clear trends in the final BH and stellar masses.

- Increasing the mechanical coupling efficiency raises the energy budget for feedback through the jet mode, this typically results in stronger heating of the group and clusters, raising the entropy, lowering the density and resulting in less star formation.

- Varying the radiative coupling efficiency does not yield simple trends in the gas properties, however the stronger quasar-mode heating is more effective at disrupting the spurious cold knots and reducing artificial accretion

- The star formation and BH accretion in the group and cluster objects simulated with hybrid feedback are dependent on the resolution used. The variation, however do not show clear trends as multiple non-linear effects interact. The level of gas clumping and the prevalence of cold blobs is one such effect. Despite this, the effects within a given resolution are likely to be genuine.

- Group and cluster gas properties are largely converged between resolution levels outside of the core region despite the discrepancy in the BH and stellar masses, suggesting that the changes are only important on small scales.

The hybrid AGN model presented is therefore at least as successful as contemporary AGN models in group and cluster scales. The feedback continues to suffer from a tuning problem whereby outflows are over-powerful in lower mass objects and do not provide sufficient feedback on rich cluster scales, however this may improve with additional resolution. The inclusion of the central quasar component acts to make the model more numerically stable as well as dispersing the artificial cold knots of gas commonly seen in SPH simulations of groups and clusters without producing central entropy inversions.

Direct comparison with observations is difficult due to the low number of objects considered in this study, however our findings are valid for drawing broader conclusions. We find that bubble and jet feedback is successful in explaining observational features such as radio lobes and X-ray cavities. Furthermore, we find that the galaxy groups are highly sensitive to AGN activity (first discussed in Chapter 4 Section 4.3) as the directional outflows continue to interact with large amounts of the IGM. Our findings also indicate that

compressions in the ICM due to feedback events may seed star formation, although possibly due to numerical errors (due to the spurious SPH surface tension), this source of positive feedback could be investigated observationally by future studies.

A key finding of this work (and that of Chapter 4) is that the uncertainties involved in current cosmological AGN models mean that it is not yet possible to reliably investigate interesting properties of the AGN such as activity timescales, the temperature of heated gas, and detailed accretion rates.

Chapter 6

Summary and future work

If I have ever made any valuable discoveries, it has been owing more to patient attention, than to any other talent.

SIR ISAAC NEWTON

The leading BH model in use in cosmological simulations was pioneered by Springel et al. (2005) and Di Matteo et al. (2005, 2008), it makes use of the simple Bondi accretion (Hoyle & Lyttleton 1939; Bondi & Hoyle 1944; Bondi 1952) model and the numerically-convenient kernel-weighted feedback method. We analyse this and other existing models (Booth & Schaye 2009 and a model derived from Power et al. 2011) as well as novel feedback methods in a range of environments in order to better understand and improve the numerical modelling of AGN feedback.

Despite ongoing work (e.g. Debuhr et al. 2011; Fanidakis et al. 2011; Hobbs et al. 2012; Planelles 2012; Vogelsberger et al. 2013) the current generation of AGN models such as those incorporated in this study are unable to perform well over the full mass range in cosmological objects, from dwarf galaxies to clusters. It is therefore important that the development of a flexible, resolution independent AGN feedback model continues.

We began in Chapter 1 outlining and summarising previous research and theory behind AGN and galaxy formation, before discussing the relevant numerical methods and models appropriate to our work in Chapter 2.

In Chapter 3 we presented results from simulations of isolated and merging disc galaxies simulated with different AGN and supernovae models. In this study, we found supernova feedback dominates the star formation suppression in isolated Milky-Way-mass model disc galaxies, whereas even strong AGN feedback has no impact for any of the

tested models. However, in merging galaxies the picture reverses and AGN feedback plays a much larger role. Strong AGN heating may even eliminate the starburst entirely. We found that the most important factor determining the strength of AGN feedback on the host galaxy is the temperature to which gas is heated and correspondingly the feedback mass loading. We also found that the numerical resolution strongly affects the black hole mass due to under-resolved feedback and accretion. Concerning the interaction between AGN and supernova feedback, we found that they act largely independently; this is an apparent contradiction to the recent work of Booth & Schaye (2013).

We then went on in Chapter 4 to apply the same models to galaxy group and cluster scales as well as presenting a new anisotropic AGN model. We found strong feedback models lower (raise) the central density (entropy) in a galaxy group, but provide insufficient energy to halt cooling in the higher mass clusters. However, the weaker kernel-weighted feedback model is unable to halt the cooling even in the lowest mass object and has an even less significant impact on the cluster gas profiles. Generically the stock AGN models do not balance the amount of energy lost through cooling over the course of the simulation in any object; either providing too much or too little feedback. We found that the level of BH growth observed in tests of the anisotropic feedback model were not linked to the large-scale properties of the cluster. Detailed analysis found that a large fraction of the accretion is chaotic and of a numerical origin, with anomalously high rates linked to the accretion of cold lumps of gas. The cold gas was found to be formed by outflowing winds compressing gas and/or lifting it to larger radii causing it to cool rapidly, falling back into the central region. However, the cold blobs are artificially stablised by the spurious surface pressure inherent in the formulation of SPH used here; we therefore wish to reduce the impact of this numerical artefact

In Chapter 5 we presented and analysed in detail, a novel hybrid AGN model acting on groups and clusters for a fiducial jet geometry, before performing a detailed interrogation of the various aspects of the model. Firstly, we note that by including the central quasar-mode heating component, the spurious accretion encountered in Chapter 4 was reduced significantly, if not eliminated. We found across the different models and objects simulated, the distance to which AGN winds reach has a large impact on the group/cluster gas profiles as well as the star formation and final BH mass. When imposing an AGN duty cycle, a longer time between feedback events means that the AGN winds interact with more gas as outflows are larger and hotter. This effect is also linked to the winds on short time intervals forming ‘trickle’ jets, whilst the longer time intervals fragment into bubbles which follow less defined paths. Generically, models which drive strong AGN winds, which interact with more gas, result in higher levels of star formation through positive feedback as they compress more of the ambient gas. The randomly-oriented jet

simulations therefore cause higher star formation than the corresponding fixed-axis jet simulations, whilst wider jets and longer time interval jets likewise form more stars.

Looking now to future work, we note that there is a growing consensus that the standard SPH algorithm has flaws which are affecting the results of modern high resolution hydrodynamical simulations (e.g. Ritchie & Thomas 2001; Agertz et al. 2007; Read et al. 2010; Read & Hayfield 2012; Sijacki et al. 2012; Saitoh & Makino 2013). As we have noted, the spurious surface tension is particularly troublesome for simulations including AGN feedback through the use of a BH particle as cold clumps gather around it. Therefore, it is important for future work that this issue is resolved or reduced before further inroads can be made into improving the current generation of AGN models in cosmological simulations.

On galaxy-scales, future work would include the hybrid model presented here, however performing such simulations would necessitate a self-consistent treatment of the jet axis orientation rather than the crude approximations used here. An un-physical jet orientation could otherwise lead to the destruction of a disc galaxy.

As we found that our investigation of the jet opening angle was limited by the SPH smoothing, performing simulations at still higher resolution would be of interest to see if more agreement could be found with grid-based simulations (e.g. Gaspari et al. 2011). Similarly, investigations utilising mechanical feedback could be investigated as not only would they give greater control over the jet/wind direction, but current observations suggest that the majority of AGN energy is thought to be deposited in this fashion (McNamara & Nulsen 2007; we have so far implicitly assumed it has been thermalised on sub-grid scales).

On galaxy group and cluster scales, future work investigating the role of AGN feedback in the maintenance mode would be improved by the inclusion of conduction, which is thought to be important in redistributing energy (e.g. Bertschinger & Meiksin 1986; Bregman & David 1988; Dolag et al. 2004; Ruszkowski et al. 2011; Smith et al. 2013). The incorporation of conduction would be complemented by the modelling of magnetic fields, which can either inhibit or enhance thermal conduction depending on the orientation of the field lines. The simulation of a central radio AGN distorting the field with outflows would therefore be particularly interesting.

Ultimately, performing full cosmological and high resolution zoom simulations would give better statistics on simulated objects and provide more realistic objects for study. We therefore aim to perform such simulations as an investigation into AGN modelling, to complement the high resolution idealised simulations.

Bibliography

Aarseth S. J., Turner E. L., Gott, III J. R., 1979, ApJ, 228, 664

Agertz O. et al., 2007, MNRAS, 380, 963

Aghanim N., Majumdar S., Silk J., 2008, Reports on Progress in Physics, 71, 066902

Alexander D. M., Hickox R. C., 2012, New Astronomy Reviews, 56, 93

Appel A., 1985, SIAM Journal on Scientific and Statistical Computing, 6, 85

Babul A., Sharma P., Reynolds C. S., 2013, ApJ, 768, 11

Balsara D. S., 1995, Journal of Computational Physics, 121, 357

Barnes J., Hut P., 1986, Nature, 324, 446

Baumann D. et al., 2009, in American Institute of Physics Conference Series, Vol. 1141, American Institute of Physics Conference Series, Dodelson S., Baumann D., Cooray A., Dunkley J., Fraisse A., Jackson M. G., Kogut A., Krauss L., Zaldarriaga M., Smith K., eds., pp. 10–120

Bellovary J., Volonteri M., Governato F., Shen S., Quinn T., Wadsley J., 2011, ApJ, 742, 13

Bennert V. N., Auger M. W., Treu T., Woo J.-H., Malkan M. A., 2011, ApJ, 742, 107

Bennett C. L. et al., 2012, ArXiv e-prints

Benson A. J., Bower R. G., Frenk C. S., Lacey C. G., Baugh C. M., Cole S., 2003, ApJ, 599, 38

Benson A. J. et al., 2013, MNRAS, 428, 1774

Bertschinger E., Meiksin A., 1986, ApJL, 306, L1

Binney J., 2004, MNRAS, 347, 1093

Binney J., Tremaine S., 1987, Galactic dynamics, Binney, J. & Tremaine, S., ed.

Bîrzan L., Rafferty D. A., McNamara B. R., Wise M. W., Nulsen P. E. J., 2004, ApJ, 607, 800

Blandford R. D., Znajek R. L., 1977, MNRAS, 179, 433

Blumenthal G. R., Faber S. M., Primack J. R., Rees M. J., 1984, Nature, 311, 517

Blumenthal G. R., Faber S. M., Primack J. R., Rees M. J., 1985, Nature, 313, 72

Böhringer H. et al., 2007, A&A, 469, 363

Bois M. et al., 2011, MNRAS, 416, 1654

Bondi H., 1952, MNRAS, 112, 195

Bondi H., Hoyle F., 1944, MNRAS, 104, 273

Booth C. M., Schaye J., 2009, MNRAS, 398, 53

Booth C. M., Schaye J., 2013, Nature Scientific Reports

Borgani S., Kravtsov A., 2009, ArXiv e-prints

Bower R. G., Benson A. J., Crain R. A., 2012, MNRAS, 422, 2816

Bower R. G., Benson A. J., Malbon R., Helly J. C., Frenk C. S., Baugh C. M., Cole S., Lacey C. G., 2006, MNRAS, 370, 645

Bregman J. N., David L. P., 1988, ApJ, 326, 639

Bridle A. H., Perley R. A., 1984, ARA&A, 22, 319

Bryan G. L., Norman M. L., Stone J. M., Cen R., Ostriker J. P., 1995, Computer Physics Communications, 89, 149

Bryan S. E., Kay S. T., Duffy A. R., Schaye J., Vecchia C. D., Booth C. M., 2013, MNRAS, 429, 3316

Campanelli M., Lousto C., Zlochower Y., Merritt D., 2007, ApJL, 659, L5

Campbell H. et al., 2013, ApJ, 763, 88

Cattaneo A., Teyssier R., 2007, MNRAS, 376, 1547

Cavagnolo K. W., McNamara B. R., Nulsen P. E. J., Carilli C. L., Jones C., Bîrzan L., 2010, ApJ, 720, 1066

Chomiuk L., Povich M. S., 2011, AJ, 142, 197

Churazov E., Sazonov S., Sunyaev R., Forman W., Jones C., Böhringer H., 2005, MNRAS, 363, L91

Colella P., Woodward P. R., 1984, Journal of Computational Physics, 54, 174

Couchman H. M. P., 1991, ApJL, 368, L23

Couchman H. M. P., Thomas P. A., Pearce F. R., 1995, ApJ, 452, 797

Croston J. H. et al., 2008, A&A, 487, 431

Croton D. J. et al., 2006, MNRAS, 365, 11

Cullen L., Dehnen W., 2010, MNRAS, 408, 669

Dalla Vecchia C., Bower R. G., Theuns T., Balogh M. L., Mazzotta P., Frenk C. S., 2004, MNRAS, 355, 995

Dalla Vecchia C., Schaye J., 2008, MNRAS, 387, 1431

Dalla Vecchia C., Schaye J., 2012, MNRAS, 426, 140

Davis M., Efstathiou G., Frenk C. S., White S. D. M., 1985, ApJ, 292, 371

Debuhr J., Quataert E., Ma C., Hopkins P., 2010, MNRAS, 406, L55

Debuhr J., Quataert E., Ma C.-P., 2011, MNRAS, 412, 1341

DeGraf C., Di Matteo T., Khandai N., Croft R., 2012, ApJL, 755, L8

Dehnen W., Aly H., 2012, MNRAS, 425, 1068

Di Benedetto G. P., 2013, MNRAS, 430, 546

Di Matteo T., Colberg J., Springel V., Hernquist L., Sijacki D., 2008, ApJ, 676, 33

Di Matteo T., Springel V., Hernquist L., 2005, Nature, 433, 604

Dolag K., Jubelgas M., Springel V., Borgani S., Rasia E., 2004, ApJL, 606, L97

Dubois Y., Devriendt J., Slyz A., Teyssier R., 2012, MNRAS, 420, 2662

Duffy A. R., Schaye J., Kay S. T., Dalla Vecchia C., 2008, MNRAS, 390, L64

Durier F., Dalla Vecchia C., 2012, MNRAS, 419, 465

Efstathiou G., Davis M., White S. D. M., Frenk C. S., 1985, ApJS, 57, 241

Einasto J., Saar E., Kaasik A., Chernin A. D., 1974, Nature, 252, 111

Ekers R. D., Fanti R., Lari C., Parma P., 1978, Nature, 276, 588

Emsellem E. et al., 2007, MNRAS, 379, 401

Fabian A. C., 1999, MNRAS, 308, L39

Fabian A. C., 2012, ARA&A, 50, 455

Fabian A. C., Sanders J. S., Taylor G. B., Allen S. W., Crawford C. S., Johnstone R. M., Iwasawa K., 2006, MNRAS, 366, 417

Fabjan D., Borgani S., Tornatore L., Saro A., Murante G., Dolag K., 2010, MNRAS, 401, 1670

Fan X. et al., 2001, AJ, 122, 2833

Fanaroff B. L., Riley J. M., 1974, MNRAS, 167, 31P

Fanidakis N., Baugh C. M., Benson A. J., Bower R. G., Cole S., Done C., Frenk C. S., 2011, MNRAS, 410, 53

Fender R., Belloni T., 2012, Science, 337, 540

Ferrarese L., Merritt D., 2000, ApJL, 539, L9

Fluke C. J., Barnes D. G., Barsdell B. R., Hassan A. H., 2011, PASA, 28, 15

Freedman W. L. et al., 2001, ApJ, 553, 47

Frenk C. S., White S. D. M., 2012, Annalen der Physik, 524, 507

Frenk C. S. et al., 1999, ApJ, 525, 554

Fryxell B. et al., 2000, ApJS, 131, 273

Gaspari M., Brighenti F., Ruszkowski M., 2013, Astronomische Nachrichten, 334, 394

Gaspari M., Melioli C., Brighenti F., D'Ercole A., 2011, MNRAS, 411, 349

Gebhardt K. et al., 2000, ApJL, 543, L5

Genzel R., Eisenhauer F., Gillessen S., 2010, Reviews of Modern Physics, 82, 3121

Gingold R. A., Monaghan J. J., 1977, MNRAS, 181, 375

Giodini S., Lovisari L., Pointecouteau E., Ettori S., Reiprich T. H., Hoekstra H., 2013, ArXiv e-prints

Giodini S. et al., 2009, ApJ, 703, 982

Godunov S. K., 1959, Matematicheskii Sbornik, 89, 271

Goldberg D. M., Strauss M. A., 1998, ApJ, 495, 29

Guo Q. et al., 2011, MNRAS, 413, 101

Hahn O., Abel T., Kaehler R., 2012, ArXiv e-prints

Häring N., Rix H.-W., 2004, ApJL, 604, L89

Heinz S., Brüggen M., Young A., Levesque E., 2006, MNRAS, 373, L65

Hernquist L., 1990, ApJ, 356, 359

Hernquist L., 1993, ApJS, 86, 389

Hernquist L., Katz N., 1989, ApJS, 70, 419

Heß S., Springel V., 2010, MNRAS, 406, 2289

Hobbs A., Power C., Nayakshin S., King A. R., 2012, MNRAS, 421, 3443

Hockney R., Goel S., Eastwood J., 1973, Chemical Physics Letters, 21, 589

Hockney R. W., Eastwood J. W., 1981, Computer Simulation Using Particles

Hoeft M., Brüggen M., 2004, ApJ, 617, 896

Hopkins P. F., 2013, MNRAS, 428, 2840

Hopkins P. F., Elvis M., 2010, MNRAS, 401, 7

Hoyle F., Lyttleton R. A., 1939, in Proceedings of the Cambridge Philosophical Society, Vol. 35, Proceedings of the Cambridge Philosophical Society, pp. 405–+

Hudson D. S., Mittal R., Reiprich T. H., Nulsen P. E. J., Andernach H., Sarazin C. L., 2010, A&A, 513, A37

Ishibashi W., Fabian A. C., 2012, MNRAS, 427, 2998

Jahnke K., Macciò A. V., 2011, ApJ, 734, 92

Johansson P. H., Naab T., Burkert A., 2009, ApJ, 690, 802

Kaiser N., 1986, MNRAS, 222, 323

Kato S., Fukue J., Mineshige S., eds., 1998, Black-hole accretion disks

Katz N., Weinberg D. H., Hernquist L., 1996, ApJS, 105, 19

Kauffmann G., Haehnelt M., 2000, MNRAS, 311, 576

Kay S. T., 2004, MNRAS, 347, L13

Kay S. T., Thomas P. A., Theuns T., 2003, MNRAS, 343, 608

Kennicutt R. C., Evans N. J., 2012, ARA&A, 50, 531

Kennicutt, Jr. R. C., 1998, ApJ, 498, 541

Khalatyan A., Cattaneo A., Schramm M., Gottlöber S., Steinmetz M., Wisotzki L., 2008, MNRAS, 387, 13

King A., 2003, ApJL, 596, L27

Klypin A. A., Shandarin S. F., 1983, MNRAS, 204, 891

Kormendy J., Bender R., 2011, Nature, 469, 377

Kormendy J., Ho L. C., 2013, ArXiv e-prints

Kurk J. D. et al., 2007, ApJ, 669, 32

Laganá T. F., Martinet N., Durret F., Lima Neto G. B., Maughan B., Zhang Y.-Y., 2013, A&A, 555, A66

Leauthaud A. et al., 2012, ApJ, 744, 159

Li Y., Mo H. J., van den Bosch F. C., Lin W. P., 2007, MNRAS, 379, 689

Lovell M. R. et al., 2012, MNRAS, 420, 2318

Magorrian J. et al., 1998, AJ, 115, 2285

McConnell N. J., Ma C.-P., 2013, ApJ, 764, 184

McNamara B. R., Nulsen P. E. J., 2007, ARA&A, 45, 117

McNamara B. R., Nulsen P. E. J., 2012, New Journal of Physics, 14, 055023

Merloni A. et al., 2010, ApJ, 708, 137

Merritt D., Ekers R. D., 2002, Science, 297, 1310

Mihos J. C., Hernquist L., 1996, ApJ, 464, 641

Mo H. J., Mao S., White S. D. M., 1998, MNRAS, 295, 319

Monaghan J., 1997, Journal of Computational Physics, 136, 298

Monaghan J., Gingold R., 1983, Journal of Computational Physics, 52, 374

Monaghan J. J., 1992, ARA&A, 30, 543

Mortlock D. J. et al., 2011, Nature, 474, 616

Moster B. P., Macciò A. V., Somerville R. S., 2012, ArXiv e-prints, 1210.5522

Moster B. P., Maccio' A. V., Somerville R. S., Naab T., Cox T. J., 2011, ArXiv e-prints

Moster B. P., Somerville R. S., Maulbetsch C., van den Bosch F. C., Macciò A. V., Naab T., Oser L., 2010, ApJ, 710, 903

Muldrew S. I., Pearce F. R., Power C., 2013, ArXiv e-prints

Navarro J. F., Eke V. R., Frenk C. S., 1996a, MNRAS, 283, L72

Navarro J. F., Frenk C. S., White S. D. M., 1996b, ApJ, 462, 563

Ogiya G., Mori M., 2012, ArXiv e-prints

O'Shea B. W., Bryan G., Bordner J., Norman M. L., Abel T., Harkness R., Kritsuk A., 2004, ArXiv e-prints, 0403044

Ostriker J. P., Peebles P. J. E., 1973, ApJ, 186, 467

Ostriker J. P., Peebles P. J. E., Yahil A., 1974, ApJL, 193, L1

Peebles P. J. E., 1967, ApJ, 147, 859

Peebles P. J. E., 1984, ApJ, 277, 470

Penzias A. A., Wilson R. W., 1965, ApJ, 142, 419

Percival W. J. et al., 2010, MNRAS, 401, 2148

Planck Collaboration et al., 2013a, ArXiv e-prints

Planck Collaboration et al., 2013b, ArXiv e-prints

Planck Collaboration et al., 2013c, A&A, 550, A131

Planelles S., 2012, in Galaxy Clusters as Giant Cosmic Laboratories, Ness J.-U., ed., p. 44

Portegies Zwart S. F., Belleman R. G., Geldof P. M., 2007, New Astronomy, 12, 641

Power C., Navarro J. F., Jenkins A., Frenk C. S., White S. D. M., Springel V., Stadel J., Quinn T., 2003, MNRAS, 338, 14

Power C., Nayakshin S., King A., 2011, MNRAS, 412, 269

Power C., Read J. I., Hobbs A., 2013, ArXiv e-prints

Pratt G. W. et al., 2010, A&A, 511, A85

Price D. J., 2012, Journal of Computational Physics, 231, 759

Puchwein E., Sijacki D., Springel V., 2008, ApJL, 687, L53

Read J. I., Gilmore G., 2005, MNRAS, 356, 107

Read J. I., Hayfield T., 2012, MNRAS, 422, 3037

Read J. I., Hayfield T., Agertz O., 2010, MNRAS, 405, 1513

Ritchie B. W., Thomas P. A., 2001, MNRAS, 323, 743

Robertson B., Hernquist L., Cox T. J., Di Matteo T., Hopkins P. F., Martini P., Springel V., 2006, ApJ, 641, 90

Rubin V. C., Ford, Jr. W. K., 1970, ApJ, 159, 379

Russell H. R., McNamara B. R., Edge A. C., Hogan M. T., Main R. A., Vantyghem A. N., 2013, MNRAS

Ruszkowski M., Lee D., Brüggen M., Parrish I., Oh S. P., 2011, ApJ, 740, 81

Saitoh T. R., Makino J., 2009, ApJL, 697, L99

Saitoh T. R., Makino J., 2013, ApJ, 768, 44

Sandage A., Tammann G. A., Saha A., Reindl B., Macchetto F. D., Panagia N., 2006, ApJ, 653, 843

Schaye J., Dalla Vecchia C., 2008, MNRAS, 383, 1210

Schaye J. et al., 2010, MNRAS, 402, 1536

Schneider A., Smith R. E., Reed D., 2013, ArXiv e-prints

Shakura N. I., Sunyaev R. A., 1973, A&A, 24, 337

Sijacki D., Springel V., 2006, MNRAS, 366, 397

Sijacki D., Springel V., Di Matteo T., Hernquist L., 2007, MNRAS, 380, 877

Sijacki D., Vogelsberger M., Kereš D., Springel V., Hernquist L., 2012, MNRAS, 424, 2999

Silk J., 1968, ApJ, 151, 459

Silk J., Rees M. J., 1998, A&A, 331, L1

Sinha M., Holley-Bockelmann K., 2009, MNRAS, 397, 190

Smith B. D., O'Shea B. W., Voit G. M., Ventimiglia D., Skillman S. W., 2013, ArXiv e-prints

Springel V., 2005, MNRAS, 364, 1105

Springel V., 2010a, MNRAS, 401, 791

Springel V., 2010b, ARA&A, 48, 391

Springel V., Di Matteo T., Hernquist L., 2005, MNRAS, 361, 776

Springel V., White S. D. M., 1999, MNRAS, 307, 162

Story K. T. et al., 2012, ArXiv e-prints

Sugimoto D., Chikada Y., Makino J., Ito T., Ebisuzaki T., Umemura M., 1990, Nature, 345, 33

Sunyaev R. A., Zeldovich Y. B., 1970, Astrophysics and Space Science, 7, 3

Sutherland R. S., Dopita M. A., 1993, ApJS, 88, 253

Tasker E. J., Brunino R., Mitchell N. L., Michielsen D., Hopton S., Pearce F. R., Bryan G. L., Theuns T., 2008, MNRAS, 390, 1267

Thomas P. A., Couchman H. M. P., 1992, MNRAS, 257, 11

Tormen G., Bouchet F. R., White S. D. M., 1997, MNRAS, 286, 865

Tremaine S. et al., 2002, ApJ, 574, 740

van Leer B., 1984, SIAM Journal on Scientific and Statistical Computing, 5, 1

van Leer B., 2006, Communications in Computational Physics, 1, 192

Vogelsberger M., Genel S., Sijacki D., Torrey P., Springel V., Hernquist L., 2013, ArXiv e-prints

Voit G. M., 2005, Reviews of Modern Physics, 77, 207

Voit G. M., Kay S. T., Bryan G. L., 2005, MNRAS, 364, 909

Volonteri M., Natarajan P., Gültekin K., 2011, ApJ, 737, 50

White S. D. M., Frenk C. S., 1991, ApJ, 379, 52

White S. D. M., Frenk C. S., Davis M., 1983, ApJL, 274, L1

White S. D. M., Rees M. J., 1978, MNRAS, 183, 341

Wurster J., Thacker R. J., 2013, MNRAS, 431, 539

Xu G., 1995, ApJS, 98, 355

Yu Q., Tremaine S., 2002, MNRAS, 335, 965

Zwicky F., 1933, Helvetica Physica Acta, 6, 110